

**Optimised Part Programs for Excimer Laser-Ablation
Micromachining Directly from 3D CAD Models**

by

Emir Mutapcic

A thesis submitted to the Industrial Research Institute Swinburne, Faculty
of Engineering and Industrial Sciences, in fulfillment of the requirements
for the degree of Doctor of Philosophy

SWINBURNE UNIVERSITY OF TECHNOLOGY
HAWTHORN, VICTORIA
AUSTRALIA
October 2006

Abstract

Fabrication of a 3D structure and surface texture using excimer laser mask projection ablation processes typically requires the machine operator to develop a specific NC part program for the desired structure geometry, and also incorporate appropriate machine parameters to achieve the desired surface finish. The capability of the laser ablation process could therefore be significantly improved by developing a CAD/CAM system that automatically generates the NC part program using the 3D information of the CAD model of the desired structure. Accordingly, the focus of this research was to develop such a system – that is, an effective CAD/CAM system specifically for excimer laser mask projection micromachining tools.

To meet these requirements, a unique combination of commercially available systems was used to develop the new CAD/CAM system. The systems used comprised of a computer aided, feature based parametric design system (SolidWorks®), together with its extended programming capabilities based on Automated Programming Interface (API) functions for Windows applications, and Visual Basic (VB) 6.0 programming utilities. The system's algorithms use a novel methodology to extract the 3D geometry of a microstructure. Two different techniques have been developed to extract the 3D data. First, where 3D geometry information from a CAD model was defined as a Stereolithography (STL) file, and second, where this information has been contained in a set of bit-map (BMP) files that represent a sliced or layered structure of a CAD model. Based on this, first an algorithm to create NC part programs to support Step-and-repeat micromachining technique was developed and then successfully extended to be applicable for another commonly used micromachining method, Workpiece-Dragging technique.

The system's algorithms for both techniques are based on the raster-colour programming technique, resulting in substantially reduced mathematical complexity and computational time. This is the first time this approach has been used to support direct conversion of 3D geometry from a CAD model into an NC part program compatible with the excimer laser CNC controller. 2D mathematical models for controlling edge and stitching errors were also implemented in the system.

An additional technique, named as “Common Nest” has been developed with the aim to enable automatic NC part programming when microstructure design to be

completed successfully, requires use of multiple complex mask patterns as a projection tool instead of just a single square aperture.

The effectiveness of the system was verified by NC part program generation for several 3D microstructures and subsequent machining trials using polycarbonate (PC) and Polyethylene terephthalate (PET), and optimised processing parameters. Excellent agreement was obtained between the laser machined geometries and the microstructure CAD models. The Laser Scanning Confocal Microscope (LSCM) measured the lateral dimensions tolerance of $\pm 2 \mu\text{m}$.

The system was also successfully applied for a practical micro-engineering application, for the development of a microfluidics cell transportation device.

Acknowledgements

This research work is a culmination of a pursuit, which involved the time, and efforts of many people, whom I wish to acknowledge.

I would like to express my sincerest appreciation and gratitude to Dr. Pio Iovenitti and Dr. Jason P. Hayes who have been the primary source of encouragement right from the problem conception stage, to the final write-up of this thesis. This thesis would not have been completed without their guidance, counsel and moral support. I would especially like to thank Professor Erol C. Harvey from IRIS for his help and assistance.

I wish to thank to all my colleagues who encouraged and supported me. They all tried to be helpful and supportive as much as it was possible, but I would like to thank the colleagues who gave me advice about my research project and helped me with my laboratory work. Dr. Karlo Jolic and Andrew Dowling who have discussed all sorts of problems on a number of occasions. Dr Matthew Solomon for his help with the laboratory work and equipment procedure explanations and guidance.

I had the opportunity to visit two major players in my research project field. A world class laser company (Exitech Ltd., Oxford, UK), where I wish to thank Dr. Heather Booth and Miss Ines Bohelaen for sharing their experience and findings on the same topic and showing me their factory and laboratories.

I also visited one of the leading institutes for micro and nano-technologies (Laser Zentrum, Hannover, Germany), and I wish to thank Dr. Frank Mayer and Mr. Temme Thorsten for spending much time on discussing their work on the same topic and showing me around their laboratories.

Some papers in the references were not possible to obtain from the local libraries. I should thank Ms. Fiona O'Donnell for taking care and providing copies of these papers. She always responded promptly and completed her job with high professionalism and no delays.

This research was funded by the CRC for Microtechnology, and I wish to thank the people from CRC as well.

I would also like to especially thank my parents, brother and sister for their inspiration and encouragement, without which this pursuit would have been incomplete.

Contents

List of Figures.....	xii
List of Tables	xix
List of Variables	xx
List of Abbreviations	xxii
Chapter 1. Introduction.....	1
1.1 Background and Significance of the Research	1
1.2 CAD/CAM System Development	2
1.3 Stitching Error Effects	5
1.4 Objectives and Scope of the Research.....	7
1.5 Outline of Thesis	8
Chapter 2. Literature Review	9
2.1 Overview	9
2.2 Background.....	9
2.3 Excimer Laser Ablation Mechanism	10
2.4 Laser Machining Methods.....	17
2.4.1 Mask Projection Design Principles	18
2.4.2 Energy Density.....	19
2.4.3 Image Size.....	20
2.5 Mask Projection Ablation Techniques	21
2.5.1 Machining with Static Mask and Workpiece.....	21
2.5.1.1 Step-and-Repeat Machining.....	24

2.5.1.2	Mask Indexing Technique.....	25
2.5.2	Synchronised Mask Scanning.....	26
2.5.2.1	Machining with Moving Mask.....	28
2.5.2.2	Machining by Moving Workpiece (Workpiece-Dragging)	29
2.5.3	Synchronised Overlay Scanning.....	33
2.6	Serial Scribing (Direct Machining)	34
2.6.1	Bow-Tie Scanning	35
2.6.2	Sync Scan.....	36
2.7	Anvik Corporation HexScan™ Series Laser Projection System	37
2.8	CAD/CAM Systems for Excimer Lasers	38
2.8.1	Other Techniques and CAD/CAM Tools of Relevance	46
2.9	Machining Process Sequence	47
2.10	STL File Generation.....	48
2.11	Slicing Techniques	48
2.12	Summary.....	49
 Chapter 3. Development of a CAD/CAM System For Excimer Laser		
Micromachining		51
3.1	Overview	51
3.2	Motivation	51
3.3	System Requirements	53
3.4	System Concept Design.....	55
3.4.1	Design Module Component	56
3.4.2	“External” CAD Modelling	58
3.4.3	STL File Approach	58
3.4.3.1	Facet Orientation.....	59

3.4.3.2	Vertex to Vertex.....	59
3.4.3.3	Slice File Format.....	59
3.4.3.4	Example of “External” CAD Modelling Process Steps.....	60
3.4.3.5	“Internal” CAD Modelling	62
3.4.3.6	Machining Module Component	62
3.4.4	Bit Map Approach.....	65
3.4.4.1	Raster Graphics.....	65
3.4.4.2	Pixel Colours.....	66
3.4.4.3	Color Patterns Extraction.....	67
3.4.4.4	Scan-Line Polygon Fill Algorithm.....	67
3.4.4.5	Boundary-Fill Algorithm	69
3.4.4.6	Bresenham's Line Drawing Algorithm	69
3.4.4.7	Generalising the Bresenham Algorithm.....	75
3.5	Toolpath Optimisation Algorithms.....	76
3.5.1	Adaptation to Traveling Salesman Problem	76
3.5.2	Left-to-Right	80
3.5.3	Zig-Zag Algorithm.....	81
3.5.4	Star Algorithm	82
3.6	Pulse Minimisation Algorithm	84
3.7	Experimental Set Up and Equipment	89
3.7.1	Design of Experiment Technique	89
3.7.2	Materials	90
3.7.3	Masks	91
3.7.4	Excimer Laser Series 8000 (Exitech Ltd.,UK)	93
3.7.4.1	Excimer Laser Machining.....	94

3.7.5 Laser Scanning Confocal Microscopy	96
3.7.6 Optical Microscopy	99
3.8 Evaluation of the System	100
3.8.1 Step and Repeat Algorithm	102
3.8.2 Workpiece-Dragging Technique	103
3.8.3 Multi-Layer Technique	104
3.8.4 Ramp Removal using Synchronised Mask Scanning Technique	105
3.8.5 Material Database System	106
3.8.6 System Limitations	106
3.9 Summary	106
Chapter 4. Mathematical Model for Edge Error	108
4.1 Overview	108
4.2 Introduction	108
4.3 C.L.A. Definition	109
4.4 Edge Error	110
4.4.1 Algorithm for Determining Minimum Edge Error	116
4.4.2 Experiments to Determine Edge Error For Outside Boundaries	118
4.4.3 Comparison of Theoretical and Experimental Results for Edge Error	118
4.5 Summary	124
Chapter 5. Stitching Errors Correction	126
5.1 Overview	126
5.2 Introduction	126
5.3 Ablation Process Model	127
5.4 Characterisation of PC and PET	128

5.4.1 Dependence of the Ablation Depth on the Number of Pulses	128
5.4.2 Etch Rate versus Fluence	129
5.4.3 Wall Angle versus Fluence	132
5.5 Theoretical Model of Overlap Error	133
5.6 Overlap Size Calculation	137
5.7 Main Process Parameters	140
5.7.1 Taguchi Control Parameters	141
5.7.2 Optimisation of Process Parameters	141
5.8 Experimentation using Optimised Parameters	148
5.8.1 Surface Ablation using Workpiece Dragging Technique	148
5.9 Summary	152
Chapter 6. Method for Micromachining using Origin Related Mask Patterns	154
6.1 Overview	154
6.2 Introduction	154
6.3 Limitations of Existing Approaches	155
6.3.1 Stitching Errors	155
6.3.2 Additional Programming for Offsets	156
6.3.3 Mask Positional Error in respect to Mask Holder	161
6.3.4 Chrome-on-Quartz Masks	162
6.4 Description of “Common Nested” Approach	163
6.5 CN Mask Design Tool	168
6.6 Experiments to Evaluate CN Approach	171

6.6.1 Results and Discussion	171
6.6.2 Y-Shape Microstructure Produced by “Common Nest” (CN) Technique.....	175
6.6.3 Serpentine Microstructure.....	180
6.7 Summary.....	193
Chapter 7. Case Study: Fabrication of a Microfluidic Device For Cell Transportation	194
7.1 Overview	194
7.2 Cell Transportation Device.....	194
7.3 Microfluidics System Design using the CAD/CAM Tool	195
7.4 Comparison between CAD Models and Machined Structures.....	196
7.4.1 In-line Obstacles - Design 1	196
7.4.2 Circular Layout - Design 2	204
7.5 Summary.....	208
Chapter 8. Conclusions and Further Research.....	210
8.1 Overview	210
8.2 Contributions of the Research	210
8.3 Limitations of the Research.....	213
8.4 Recommendations for Future Research.....	214
8.5 Summary.....	216
References.....	218
Appendix A.....	229
A List of Publications	229
A.1 Journal Publications	229
A.2 International Conferences Publications	229
A.3 Local Publications and Presentations.....	230

Appendix B	231
NC Part Programs and Actual Microstructures Produced by Ex-Expv1.0 System.	231
B.1 Creating 2D and 3D Geometry.....	231
B.2 Creating STL File.....	233
B.3 Creating Sliced File Structure	234
B.4 Samples of Part Programs and Machined Structures using Different Machining Techniques	236
B.5 User-interface for Selection of Materials and Machining Process Parameters.	240
B.6 Aerotech Unidex 500 Programming Language.....	241
Appendix C	247
Flow chart of main input and output parameters for Design 1 (in-line obstacles) and Design 2 (circular layout).	247
Appendix D	253
Comparison between functionalities and similarities of the main modules described in Charrier et al. [101] approach and this research work.....	254

List of Figures

Figure 1.1: CAD/CAM system layout.	4
Figure 1.2: (a) and (b) SEM images showing stitching micromachining errors of a polycarbonate structure produced by excimer laser ablation.	6
Figure 2.1: Excimer laser ablation process steps.	10
Figure 2.2: Ultraviolet absorption spectrum of PMMA. The arrows point to the wavelengths of the strong emission lines from an excimer laser [15].	11
Figure 2.3: (a) Material removal process for heat conductors and (b) material removal process for heat insulators for short pulse duration laser ablation process [9, 16]. ...	13
Figure 2.4: Etch depth per pulse versus energy density for 14ns, 193nm pulses on PMMA. A pulse of energy density 20 J/cm^2 removed only $0.48\mu\text{m}$, emphasizing the strong saturation behavior [14].	14
Figure 2.5: Theoretical near-field imaging setup. (Image reproduced by courtesy of RESONETICS http://resonetics.com/).	19
Figure 2.6: Schematic of an excimer laser mask projection system [31].	22
Figure 2.7: Step-and-repeat mask projection process (Image reproduced by courtesy of RESONETICS http://resonetics.com/).	25
Figure 2.8: Microstructures produced by Indexed mask projection [21].	26
Figure 2.9: Synchronised mask scanning technique: (a) where workpiece movement is a translation and (b) where workpiece movement is rotation [31].	27
Figure 2.10: Mask Dragging Method.	28
Figure 2.11: Workpiece moving or workpiece-dragging method.	29
Figure 2.12: Principle of SIS showing the first three shots with moving workpiece and static mask. The laser beam illuminates all apertures with a single pulse [38].	32
Figure 2.13: Technique of synchronised overlay scanning [41].	33
Figure 2.14: Schematic of the direct machining method using a galvo-scanner and motorised X-Y translation stages [42].	35
Figure 2.15: Schematic of BTS technique - motion compensation with a typical bow tie shape of the scanner movement to provide straight line processing [38].	36
Figure 2.16: Anvik's high-resolution, high-throughput laser projection imaging technology, showing scanning with a planar stage and hexagonal beam [45].	38
Figure 2.17: Excimer laser micromachining of a 3D microstructure with a laser mask and sample-rotation method [46].	40

Figure 2.18: Multiple masks used for machining of corner cube structures [48].	41
Figure 2.19: Machining steps employed and pulse-by-pulse formation of structures in the workpiece [48].	42
Figure 2.20: Schematic build up of 3D structure by applying different machining process sequences: a) starting with the smallest and b) starting with the biggest aperture [38].	48
Figure 3.1: Ex-Expv1.0 system software structure showing main process parameters.	56
Figure 3.2: Ex-Expv1.0 system design module structure allows for CAD modelling to be accomplished “externally” by other CAD packages (left path) or “internally” through internal link to Solidworks (right path).	57
Figure 3.3: Triangular mesh for different geometric shapes.	59
Figure 3.4: First step - 3D Model of a triangular structure on a surface.	60
Figure 3.5: Second step - Tessellated representation of a triangular structure.	61
Figure 3.6: Third step - Sliced 3D model of a triangular structure.	61
Figure 3.7: Ex-Expv1.0 system machining module showing alternative machining options (Step-and-repeat and Workpiece-dragging).	63
Figure 3.8: Masks layout for a layer of triangular structure produced by Ex-Expv1.0. The colours and dimensions represent the different size masks incorporated into the CNC by the system.	64
Figure 3.9: Interior pixels along a scan line. The 4 pixel intersection points with polygon boundaries determined the area to be filled with different color [72].	68
Figure 3.10: Scan line y generates an odd number of intersections, but scan line y' generates an even number of intersections that can be paired to identify correctly the interior pixel spans [72].	69
Figure 3.11: Line drawing using pixels showing how the line rises, as x value increases by one, where value of dimension m defined line slope.	70
Figure 3.12: Lines of slope ≤ 1 .	71
Figure 3.13: Bresenham line drawing algorithm where position of the next pixel is determined by using the known position of the previous pixel.	72
Figure 3.14: Adaptation to TSP algorithm where the shortest toolpath (shown as continuous line that connects different machining regions) was determined by the nearest insertion method.	78
Figure 3.15: Toolpath optimization algorithm based on heuristic insertion method.	79

Figure 3.16: (a) Left-to-Right algorithm (Top to Bottom) used to generate an optimal masks layout for toolpath determination. (b) An example of masks layout and toolpath produced by Left-to-Right algorithm.....	81
Figure 3.17: (a) Zig-Zag algorithm used to generate an optimal masks layout for toolpath determination. (b) An example of mask layout and toolpath produced by Zig-Zag algorithm.	82
Figure 3.18: Star Algorithm showing toolpaths generated for each quarter of the structure for 8, 4, and 2 mm mask sizes.....	83
Figure 3.19: Mask layout simulation and pulse minimization process using adapted Bersenham algorithm.	86
Figure 3.20: Design with square and hexagonal patterns drawn in AutoCAD and used by PG/IR photo-plotting machine for manufacturing of conventional Chrome-on-Quartz mask.	92
Figure 3.21: Excimer laser Series 8000 Exitech Ltd.	93
Figure 3.22: Optical arrangement of the excimer laser micromachining system.	94
Figure 3.23: LSCM (OLS 1200, Olympus Pty.Ltd.).	97
Figure 3.24: A schematic of LSCM.....	98
Figure 3.25: (a) Optical microscope (Olympus BX60).	100
Figure 3.26: SEM image of a triangular structure produced by Step and repeat machining method. Material; PC, $PRF = 5\text{Hz}$, Fluence 1.1 J/cm^2 , Number of pulses per area $n = 100$	103
Figure 3.27: LSCM image of an octagonal 3D microstructure. Material; PC, $PRF = 10\text{Hz}$, Fluence 1.2 J/cm^2 , Number of pulses per area $n = 250$	104
Figure 3.28: (a) CAD model and (b) LSCM image of a 3D multi-layered pyramidal microstructure. Material; PC, $PRF = 70\text{Hz}$, Fluence 0.5 J/cm^2 , Number of pulses per area $n = 100$	105
Figure 4.1: Graphical representation of C.L.A. by the collection of ordinates (h_n) [84].	109
Figure 4.2: Graphical representation of C.L.A. by the collection of areas (A_n) [84]......	110
Figure 4.3: Masks layout in accordance to Bresenham ideal line drawing algorithm. Grid size is equal to mask size, and mask size could be any integer number.	111
Figure 4.4: Edge error representation for 15° sloped straight lines.	113
Figure 4.5: Edge error representation for 30° sloped straight lines.	114
Figure 4.6: Edge error representation for 45° sloped straight lines.	115

Figure 4.7: Mathematical algorithm to determine minimum edge error for lines with slope angle between 0-45°.	117
Figure 4.8: LSCM image of edge error measurements when slope angle is 15°. Labels (A1-A5) are area measurements calculated by LSCM.	119
Figure 4.9: LSCM image of edge error measurements when the slope angle is 30°. Labels A1-A7 are area measurements calculated by LSCM.	120
Figure 4.10: LSCM image of edge error measurements when slope angle is 45°. Labels A1-A9 are area measurements calculated by LSCM.	121
Figure 4.11: Slope angle versus C.L.A. for a constant mask size.	123
Figure 5.1: Characteristic cross-section of a single ablation site.	127
Figure 5.2: Ablation Depth, D_p , versus Number of pulses, n , at a fluence, $F_d = 1.1 \text{ J/cm}^2$ for PC and PET.	129
Figure 5.3: The relationship between the etch rate and fluence for the excimer laser firing 128 and 8 pulses respectively at 10Hz showing an etch rate of $0.39\mu\text{m/pulse}$ and $0.35\mu\text{m/pulse}$ respectively at fluence of 0.4 J/cm^2 . Sample material was PC.	130
Figure 5.4: The relationship between the etch rate and fluence for the excimer laser firing 128 pulses at 10Hz showing that PET has slightly higher etch rate then PC for the same process conditions.	131
Figure 5.5: Wall angle changes for fluence range from 0.2 to 1.1 J/cm^2 for a constant number of pulses $n = 100$, image size $100 \times 100\mu\text{m}^2$ in PC.	132
Figure 5.6: Wall Angle vs. Fluence for PET.	133
Figure 5.7: Mathematical model based on the laser pulse overlap (OL) geometry.	134
Figure 5.8: Five types of overlay error for different size of overlap OL where (a) $OL=0$, (b) $OL=CT$, (c) $OL<CT$, (d) $CT<OL<2*CT$, and (e) $OL=2*CT$.	136
Figure 5.9: Type 1 overlay error where mask image projection overlap $OL = 0$, $n = 100$ laser pulses, F_d is equal to 1.1 J/cm^2 .	137
Figure 5.10: Cross-section of ablated surface of Type 1 overlay error where overlap $OL = 0$, image size $210 \times 210\mu\text{m}^2$, $n = 100$, $F_d = 1.1 \text{ J/cm}^2$. Points A1-B1 and A2-B2 were used to measure wall angle θ .	138
Figure 5.11: (a) Peak error calculation by the ExExpv1.0 when $OL = 0$, (b) Optimised parameters for overlap OL .	139
Figure 5.12: Optical images of overlap error with $F_d = 1.1 \text{ J/cm}^2$, $n = 500$, material PC when: (a) Type 1 $OL=0$, (b) Type 2 $OL=CT$, (c) Type 3 $OL<CT$ and $\max(+)>\min(-)$,	

(d) Type 3 $OL < CT \max(+) = \min(-)$, (e) Type 4 $CT < OL < 2*CT$, (f) Type 5 $OL = 2*CT$	140
Figure 5.13: Ablation depth of a 100 μ m wide channel at a constant fluence, 1.1 J/cm ² , in polycarbonate, when number of pulses per area varies from 10-100.	142
Figure 5.14: Typical cross-section of an ablation site as measured by the LSCM. Points A1-B1, A2-B2, and A3-B3 were used to measure the wall angle.	143
Figure 5.15: Schematic of the wall angles θ_1 and θ_2	144
Figure 5.16: Design schematics of (a) Hexagonal and (b) Square mask with integrated overlap size for stitching error minimization.	147
Figure 5.17: LSCM image showing surface texture created by 100x100 μ m square image at fluence $F_d = 0.5$ J/cm ² , $PRF = 80$ Hz, $n = 70$ shots per area and material PC.	148
Figure 5.18: LSCM image showing stitching error effect of $13.4 \pm 2.2\mu$ m width and $1.4 \pm 0.9\mu$ m height horizontal defects in one axis only during workpiece-dragging ablation process, with square shaped 1.014 mm mask.	149
Figure 5.19: LSCM image showing stitching error effect of $2.4 \pm 0.2\mu$ m wide and $1.4 \pm 0.2\mu$ m high horizontal defects during workpiece dragging ablation process with hexagonal shaped mask.	150
Figure 5.20: LSCM image showing surface texture, with circle around aliasing effects at the edge of machined structure during mask dragging ablation process.	151
Figure 6.1: Typical stitching error effect (indicated by rectangles) at junction between four imaged patterns. Y-shape channel width is equal to 100 μ m.	156
Figure 6.2: (a) Desired alignment position indicated by rectangle and (b) Mask patterns offsets and misalignment problem.	157
Figure 6.3: (a) Top and bottom view of microfluidic chip layer with dimensions of the channel and holes for fluidic connectors. (b) Y-Shape assembly of two-layered microfluidic device. All dimensions are shown in millimeters.	158
Figure 6.4: Three different mask design solutions. (a) Y-shape made in one mask pattern. (b) Four mask patterns that can be used to produce the Y-shape. (c) Four mask patterns where two of the patterns are spaced in accordance to design requirements for center distance between fluidic connectors.	160
Figure 6.5: Mask rotational error in respect to mask holder.	161
Figure 6.6: (a) Chrome-on-quartz mask, (b) steel mask (precision stencil).	162

Figure 6.7: The main process steps 1-8 illustrate how CN approach was used to create a Y-shape structure. Four mask patterns were extracted from the main target design and when overlapped using a CN point, they would create the required structure.	164
Figure 6.8: An existing approach shows mask patterns with origins unrelated to a common point. Mask patterns offsets and overlaps were not included into design stage.	165
Figure 6.9: Four mask patterns extracted from target design were used to produce same Y-shape structure using principles of CN approach.	166
Figure 6.10: (a) Mask design including overlap features. Mask includes features used for correction of mask rotational error in relation to direction of travel of the stage axis. (b) Final mask design.	169
Figure 6.11: Typical toolpath to generate a serpentine structure for microfluidics applications. Arc and line blocks used to make this structure are also shown.	170
Figure 6.12: 3D LSCM image of a serpentine structure 100µm wide and 100µm deep. Process conditions: $F_d = 1.2 \text{ J/cm}^2$, $PRF = 5\text{Hz}$, $n = 50$.	172
Figure 6.13: 2D CAD model of a more complex serpentine structure designed in accordance with the CN method requirements.	173
Figure 6.14: 2D LSCM image showing a complex serpentine structure. Process conditions: $F_d = 1.2 \text{ J/cm}^2$, $PRF = 5\text{Hz}$, $n = 50$.	174
Figure 6.15: Steps 1- 4 for production of a Y-shape microstructure using CN method.	180
Figure 6.16: Serpentine structure element.	181
Figure 6.17: Metal shim mask with eight patterns for machining serpentine structure.	181
Figure 6.18: Steps 1-13 to fabricate serpentine structure using CN method.	192
Figure 7.1: 2D model representation of Design 1 - a microfluidic device for cell transportation (in-line obstacles). All dimensions are shown in millimeters after 10x demagnification.	195
Figure 7.2: 2D model representation of Design 2 - a microfluidic device for cell transportation (circular layout). All dimensions are shown in millimeters after 10x demagnification.	196
Figure 7.3: 2D LSCM image of micro fluidic device for cell transport – Design 1 produced by workpiece-dragging technique using NC code generated by Ex-Expv1.0. Process parameters: $F_d = 1.1 \text{ J/cm}^2$, $PRF = 50\text{Hz}$, $n = 25$, material:PC.	197

Figure 7.4: A detail view of 2D CAD model of Design 1 with lateral dimensions (μm) for comparison, taken in the area indicated in Figure 7.3 by the dashed box.	198
Figure 7.5: 2D LSCM image of microstructures produced by excimer laser micromachining, with lateral dimensions for comparison. The detail is taken in the indicated area in Figure 7.3 by the dashed box.....	200
Figure 7.6: 2D LSCM image showing saw-tooth effects, i.e. a problem of straightness along the square feature vertical sides. The detail taken is indicated area in Figure 7.5 by the dashed box.....	201
Figure 7.7: 2D LSCM image showing locations for wall angle measurements. The detail taken in the indicated area in Figure 7.3 by the dashed box.	202
Figure 7.8: LSCM cross-sectional wall angle line profile 1. Line profile 1 was taken in the highlighted area in Figure 7.7 by the dashed box.	203
Figure 7.9: 3D model of Design 2 (Circular) produced by developed CAD/CAM system.	204
Figure 7.10: 2D LSCM image of a micro fluidics device for cells transportation (Design 2 - circular layout). Process parameters: $F_d = 1.1 \text{ J/cm}^2$, $PRF = 50\text{Hz}$, $n = 25$, material:PC.	205
Figure 7.11: 2D LSCM image showing locations for wall angle measurements.	206
Figure 7.12: LSCM cross-sectional wall angle line profile 1. Line profile 1 was taken in the highlighted area in Figure 7.11 by the dashed box.	207
Figure B.1.1: Steps (a) – (d).....	232
Figure B.4.1: (a) CAD model of a complex microfluidics channels network, (b) and (c) 2D and 3D LSCM image of the machined structure.....	237
Figure B.4.2 (a)-(f): CAD models and 2D LSCM images of different machined structures produced by Ex-Expv1.0 system.	239
Figure B.5.1: Part of GUI for machining.	240
Figure B.5.2: Part of GUI for selection of process parameters from database of the system.	241
Figure C.1: Design 1: In-line obstacles - Flow Chart	249
Figure C.2: Design 2: Circular Layout - Flow Chart	252
Figure D.1: Comparison between Charrier et al. [101] approach and this research work.	253

List of Tables

Table 2.1: Summary of studies for CAD/CAM system development for excimer laser processing.	45
Table 3.1: System input and output parameters.	54
Table 3.2: Pulse minimisation using different algorithms.	87
Table 3.3: Experimental investigations undertaken in this research.	95
Table 3.4: Comparison of the process steps in the existing and new approach from early design stage to final product.	101
Table 4.1: Edge error measurements when slope angle is 15°.	119
Table 4.2: Edge error measurements when slope angle is 30°.	120
Table 4.3: Edge error measurements when slope angle is 45°.	122
Table 4.4: Theoretical and experimental results for C.L.A. values.	123
Table 5.1: Measurements of the wall angle as measured by LSCM.	138
Table 5.2: Excimer laser optimised process parameters for PC samples.	141
Table 5.3: Ablation parameters for workpiece-dragging machining method of channels in PC.	143
Table 5.4: Measurements of the wall angle of the channel machined in PC using results in Figure 5.14.	144
Table 5.5: Input parameters to the Taguchi Design of experiment and their values.	145
Table 5.6: Taguchi Orthogonal Array (<i>OA</i>) for optimising wall angle and ablation depth.	145
Table 5.7: Predicted results from Taguchi <i>OA</i> experiments.	146
Table 5.8: Results summary of stitching error reduction.	150
Table 6.1: CN approach reduction in coding compare to existing approach.	167
Table 7.1: Wall angle measurements data along line profile 1 as shown in Figure 7.8.	203
Table 7.2: Wall angle measurements data along line profile 1 as shown in Figure 7.12.	207
Table B.6.1: Exitech Series 8000 laser machine.	242
Table B.6.2: RS-274 “G” code and Aerotech commands.	243
Table B.6.3: PSO Commands.	245

List of Variables

The symbols listed in the chapters follow the convention of international system of units (SI), SI base units and SI derived units.

Symbol	Description	SI unit
CT	Wall Angle Projection on Top Surface	μm
D	Demagnification Ratio	-
D_p	Ablation Depth	μm
$E_{d(IP)}$	Energy Density at the Image Plane	J/cm^2
E_s	Encoder Steps per 1 mm	-
f	Focal Length of the Image Lens	mm
F_d	Laser Fluence	J/cm^2
F_{th}	Threshold Fluence	J/cm^2
$h(r)$	Machining Depth at Radius r	μm
I	Image Distance	mm
I_x	Beam size at the Workpiece along X-axis	mm
L	Orthogonal Array	-
L_{ty}	Top Length of Ablated Volume	μm
$max(+)$	Peak Error	μm
$min(-)$	Trough Error	μm
n	Number of Pulses per Area	-
N	Total Number of Fired Laser Pulses	-

O	Object Distance	mm
OL	Actual Overlap Size	μm
PRF	Pulse Repetition Frequency	Hz
$PSOD$	Position Synchronised Output Distance	-
r	Radius	mm
R	Corner Radii	μm
R_a	Roughness Average	μm
R_z	Average Maximum Height of the Profile	μm
$S(\rho)$	Arc Length of Aperture at Radius r	mm
t	Total Machining Error in Depth	μm
v_x	Velocity of the Workpiece along X-axis	mm/min
Wbx	Bottom Width of Ablated Volume	μm
Wtx	Top Width of Ablated Volume	μm
x	Number of Experiments	
y	Number of Input Parameters	-
Z	Number of Value Settings for Each Parameter	-
α	Absorption coefficient	cm^{-1}
ε	Etch Rate	$\mu\text{m}/\text{pulse}$
θ	Wall Angle	°
ρ	Radius at the Mask	mm

List of Abbreviations

The list of abbreviations used in this thesis is shown below.

Abbreviation	Description
API	Automatic Programming Interface
ASCII	American Standard Code for Information Interchange
ANOVA	Analysis of Variances
BMP	Bit-Map File Format
CAD	Computer Aided Design
CAM	Computer Integrated Manufacturing
CRC	Cooperative Research Center
CNC	Computer Numerical Control
DXF	Drawing Interchange File Format
DB	Data Base
DOE	Design of Experiment
DIN	German Industrial Norm Standard
EGA	Enhanced Graphics Adapter Display
FIB	Focused Ion Beam
FDM	Fused Deposition Modelling
GUI	Graphical User Interface
LSCM	Laser Scanning Confocal Microscope
LIGA	Lithography-Galvanoformung-Abformung

LUT	Color Look-Up Table
MEMS	Micro-Electro-Mechanical-Systems
MOEMS	Micro-Optical-Electro-Mechanical-Systems
MIA	Multiple Image Alignment
NC	Numerical Control
OS	Operating System
OA	Orthogonal Array
PC	Polycarbonate
PET	Poly-terephthalate
PMMA	Polymethyl methacrylate
RP	Rapid Prototyping
R&D	Research and Development
RAM	Random Access Memory
SEM	Scanning Electron Microscope
STL	Stereo-Lithography File Format
VRAM	Video RAM
VGA	Video Graphics Array Display

Optimised Part Programs for Excimer Laser-Ablation Micromachining Directly from 3D CAD Models

Declaration

This thesis contains no material which has been accepted for the award of any other degree or diploma at any University and to the best of my knowledge and belief contains no material previously published or written by another person or persons except where due reference is made.

Emir Mutapcic

October 20, 2006

Chapter 1. *Introduction*

1.1 Background and Significance of the Research

This work was carried out at the Industrial Research Institute Swinburne (IRIS) during the years from 2001 to 2006. It was part of the Microfluidics project supported by CRC for Microtechnology in Australia.

CAD/CAM tools have become increasingly important in Micro-Electro-Mechanical-Systems (MEMS) and Microfluidics technology, where they are used to design a product, assess the effect of design changes, evaluate manufacturing and reduce the time to market. Achievement of successful micro-engineered structures requires incorporating the microstructure functionality early in design stage. Many research groups are attempting to address this problem, and correspondingly an active CAD community has developed to help scientists and engineers model and understand microdevices. While significant advances have taken place in some areas of microengineering, such as lithographic and chemical-etching techniques, a structured methodology for many other micro-fabrication processes is yet to be developed.

In particular, CAD/CAM systems for excimer laser mask projection micromachining tools have received little attention, and indeed few attempts have been reported on CAD/CAM systems that fully capitalize on the unique capability of the excimer laser process. Two of the possible reasons are that these systems are still costly even though some dramatic changes happened in recent years that make them more affordable (development of low-cost Solid-State laser systems) and that market demand for these tools is still relatively undeveloped.

The only reported implementation of CAD/CAM systems for excimer laser mask projection is based on the DXF file format and uses a polygonal mesh to approximate the 3D models [1-3]. The system was used only for internal R&D, and has complex procedures for extracting 3D geometry data. It was developed specifically for an excimer

laser tool with a flexible beam shaping system, comprising of four additional NC axes for controlling special blades to shape the laser beam. Although this system provides greater machining flexibility, it has disadvantages including increased machining time, due to the additional time required to open and close the blades. Furthermore, four additional driving stages must be aligned to ensure proper beam size and adequate dimensional accuracy in the machined structures. Finally, the cost of this complex system is very high compared to conventional excimer laser tools, the vast majority of which incorporate fixed mask geometry to shape the beam.

The specific aim of this research, therefore, was to develop a novel CAD/CAM system for prototyping and small-scale production of microdevices using conventional excimer laser tools that incorporate a fixed mask geometry system to shape the beam. A further important aim was to develop a system capable of incorporating the error effects of stitching that are inherently present in microstructures made using this unique micromachining process.

The following section 1.2 explains in more detail the type of system that this research work will focus on and describe it in the context of system evolution. Section 1.3 shows how this approach also addresses problems of stitching error effects. Furthermore, section 1.4 states the research objectives of this work, and finally, section 1.5, provides a road map of this dissertation.

1.2 CAD/CAM System Development

A unique combination of commercially available software systems was used to develop the new CAD/CAM system. The systems used comprised of a computer aided, feature based, parametric design system (SolidWorks®), together with its extended programming capabilities based on API functions for Windows applications, and Visual Basic 6.0 programming utilities.

Based on the principle of layer manufacturing (LM) and rapid prototyping (RP) processes [4], the new CAD/CAM system will use the information obtained from the intersection of a 3D model from a CAD system (in the form of a STL file) with layers of horizontal planes. As a result, a stack of 2D geometry contours is obtained, each

representing a cross-section of the 3D model. Next the system takes the top slice of the geometric contour and creates the optimal toolpath for the excimer laser tool. After having placed each pulse on the location as required by the geometric contour the new layer is processed. The process is repeated one slice after another from top to bottom until a complete 3D part is scanned. Theoretically, as the slice thickness is only few microns, the 3D part should be identical with the 3D model constructed by CAD system. However, in reality, materials used in excimer laser ablation process all have their limits (density, heat capacity, thermal conductivity, melting or glass transition temperature, absorptivity) [5], thus generating an error. There are also other factors that may affect excimer laser ablation process. Since these errors have a crucial influence on the entire process they will be discussed in greater deal in a separate chapter.

The developed system is the first of its kind that extracts information from a STL file to automatically generate Numerical Control (NC) code data for excimer laser ablation manufacturing using optimised processing parameters.

To overcome the problem of geometrical information loss when approximate surfaces using STL file representation, a BMP file approach has been developed. In this approach each layer or slice represents an individual BMP file that contains geometric contour information of the model. The system simplifies part program creation and is useful for excimer laser operators who currently use a tedious trial and error process to create programs and complex masks to generate microstructure parts. The system enables components with feature resolution down to $\sim 10\mu\text{m}$ to be produced for small batch production of MEMS devices and Microfluidics applications. The system can also be utilised as a rapid prototyping tool for the excimer laser ablation process, and reduces the overall design and production time from a day to an hour, reducing the cost of the process itself. The system algorithms deployed are currently developed only for square and hexagonal mask patterns, however, the algorithms can be extended to accommodate a range of different shaped masks and other processes. Furthermore, the system is cost-effective because it does not require additional expensive lithography masks to be produced for every change in design of microstructures. The system was specifically designed for fixed mask geometry to shape the laser beam. Additionally, a pulse minimization algorithm is integrated, allowing reduction of manufacturing time by the use of specific multiple patterned masks.

The described CAD-CAM system is adapted to the special demands of microstructuring with excimer lasers by the implementation of different features as shown in Figure 1.1

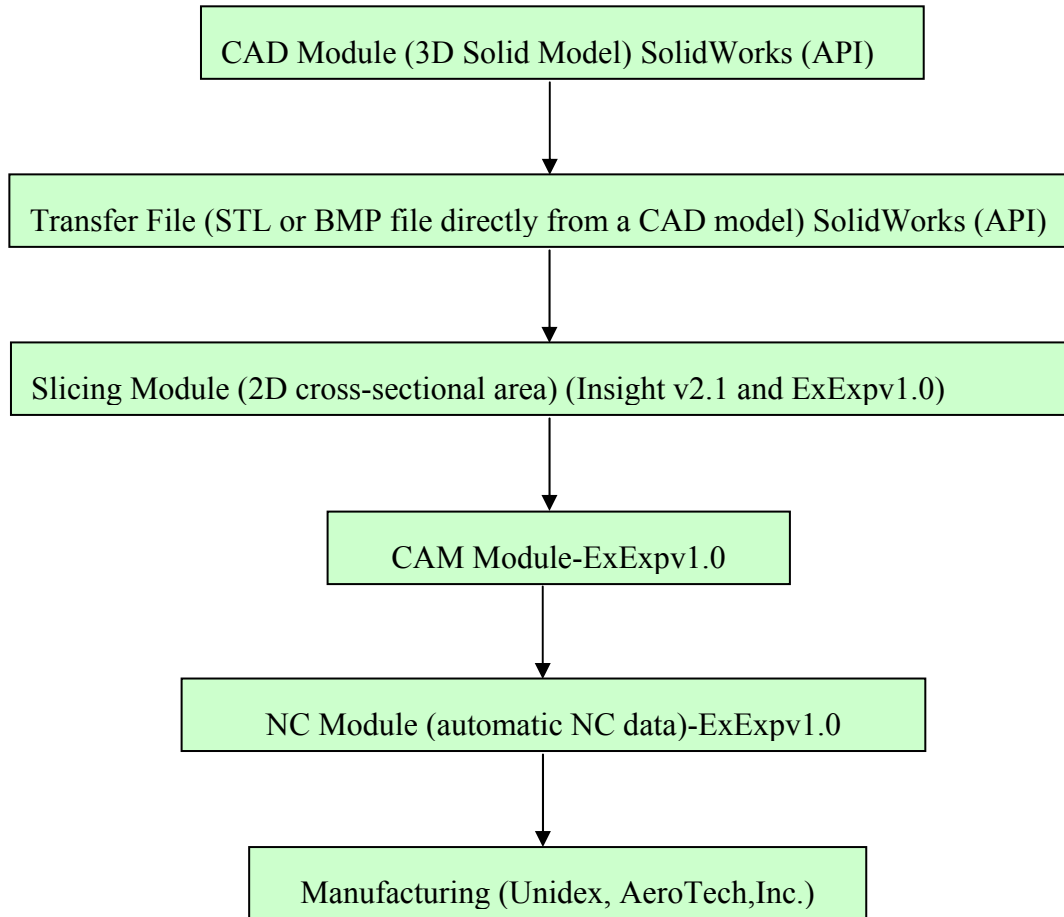


Figure 1.1:CAD/CAM system layout.

A CAD/CAM system needs to be developed in accordance to the following requirements:

- Graphical User Interface (GUI) to provide user friendly design environment
- Output file format of commonly used CAD systems as input to new system

- High flexibility concerning size, resolution, and producible geometry, modelling and accuracy at microstructure level
- Expertise and knowledge of an experienced user and existing literature data should be implemented into a database (DB)
- Efficient strategies for manufacturing suggested by the system (type of material, shape and size of micro-structure, pulse minimization)

1.3 Stitching Error Effects

The excimer laser ablation process suffers from several problems such as diffraction, pulse overlapping, and stitching error effects and various methods have to be employed to achieve accuracy and satisfactory surface quality [6]. The complexity further increases with additional factors such as:

- Beam inhomogeneity
- Pulse to pulse energy variation
- Materials inhomogeneity
- Error in CNC stages.

Figure 1.2 shows typical stitching errors effects encountered in a microstructure produced by the Step-and-repeat technique.

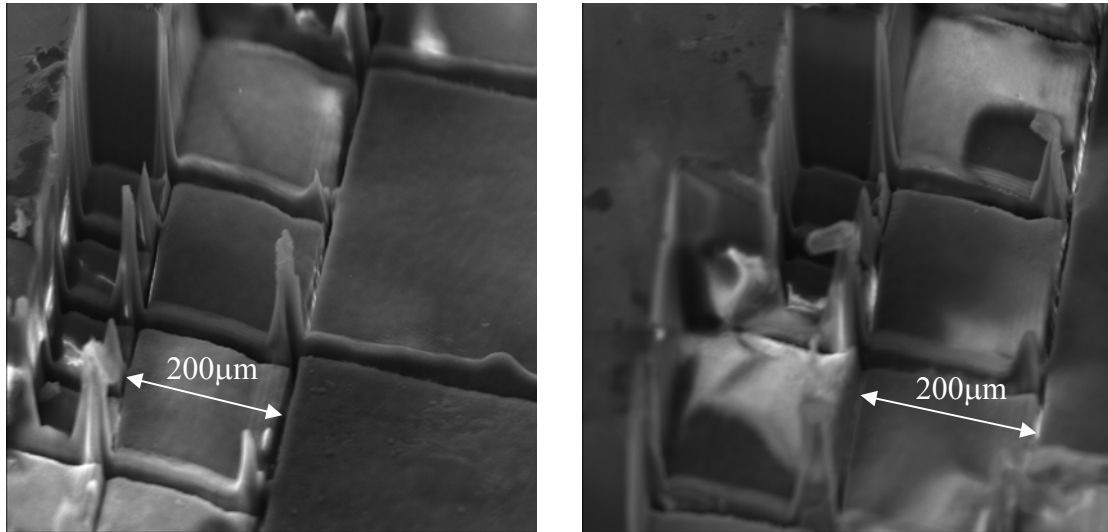


Figure 1.2: (a) and (b) SEM images showing stitching micromachining errors of a polycarbonate structure produced by excimer laser ablation.

The number of parameters involved in the actual process is large and this research effort concentrated on the impact of several the most influential ones, i.e.: laser fluence F_d , number of laser pulses per area n , pulse repetition frequency PRF , feature size, wall angle θ , ablation depth D_p , and stitching error.

The Taguchi Design of Experiments (DOE) [7] method was used for the parameter optimisation process, as the number of experiments needed to determine these parameters using other means was impractically high, owing to the large number of parameters involved. The Taguchi method reduced the number of process characterization experiments from 27 to 9. Optimisation of the stitching errors was also performed using the Taguchi method.

A 2D mathematical model for controlling stitching errors was developed and implemented in the system. This model relates the width and height of the stitching error to the mask shape and overlap size. The model may be used to determine the optimal overlap size to achieve minimum stitching error.

1.4 Objectives and Scope of the Research

The main objective of this research was to develop an intelligent part programming NC code generation system for excimer laser ablation processes. A second objective was to provide a GUI that would significantly reduce the time to market of new products and reduce the trial and error processes to the minimum. A third and final objective was to provide a set of techniques and methodologies that would help the excimer laser user to select the optimum process parameters for improved surface quality and roughness control of the produced microstructures.

These objectives were to be accomplished by:

- Developing a generic approach that will provide processing of any surface of any complexity suitable for an excimer laser ablation process
- Developing techniques and algorithms for automatic tool path generation analytically using primitive mask shapes such as squares and hexagons
- Developing techniques and algorithms for STL file conversion
- Developing a methodology for computing the layered structure
- Developing techniques and algorithms for stitching error reduction
- Developing a database system that will contain optimal machining data for commonly used materials. Experimental data as well as data available from existing literature should be implemented
- Determining experimentally various parameters of the excimer laser ablation process that would be subsequently used as input parameters for the optimisation module
- Verifying the accuracy of the system by comparing the analytical results and experimental results for selected simple parts and primitive structures
- Testing the system with a range of simple and complex parts to obtain the best possible surface quality and roughness.

1.5 Outline of Thesis

The research presented in this thesis is organised into several chapters as outlined below.

Chapter 2 presents a brief overview of laser-ablation technologies and current process limitations and includes a literature survey on the current work that relates to CAD/CAM problems and software development in this field.

Chapter 3 describes the methodology used to develop a CAD/CAM system for direct conversion of 3D geometry from a CAD model into an NC part program compatible with the excimer laser machine (Exitech S8000 with Unidex 500 Controller, Aerotech Inc).

Chapter 4 discusses development of a mathematical model for edge error control. The model involves the determination of staircase area error on the outer edge of each layer of the object.

Chapter 5 covers development of a model concept for stitching error effects controls that involves optimisation of several process parameters. Optimisation of these parameters was supported by the DOE Taguchi method.

Chapter 6 presents the development of a new micro-machining design and programming strategy based on a mask design technique named “Common Nest” (CN) and the software algorithm development to support this strategy. The strategy is presented and the results are verified by comparison with analytical and experimental results.

Chapter 7 presents the application of the system through a case study on quick prototyping of a microfluidic device for cell transportation. It evaluates the system capabilities in terms of device design and production time, lateral dimensions accuracy compared to CAD model, wall angle, edge error and system adaptation to quick changes in design. The results for the two different design concepts (in-line obstacles and circular design) produced by the system in a polycarbonate (PC) sheet are presented.

Chapter 8 presents; conclusions, major contributions of this research, limitations and recommendations for future research work in this field.

Chapter 2. *Literature Review*

2.1 Overview

The literature review for this research was conducted over a period of several years, from 2001-2006. The objective of the review was to acquire an understanding of the current state of knowledge in the field of CAD/CAM systems for excimer laser mask projection ablation process and to identify the areas of research which form the basis of the present research. The fundamentals of excimer laser ablation mechanism are first reviewed in sections 2.2 and 2.3 to understand the main factors and physical principles behind this unique micromachining process. The mask projection theory and existing machining techniques are discussed in sections 2.4 and 2.5 respectively. Focal point and scanner based techniques are covered in section 2.6 and a new system for large area patterning from Anvik corporation is discussed in section 2.7. Section 2.8 surveys the current research in the field of CAD/CAM systems for microstructuring by excimer lasers. Sections 2.9, 2.10 and 2.11 cover related work on machining process sequence, STL file generation and slicing techniques respectively. Finally, in section 2.12 the findings of the literature review are summarised.

2.2 Background

Excimer lasers are pulsed lasers that use a mixture of gases to provide emission at a series of discrete wavelengths in the UV or deep UV region of the spectrum. Commonly used excimer lasers for micromachining are: Argon-Fluoride (ArF) 193 nm, Krypton-Fluoride (KrF) 248 nm, and Xenon-Chlorine (XeCl) 308 nm pulsed lasers. They are capable of machining microstructures having feature size of the order of 1 to 100 μ m, and can be used on various materials, including polymers, metals, and ceramics [8-10].

Excimer lasers' mechanism of material removal is based on laser-material interactions that may induce thermal ablation and/or photo-ablation [9, 11-13].

2.3 Excimer Laser Ablation Mechanism

A comprehensive review of the early research work on laser ablation phenomenon was summarized by Srinivasan and Braren in 1989 [14].

Laser ablation is the direct removal of material by the interaction of the laser light with the sample. The main process steps are shown in Figure 2.1.

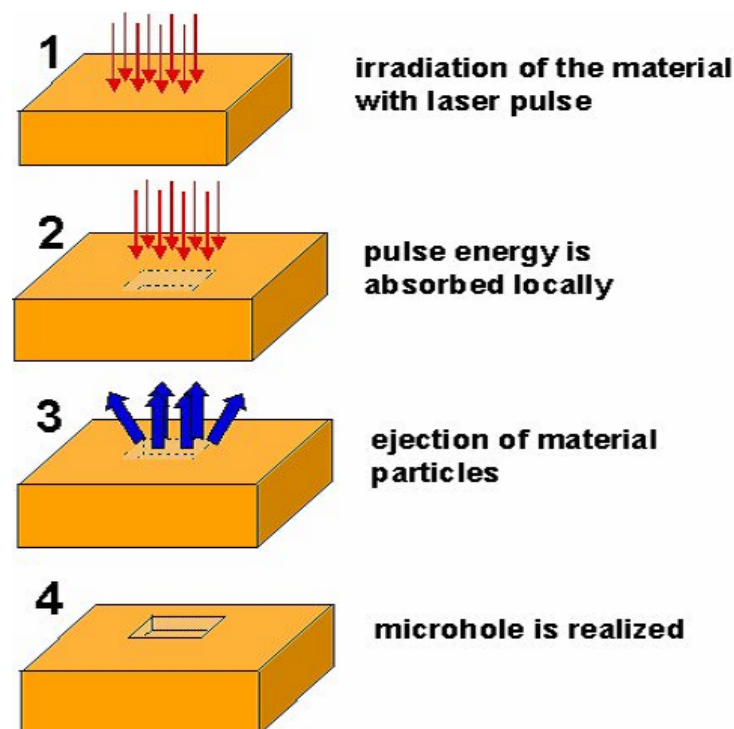


Figure 2.1:Excimer laser ablation process steps.

As a result of the irradiation of material with high-energy excimer laser photons at sufficient fluence immediate bond breaking due to electronic excitation is induced. In combination with short-term laser-material interaction of only 10 to 30 ns excimer pulse duration, material ablation proceeds via fast vaporization and consecutive ejection of material with only negligible dissipation of heat transfer to the surrounding zone. Hence,

photo-ablation mechanism dominates the material removal [8]. Excimer laser micromachining is particularly suitable for polymers materials because the covalence bonding energy in polymer materials is relatively low (all polymers contain the C-H bond with a bond energy of $\approx 3.5\text{eV}$) to withstand the high photon energies ranging from 3.5 to 7.9 eV emitted by excimer lasers [8]. Changes start occurring as soon as the laser pulse arrives at the surface of the ablated substrate, and continues a little time after the pulse has ended. Ablation occurs if the incident fluence is higher than the ablation threshold of the ablated material. Material ablation threshold is function of laser light wavelength (λ) and material properties (i.e., absorption coefficient) Figure 2.2 shows the ultraviolet absorption spectrum of a commercial polymer polymethyl methacrylate (PMMA)[15].

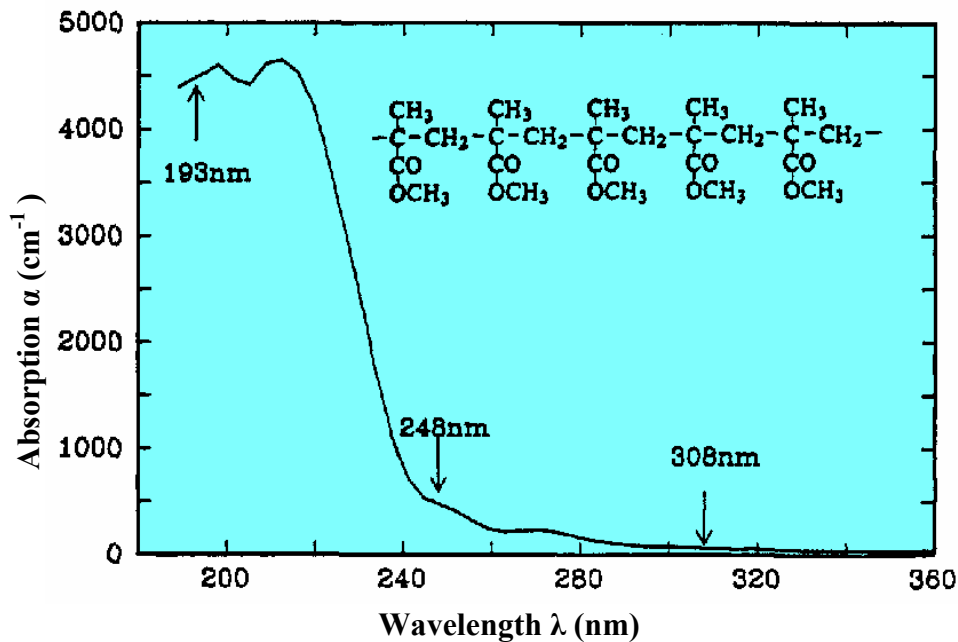


Figure 2.2: Ultraviolet absorption spectrum of PMMA. The arrows point to the wavelengths of the strong emission lines from an excimer laser [15].

At the three principle wavelengths of the excimer laser which are noted in Figure 2.2, both absorption and etching characteristics of the material vary significantly [15]. It can be noted in Figure 2.2 that 193nm wavelength would be the most suitable for machining of PMMA material comparing with the other two principle wavelengths that would produce poor machining results.

Thermal damage resulting from excimer laser ablation is usually small, provided the right conditions are employed. The penetration depth of light is very small (fraction of microns 0.1-0.5 μm) when a material absorbs strongly (absorptivities of $> 4000 \text{ cm}^{-1}$) at the irradiated wavelength. When the material has a low absorption coefficient at the wavelength of the light source, the radiation will penetrate to a greater depth (many tens of microns) but not all of it will cause ablation unless the light intensity at the depth in consideration crosses the ablation threshold. The ablation threshold is defined as fluence level at which ablation is onset. The energy density for machining operations is selected at the lowest fluence level where the ablation rate holds constant. This gives a reproducible result without stressing the laser system [97]. The threshold energy fluence is low for polymers (typically in the range 10-100 mJ/cm^2). Whenever the fluence is less than the threshold for ablation, thermal effects will be pronounced. Conversely, whenever the fluence is greater than the threshold value, there will be less thermal damage and more of ablative photodecomposition. This ablated area will have the shape of the incident light beam, and heat affected zone (HAZ) outside this area will be limited because of the very short duration of the pulse and the poor thermal diffusivity of material [14]. Hence, for pulsed lasers the extent of the HAZ, L , has been given by the equation 2.1:

$$L = 2\sqrt{\kappa\tau} \quad (2.1)$$

Where:

κ - thermal diffusivity constant

τ - the pulse duration

It is noticable from Figure 2.3 (a) that for heat conducting materials (metals, ceramics, etc) machining is mainly due to thermal degradation process and thermal penetration depth L can be minimised by using short laser pulses. On the other hand for heat insulators (e.g. polymers, glasses) machining is more due to localised evaporation and explosion, and L can be minimised by using wavelengths with maximum photon absorption [9, 16].

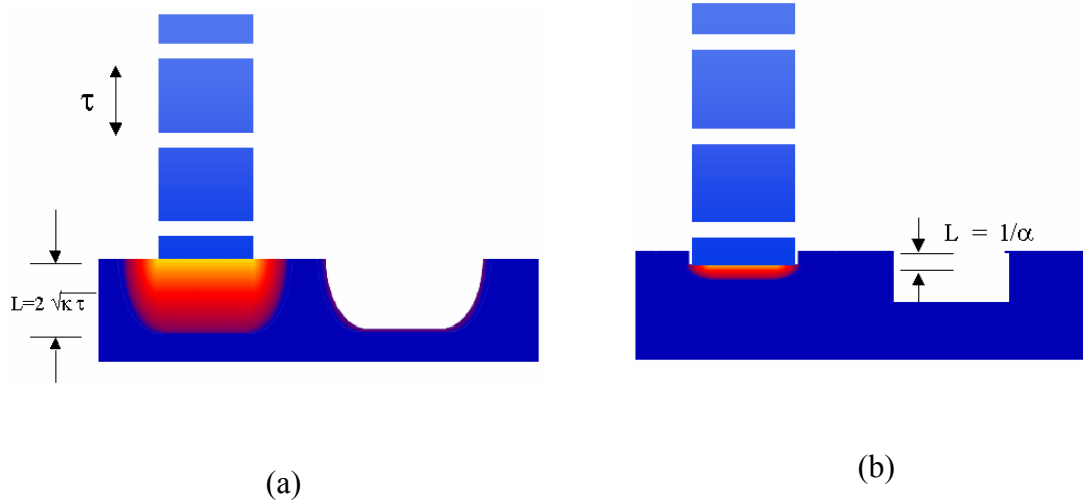


Figure 2.3: (a) Material removal process for heat conductors and (b) material removal process for heat insulators for short pulse duration laser ablation process [9, 16].

Another property of the process is that the threshold for ablation of metals is significantly higher than for polymers. For metals, the higher thermal conductivity results in a larger volume of deposited energy, and therefore a higher threshold for ablation. In the case of patterning polymers over a metal, the metal acts as an extremely effective etch stop for the process [17].

An important quantity for excimer laser micro machining is the etch rate of the material – that is, the amount of material which is removed per laser pulse at a particular laser fluence. For absorption processes independent of intensities the Lambert-Beer's law is given by equation 2.2:

$$D_p = \ln(F_d / F_{th}) / \alpha \quad (2.2)$$

where

D_p - ablation depth per pulse

α - absorption coefficient

F_d - incident fluence

F_{th} - threshold fluence [96].

Figure 2.4 shows etch rate curve for PMMA at 193nm excimer laser wavelength. It can be seen that there is an initial linear form for the etch rate as the laser fluence increases but then the etch rate levels off or saturates [14].

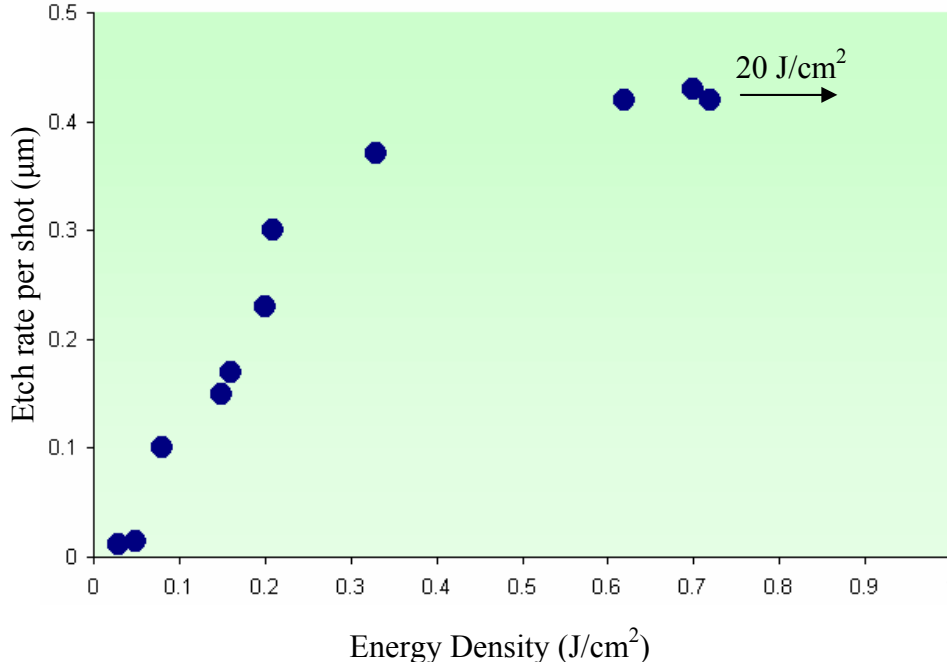


Figure 2.4: Etch depth per pulse versus energy density for 14ns, 193nm pulses on PMMA. A pulse of energy density 20 J/cm² removed only 0.48μm, emphasizing the strong saturation behavior [14].

This effect can be explained in simple terms in the following manner.

Consider that the laser exposes an area A . Due to the finite absorption of the material at the laser wavelength, there is a maximum depth d over which the laser light is absorbed. Hence, the volume $A*d$ can be considered to be the interaction volume. Initially, at low fluences, all the laser photons, which are incident on the exposure area, are absorbed and participate in bond breaking, and therefore promote laser ablation of material. As the laser fluence increases, however, a point is reached where all the material in the interaction volume is being acted on by the incoming photons – all the molecular bonds are being broken – and so any increase in fluence has little effect in increasing the

etch rate. The etch rate therefore saturates and the rate of material removal cannot be increased [15].

Another important property of the etch rates is that the material removal rate is very small – only tenths of micron per pulse.

Therefore, the depth of ablation is simply given by equation 2.3:

$$D_p = \varepsilon * n \quad (2.3)$$

Where D_p = Ablation Depth (μm), ε = Etch Rate ($\mu\text{m}/\text{pulse}$) and n = Number of pulses per area (-).

Once a laser has been chosen for a particular application (i.e. the spectral properties of the laser output have been matched with the absorption of the material), then the important parameters to optimise are the laser fluence at the sample, the number of pulses used, the nature of processing and the repetition rate of the laser [11, 18, 19].

Excimer laser micromachining techniques have been developed for more than 20 years and are now well-established for fabricating 2D and 3D microstructures [6, 8, 20-22].

The machining is essentially 2D and binary, which means one single laser pulse removes a certain depth of material within the machining pattern defined by the laser mask. However, by combining the mask design and moving of the mask or the sample, 3D surface profiles can be achieved [23, 24], [10].

Excimer laser ablation techniques can be used to control the geometry of a microstructure being produced in various dimensions:

- Lateral dimensions (x and y): Controlled by the resolution of the optical system used to produce the feature and machining method;
- Ablation Depth D_p (controlled by wavelength and fluence but primarily by number of shots)

- Wall Angle θ (controlled by the fluence and numerical aperture (NA) [10]). The magnitude of the wall angle is mainly a function of:
 - Material composition
 - Laser wavelength
 - Numerical aperture of the optical system
 - Laser fluence.

The designs of the optics used in excimer laser micromachining systems are varied and can be quite complicated, depending on the exact application. The determining factors in choosing a particular design can be:

- the material to be used (which affect the laser, the wavelength and the fluence needed)
- the types of features required (where the resolution needed may be the most important criterion)
- the area to be covered by the laser processing
- damage threshold limitations of any optical component
- the magnification of the system, if mask projection technique is being employed.

When a particular design has been chosen, then the wall angle can usually be characterised by a combination of the laser fluence and the numerical aperture (NA). Having chosen a particular NA (which is usually the case since other factors such as resolution also affect the choice of optical system), the most convenient parameter, which can be readily changed, is the laser fluence. Using this process, the wall angle can be controlled and a change in the fluence alters the wall angle of the feature [18, 25].

2.4 Laser Machining Methods

Two methods of laser machining are widely used in industry. The beam focusing or focal point machining typically used with solid-state lasers, such as Nd: YAG (A solid-state laser that uses a crystal of Yttrium Aluminum Garnet (YAG), doped with Neodymium (Nd) as the lasing medium) or Carbon-Dioxide (CO₂) lasers (which usually have good beam propagation characteristics). The motion of either the laser beam or the sample (or sometimes both) is then used to produce the microstructures in the sample. The two main advantages of direct writing are that:

- it does not require a mask
- the path to be machined can be fed directly into the control of the machining system (i.e. the laser system can be directly interfaced to the CAD generation of the pattern) [28].

Here the material to be machined is placed at the focal point of the nearly Gaussian, or single mode, beam as it passes through a lens. An extension of focal point machining is the technique of beam scanning where the laser beam is moved rapidly over a small sample area by galvanometer XY scanning mirrors and the control of the scanning mirrors determines the features to be produced [22] .

Excimer lasers are pulsed laser sources emitting in the ultra-violet region of the spectrum. They are relatively broadband sources and usually have a rectangular beam output of the order of ~25mm x ~10mm. The beam divergence is usually ~1-5mrad and it is different in two orthogonal beam directions. Due to this relatively large and non-uniform beam divergence, and the fact that the beam has poor spatial coherence, the direct focusing of excimer lasers is generally unattractive. Hence, the technique of mask projection is commonly used in a large number of applications [22].

2.4.1 Mask Projection Design Principles

Near-field imaging involves use of a mask to project a pattern of light onto a part. The features of the mask are etched into the target material at a magnification determined by the relative positioning of the optical elements [26].

The relationship between mask, imaging lens and image on the target material is described by the *thin lens* equation 2.4:

$$\frac{1}{O} + \frac{1}{I} = \frac{1}{f} \quad (2.4)$$

Where:

O = object distance (mm)

f = focal length of the image lens (mm)

I = image distance (mm)

The term magnification in optics is normally used to describe the ratio of the image size to the size of the object. Hence, the term demagnification implies that the image is smaller than the object, as shown in Figure 2.5 and is described by the equation 2.5:

$$D = \frac{O}{I} \quad (-) \quad (2.5)$$

Where:

D is the demagnification ratio [26].

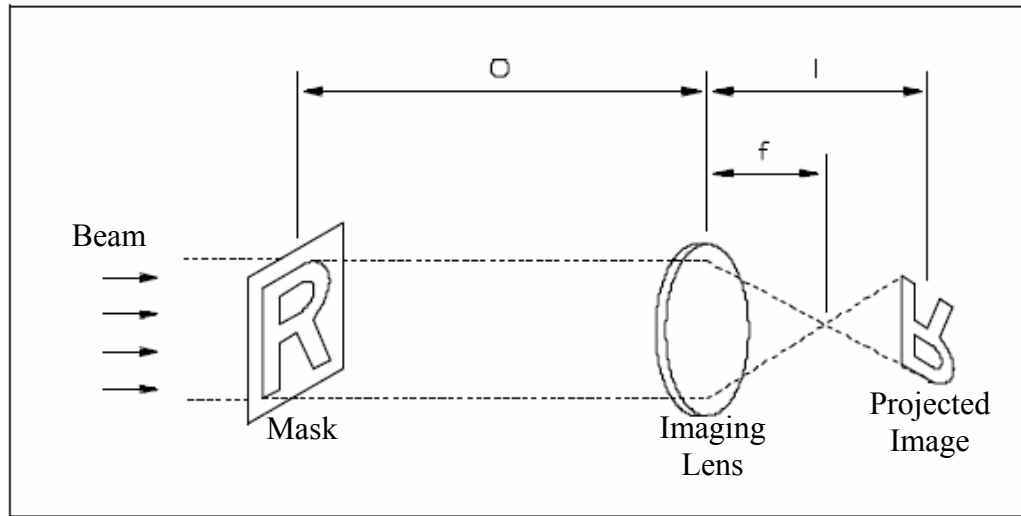


Figure 2.5: Theoretical near-field imaging setup. (Image reproduced by courtesy of RESONETICS <http://resonetics.com/>).

2.4.2 Energy Density

Changing the demagnification ratio affects the energy density as shown by equation 2.6:

$$E_{d(IP)} = F_d * D^2 \quad (2.6)$$

Where:

$E_{d(IP)}$ = Energy Density at the Image Plane (J/cm²)

F_d = Laser Fluence (J/cm²)

D = Demagnification Ratio (-)

For example, if the excimer laser has a pulse energy of 300mJ within a beam size of 24mm x 10mm, one expects a laser fluence of approximately 125mJ/cm². Therefore, at a demagnification of 10, the energy density at the workpiece will be 12.5J/cm² assuming no transmission losses [27].

2.4.3 Image Size

Changing the demagnification ratio will also affect the final image size as shown by equation 2.7.

$$\text{Image Size (mm}^2\text{)} = \text{Laser Beam Size (mm}^2\text{)} / D^2 \quad (2.7)$$

Where the laser beam size is determined by the aperture area on the mask used for laser beam projection at the workpiece. For an example: If the mask has a hole of diameter 300 μm , then at $D = 10$, the image will have a hole diameter of 30 μm [27]. This is expressed in equation 2.8.

$$\text{Hole diameter at the image plane} = \text{Hole diameter of the mask} / D \quad (2.8)$$

The mask projection technique has several attractions such as:

- The mask is distant from the sample and so damage from debris can be avoided
- Demagnification allows the mask manufacture constraints to be less severe
- The system has flexibility since only the mask has to be changed to produce another pattern
- The laser fluence is higher at the sample than at the mask due to demagnification, and hence, the mask can be used at well below its laser damage threshold. This means that lifetime issues of the mask can in general, be ignored
- Having independent control of the mask and the workpiece allows complicated processing techniques to be used
- Non-planar substrates can still be processed even with a planar mask
- Multiple features of varying size and shape can be machined simultaneously. For example, in certain applications it is possible to drill a large array of holes in a single laser burst
- Tight machining tolerances as low as ± 1 micron can be achieved [18, 22, 25].

Mask projection is a very well established technique in the manufacturing of semiconductor components such as computer microprocessors and memory chips [22].

2.5 Mask Projection Ablation Techniques

A number of different mask-imaging techniques for pulsed laser ablation are employed in many industrial applications. There are in general three main elements when looking at mask projection: the mask, the lens and the workpiece or target. Furthermore, there are three different operational modes: static, “move and stop” (also known as “step and repeat”) and continuous translation. Since it would be impractical to move the lens itself for standard mask projection systems the position of lens is normally fixed, hence the number of possible combinations is reduced to nine. In order to achieve a more sophisticated technique, more information was put into the mask. The possibilities are half tone [28], gray scale [5, 29] or object array [30] techniques. This research work concentrate on the latter in the following sections, since the new CAD/CAM system development was based on these techniques.

2.5.1 Machining with Static Mask and Workpiece

The simplest combination is to keep everything static. This gives a very straightforward setup with a fixed mask and target to expose the latter with enough laser shots until the desired depth is reached, and the hole replicated shape would reflect the mask. The basic concept of an excimer laser near field mask projection – that is, where both the mask and workpiece are static, is illustrated schematically in Figure 2.6 [31].

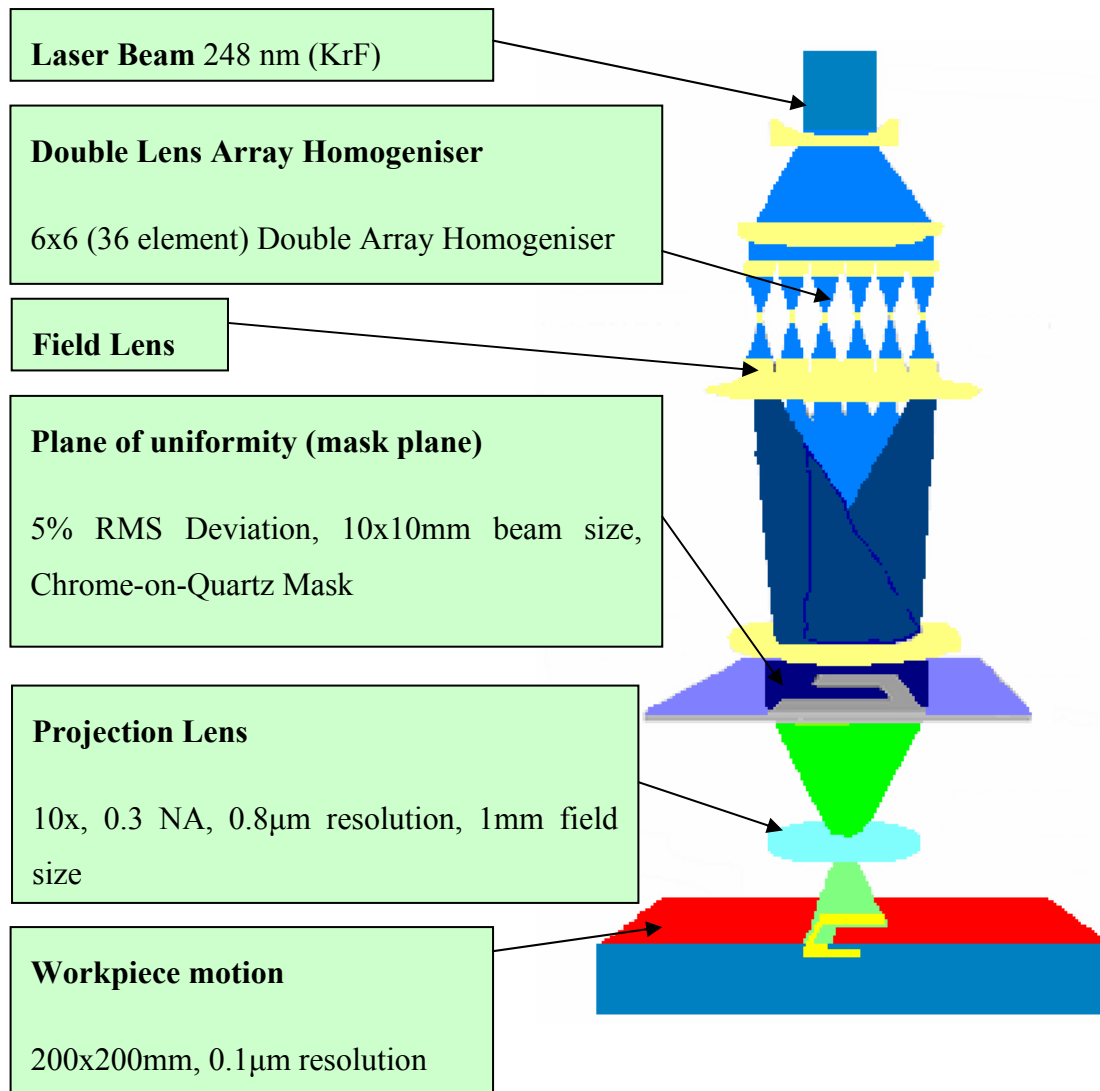


Figure 2.6: Schematic of an excimer laser mask projection system [31].
The typical near-field mask projection system comprises of:

- Laser Beam Source
- Field lens
- Beam homogeniser
- Mask
- Projection lens
- Workpiece

In a mask projection system, the excimer laser beam (typically 20x10mm) is shaped and homogenised to improve energy distribution of the beam. The purpose of a beam homogeniser is to break up the beam into small sections and recombine them in a pattern that increases the overall fluence over a smaller cross-section. Typically the lens arrays between 6 x 6 and 9 x 9 elements are used and the 36 or 81 individual beam elements are combined by overlapping them at the mask plane to average out localised variations in beam intensity and can achieve mask illumination uniformities of around $\pm 5\%$ RMS deviation. This is done since unaltered output distribution of an excimer laser is not uniform and machining with a non-uniform distribution leads to variations in the ablation depth [25].

A mask is placed at the plane of best uniformity of the homogenised beam. This plane - the mask plane - thus contains a pattern (the mask), which is illuminated with the uniform laser beam. A high-resolution projection lens projects the mask pattern onto the workpiece to produce an image of the mask pattern there. This is usually accomplished with a demagnification as well, so that the image is smaller than the mask pattern [22].

The lens and the optical system define the maximum resolution, which is achievable at the workpiece and the field size of the lens restrict the maximum size of the image, since neither the mask nor the workpiece move. The size of the image is thus fundamentally limited to the lens field size, which is typically in range from hundreds of microns to many millimeters. The practical limitations of this technique with a static mask and workpiece is that only patterns smaller than the beam size can be used, and hence, its applicability is restricted to only drilling type of applications. One of the most common uses of this technique is in the drilling of holes where a single hole or a small array of holes is required on a component [32, 33].

There are two enhancement of the basic process that further increased applicability of static projection. One technique is called Step-and-repeat process and the second one is called Indexed Masking process. These two methods can be considered extensions of the static projection technique since the mask and workpiece are stationary during the production of the microstructures, even though the mask or workpiece are moved in between the processing steps [31]. They are explained in more detail in the following sections.

2.5.1..1 Step-and-Repeat Machining

Adding stages in the imaging plane makes it possible to introduce a step-and-repeat process where the same object pattern is ablated in different but well-defined locations on the work piece.

The technique of step-and-repeat mask projection involves the lateral motion of the sample in between the production of structures: the laser is fired with a static mask and workpiece to produce a structure; the laser is turned off; the sample is moved laterally in X or Y direction, the laser is fired to produce the same structure again. Very large areas can be covered with the same structure by repeating this procedure since the only limitation in size of the sample is the XY motion tables [10, 11].

The patterns which can be produced range from simple holes placed at discrete position to complicated designs which are nonetheless self-repeating when place side by side. The mask does not have to contain just a single feature but can have multiple shapes on it, as long as the Step-and-repeat processing can replicate the overall pattern required. In this way, the efficiency of the processing can be increased by machining more than a single feature at the time. The advantages of step-and-repeat processing are that it is a relatively simple technique, the multiplication of repetitive features is straightforward, and complicated patterns can be produced by appropriate control of the samples. The main disadvantage is that it is only applicable to single, small patterns or ones that are self-repeating and that laser has to be switched off between each step. This technique is now commonly used in applications such as the micro-drilling of ink-jet printer nozzle heads [18, 22, 25].

The basic principle of step-and-repeat is shown in Figure 2.7.

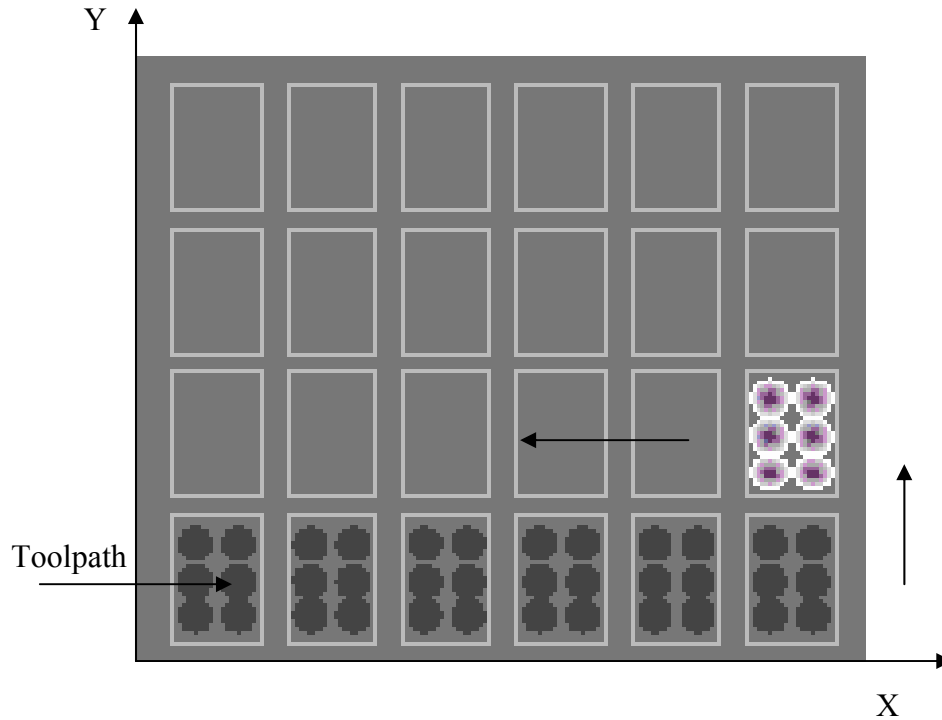


Figure 2.7: Step-and-repeat mask projection process (Image reproduced by courtesy of RESONETICS <http://resonetics.com/>).

Figure 2.7 shows 24 discrete locations that need to be machined. At each location a self-repeating pattern with 6 individual holes will be applied in an array (four rows by six columns) arrangement.

2.5.1..2 Mask Indexing Technique

The second extension of static projection involves the positioning of a new mask pattern in between production of the structures: the laser is fired with a static mask and workpiece to produce a structure, the laser is turned off, the mask is moved laterally to position another mask pattern under the laser beam, the laser is fired again over the same workpiece area to superimpose the new mask pattern over the previous one. This technique is called indexed mask projection [34]. An example of indexed mask projection technique is shown in Figure 2.8.

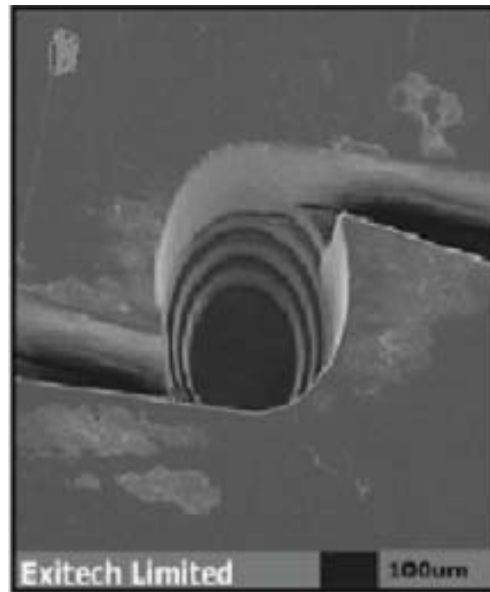


Figure 2.8: Microstructures produced by Indexed mask projection [21].

Here, the authors show a nozzle device where the central section contains a stepped structure leading down to a small hole. The steps inside the central well were produced by using different diameter apertures to define the different steps - a particular diameter circular section was machined to a specified depth, the mask changed for another one and the machining repeated for the new diameter and depth [21]. The authors highlighted two important points; first that the positioning accuracy of the holes is governed by the accuracy of the workpiece stages and second the reproducibility of the quality of the holes is determined mainly by the laser stability [31].

2.5.2 Synchronised Mask Scanning

Synchronised mask scanning is the most versatile of the projection techniques used in excimer laser micromachining, and basic concept of this method is shown in Figure 2.9. This technique can be used to manufacture microstructures, which are in a non-repeating pattern, with micron resolution and over areas of many thousands of square millimeters. This is accomplished by a precise synchronization of the travel of the mask and workpiece stages in conjunction with the firing of the laser. Any pattern, which is not discrete and self-repeating, and hence, cannot be produced by other techniques, can be

produced by synchronised mask scanning provided that it can be produced on an appropriate mask [18, 22, 25].

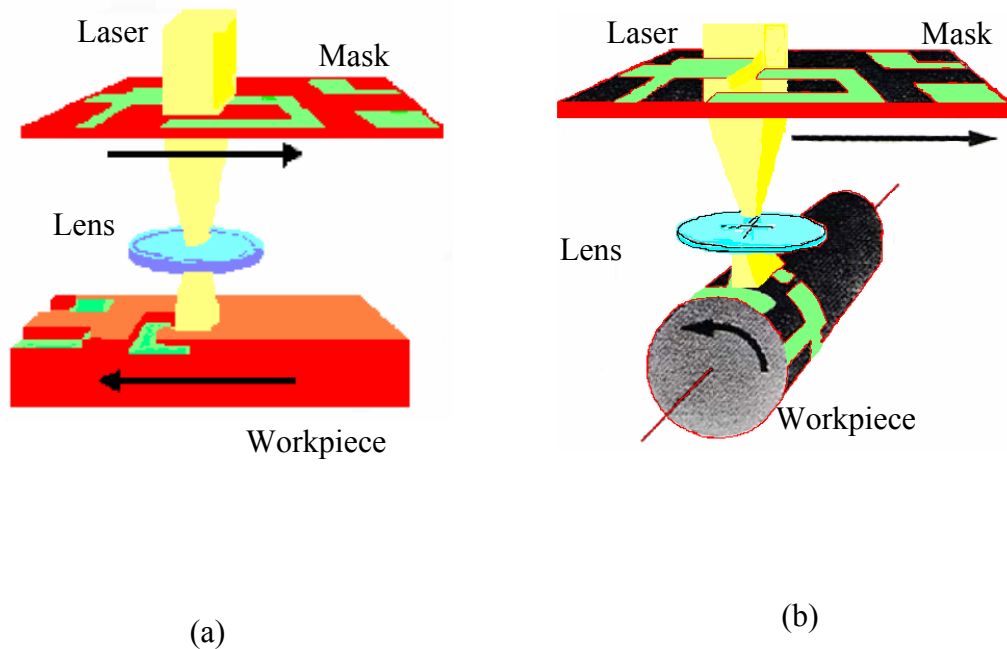


Figure 2.9: Synchronised mask scanning technique: (a) where workpiece movement is a translation and (b) where workpiece movement is rotation [31].

Examples where this method is used include:

- Laser engraving (the production of complex patterns printing, publicity, marking or coding purposes) (RESONETICS <http://resonetics.com/>).
- Demetalization (the production of electrode and other active electrical features for circuits, sensors and displays or marking applications) (RESONETICS <http://resonetics.com/>).
- Marking (the production of marks for aerospace, automotive, computer industries) (RESONETICS <http://resonetics.com/>).
- Deep ablation (the production of 3D prototypes for LIGA (German acronym for Lithography-Galvanoformung-Abformung), type applications) [18, 22, 25].

2.5.2..1 *Machining with Moving Mask*

Mask dragging is one of the techniques where only the mask is moved during the part processing. This method is shown in Figure 2.10.

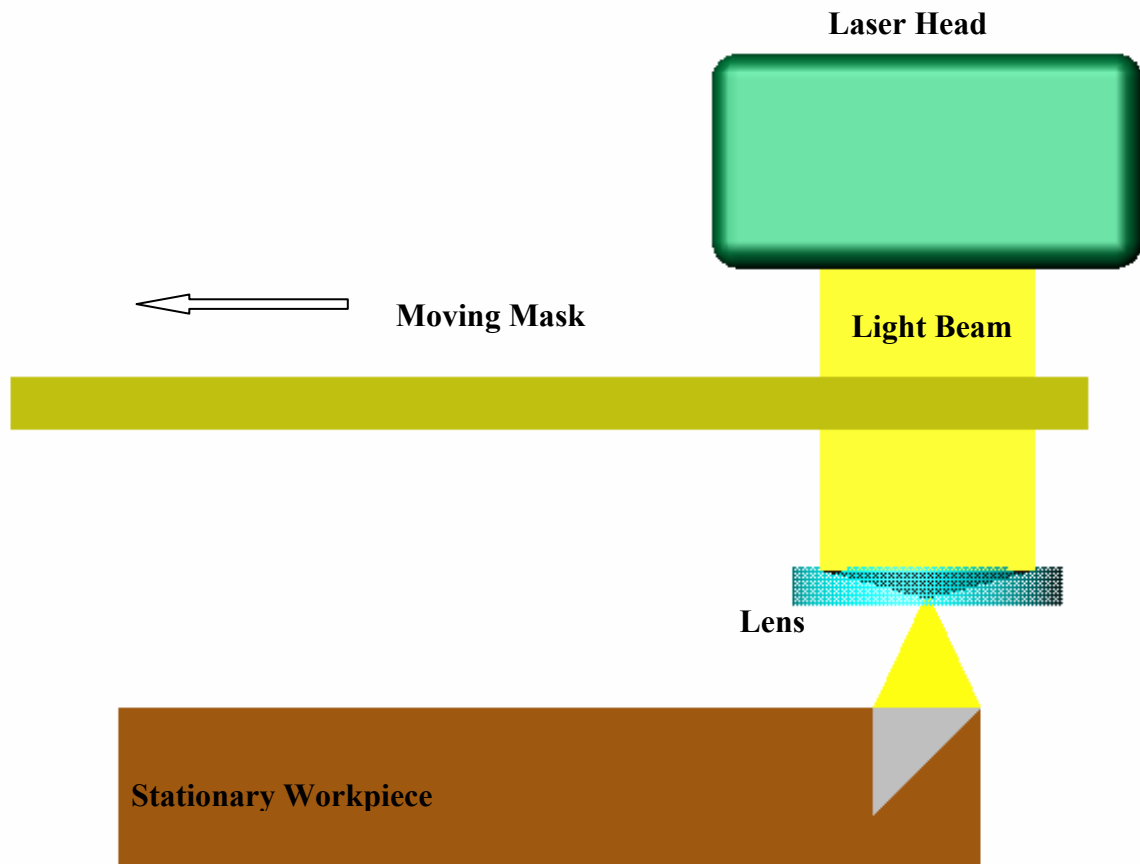


Figure 2.10: Mask Dragging Method.

The system has a pattern contained in a mask, a projection lens to image the mask onto the workpiece and motion stages for both the mask and the workpiece. Keeping the workpiece stationary while moving the mask can produce ramps if the laser fires at the constant repetition rate, because it can be arranged that one side of the exposed area receives more laser shots than the other side during the motion of the sample under the laser beam [35].

Another common use of the mask dragging technique is for the production of tapered holes where the application demands some contouring of the whole profile, for example in the production of ink-jet printer nozzles. Thus, instead of performing static

mask and workpiece drilling, the motion of the mask – usually a circular aperture – while drilling can lead to controllable profiling. The exact shape of the hole contour, which is produced, is governed by the size of the mask and the way in the motion of the mask and the laser firing is combined [18, 22, 25].

2.5.2..2 *Machining by Moving Workpiece (Workpiece-Dragging)*

Upgrading the stages by numeric control enables the use of “workpiece-dragging” [25, 28]. The principle of this technique is shown in Figure 2.11, where it can be seen that only the workpiece is moved during the laser processing.

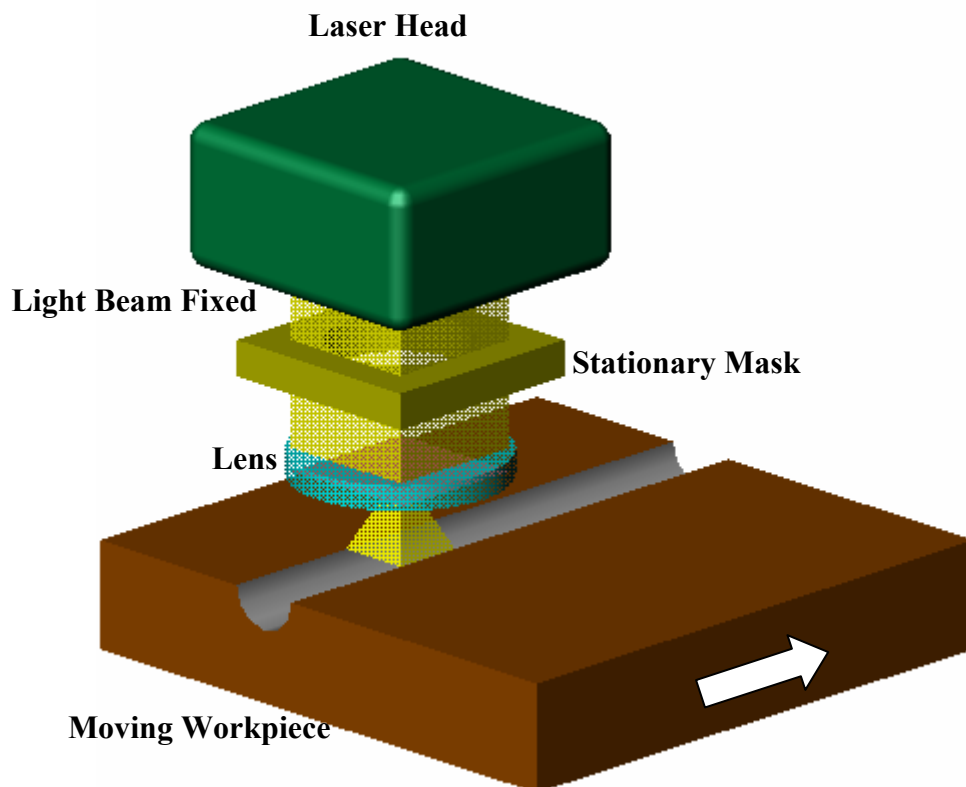


Figure 2.11: Workpiece moving or workpiece-dragging method.

Usually a simple aperture is used at the mask plane and the laser fired during the movement of the sample to produce a trench or track. Furthermore, by finding the right balance between the repetition rate of the laser and the velocity of the stages it is possible to vary the channel profiles, which represent the mask shape. This is commonly achieved

by a special Position Synchronised Output (PSO) card (see Appendix B), which generates the laser trigger pulses. The most powerful use of the PSO is as a position synchronised trigger source when the PSO counts stage encoder pulses and issues a pulse at a programmable incremental number of encoder counts (or stage steps) [36]. This is shown by equation 2.9:

$$PSOD = E_s * \frac{I_x}{n} \quad (-) \quad (2.9)$$

Where:

$PSOD$ = Position synchronized output distance (-)

E_s = Encoder steps per 1 mm (-)

I_x = Beam size at the workpiece along X-axis (mm)

n = Number of pulses per area (-)

Any mask object designed will be reproduced as an equivalent channel as long as there are no undercuts and the depth of the channel is within process designed limits; e.g. a circular mask will give a groove with a cylindrical bottom.

Applying different velocity profiles provides more flexibility to micro-structuring materials. With a simple square aperture it is possible to machine steps, ramps and curves.

When the workpiece traveling along X-axis then velocity of the workpiece is usually given by equation 2.10:

$$v_x = \frac{I_x}{n} * PRF * 60 \quad (\text{mm/min}) \quad (2.10)$$

Where:

v_x = Velocity of the workpiece along X-axis (mm/min)

I_x = Beam size at the workpiece along X-axis (mm)

PRF = Pulse repetition frequency (Hz)

n = Number of pulses per area (-)

The production of straight channels or grooves can be considered as one-dimensional dragging along the length of the channels. One of the reasons why workpiece dragging is an important technique is because it can be used for the production of controlled, multi-shaped 3D microstructures. This is achieved by using workpiece dragging in two dimensions – making channels or shapes in two directions on the same sample. This can result in features such as pyramids, cones, lenses etc.

There are advantages to using the technique of workpiece dragging rather than that of synchronised scanning, namely:

- a mask containing all the features does not have to be produced
- there is great flexibility in changing the design of the pattern to be produced just by appropriate programming of the workpiece motion
- the profile of the channel can be changed by correct choice of the aperture used at the mask plane [18, 22, 25].

2.5.2..2.1 Synchronised Image Scanning Technique

Synchronised Image Scanning (SIS) is a laser micro-machining technique where the information for the ablation of a specific 3D feature is stored as a linear array on a photolithography mask [37]. The feature is then written by synchronised motion and laser firing such that the firing frequency of the laser corresponds to the spatial pitch of the features. The starting point is the micro-feature that has to be machined. There are virtually no limits to the design of the feature as long as there are no undercuts [21].

In Figure 2.12, the authors demonstrated the basic principle of SIS in three steps, the first laser pulse imprints the three squares on the mask into the workpiece, and the next pulse will be triggered as soon as the workpiece has traveled exactly the pitch distance.

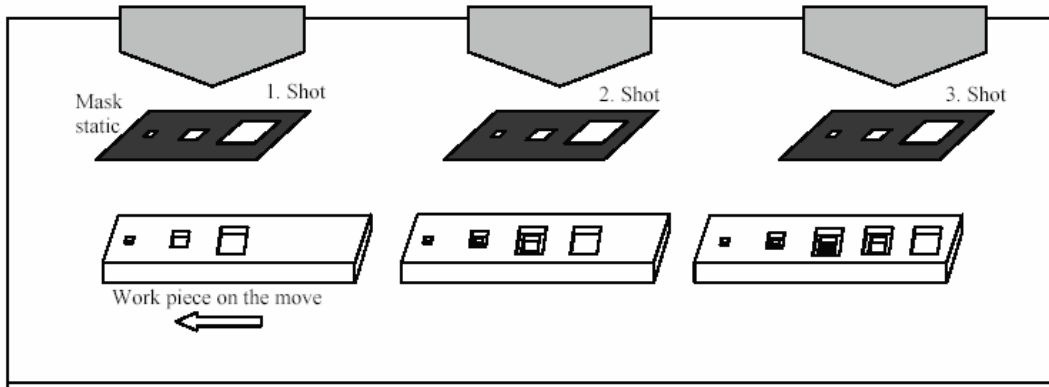


Figure 2.12: Principle of SIS showing the first three shots with moving workpiece and static mask. The laser beam illuminates all apertures with a single pulse [38].

Positions 2 and 3 on the workpiece have now received two exposures. By moving the workpiece further and triggering the laser again at the pitch distance, the third laser pulse will finish off the feature on position 3. Continuing this process will produce three-step pyramid every next laser pulse. To make the whole process efficient the work piece has to move continually, the laser being triggered on the fly. This requires highly accurate laser triggering with low-jitter signals, and highly accurate stages and encoders [21].

The authors use a simple square pyramid as an example to demonstrate efficiency of this technique. They assumed a footprint of $30\text{ }\mu\text{m} \times 30\text{ }\mu\text{m}$ and a depth of $30\text{ }\mu\text{m}$ and that the pyramids should be on a $30\text{ }\mu\text{m}$ pitch on the substrate. The next step was to slice this feature. This technique is well known in stereolithography [39]. The thickness of the steps were equal to an ablation rate between $\sim 40\text{ nm}$ and $\sim 300\text{ nm}$ per shot, depending on which polymer was used [40].

The slice thickness of 150 nm was chosen, which resulted in 200 cuts, every cut being a square. By bringing these squares into a linear array at a $30\text{ }\mu\text{m}$ pitch an object of 200 squares contained in an envelope of $6\text{ mm} \times 30\text{ }\mu\text{m}$ was obtained. It can now be magnified to match the demagnification of the imaging lens and for a 5x lens objective generates a mask object of $30\text{ mm} \times 150\text{ }\mu\text{m}$. To make best use of the given laser energy authors array 200 of those objects on a $150\text{ }\mu\text{m}$ pitch leaving a mask pattern of $30\text{ mm} \times 30\text{ mm}$. Moving the work piece linearly at a speed of 6 mm/s , and triggering the laser to fire a pulse every $30\text{ }\mu\text{m}$ of travel, will yield 40,000 copies of the designed pyramid in

one second. One area where this plays an important part is in display applications, where there are high-density micro-imaging elements on large areas. This simple example support the authors claim that SIS is a highly efficient technique to produce micro-features.

2.5.3 Synchronised Overlay Scanning

The basics of standard synchronised mask scanning systems have been described in section 2.5.2. To extend this technique and add depth information, the synchronised overlay scanning (SOS) method additionally shapes the laser beam, which is used, and it is this choice of beam shape that determines the depth profile imparted to the microstructures [21]. The concept of synchronised overlay scanning is depicted in Figure 2.13.

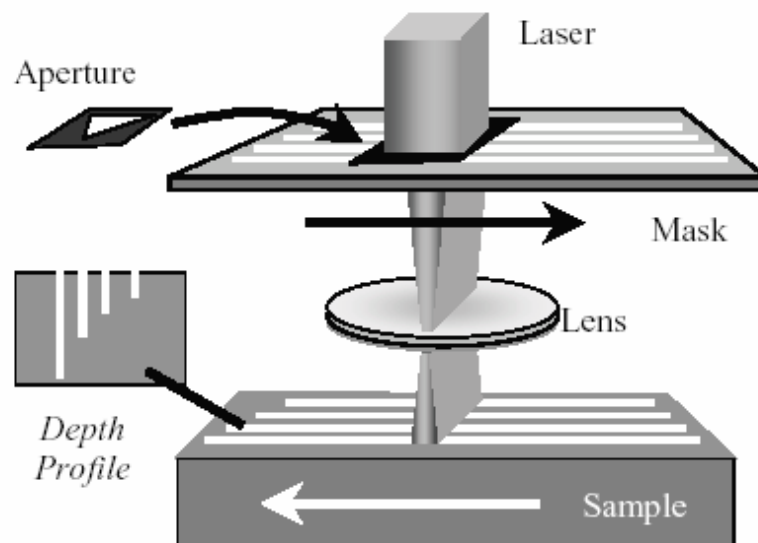


Figure 2.13: Technique of synchronised overlay scanning [41].

The SOS technique uses standard synchronised scanning where the mask and the workpiece are moved in unison but in addition to this, an aperture is also placed above the

mask to tailor the shape of the beam. The shape of the aperture determines the depth profile in the workpiece, as shown in Figure 2.13, and a triangular aperture shape gives rise to a triangular depth variation in the material as seen in cross-section. Another feature of the SOS method is that the choice of mask (which determines the features to be made) is independent of the choice of beam shape aperture (which controls the depth profiling). This means that there is great scope for selecting appropriate combinations of masks and apertures depending on the specific requirements of the application. Synchronised overlay scanning techniques are now being applied in many different development areas such as; microfluidic transport systems and mixing devices, lubrication equipment, components for optical devices and for display panel enhancement where the combinations of high-resolution microstructures and changes in feature height can be of benefit in the micro product designs [41].

2.6 Serial Scribing (Direct Machining)

Figure 2.14 describes technique of machining where the laser beam is focused to a small spot and it is moved over the workpiece to produce the desire patterns. Movement of the workpiece relative to the beam would produce the same effect. The laser beam movement relative to the workpiece is synchronised with the firing of the laser. The relative movement of the beam is ensured using galvo-scanner and motorised stages [42].

This technique is used in a wide range of micromachining applications where high precision and small feature sizes ($0.01\text{ }\mu\text{m}$) are essential, including micro via drilling, fuel injector drilling, gas sensor drilling, solar cell scribing and MEMS prototyping [18, 34].

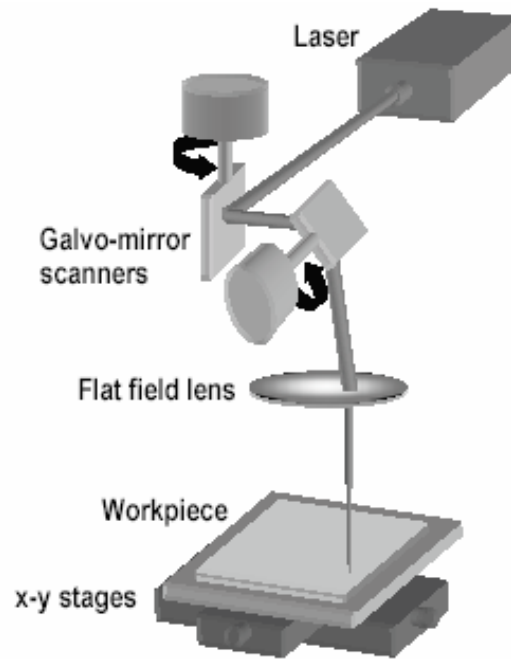


Figure 2.14: Schematic of the direct machining method using a galvo-scanner and motorised X-Y translation stages [42].

2.6.1 Bow-Tie Scanning

Bow-Tie Scanning (BTS) is another extension of Serial Scribing or “direct” machining technique based on recent developments in the area of speed and accuracy of modern stages and galvanometer mirror scanner systems to allow the accurate and rapid regular patterning on large planar substrates. This technique is particularly suited to applications in which regular lines or dense patterns of contact holes in a regular array are required (e.g. solar panels and flat displays). Figure 2.15 shows a schematic of the BTS technique where a focused laser beam is scanned in a straight line at high speed across a section of the substrate whilst the substrate is moved on a linear stage at constant speed in the direction perpendicular to the galvo-scanner beam scan path. The galvo-scanner deflects the beam in a ‘bow tie’ trajectory to track the motion of the substrate whilst the laser is gated on and then returns to the start of the next track (separated by defined pitch from the first) when the laser is gated off. This type of combined beam scanning and substrate motion has been used extensively for scribing, marking, and micro via drilling, however, it has only recently been employed successfully in the processing of large substrates for flat panel displays and solar panels [38].

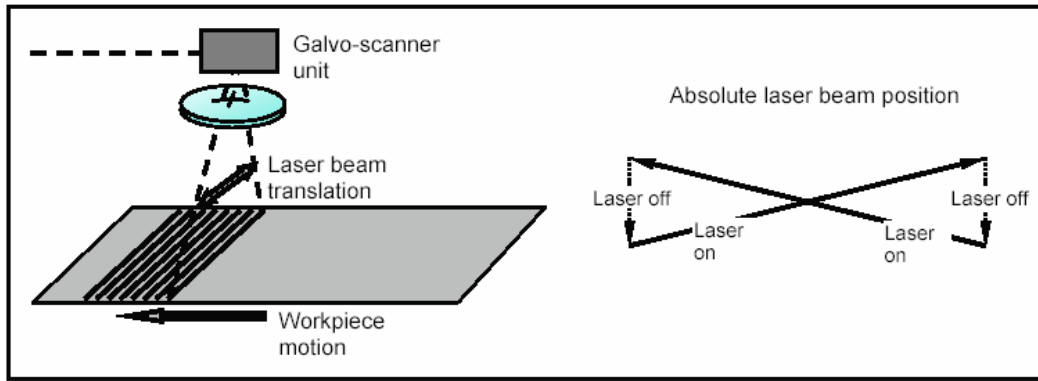


Figure 2.15: Schematic of BTS technique - motion compensation with a typical bow tie shape of the scanner movement to provide straight line processing [38].

2.6.2 Sync Scan

In order to machine a large area patterns using galvo-scanner unit based systems has always inherited problems of stitching together individual scan fields. Laser firing has to be turned off for the workpiece to be moved to the position of the next scan fields. This causes an increase in the total processing time. A solution to this problem is to have system that can continuously move workpiece during machining while scanner scans the beam over the area in the scan field. The recent series of digital signal processing systems enables synchronization of the workpiece position and the scan field. This technique is termed as Sync Scan [41]. The system does not require a mask comparing to standard mask projection systems and another advantage is that design data can be directly imported from a CAD package.

Sync Scan technique works by dividing the patterns into rectangular sections where the length of the rectangle represent the size of the scan area, while the width of the rectangle is typically a trajectory for the workpiece stage travel path, i.e., the scanner mirrors are constantly updating with pattern data so the constant machining can be performed. Typical scanning speeds are in range of a few meters per second and the workpiece stages moves at speeds of 10-20mm/sec. Scan field size is between 20-100mm and positioning accuracy obtainable in microns range. The use of Sync Scan in the manufacture of display devices is likely to be a major application [41].

2.7 Anvik Corporation HexScan™ Series Laser Projection System

The core technology developed for the Anvik large-area lithography systems is schematically illustrated in Figure 2.16. The panel and the mask are rigidly mounted on a single planar stage that is capable of moving them synchronously in both x- and y-directions. The illumination system comprises a UV excimer laser light source (248nm KrF) and a beam-processing optical system. The beam processing system illuminates the mask from below (through a cutout in the stage) in a uniform, hexagon-shaped illumination region that is typically 50 mm in size. The hexagonal illumination configuration ensures that the whole exposure is completely seamless and uniform. The new laser projection imaging system provides not only high resolution (10 μ m) and precise alignment ($\pm 2.5\mu$ m), but also high throughput (120 panels/hr, panel exposure area: 460x610 mm) with commonly used dry-film and liquid photoresists. The Anvik laser projection imaging systems are the cost effective solutions for volume production of high performance printed circuit boards, displays, flex circuits and other microelectronics system fabricated on large substrates ([43, 44], [45]). The Anvik systems technique of hexagonal-seamless scanning eliminates stitching errors between adjacent segments on the substrate during imaging since the mask and substrate are mounted rigidly on a single planar stage, hence issues concerning relative mask-substrate movement during imaging are eliminated. This approach also provides a solution to control the exposure dose stitching errors, therefore it was of particular interest for this research work.

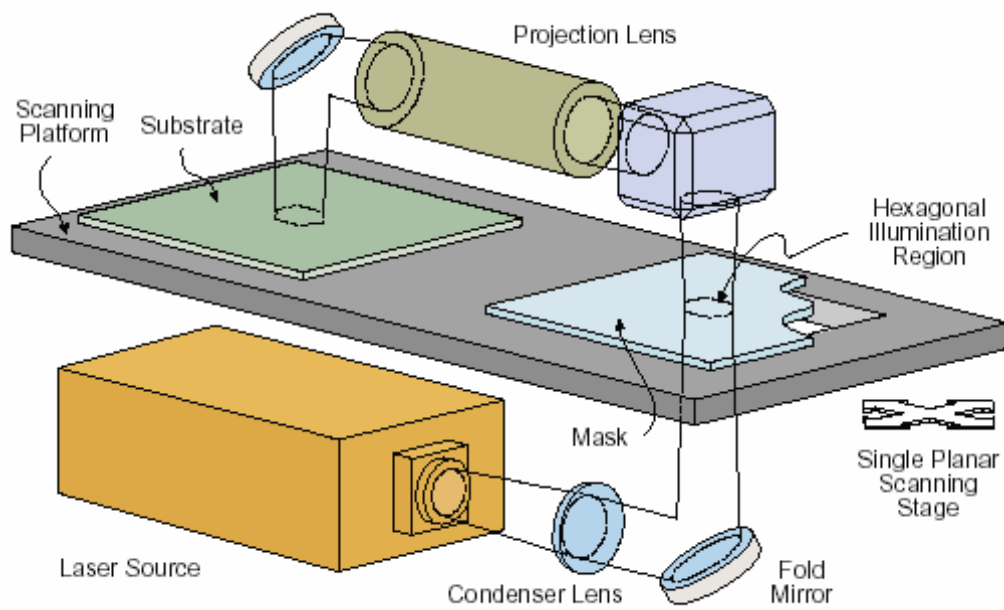


Figure 2.16: Anvik's high-resolution, high-throughput laser projection imaging technology, showing scanning with a planar stage and hexagonal beam [45].

2.8 CAD/CAM Systems for Excimer Lasers

The determination of proper mask and excimer laser process parameters that optimise part processing has been a major problem to be resolved by the users of excimer laser systems. There has been several works presented on developing methods to determine optimised tool path, mask design, and laser processing methodology based on different criteria. Since laser ablation processes always involve a certain amount of error in the process, research has also been done on developing a strategy to significantly reduce the amount of error. Some work has also been conducted on NC advanced control methods related to the minimization of tool paths required during laser ablation processes.

Lee et al. [46] presented their new method for fabricating axially symmetric 3D microstructures based on a KrF 248 nm excimer laser micromachining system. A novel mask contour scanning method is developed for obtaining a pre-described continuous surface profile with high accuracy and fast machining speed. Rotating the sample and

firing the laser pulses continuously produce a 3D axially symmetrical structure. The profile of the machined structure depends on the design of the mask pattern and machining parameters.

Figure 2.17 (a) shows an example of mask design for making nozzle type convex microstructure. The window opening area is where the laser beam can pass through and then project onto the sample surface for the machining. Figure 2.17 (b) shows that machining depth is a function of the radius and can be expressed with a simple equation:

$$h(r) = d * N * \frac{S(\rho)}{2\pi\rho} \text{ and } r = \frac{\rho}{10} \quad (2.11)$$

where $h(r)$ is the overall machining depth at radius r , d is the machining depth per laser pulse, $S(\rho)$ the total arc length of opening aperture at radius ρ of the mask, and N total number of laser pulses fired during the machining. The relationship between ρ and r is due to the 10x demagnification factor of the imaging system settings. In short, the term $\frac{S(\rho)}{2\pi\rho}$ in equation 2.11 represents a probability function at radius ρ or r . The product of the probability function and the total number of laser pulses determines the number of laser pulses received at position r , and therefore the overall machining depth $h(r)$.

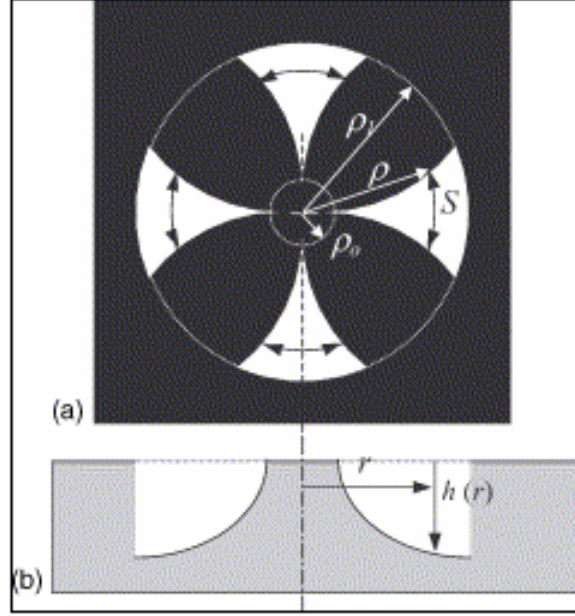


Figure 2.17: Excimer laser micromachining of a 3D microstructure with a laser mask and sample-rotation method [46].

The key idea is to conduct a planetary motion of the sample so that the singularity problem in mask design can be resolved. It uses the laser energy effectively by allowing a maximum portion of laser beam to pass through the mask window for the machining. The method has great flexibility in the mask design and sample movement, and thus the profile shapes. Therefore, it can be applied to fabricate surface profiles in various applications of 3D microstructures. The proposed method has great potential in fabricating micro-optical elements, especially the refractive type of microlenses. The concept of the proposed excimer laser micromachining method can be extended to non-axially symmetrical surface contour by conducting a non-circular stage movement.

Choi et al. [47] introduced a new approach called Hole Area Modulation (HAM) for machining 3D feature using the excimer laser. When micromachining by using HAM-based excimer laser, laser ablation depth is influenced by the hole diameter on the mask, pitch, transferring velocity, transferring distance and the number of pulses. The ablation depth is proportional to the area of hole diameter on the mask.

Charrier et al. [101] represented a novel method to produce a high precision pattern of copper tracks on both sides of a 4-layer conformal radar antenna made of PEI polymer and shaped as a truncated pseudo-parabolic cylinder. After 2D layer design in Allegro

v1.2, the resulting Gerber file-format circuits are wrapped around the antenna shape, resulting in a cutter-path file, which provides the input for a postprocessor that outputs G-code for robot and laser control. A rules file contains embedded information such as laser parameters and mask aperture related to the Allegro symbols. Comparison between functionality and similarities of the main modules described in Charrier et al. [101] approach and this research work was explained in Appendix D.

Jolic et al. [48] developed a multiple mask technique used for micromachining of corner cube structures. The laser micromachining method used in this work consists of varying the projection aperture during machining by applying relative motion of two overlapping masks as shown in Figure 2.18. The effective projection aperture is the two-dimensional area defined by intersection of the apertures of each mask. During machining, the volume of material removed per pulse is defined by the etch rate and the effective projection aperture. Figure 2.18 shows the mask patterns used for excimer laser micromachining of corner cube structures. The rectangular apertures shown in Figure 2.18 (a) were produced from a stainless steel shim using a Nd:YAG laser, while the equilateral-triangle shaped apertures shown in Figure 2.18 (b) were realized on a conventional chrome-on-quartz mask. The rectangular apertures were aligned parallel to the triangles, and positioned to completely enclose them as shown in Figure 2.18 (c).

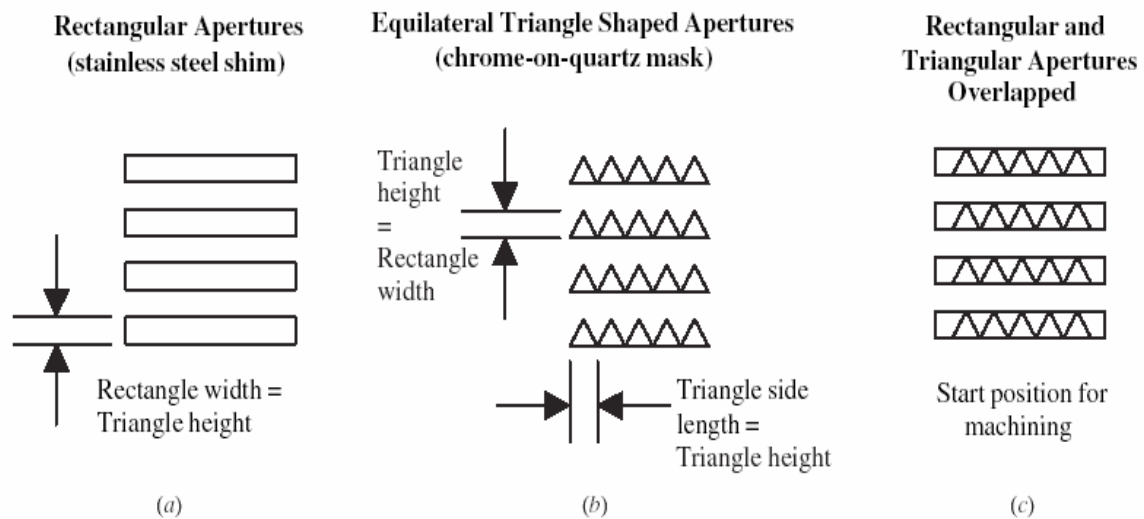


Figure 2.18: Multiple masks used for machining of corner cube structures [48].

Figure 2.19 illustrates the machining steps employed and the pulse-by-pulse formation of structures in the workpiece. The left-hand side of Figure 2.19 shows the mask positions employed for each laser pulse, while the right-hand side shows the patterns formed on the workpiece after each laser pulse. The triangular apertures are moved perpendicular to the fixed rectangular apertures in the direction indicated in Figure 2.19, in order to maintain an equilateral-triangle-shaped effective projection aperture of gradually reducing size. The total distance moved by the triangular apertures is equal to the rectangular apertures width. The triangular aperture speed is proportional to the selected laser repetition rate and is set equal to the rectangular aperture width divided by the number of laser pulses required to achieve the corner cube depth, multiplied by the laser repetition rate [48].

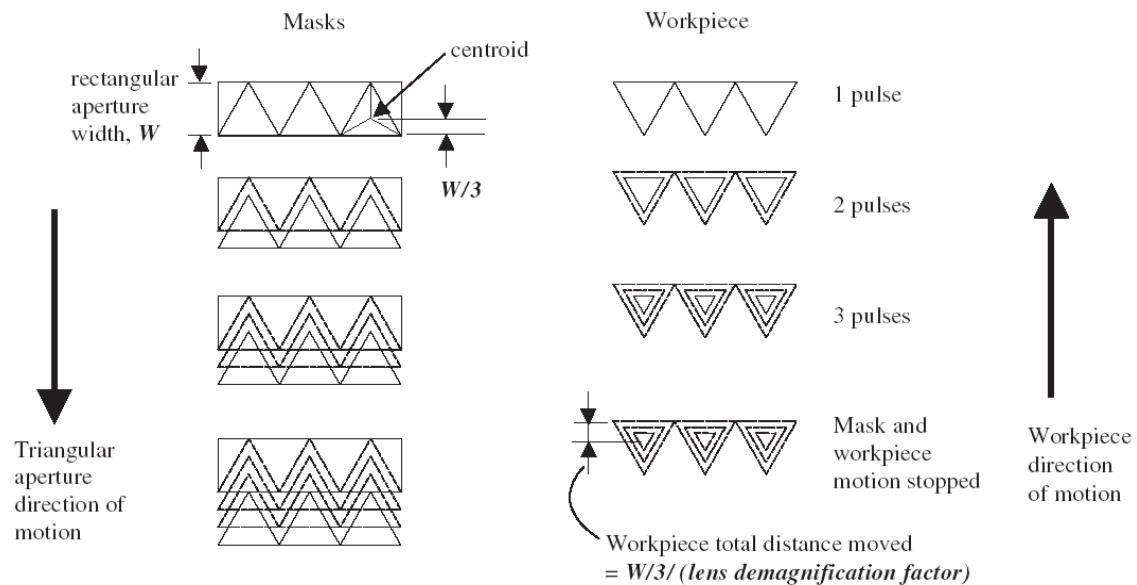


Figure 2.19: Machining steps employed and pulse-by-pulse formation of structures in the workpiece [48].

Boehlen et al. [49] developed a new approach using existing CAD/CAM software (alphaCAM by Licom Systems Ltd.) as a basis for a GUI and using the API to communicate with alphaCAM software, to generate their own tool paths. The following laser machining options have been implemented: cutting, hole drilling, slot cutting, 2D area clearing, pocketing and 2.5D surface machining. Once the toolpaths are available, a

post processor translates this information into CNC commands that control a scanner head. This scanner head then guides the beam of a UV solid-state laser to machine the desired structure by direct laser ablation.

Perkins [50] in his thesis work produced CNC scripts to be used to control an Exitech's S8000 series excimer laser micro-machining workstation. Using a Visual Basic tool kit he was able to produce software that allows CNC scripts to be processed, lifting the restrictions and letting the full potential of the system be realised. The developed software fulfilled the project objective, which was to allow large CAM produced CNC scripts to be used to control an Eximer S8000 series micro-machining workstation. This was met firstly by a stand-alone piece of software, then secondly by incorporating a limited version of this software into a commercially available CAM package using Visual Basic for Application (VBA)

Tonshoff et al. [3] reported on the fundamental basis of controlling and modelling the structuring process and the existing tools for the 3D micro structuring with Fluorine (F₂), 157nm, excimer lasers. They developed a software tool that makes simulation of manufacturing micro-components possible. It is based on the complex NC code and on the exact model of the single ablation.

Tonshoff et al. [1] developed a 3D-CAD interface for micromachining with an excimer laser. They developed special CAD/CAM software that includes the excimer laser specific aspects of workpiece modelling and the process itself such as facts that the process of 3D microstructuring with excimer lasers is based on the ablation of discrete removal volumes and to produce complex microstructures a large number of discrete ablations is necessary. Due to the limited repetition rate of conventional excimer lasers (less than or equal to 400Hz), the production takes up to hours.

Therefore, strategies to minimize the processing time using flexible beam shaping with an NC mask were implemented. In regards to single ablations with a varying shape and depth, a special path calculation was programmed, that allows the processing of all laser pulses within a short time. All these functions were assembled within a program with a user interface that allows more simple and economic manufacturing of prototypes and small batch series. Unfortunately, more details about the software efficiency and processing speed couldn't be established from the data reported.

Tonshoff [2] described the potential of 193nm treatment of 3D micro surfaces with a process-optimised machine and data handling system. Due to limitations of conventional micromachining technology for brittle transparent materials in the micro range, a new laser machining beam guiding and data handling system was designed and built. The paper shows the possibilities of 193nm treatment of brittle materials such as glasses. The excellent absorption behavior of materials at 193nm compared to 248nm leads to damage free microstructures, therefore, to achieve good surface roughness for the majority of glasses including aluminum oxide, the chosen wavelengths needs to be 193nm. Smooth surfaces are only possible with a high process stability of the ablation geometry and controlling the depth per pulse as well as the beam spot size and geometry. Compared with 248nm where commercial mirrors are available, no mirrors have been found to have long-term stability for 193nm radiation. Due to this fact, a mirror free machining concept was built and described. By developing new software tool for automatically generating microstructures the micro machining station becomes an effective and powerful production tool for various areas of micro components. The software is capable of breaking down the total removal volume of the structure into laser specific volumes, which can be processed by one laser pulse. By using a flexible mask instead of a fixed mask with an imaging scale of 1:40, it is possible to change the contour and the cross-section of the removal area between $1 \times 1 \mu\text{m}^2$ and $150 \times 150 \mu\text{m}^2$ onto the workpiece surface. When changing the energy density of the laser beam between 1 and 40 J/cm^2 , a removal depth between 0.1 and $1,5 \mu\text{m}$ per laser pulse can be achieved, depending on the material and the adjusted wavelength.

Laser Zentrum Hannover, revealed current status and development of several projects; “ELPEC II” excimer laser processing system developed by cooperation between Laser Zentrum Hannover and Kugler GmbH [51]. The system is capable of micro and precision machining, flexible processing, single and serial fabrication, research and development. The system optionally provides CAD/CAM CAGILA® software. This software provide as stated by authors the following characteristics:

- Easy to use and simple training
- Interfacing with other CAD/CAM software (AutoCAD, 3D Max Studio)

- Variety of application possibilities

“PROMIS” (Production Technology for Flexible Micro-structuring of Passive Optical Components) project was also discussed [51]. The main objective of this project was the industrial implementation of a shaping process method for the microstructuring of glass components using UV-radiation. The process is based on material removal using excimer laser radiation, which allows a defined volume to be removed per laser pulse. Thus, only a mathematical description of the desired contour is required for an automated process. The system for the manufacturing of micro-lenses consisted of a high-acceleration, air-supported positioning system under development by Kugler GmbH, and an excimer laser with a high pulse frequency by Lambda Physics GmbH [51].

Table 2.1: Summary of studies for CAD/CAM system development for excimer laser processing.

Author:	Software Platform	Input File Format	Output File Format	Machining Method and mode
Tonshoff et al.[1]	3D Max Studio	DXF	NC-data File	Step and repeat
Bohelen et al.[45]	AlfaCam	Script File	NC-data File	Direct Writing
Perkins [80]	AlfaCam + VB	Script File	NC-data File	
Charrier et al.[101]	2D Allegro v12	Gerber File	G-Code	
This research	Solidworks +VB Studio	STL+BMP	G-Code	Step and repeat, Workpiece dragging

2.8.1 Other Techniques and CAD/CAM Tools of Relevance

Zhao et al. [52] have been developing a CAD/CAM system for generating the massive tool electrode paths and related NC code. This system is very useful for micro-electro discharge (ED) -milling of small free form cavity. The system is based on the Initial Graphics Exchange Specification (IGES) file format to describe the information of the solid model and the information of slicing contour can be obtained precisely and tool path can also be generated.

Takayuki et al. [53] have been developing an original fabrication method named FORMULA (Formation of μ -structures by lamination) for 3D microstructures using surface-activated bonding (SAB) of thin films at room temperature. This method is a kind of layer manufacturing method-using stacking of thin film patterns with an accuracy of sub-micrometer order. For now, they have demonstrated that this method is applicable to batch fabrication of microstructures of approximately 100 μm in size and several micrometers in height.

He et al. [54] discussed the architecture and main features of the IntelliCAD developed by IntelliSense to address the need for predictive MEMS development. IntelliCAD[™] is an integrated software system which assists designers in optimizing MEMS devices by providing them with needed manufacturing databases, allowing them to model the entire device manufacturing sequence, and to simulate behavior without having to enter a manufacturing facility. IntelliCAD has predicted the behavior of complex structures to within 10% accuracy by utilizing fully coupled thermo-electromechanical analysis. Its use has resulted in device designs that are easier to manufacture and has reduced development time and cost.

Harris et al. and Maseeh et al. [55, 56] presented CAD architecture for microelectromechanical systems in which conventional mask layout and process simulation tools were linked to three-dimensional mechanical CAD and finite-element tools for analysis and simulation. Architecture for an object-oriented material property simulator is also presented in which material properties and their process dependence are stored and accessed based on the specific process conditions.

Koppelman et al. [57] has developed a program called OYSTER, which permits construction of a 3-D polyhedral-based solid model from a mask set and primitive process description, but as yet, there is no provision to Finite Element Modelling (FEM) tools or to standard layout and process modelling tools, and no database for prediction of material properties from the process sequence.

2.9 Machining Process Sequence

There are two machining process sequences to machine a 3D feature by the layer-by-layer method; one is starting with the smallest aperture as shown in Figure 2.20 (a), and the other starts with the biggest aperture at the mask (b). As long as the total depth of the machined feature does not exceed the depth of focus of the imaging lens it will reach the same depth regardless of the process sequence. Nevertheless the process sequence has an effect on the surface quality. The ever-increasing aperture of the sequence procedure starting with the smallest one will smooth the edges of the ablation steps and thus decrease the roughness of the surface significantly. When machining into polymers, it is sometimes the case that the very top layer of the material has a slightly higher ablation threshold than the rest; by using sequence mode (a) this can then cause some distortion of the ablation curve since every single aperture has to remove a small part of the top layer, while in sequence mode (b) the very first aperture will remove all of the top layer where the feature will be created and for the subsequent shots the material will be homogenous from a ablation point of view [38].

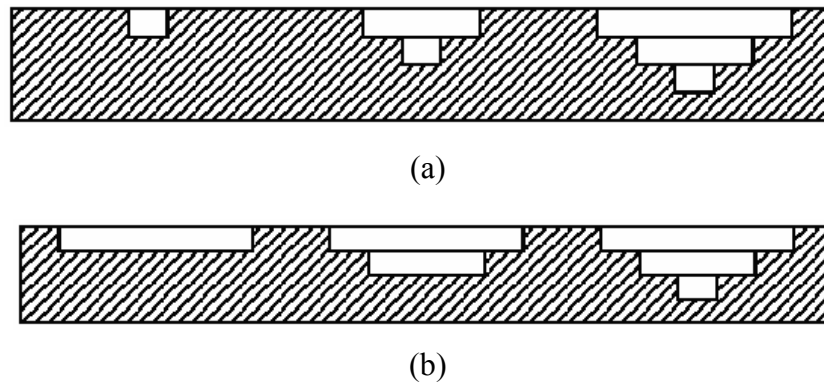


Figure 2.20: Schematic build up of 3D structure by applying different machining process sequences: a) starting with the smallest and b) starting with the biggest aperture [38].

2.10 STL File Generation

Most recent commercial CAD/CAM software systems are capable of generating STL files directly from a surface model. The majority of triangulation methods are based on a known surface model [58]. Triangulation of scattered data in 3D space often has the objective of constructing smooth surfaces [58, 59]. In this research work STL files were generated by SolidWorks and Pro/ENGINEER CAD packages.

2.11 Slicing Techniques

The determination of a proper slicing strategy has been an important problem to be resolved by the users of RP systems. Several works have been published on developing methods to determine the best slicing algorithms based on different criteria.

Dolenc and Makela [60] and Mani et al. [61] addressed the problem of reducing the stair stepping effect by means of adaptive slicing. They used heuristic methods on faceted models since they were concerned with STL files. Kulkarni and Dutta [62] addressed the problem of determining adaptive slicing for a surface from its analytical presentation. They also use cusp height to quantify the error associated with stair stepping effect. Suh and Wonzy [63] developed a procedure of adaptive slicing using a parametric CAD model of the object. Their algorithms improved part accuracy and minimised building time especially for the parts with highly curved surfaces.

Slicing strategies can be borrowed from current RP techniques. There are two methods when using the slicing method to produce a 3D part. The most common approach is top-down slicing. In this method the intersection point between the triangle facet and slicing plane is calculated and extended down to the thickness of the layered material. In this research work slicing was performed by using a commercial slicing algorithm developed by Stratasys® for their Fused Deposition Modelling (FDM) RP machines.

2.12 Summary

A major hurdle in manufacturing MEMS is reducing the expensive and long product development cycles. Adequate design and simulation tools have not been available and manufacturers were forced to undertake many trial-and-error iterations when manufacturing devices since it was difficult to model accurately the physical behavior without having to enter a manufacturing facility.

Compared to conventional CAD/CAM technology, research in simulation of laser micromachining is still in the primitive stage and only a few research groups have attempted such work. This thesis will build on the small amount of published work and explores the development of a novel system for excimer laser ablation process that implements the optimised parameters that influence and specifically determine this unique process, to automatically derive a precise NC part program for the excimer laser machine. A CAD/CAM system should address the need for predictive MEMS development by excimer laser mask projection process. The system needs to provide designers with material database and a modelling simulator, which allows them to model the entire device manufacturing, and load simulation without ever having to enter manufacturing facility. The results will decrease development time and reduce the cost for the user.

With the development of increasingly sophisticated microelectromechanical devices, including microsensors, pumps, valves, and micromotors, and with the increasing performance demands being placed on these devices, notably in the precision and accuracy of microsensors, there is a critical need for CAD tools which will permit rational design of devices. There are two fundamental problems that confront the designer: (a) the

need to construct a three-dimensional solid model from a description of the mask set and process sequence to be used in fabrication of a micromechanical device; and (b) the need to be able to predict the material properties of each of the constituent components in a device, including possible process dependences of these properties. At the present time, there is no CAD system, either mechanical or microelectronic, which successfully addresses these problems in a coherent way.

Most of the research to date has focused on one of a few mask projection systems, and full understanding of 3D microstructuring, and their influence on system performance has not yet been achieved. In this research, existing systems will be systematically studied to understand the influence of these on machining performance.

Chapter 3. *Development of a CAD/CAM System For Excimer Laser Micromachining*

3.1 Overview

This chapter describes in detail the methodology proposed for the development of a CAD/CAM system for excimer laser mask projection ablation process. The motivations and system requirements for the approach developed are presented in sections 3.2 and 3.3 respectively. A detailed concept overview of the entire methodology is introduced in section 3.4. The design component of the system and “external” modelling option are described in sections 3.4.1 and 3.4.2 respectively. The STL file approach is detailed in section 3.4.3. In section 3.4.3..5 the “internal” CAD modelling option is described and the machining module algorithms are covered in section 3.4.3..6. The Bit-Map approach used to overcome deficiencies of STL approach is detailed in section 3.4.4. The heuristics algorithm used in toolpath optimisation method appears in section 3.5. The details of the algorithms for pulse number minimisation using bit-map approach appear in section 3.6. The experimental setup and equipment used are explained in section 3.7. The system capabilities and limitations are presented in section 3.8 and finally, in section 3.9, a summary of this chapter is presented. The essence of the work presented here has been published in summary form in Mutapcic et al., 2002 [64], and in more detail in Mutapcic et al., 2004 [65].

3.2 Motivation

The design and fabrication tools for MEMS design are still limited. Many of today’s CAD systems are inappropriate because they do not have the necessary MEMS design, material or fabrication information. As a result, manufacturers are forced to use time consuming and expensive trial and error approaches to develop MEMS devices, as is the case with excimer laser ablation process.

The excimer laser micromachining is used to produce various MEMS parts including filters, nozzles, microchannels, textured surfaces and optical elements [22]. The suitability of laser-ablation in micro-optics depends on the required surface finish and accuracy of geometry produced. Optical components can be designed and their theoretical performance established using current software tools, however, the fabrication of these parts is still a difficult task [20]. The ability to produce a given 3D structure and surface quality is often dependent on the machine operator to produce the NC part program for a desired shape and to set the appropriate machine parameters to achieve the required finish.

To significantly improve the capability of the laser ablation process, any desired 3D surface should be able to be produced by taking the 3D information from a CAD system and automatically generating the NC part program. In addition, surface quality should be able to be controlled by specifying optimised parameters.

The development of new techniques that can rapidly reduce the cost of fabrication for the most complex microstructures and at the same time reduce the product time to the market are the basis for full integration and more wider application of these structures in the micro world [11].

One important goal of current CAD research is the development of highly integrated and seamless tools for use in design environments. Achieving this goal would presumably increase the efficiency of design processes, shorten lead times, increase product quality, and free designers from a number of relatively mundane tasks to concentrate on producing the best possible designs.

The computer integrated product development has a key position for optimising the development processes. Using CAD/CAM software tools in a production chain from the design to the NC code generation and manufacturing of workpiece is state-of-the-art in common technologies such as milling or turning [66]. Today's CAD systems contain complete contour information that can easily be exported in a number of different graphical file formats, and it is this information that can be used for automatic generation of data necessary for a CNC system to produce a desired structure. Hence, intelligent software as a 3D CAD-interface that can calculate the CNC-data for laser triggering, XYZ-table movements and the CNC-mask control is desirable. Such software should

allow the conversion of STL-files into NC code for excimer laser ablation based micro machining. With such a system micro components for MEMS and Micro-Opto-Electro-Mechanical Systems (MOEMS) [8] can be manufactured without using expensive and time consuming programming work. An excimer laser system with additional equipment of CNC-controlled handling devices is a logical step towards a more efficient and reliable system for more complex microstructure components [1]. Hence, this research work is interested in developing a particular type of automated system to provide support for excimer laser ablation process.

3.3 System Requirements

The CAD/CAM system generates optimised NC part programs from given 3D solid models of the desired microstructures. In achieving this goal, there are several criteria that the system should fulfill:

1. **System flexibility:** The CAD/CAM system should provide flexibility of interfacing with standard commercial CAD modelling package such as SolidWorks. Hence, for interfacing, the STL file format was selected because it can be generated with most CAD modeller packages (Inventor, Pro/ENGINEER, SolidEdge).
2. **Design capabilities:** The CAD/CAM system developed should be applicable to production of 3D microstructures and be able to cope with complexity of quick changes to design, i.e. should be parametric. This is especially important if the system is to be used as a quick prototyping tool for proof of concept design stage. This has been resolved by using a commercial 3D CAD modeler and its API programming capabilities to develop the CAD/CAM system. In terms of simplicity of system use, the CAD/CAM system will provide a number of design tools and features (fully parametric design environment, 3D modelling, Feature-Extrusion, Cut-Features, 3D Viewing, Macros, etc.), that will allow rapid design changes and testing of 3D models of microstructures regardless their size and design complexity.

3. Dimensions and accuracy: Requirements are to be appropriate for the micro structuring environment with features resolution down to 10µm.
4. A database is required for retrieving the optimal machining parameters for common materials. One of the pitfalls of the excimer laser micromachining process is that the user has to have expertise in the field to be able to efficiently operate system and produce quality structures. In the proposed system, a database is employed with data already available from existing literature or data experimentally determined for typically used materials such as Polycarbonate (PC) and Polyethylene Terephthalate (PET).

The main input and output parameters and their specifications for CAD/CAM system developed has been listed in Table 3.1

Table 3.1: System input and output parameters.

	Parameter	Specification
Inputs	Fluence	0.1-3 J/cm ²
	PRF	5-80 Hz
	Number of pulses	1-500
	Depth of Cut	1-250 µm
	Wall Angle	2-80 °
	Overlap Size	4-10 µm
	CAD Model	(STL file, BMP file)
	Materials	PC, PET
Outputs	Part Program	G- Code

The CAD/CAM system has been developed for a purpose-built laser micromachining tool, the Exitech Series 8000. However, the system is not restricted to this particular tool and should be used on other similar mask projection tools.

3.4 System Concept Design

The first goal of this thesis was to develop a 3D CAD/CAM system that will help to design and machine microstructures by an excimer laser ablation process. This unique process has complex and dynamic process parameters that are continuously changing and require regular calibration. The ablation process is driven and controlled by NC part programs, which are currently written manually to achieve the desired microstructure shape. The creation of the part programs is a time-consuming process, and relies on operator expertise and a trial-and-error approach to generate the programs to machine the microstructures.

To overcome these problems the 3D CAD modelling software Solidworks and its API, in conjunction with VB programming tool kit, were used to develop the system. This system should enable design, analysis and machining of complex microstructures.

The development methodology is depicted in the flow chart in Figure 3.1. Initially a prototype system was chosen to serve as a framework. It was defined as a composition of four main modules: design module, machining module, mask module, and materials data base module. In particular, the structure of design and machining module are discussed. These modules are based on a combination of two different sets of algorithms. Firstly, the STL File approach and secondly, the Bit-Map file approach. The following sections describe the entire process.

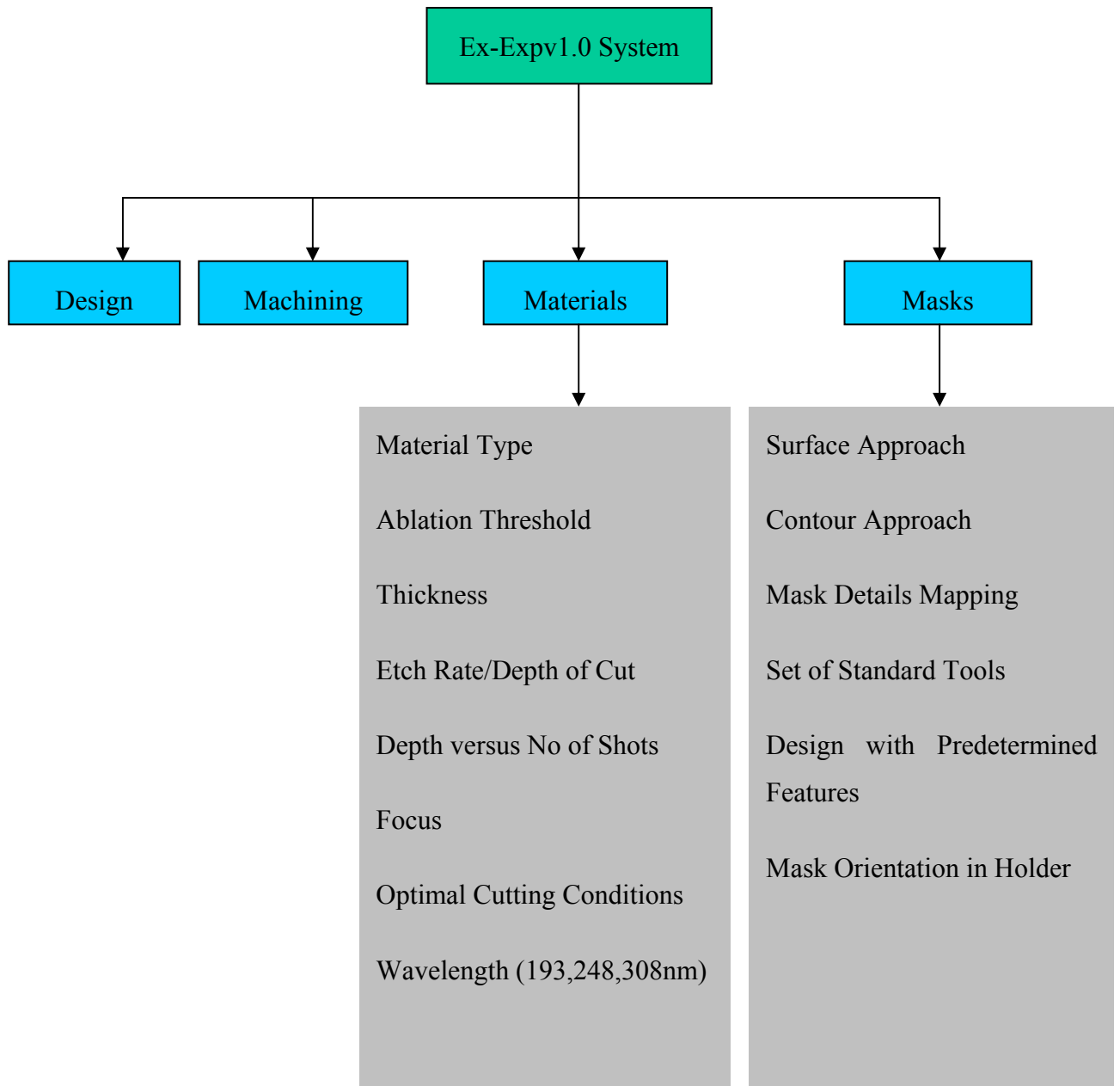


Figure 3.1: Ex-Expv1.0 system software structure showing main process parameters.

3.4.1 Design Module Component

Figure 3.2 shows the design module component of the Ex-Expv1.0 system. The design module integrates two independent streams.

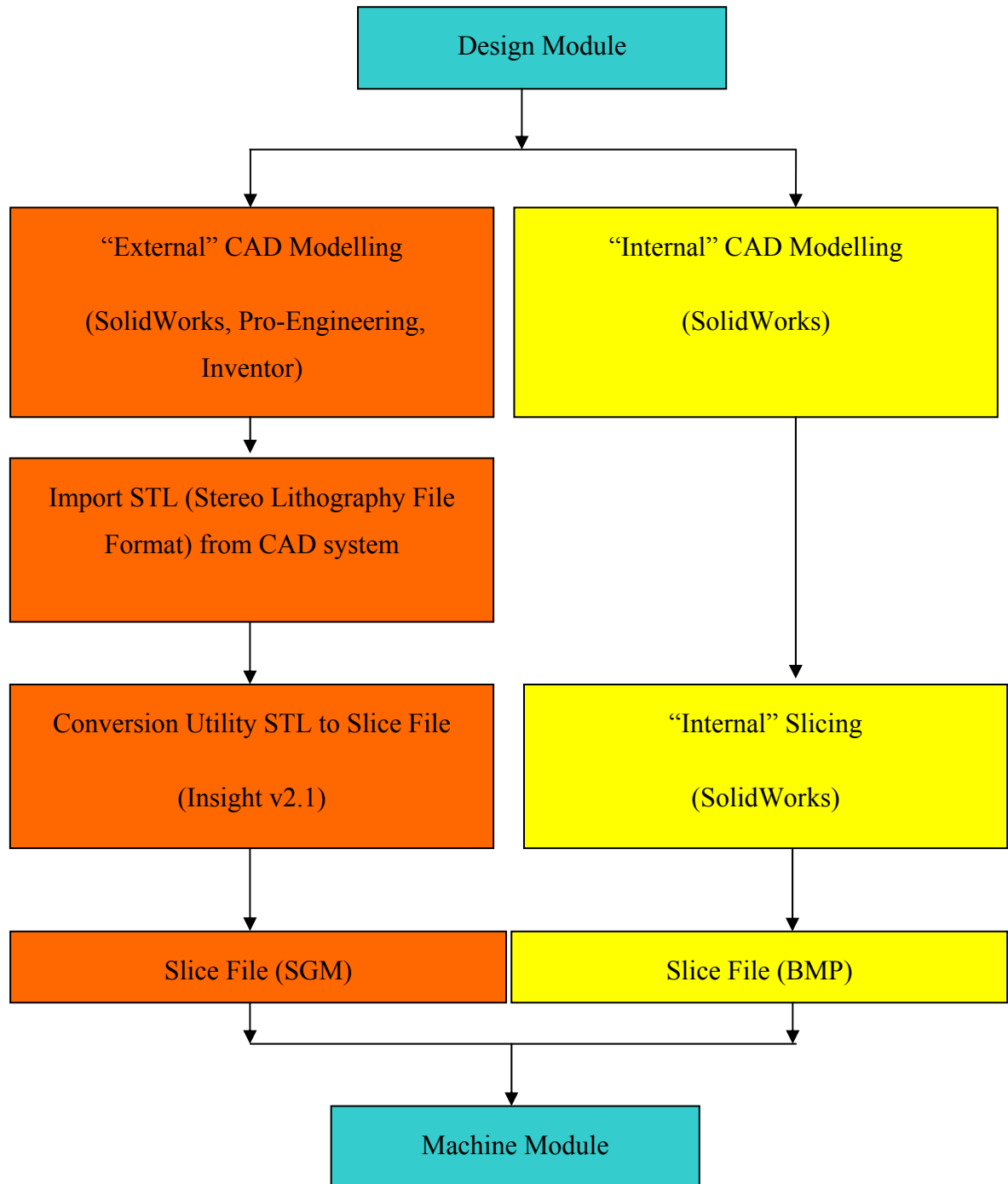


Figure 3.2: Ex-Expv1.0 system design module structure allows for CAD modelling to be accomplished “externally” by other CAD packages (left path) or “internally” through internal link to Solidworks (right path).

This module is used as a data translator that allows the microstructure design to be completed “externally” by any CAD software that has capabilities to export data as a STL file. The STL file is then sliced using Stratasys® InsightV2.1™ software. Alternatively, the module can be used as an “internal” CAD modelling tool where the design and slicing process is completed by Ex-Expv1.0 system through its internal link to SolidWorks and output is in a form of a Bit-Map File.

3.4.2 “External” CAD Modelling

The first step towards development of a CAD/CAM interface for the excimer laser ablation process starts with 3D CAD modelling of a microstructure, using Solid Works (or Inventor, Pro-Engineering, SolidEdge) and then converting the solid model to an STL File (see Appendix B). This file was then imported to InsightV2.1™ to create a slicing file in a format suitable for the excimer laser ablation process.

The slicing algorithm was used to create horizontal planes and divide a 3D model into 2D cross-sectional areas. This sliced structure was used as an input to the ExExp v1.0 system developed to create part program for the excimer laser. The system software was developed with the Visual Studio Developer Kit to interface a Microsoft Access database using the VB 6.0 programming tool. The system is the CAD/CAM interface for the excimer laser machine (Exitech S8000 with Unidex 500 Controller, Aerotech Inc).

3.4.3 STL File Approach

The STL file format represents the shape of the object as a mesh of tiny triangles laid over the surfaces, as shown in Figure 3.3. The triangles must meet up exactly with each other, without gaps or overlaps, if the object is to be built successfully [58]. The "slice files" which were used to build each individual layer were calculated from the STL file, and if there were any gaps between the triangles, then the edges of the slices were not properly defined [60].

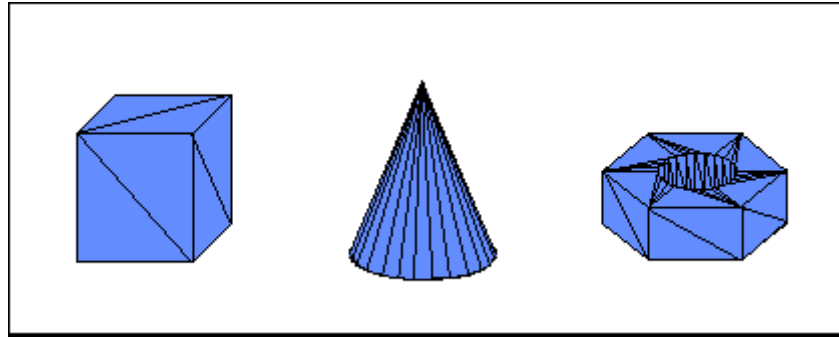


Figure 3.3: Triangular mesh for different geometric shapes.

An STL file consists of a list of triangular facet data (see Appendix B). A unit normal and three vertices uniquely identify each facet. Three coordinates each specify the normal and each vertex, so there is a total of 12 numbers stored for each facet. Apart from this, triangular facets in an STL file must also obey the following two rules.

3.4.3..1 Facet Orientation

The facets define the surfaces of a 3D object. Each facet is part of the boundary between the interiors and exterior of the object. The orientation of the facet is specified redundantly in two ways, which must be consistent.

First, the direction of the normal is outward. Second, the vertices are listed in counterclockwise order when looking at the object from the outside.

3.4.3..2 Vertex to Vertex

Each triangular facet must share two vertices with each of its adjacent triangles. In other words, a vertex of one triangle cannot lie on the side of another.

3.4.3..3 Slice File Format

The STL file was used as input to InsightV2.1™ (Stratasys. Inc.) FDM software to create a slicing file. This slicing file was created in a format that contains the original information from the CAD model and was suitable for the excimer laser ablation process. A slice file is a collection of the 2D vertices where all vertices that belong to the same

layer have the same value of Z-coordinate. Each layer represents a cross section of a 3D model (a listing of a slice file is shown in Appendix B).

3.4.3..4 Example of “External” CAD Modelling Process Steps

First step: A simple 3D model and STL file structure are presented as an example of this process. The 3D model consists of a rectangular base with a triangular recess as shown in Figure 3.4. The triangular recess represents the volume of material to be removed by the laser ablation process. This model was created using SolidWorks®.

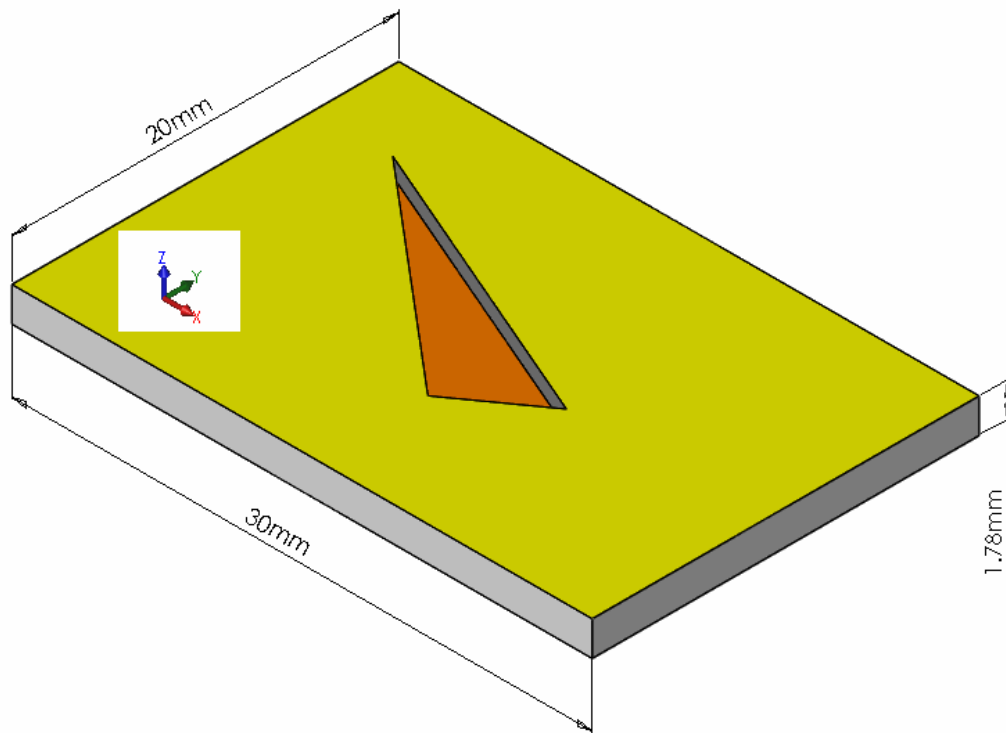


Figure 3.4: First step - 3D Model of a triangular structure on a surface.

Second step: A tessellated (triangular) representation of this model is shown in Figure 3.5. This figure shows that this model has 24 facets.

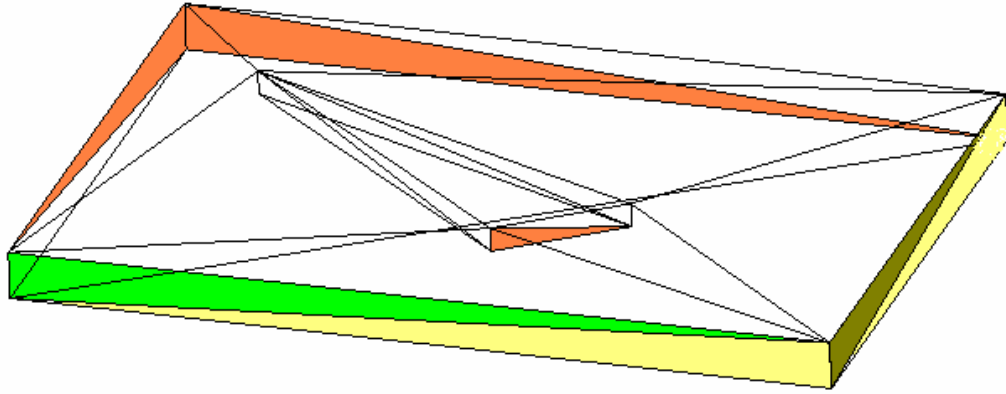


Figure 3.5: Second step - Tessellated representation of a triangular structure.

Third step: The slice thickness is limited by the InsightV2.1 software to 0.178 mm and the example 3D model has a thickness of 1.78 mm in the direction of Z-axis. Hence, this model is sliced into 10 equal layers, using the maximum precision possible by the current settings of an FDM 3000 modeller [67]. Before starting the slice file generation the model is oriented in such way that the 2D cross-sectional areas generated after slicing will be suitable for further processing. The layered structure is represented in Figure 3.6.

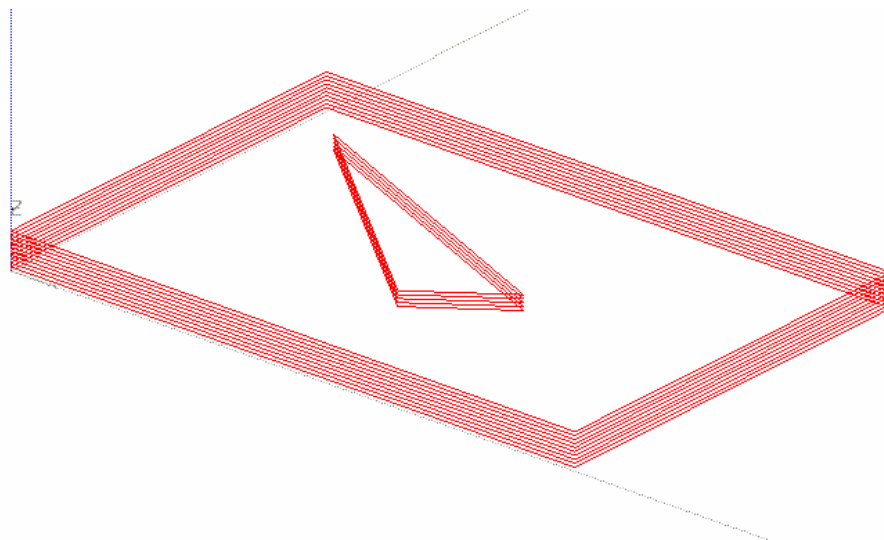


Figure 3.6: Third step - Sliced 3D model of a triangular structure.

The sliced model in Figure 3.6 is a collection of 2D vertices where all vertices that belong to the same layer have the same value of Z-coordinate. Each layer represents a cross-section of a 3D model. This layered structure was used as an input to the machining module of the system to create the toolpath for the excimer laser ablation tool, and using this information automatically generate the NC code. This example proved that STL file format, normally used in RP techniques, was suitable for extracting 3D geometrical information that can be used for automatic generation of NC code in excimer laser micromachining process.

3.4.3..5 “Internal” CAD Modelling

CAD modelling can be accomplished directly by Ex-Expv1.0 system through its internal link to Solidworks’ drawing and visualization tools for design of microstructure. To achieve slicing of the model by Ex-Expv1.0 system an algorithm was developed through API programming interface to control Solidworks’ Feature-Cut function. A parametric part that represents substrate is extruded then cut into slices. Each individual slice is generated as a BMP format file. These files contain the contour information of CAD model for each layer, i.e., the areas are defined by pixels and depth information by each layer thickness. This approach overcame the redundancy problems associated with STL file that could cause some information to be lost when approximate surfaces were used. This is discussed in section 3.4.4.

3.4.3..6 Machining Module Component

Figure 3.7 shows a description of machining CAM module of the system. This module is directly connected to the system database where optimal data for different materials was stored.

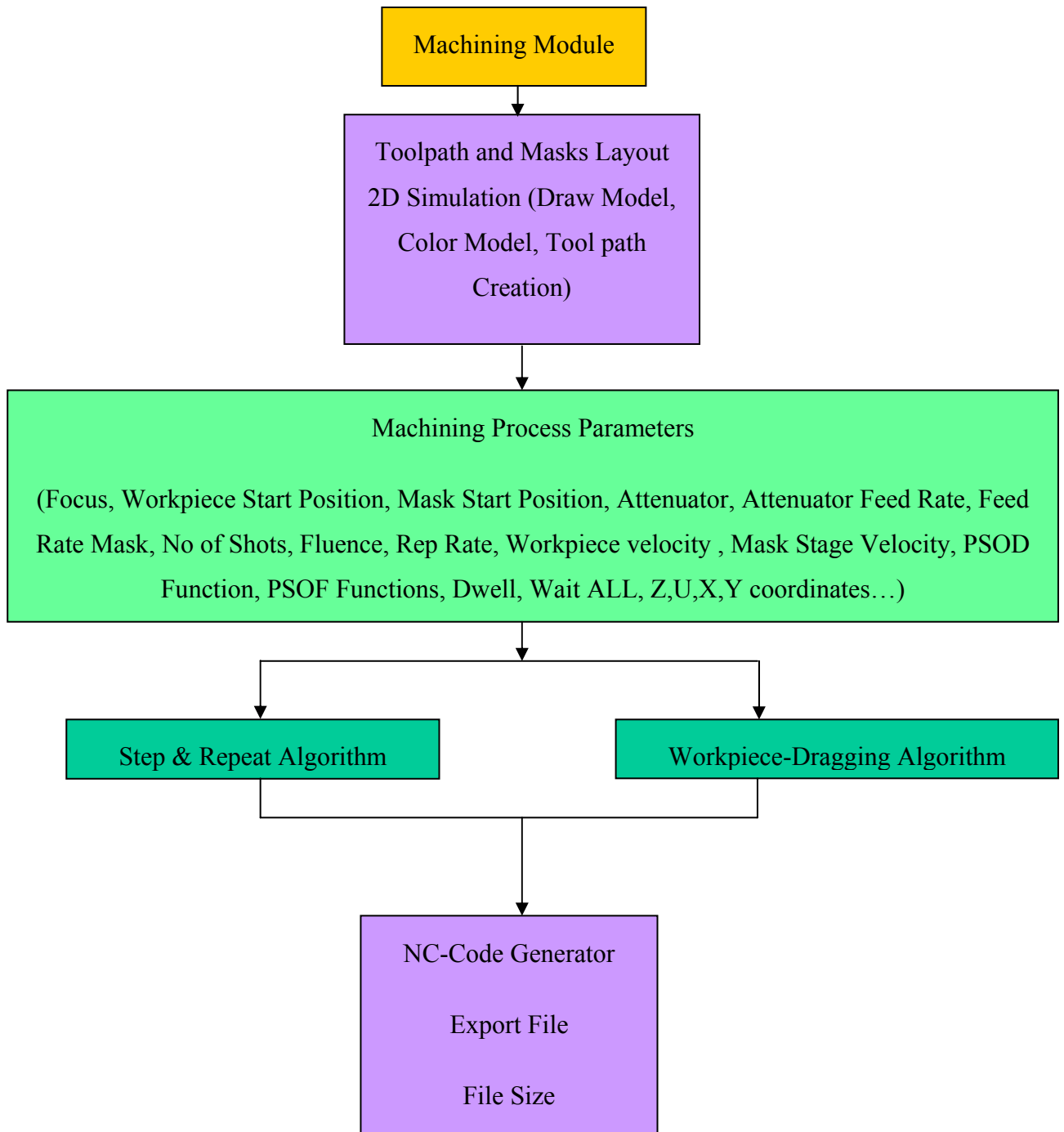


Figure 3.7: Ex-Expv1.0 system machining module showing alternative machining options (Step-and-repeat and Workpiece-dragging).

The machining module performs the actual simulation of the mask layout depending on the machining strategy chosen. Machining strategies are explained in section 3.5. The toolpath and pulse minimization algorithms are integrated in this module.

An inside triangular boundary of a layer of the 3D model shown in Figure 3.6 with different size masks layout is shown in Figure 3.8, which was produced by ExExpv1.0 system.

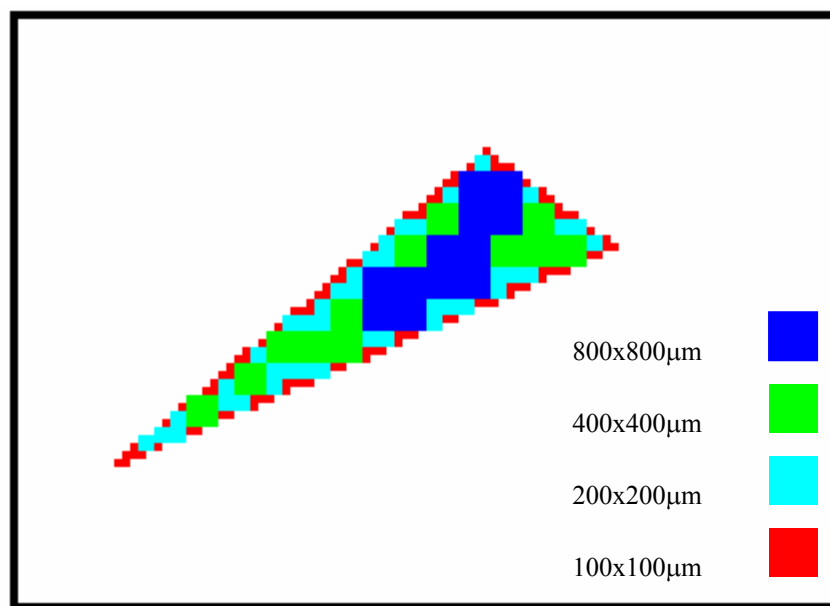


Figure 3.8: Masks layout for a layer of triangular structure produced by Ex-Expv1.0. The colours and dimensions represent the different size masks incorporated into the CNC by the system.

After all the 2D cross-sectional areas were defined by the Ex-Expv1.0 system and all necessary masks are mapped into their exact locations using different pulse number and toolpath optimisation criteria, the system was able to automatically extract the NC code. This example proved that the approach is able to generate masks layout and subsequently generate NC code for shapes with non-orthogonal boundaries, i.e., shapes that have some of their edges with a slope angle. This enabled shapes of any complexity to be designed, and was not limited just to square or rectangular, i.e. shapes with orthogonal edges.

The NC code generation then had to be optimised, in order for the laser ablation process to be efficient and less time consuming. Optimisation processes and criteria are discussed later in section 3.5 and section 3.6 respectively.

3.4.4 Bit Map Approach

As mentioned earlier in Chapter 1 the STL file approach enabled approximation of any 3D surface and after slicing of the structure create the way for 3D microstructures to be machined using excimer laser machining process. However, as the STL file is based on a triangular approximation process where each surface is represented as a mesh of triangles, and if certain conditions are not met the file will contain redundancy data (see 3.4.3..1) that will result in an inaccurate model representation. In order to overcome these difficulties an alternative approach was developed based on the Bit-Map file. The background theory and adaptations to existing algorithms used are explained in the following sections. This approach is more suitable to the excimer laser micromachining process, which is in its nature 2D and binary, and an analogy can be drawn between laser micromachining principle and raster graphics theory.

3.4.4..1 Raster Graphics

Most modern output devices are raster displays (e.g. PC monitor, laser printer, ink-jet printer, and flat-panel display). A raster display consists of a display surface on which the image is presented. The surface is divided into a finite number of small square regions, each called a pixel (picture element), which are arranged in a regular grid of rows and columns. The number of pixels in the display determines its resolution. The resolution is usually given as the number of columns by the number of rows (e.g. 640x480). Each pixel is referred by specifying its column number and its row number. The rows are usually numbered from left to right starting at zero. The columns are usually numbered from top to bottom, starting at zero [68].

Raster displays have an associated frame buffer; which is a region of memory large enough to store a value for each pixel on the display. Each time the image needs to be displayed a scan controller reads each value in the frame buffer and 'draws' a spot at the

appropriate location (pixel) on the display. The intensity or colour of the pixel is determined by the value in the frame buffer. [68].

Because of the nature of raster displays, images, text, user-interface controls or anything that appears on screen must be converted into a set of discrete pixel values. This process is called rasterization, and usually produces a blocky approximation of the object being processed, with jagged edges. As long as the pixel size is small (high resolution), these effects are not noticeable. For low-resolution displays, there are techniques (anti-aliasing) which reduce the staircase effects [68].

3.4.4..2 Pixel Colours

As well as converting objects into sets of pixels, the rasterization process must also convert the objects' color into a value, which can be displayed. The number of colors available is dependent on the output device. Dot-matrix printers can only display a pixel as black or white, and nothing in between. Modern laser and ink-jet printers can produce a range of shades of gray from white through to black using half-toning techniques. Older monitors could only display 16 different colors, and then came 256 color monitors and today's monitors can display 16 million different colors, although, no device can reproduce the infinite range of colors seen in nature. However, it is not necessary to reproduce an infinite number of colors to produce realistic images. The human eye can only distinguish around 10 million different colors [69].

Devices, which use color look-up tables (LUTs), can increase the number of colors available to images. These allow devices to display a larger range of colors than their bit-depth would normally allow. In an 8-bit system, a LUT is a table of 256 entries; each entry represents a color and specifies the amount of red, green and blue in the color as an RGB triple. In the bit-map each pixel value represents an entry in the LUT. The bit-map would contain a header specifying the colors to be stored in the LUT. In this arrangement, a device can still only display 256 different colors (one for each entry in the table), but these colors can be selected to best match the image being displayed, e.g. if a forest scene was being displayed, the LUT may contain 100 different shades of green [70].

3.4.4..3 *Color Patterns Extraction*

A standard output primitive in general graphics package is a solid-color or patterned polygon area. There are two basic approaches to area filling on raster systems. One way to fill an area is to determine the overlap intervals for scan lines that cross the area. Another method for area filling is to start from a given interior position and paint outward from this point until the specified boundary conditions are encountered. The scan line approach is typically used in general graphics packages to fill polygons, circles, ellipses, and other simple curves. Fill methods starting from an interior point are useful with more complex boundaries and in interactive painting systems [70]. These two methods were of a particular interest for this research work because they provide an elegant solution for a mask layout problem specific for an excimer laser micromachining process. In the following section both methods are discussed in more detail

3.4.4..4 *Scan-Line Polygon Fill Algorithm*

Figure 3.9 illustrates the scan-line procedure for solid filling of polygon areas. For each scan line crossing a polygon, the area-fill algorithm locates the intersection points of the scan line with polygon edges. These intersection points are then sorted from left to right, and the corresponding frame-buffer positions between each intersection pair are set to the specified filled-color. In Figure 3.9, the four pixel intersection positions with the polygon boundaries define two stretches of interior pixels from $x = 10$ to $x = 14$ and from $x=18$ to $x= 24$ [71].

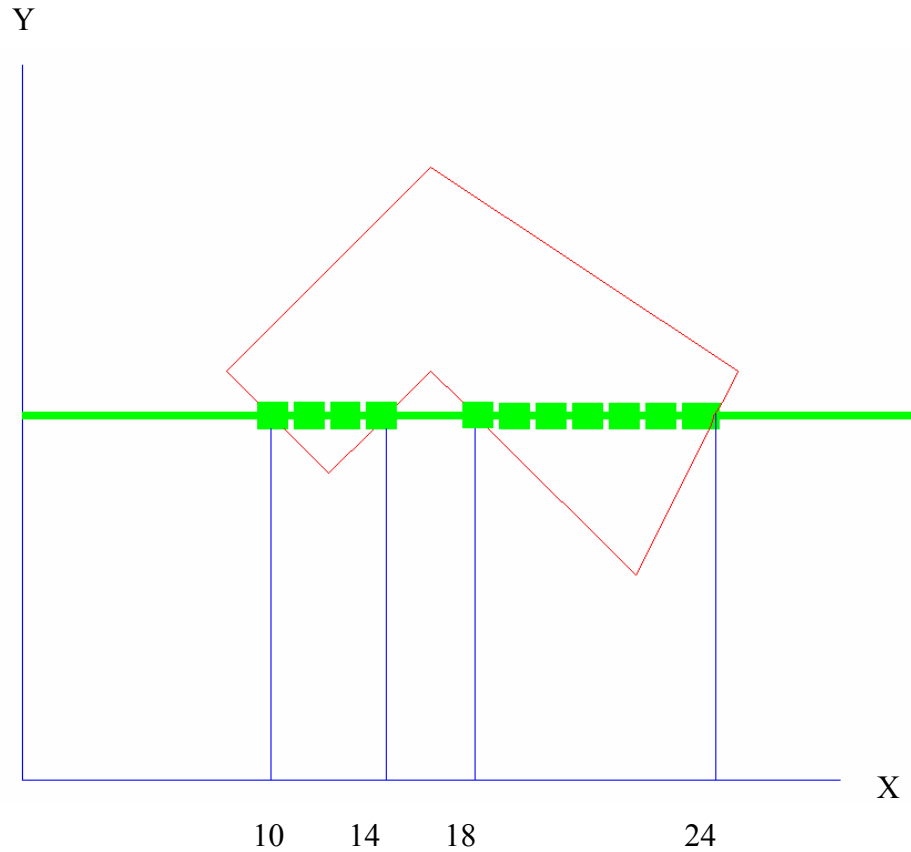


Figure 3.9: Interior pixels along a scan line. The 4 pixel intersection points with polygon boundaries determined the area to be filled with different color [72].

Some scan-line intersections at polygon vertices require special handling. A scan line passing through a vertex intersects two polygon edges at that position, and adding two points to the list of intersections for the scan line. Figure 3.10 shows two scan lines at positions y and y' that intersect edge points. Scan line y intersects five polygon edges. Scan line y' , however, intersects an even number of edges although it also passes through a vertex. Intersection points along scan line y' correctly identify the interior pixel spans. But with scan line y , additional processing to determine the correct interior points is needed [72].

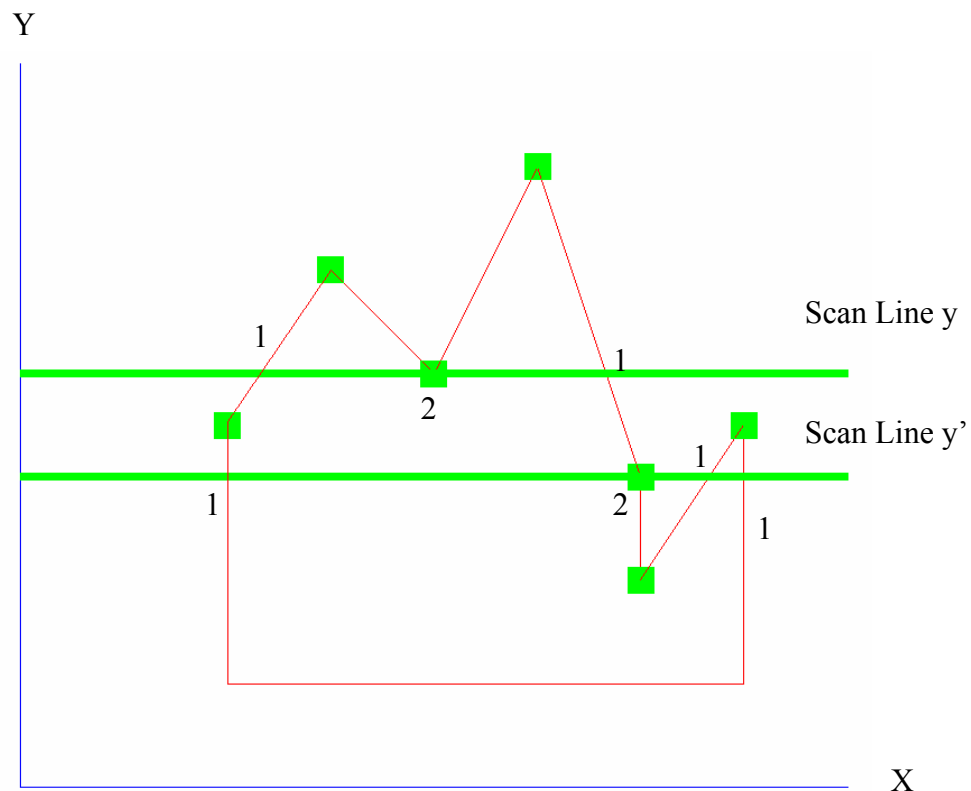


Figure 3.10: Scan line y generates an odd number of intersections, but scan line y' generates an even number of intersections that can be paired to identify correctly the interior pixel spans [72].

3.4.4..5 *Boundary-Fill Algorithm*

Another approach to area filling is to start at a point inside a region and paint the interior outward toward the boundary. If the boundary is specified as a single color, the fill algorithm proceeds outward pixel-by-pixel until the boundary color is encountered. This method, called the boundary-fill algorithm, is particularly useful in interactive painting packages, where interior points are easily selected [71].

3.4.4..6 *Bresenham's Line Drawing Algorithm*

Line drawing is fundamental to computer graphics and it is important that the rasterization technique used for line drawing be as efficient as possible [73]. In this section a highly efficient line drawing algorithm developed by Bresenham [72] is

explained in detail because Ex-Expv1.0 system was based on this approach. Lines are usually specified by giving start and end points, $A(x_1, y_1)$ and $B(x_2, y_2)$. A line drawing algorithm then tries to turn on a set of pixels, which approximates to an ideal line drawn between A and B . The equation of an ideal line is given as:

$$y = m(x - x_1) + y_1 \quad (3.1)$$

where x takes on values between x_1 and x_2 .

The slope m is calculated as:

$$m = \frac{y_2 - y_1}{x_2 - x_1} \quad (3.2)$$

To determine how high the line rises as x increases across from one pixel to the next, simply add m to the current y -coordinate and round this value to get the current pixel position (Figure 3.11).

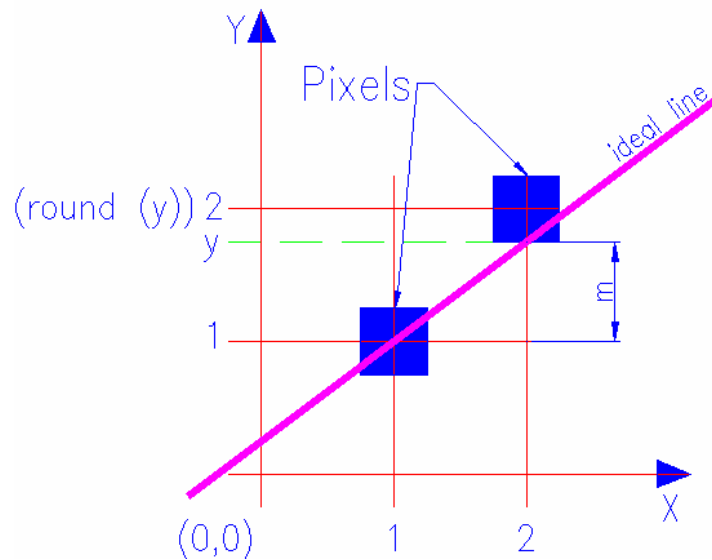


Figure 3.11: Line drawing using pixels showing how the line rises, as x value increases by one, where value of dimension m defined line slope.

Bresenham expanded this algorithm, thus giving a very efficient line drawing method [73]. The algorithm calculates the position of the current pixel, by using information about the position of the previous pixel. To simplify matters, initially only lines with slopes between 0 and 1 (0° and 45°) are considered. In this restricted case, as x increases by one for each pixel, the y co-ordinate of the next pixel either stays the same or increases by one.

Layouts of pixels (masks) for lines with slopes less than 1 are shown in Figure 3.12.



Figure 3.12: Lines of slope ≤ 1 .

In Figure 3.13, the grid intersections represent the center of pixel positions. Assume the position of the previous pixel P is known and the position of the current pixel Q need to be determined.

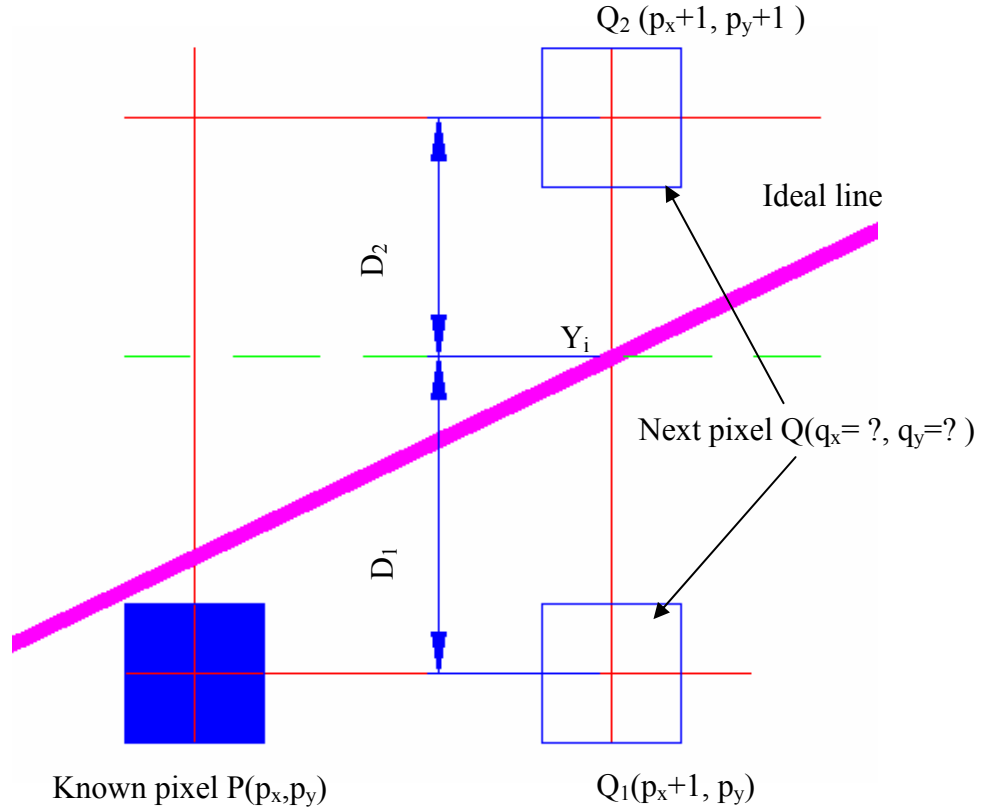


Figure 3.13: Bresenham line drawing algorithm where position of the next pixel is determined by using the known position of the previous pixel.

For lines with slopes between 0 and 1, Q will be at either $Q_1(q_x, p_y)$ or at $Q_2(q_x, p_y+1)$. Choosing between Q_1 and Q_2 is achieved by measuring the distance between these points and the y -value of the ideal line (y_i):

$$y_i = m(q_x - x_1) + y_1 \quad (3.3)$$

where (x_1, y_1) is the start point of the line.

The distance D_2 between Q_2 and y_i and distance D_1 between Q_1 and y_i are measured as follows:

$$dist(D_2) = (p_y + 1) - y_i \quad (3.4)$$

$$dist(D_1) = y_i - p_y \quad (3.5)$$

Pixel at Q_I is chosen if

$$\text{dist}(D_1) < \text{dist}(D_2) \quad (3.6)$$

or re-written, Q_I is chosen if

$$\text{dist}(D_1) - \text{dist}(D_2) < 0 \quad (3.7)$$

Thus, the y coordinate will increment if the above term is zero or positive. If the term is negative, the y coordinate stays unchanged.

If equations 3.4 and 3.5 are substituted into equation 3.7 then equation 3.8 follows;

$$\text{dist}(D_1) - \text{dist}(D_2) = (y_i - p_y) - ((p_y + 1) - y_i) \quad (3.8)$$

Now, if the value of y_i from equation 3.3 is substituted into equation 3.8, then it can be re-written

$$\text{dist}(D_1) - \text{dist}(D_2) = ((m(q_x - x_1) + y_1) - p_y) - (p_y + 1 - (m(q_x - x_1) + y_1)) \quad (3.9)$$

After regrouping, equation 3.9 can be re-written

$$\text{dist}(D_1) - \text{dist}(D_2) = 2m(q_x - x_1) + 2(y_1 - p_y) - 1 \quad (3.10)$$

The only non-integer in the above expression is m , which can be re-written as

$$m = \frac{y_2 - y_1}{x_2 - x_1} = \frac{\Delta y}{\Delta x} \quad (3.11)$$

Now equation 3.10 can be re-written as

$$\text{dist}(D_1) - \text{dist}(D_2) = 2 \frac{\Delta y}{\Delta x} (q_x - x_1) + 2(y_1 - p_y) - 1 \quad (3.12)$$

Only the sign of equation 3.12 and not its actual value is of interest, therefore, it can be multiplied across by Δx , because this will not change the sign. Therefore equation 3.12 can be re-written as

$$dist(D_1) - dist(D_2) = 2\Delta y(q_x - x_1) + 2\Delta x(y_1 - p_y) - \Delta x \quad (3.13)$$

The above expression needs to be evaluated to simply determine which distance, D_2 (increment y) or D_1 (no change in y), should be chosen.

D_1 is chosen if it is less than zero.

Now, the floating-point components are removed from the calculation, $\Delta y = (y_2 - y_1)$, $\Delta x = (x_2 - x_1)$ (all components are integers), but equation 3.13 still has multiplication operation. The multiplication can be removed as follows;

If the left-hand terms of the equation 3.13 are set equal to e_i (expression for pixel i) as in equation 3.14;

$$e_i = 2\Delta y(q_x - x_1) + 2\Delta x(x_1 - p_y) - \Delta x \quad (3.14)$$

Then the expression for the following pixel e_{i+1} will be;

$e_{i+1} = 2\Delta y((q_x + 1) - x_1) + 2\Delta x(y_1 - q_y) - \Delta x$, (where q_y is the y co-ordinate for the current pixel).

This can be re-written in terms of e_i ;

$$e_{i+1} = e_i + 2\Delta y((q_x + 1) - q_x) + 2\Delta x(q_y - p_y) \quad (3.15)$$

$$e_{i+1} = e_i + 2\Delta y - 2\Delta x(q_y - p_y) \quad (3.16)$$

Note that $(q_y - p_y)$ represents the difference between the y co-ordinates of the current pixel (Q) and the previous pixel (P). If there was no increment between P and Q , $(q_y - p_y)$ will be 0, therefore;

$$e_{i+1} = e_i + 2\Delta y \quad (3.17)$$

If there was an increment between P and Q , $(q_y - p_y)$ will be 1 and

$$e_{i+1} = e_i + 2(\Delta y - \Delta x) \quad (3.18)$$

To evaluate the term for the next pixel, only the expression for the current pixel e_i is needed and the terms $2\Delta y$ and $2(\Delta y - \Delta x)$. This method depends on knowing the result of previous pixel calculations. The first pixel is placed at the point given as the start of the line (x_1, y_1) . The term for the second pixel can be calculated as;

$$e_i = 2\Delta y - \Delta x \quad (3.19)$$

Once a value for e_i is determined, the value of e_{i+1} can be calculated quickly.

If $e_i < 0$ then

$$e_{i+1} = e_i + 2\Delta y \quad (3.20)$$

or if $e_i \geq 0$ then

$$e_{i+1} = e_i + 2(\Delta y - \Delta x) \quad (3.21)$$

Therefore, the line drawing algorithm proceeds as follows:

1. Draw first pixel (S_x, S_y) as the start-point of line.
2. Evaluate e_i .
3. If $e_i < 0$ increment x only, otherwise increment x and y .
4. Draw Pixel at (x, y) .
5. If $x < x_{endpoint}$ goto step 2.

3.4.4..7 Generalising the Bresenham Algorithm

The Bresenham's algorithm, as described above, only works for lines with slopes between 0 and 1. This limits it to drawing only one quarter of all possible lines. Hence, the Bresenham's method needs to be extended to all lines. There are two special cases of lines, which can be drawn without the Bresenham algorithm, horizontal (slope = 0) and vertical lines (slope = ∞). For horizontal lines, the x co-ordinate is incremented, while keeping y constant. Vertical lines are drawn by keeping the x co-ordinate constant and

incrementing y . These lines appear quite frequently in applications, so it is worthwhile treating them differently. Note also, that lines with slopes of 1 and -1 can also be drawn very quickly (increment x and y together). For lines with slopes greater than 1, interchange the roles of x and y . Increment y and test if the x co-ordinate needs changing (this basically turns the algorithm on its side). For lines with slope between 0 and -1, the algorithm runs as before, except that the test to determine when to decrement the y co-ordinate should be used first. For lines whose slope is less than -1, interchange the roles of x and y and decrement the x co-ordinate instead of incrementing.

The final line drawing algorithm will first test if the requested line is one of the special cases outlined above, if not a special case Δx and Δy are compared to see which “version” of the algorithm should be applied [73].

The previous sections summarised theory and algorithms behind developed Bit-Map approach. The following sections will explore how this theory and adaptations to the previously mention scan-line, fill area and Bresenham’s line drawing algorithm were used for mask layout determination and toolpath optimisation process.

3.5 Toolpath Optimisation Algorithms

Typically, a machining area consists of a set of discrete regions. On each region are located features to be machined. The position of each region is determined in advance by the design of the structure. The problem of finding the optimum sequence of machining can be represented as a Traveling Salesman Problem (TSP) and will be discussed in the following section.

3.5.1 Adaptation to Traveling Salesman Problem

The Traveling Salesman Problem (TSP) is one of the most well known problems in operations research, computer science, and mathematics. The basic idea is try to find the shortest cycle in a network such that all nodes are visited and the minimum total distance is traveled [74].

Although, the TSP is simple to characterize, it is very difficult to solve. It belongs to the class of NP – hard problems (nondeterministic-polynomial algorithms), thus, it is unlikely that any efficient algorithm will be developed to solve it. But because of its simplicity, the TSP has been one of the most studied problems in this class [75].

Since the TSP is very difficult to solve optimally, many heuristics have been developed. These heuristic procedures generally are fast and provide solutions that usually are within a few percent of the optimum. Thus, for problems of realistic sizes, heuristics represent a practical solution approach. Heuristics for the TSP can broadly be classified into two groups: tour construction heuristics and tour improvement heuristics [74]. Tour constructions heuristics generate a feasible tour (for example: optimal toolpath solution).

A second class of tour construction heuristics, called insertion procedures, was proposed by Rosenkrantz et al. [76]. The nearest insertion procedure can be described as follows:

Select one vertex to start, say vertex i . Choose the nearest vertex, say j , and form the subtour $i - j - i$. At each iteration, find the vertex k not in the subtour that is closest to any vertex in the subtour. Find the edge (i, j) in the subtour which minimizes $d(i, k) + d(k, j) - d(i, j)$. Insert vertex k between i and j . Repeat this process until a tour is constructed. Note that the iterative step trying to add the least amount of distance to the current subtour by removing edge (i, j) and adding edges (i, k) and (k, j) . How the adaptation to this heuristics method was performed has been illustrated in Figure 3.14. Islands i, j, k , and l represent different feature regions that have to be machined. They have been designed using different colors: blue, green, magenta, and red respectively. The distance between each region has been determined by the ExExpv1.0 system, and following the rules of the nearest insertion heuristics explained above, the shortest toolpath $d(i, j, k, l)$ has been calculated.

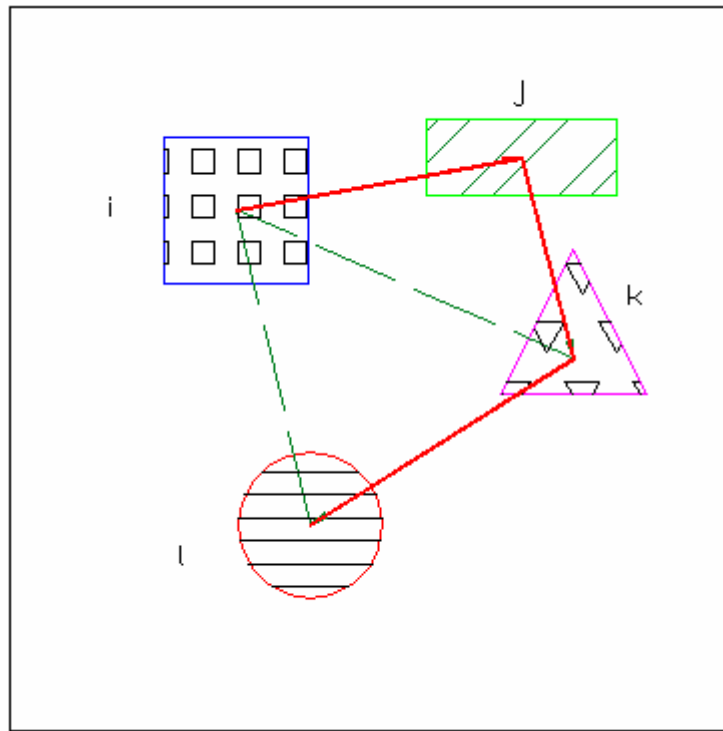


Figure 3.14: Adaptation to TSP algorithm where the shortest toolpath (shown as continuous line that connects different machining regions) was determined by the nearest insertion method.

Figure 3.15 illustrates the flow of the tool path optimization algorithm based on the heuristics insertion method.

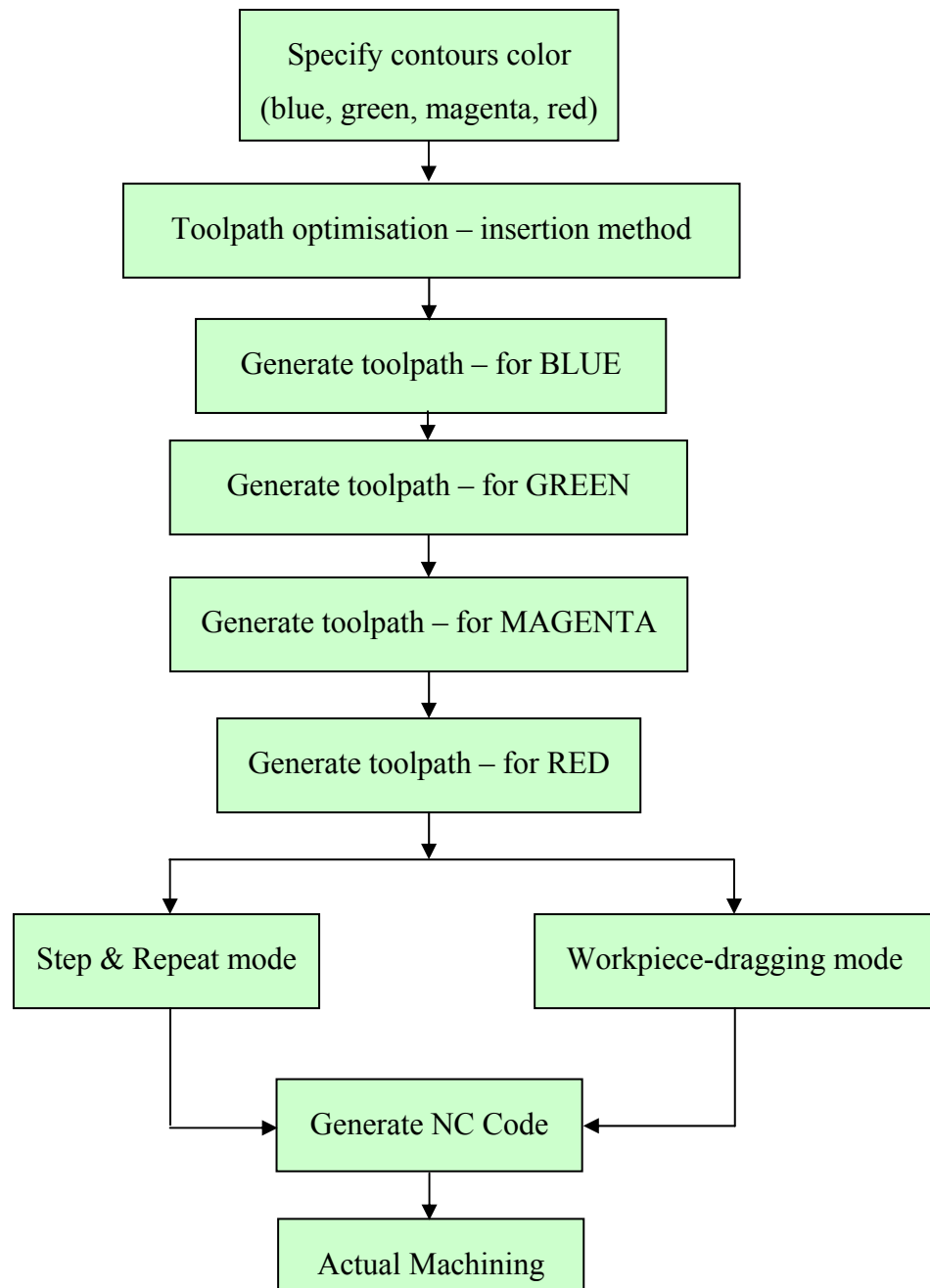


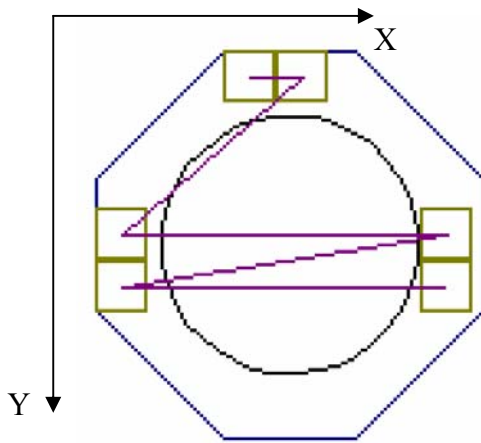
Figure 3.15: Toolpath optimization algorithm based on heuristic insertion method.

As shown in Figure 3.14 each discrete region represents a continual machining area. In order to avoid long machining times and to improve productivity, the total toolpath to machine these locations also has to be minimized.

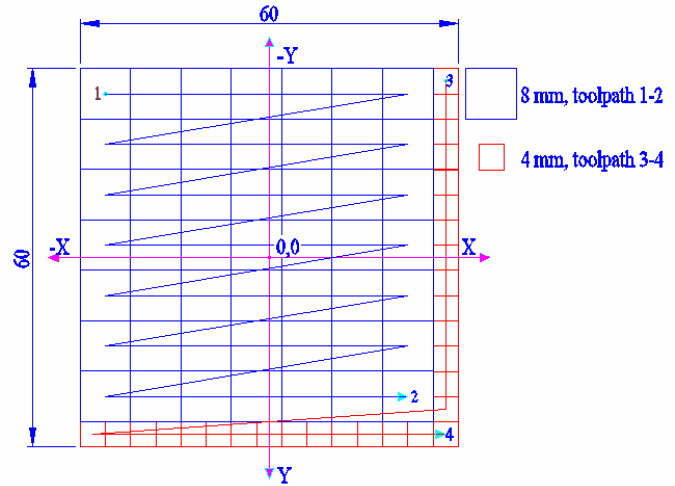
Hence, three different algorithms have been examined to achieve optimal tool path and minimize the number of pulses needed for a complete machining cycle of a discrete region of microstructure.

3.5.2 Left-to-Right

The Left-to-Right algorithm was developed to scan the area to be machined always from one side of the substrate. The algorithm works out the best possible masks layout for a given range of masks (8, 4, 2 and 1 mm) and area to be machined. Starting at the top, after one row is scanned the laser head moves to the next row, but scanning always starts first from the same side as in the previous row as shown in Figure 3.16. The main issue with the left-to-right algorithm is that masks layout is not efficient from the machining point of view. If, for example, the mask size shown in Figure 3.16 is the smallest possible size that could be used to machine that octagonal shape, then it is clear that practically it will be impossible to machine it with this mask size. Another important point is that with this algorithm, masks layout (multiple mask sizes in this case 8, 4, 2 and 1 mm) will be more stochastic and this will make toolpath inefficient and increase machining time. Another drawback of this algorithm is long idle time after the machining cycle for laser head to travel back into next position to continue machining.



(a)



(b)

Figure 3.16: (a) Left-to-Right algorithm (Top to Bottom) used to generate an optimal masks layout for toolpath determination. (b) An example of masks layout and toolpath produced by Left-to-Right algorithm.

3.5.3 Zig-Zag Algorithm

The Zig-Zag algorithm works in a similar way, but the masks are laid out in a consecutive manner, row by row. The algorithm scans in advance the predetermined area in a Zig-Zag fashion. The machining area is scanned from both sides as shown in Figure 3.17.

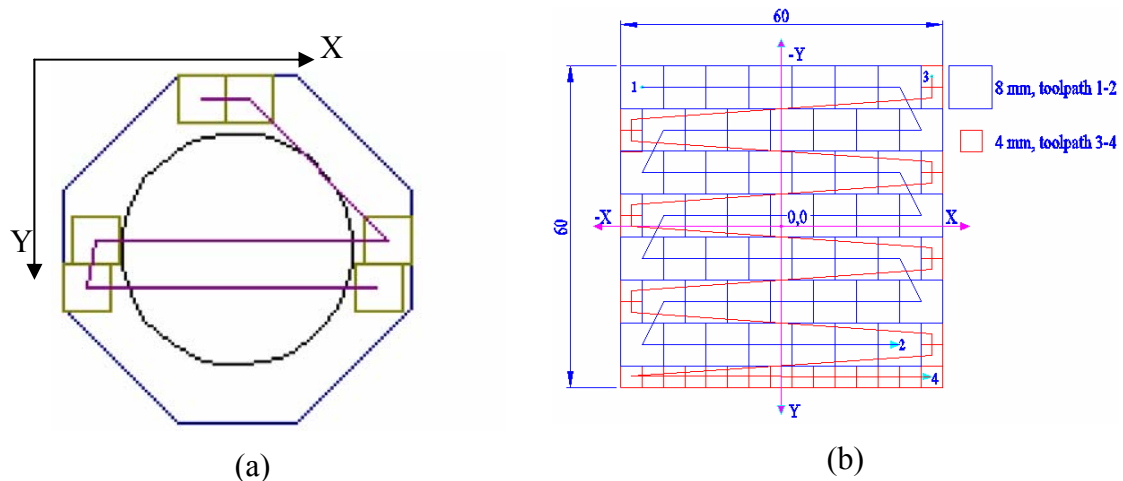


Figure 3.17: (a) Zig-Zag algorithm used to generate an optimal masks layout for toolpath determination. (b) An example of mask layout and toolpath produced by Zig-Zag algorithm.

When tested this algorithm had a similar machining efficiency problem as previously described for Left-to-Right algorithm. However, the advantage of this approach is that it halved the processing time.

3.5.4 Star Algorithm

Star algorithm resolved the machining efficiency problem (Figure 3.16 and Figure 3.17.) that appears with the other two algorithms as a result of using a standard set of square masks (8, 4, 2, 1 mm) to approximate any surface. If the area to be machined is not possible to be represented with a combination of the aforementioned range of masks, gaps in designed structure will appear in the mask layout, and consequently cause errors during machining process. This algorithm starts layout of the masks always from the centre of the machining area outwards. This ensures that the maximum possible size masks are concentrated around centre of the structure (see Figure 3.18) and the smallest masks are around border of the structure. This way the surface roughness will be improved especially for symmetrical structures because the number of shots to produce the structure will be minimum reducing the machining time, and stitching errors evenly distributed for the particular masks range used. This algorithm will approximate any shape with a

minimum number of shots and minimum stitching errors effects for the square masks range chosen.

This way the toolpath will be optimal or minimal. The real improvement of the star algorithm is not just optimal toolpath, but also minimum edge error because the smallest masks are used to machine boundaries, and even distribution of these errors especially for symmetrical parts (i.e. surface roughness improvements or stitching error reduction, and better control over these errors).

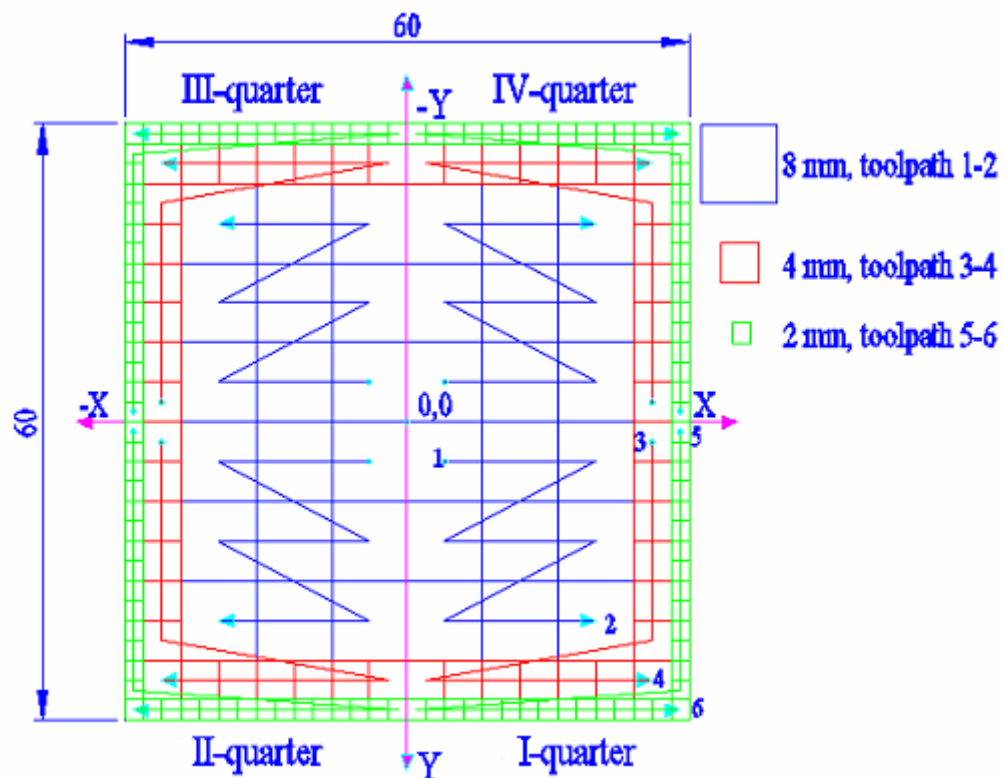


Figure 3.18: Star Algorithm showing toolpaths generated for each quarter of the structure for 8, 4, and 2 mm mask sizes.

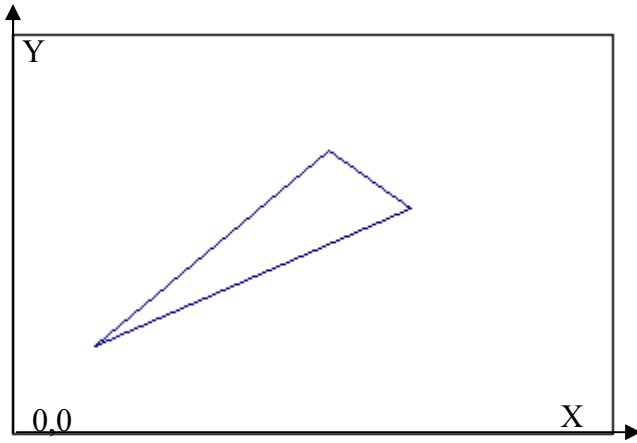
Figure 3.18 shows how this algorithm was used to layout the masks for machining of 60x60 mm square structure. The algorithm starts the layout by first using the maximum available mask size, 8mm and generate toolpath 1-2 in first quarter of the structure. Secondly, the next size down mask is used, 4mm to generate (toolpath 3-4) and finally the

2mm mask is used to generate toolpath 5-6. From Figure 3.18 it is noticeable that the smallest possible mask size from the range 1 mm was not needed to produce this particular square structure. The other important advantage of star algorithm is the minimum edge (contour) error because the algorithm always lays out the smallest possible mask size at the border of the structure. The mathematical model for edge error control is explained in Chapter 4.

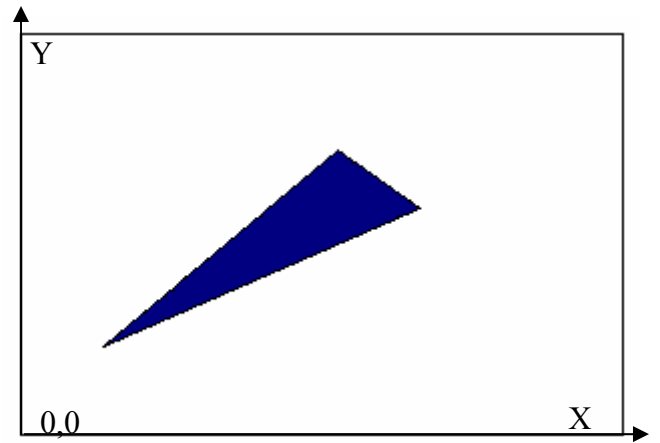
The Star algorithm is an analogous to Bresenham's ideal line algorithm, except that the algorithm was applied in a star fashion. This enables proper mask layout with maximum machining efficiency and optimal toolpath. The use of this algorithm for further optimisation of the pulse minimisation process will be discussed in more detail in the next section.

3.6 Pulse Minimisation Algorithm

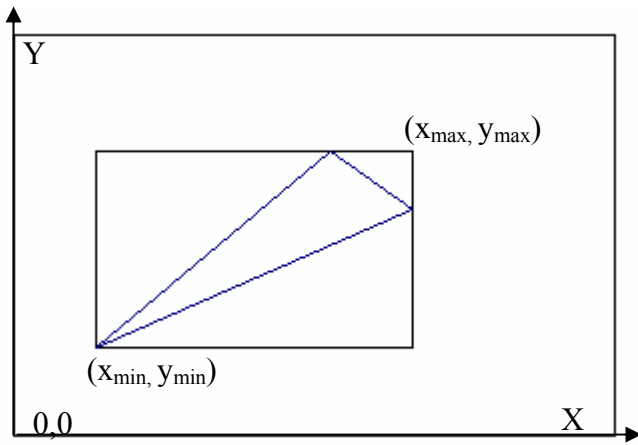
Figure 3.19 represents the process steps of the pulse minimisation process using the Star algorithm. Firstly, the desired contour is imported from a CAD model as a slice file format. Figure 3.19 (a) shows a layer of the 3D model. Secondly, the algorithm will determine the area that has to be machined and then fill this with a color as shown in Figure 3.19 (b). Then, the algorithm will find the minimum and maximum points on the contour to establish an optimal scan area, Figure 3.19 (c). When the scan limits have been determined, a complete machining area is divided into four segments as shown in Figure 3.19 (d). Next, the algorithm was designed to layout the masks from the center of the previously determined scan area outward, placing first the largest possible mask size (800 μ m) in the center of this area. When all possible masks of this size have been fitted in the area, the algorithm will look to fit next size down (400 μ m), and will scan all the area. This is repeated until the smallest possible mask size is reached. This process for each quarter is shown in Figure 3.19 (e), (f), (g), and (h) respectively. In the final step, Figure 3.19 (i), the algorithm scans through entire structure again and recombines all smaller mask sizes into larger ones wherever possible, thus reducing the number of machining pulses dramatically.



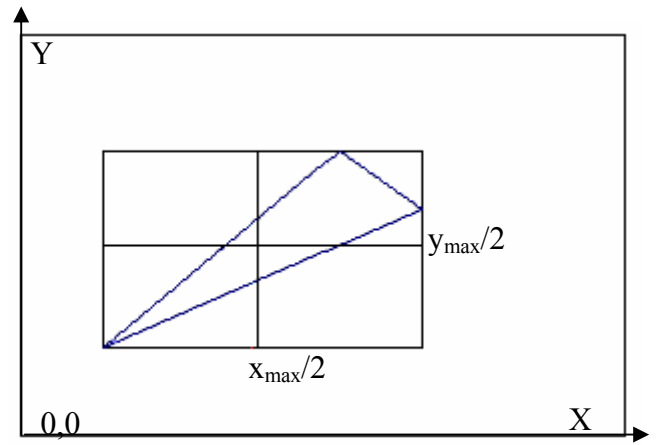
(a)



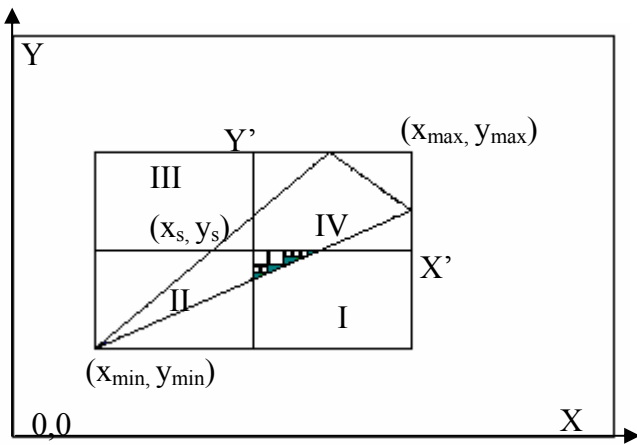
(b)



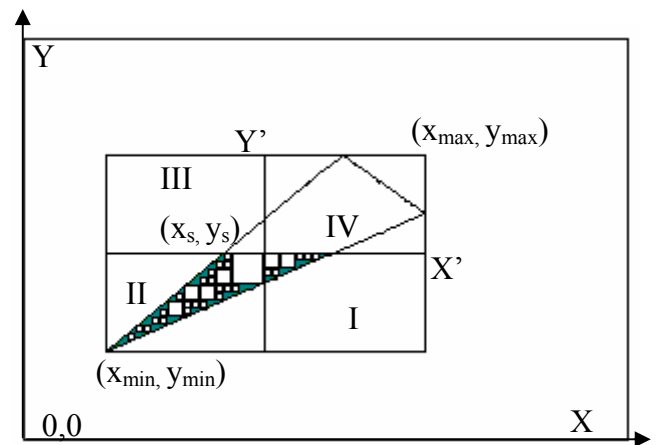
(c)



(d)



(e)



(f)

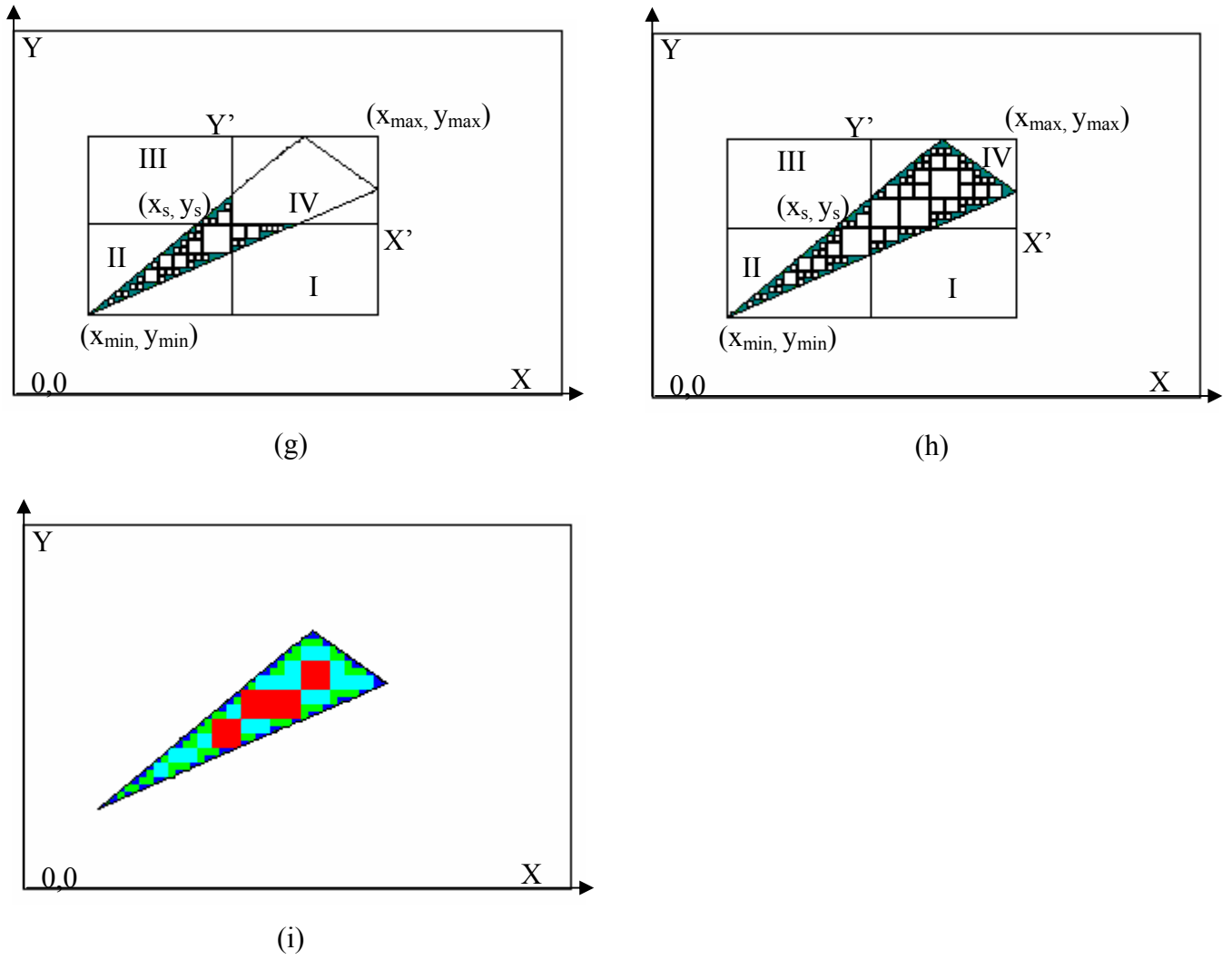
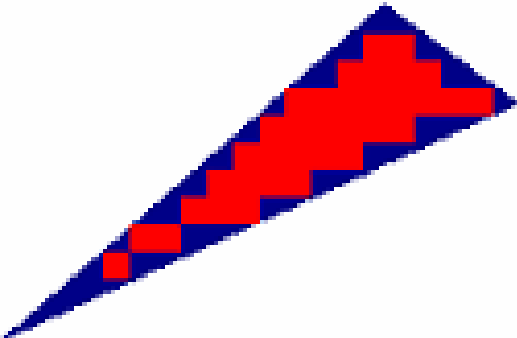
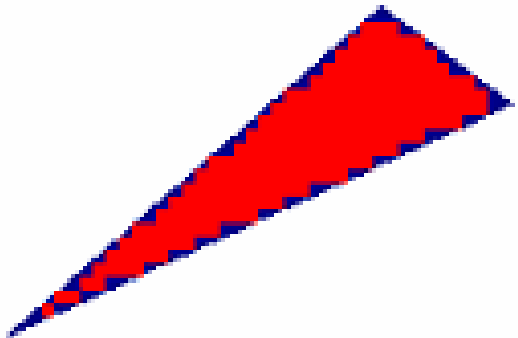
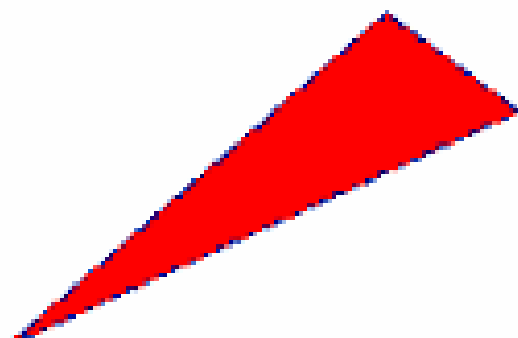
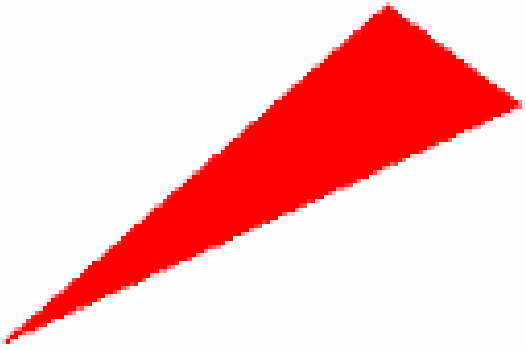
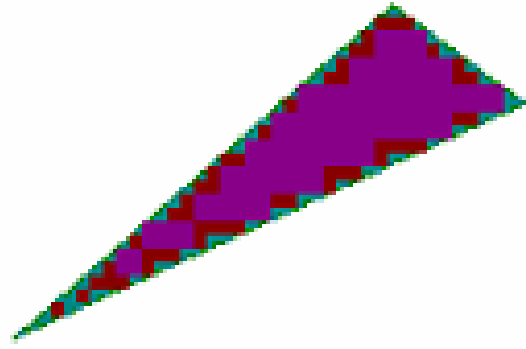
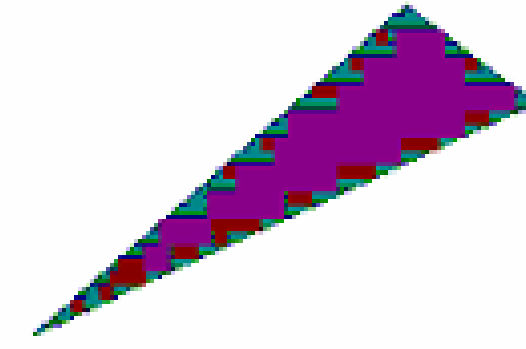
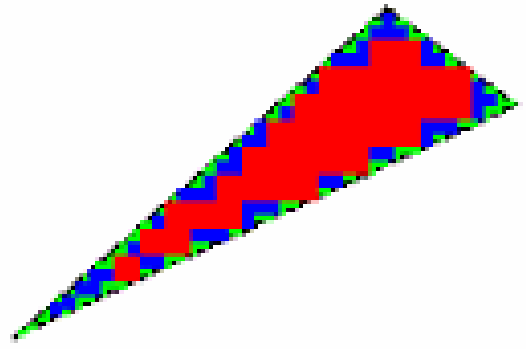


Figure 3.19: Mask layout simulation and pulse minimization process using adapted Bersenham algorithm.

Table 3.2 shows the comparison of pulse minimisation versus edge error and machining time for different algorithms employed in this research work. The comparison was performed on the same sample of triangular structure. It can be seen that for the smallest possible mask size (1x1mm), the number of pulses required to machine complete area is maximum, hence, the machining time is the longest one, but the edge error is minimum, i.e. the edge quality is the best possible with the range of masks employed (1, 2, 4 and 8 mm). On the other hand if the star algorithm were employed, the number of required pulses to machine the same area will be the minimum, and the edge error and machining time will be the minimum as well.

Table 3.2: Pulse minimisation using different algorithms.

Masks Layout	Number of pulses n	Mask Size (mm)	Edge Error	Algorithm
	35	8x8	Maximum	Single Mask, Step and Repeat
	195	4x4	Medium	
	902	2x2	Small	

	3864	1x1	Minimum	
	36	8x8	Small	Multiple Masks, Left-to- Right
	52	4x4		
	118	2x2		
	256	1x1		
	Total	462		
	17	8x8	Medium	Multiple Masks, Zig-Zag
	27	4x4		
	104	2x2		
	320	1x1		
	Total	468		
	36	8x8	Minimum	Multiple Masks, Star
	52	4x4		
	119	2x2		
	252	1x1		
	Total	459		

The tool path generation and pulse minimisation algorithms were then tested in actual machining trials. The results are reported in Chapter 6. Following successful experimental trials, complex structure designs can be produced, which were costly to achieve with existing methods. The main system features and limitations are outlined in the section 3.8.

3.7 Experimental Set Up and Equipment

3.7.1 Design of Experiment Technique

The laser ablation of material is dependent on both laser process parameters and properties of the material to be cut. For a given material, the process parameters need to be adjusted in order to achieve optimum machining performance [77].

To optimise the process parameters a design of experiment method using Design Expert v6.0 software (Stat-Ease, Inc) was implemented.

For complex research problems requiring many difficult to perform experiments, the DOE technique has become an essential part of the development process. The traditional method of collecting large quantities of data by holding each factor constant in turn until all possibilities have been tested is an approach that quickly becomes impractical as the number of factors increases. To reduce the number of experiments to a level efficient to conduct, a method termed Taguchi optimization [7] was used. This approach is based on a special set of arrays called orthogonal arrays (*OA*). An orthogonal array is usually presented in a matrix format consisting of a left-hand column and a top row, with various numbers occurring at the intersection of each column and row. Each element in the top row represents an independent input parameter and each element in the left-hand column represents an experimental run. The numbers at the intersections indicate the values of different parameters for each experimental run.

The nomenclature used is generically $L_x(Z^y)$, where L is the *OA*, y is the number of input parameters, Z is the number of value settings for each parameter and x is the number of experiments that must be run to complete the matrix. As it was necessary to conduct experiments for three main parameters with three different levels of significance for each

parameter, the most suitable *OA* array was $L_9 (3^4)$ where a fourth input factor is not included in the optimisation process [7]. Hence, the total number of experiments would be $3^3 = 27$ experiments, and is not practical to conduct.

To implement this method the following steps are needed:

1. Factors/interactions identification
2. Range of values of each factor selection
3. Orthogonal arrays selection
4. Established relation between factors/interactions to columns of the *OA*
5. Conduct the experiments at software directed conditions
6. Data analysis and optimal values selection
7. Conduct the confirmation experiment.

Statistical data analysis was completed by analysis of variance (ANOVA) software based on a linear model suggested by the software and designed to include all values for each factor. This model provides a 95% confidence interval that any individual value is expected to fall into a given range 95% of the time.

3.7.2 Materials

Standard (75 mm long x 25 mm wide) prototypes were made using 1.58 mm thick sheets of polycarbonate (PC), (8050, GE Plastics, USA). Following the ablation process, some of the channels were packaged in a lamination process. A thin PET plastic foil coated with a melting adhesive film layer was pressed by a heated lamination roller (at 150°C) onto the structure as a lid. Melinex® Polyester film type 301 (Dupont, Teijin films) having a thickness of 30µm were used for fabrication and the lamination equipment was a MEGA dry film laminator model 305 (Mega Electronics). PET (Polyethylene Terephthalate), 250 µm thick, was obtained from DuPont (Geneva) under the name type SE10 material.

3.7.3 Masks

Conventional chrome-on-quartz photolithography mask was designed using AutoCAD software and data exported in a DXF file format. ASM2500™ software tool was used to translate DXF file in a format compatible with Pattern Generator and Image Repeat machine (PG/IR) (ElectromaskII). The PG/IR machine is a specialized electromechanical photo-plotting device capable of producing precision images on photo-sensitive glass plate. The process of producing an image on a glass plate is known as Pattern Generation. Images were produced by a mosaic of rectangular shaped exposures of various sizes onto a photosensitive plate/film. To produce complex image, the individual exposures can be rotated to follow angled or curved shapes and boundaries. The “plate“ (5x5”) was resist coated Anti-Reflective (AR) Chrome Film on a glass plate. AR Chrome is available in Soda Lime, low expansion glass or pure Quartz. The mask for this work was made using AR Chrome film from pure Quartz (UV transparent). Mask was manufactured at the SES DSTO laboratory (Salisbury, SA).

The minimum possible apertures size at photographic plate was $1.25\mu\text{m}$ and maximum is equal to 3.8mm. Aperture rotation resolution was 0.1° . Two major advantages exist with this type of mask- they are extremely accurate, and free standing features can be machined since they are supported on a transparent substrate (i.e., concentric shapes) [16]. Figure 3.20 shows the mask patterns design used for this research work.

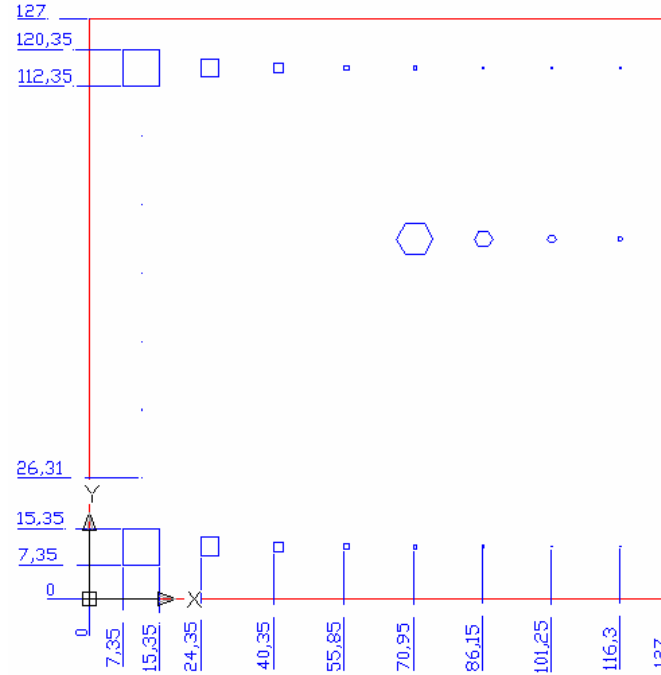


Figure 3.20: Design with square and hexagonal patterns drawn in AutoCAD and used by PG/IR photo-plotting machine for manufacturing of conventional Chrome-on-Quartz mask.

For the purpose of testing different mask shapes, prototype metal shim contour masks with arc, hexagonal and square features were produced by a frequency tripled Nd:YAG laser (AVIA 3.0W, Coherent Inc, USA). The Q-switched, pulsed output of the laser generates pulse energy of $180 \mu\text{J}$, and in this work a *PRF* of 10kHz was used. The system was set up to fire a pulse every $11\mu\text{m}$, i.e. a shot overlap equivalent to 2.7 shots per area [78]. Hence, to cut through an $80\mu\text{m}$ thick stainless steel sheet 300 passes over the designed specific toolpath (i.e. a total of 810 shots per area) were needed. There are two main problems with this type of mask, free standing shapes cannot be created, and the accuracy of the shapes is not good as chrome-on-quartz since corners tend to be round and edges have a roughness of several microns [16].

3.7.4 Excimer Laser Series 8000 (Exitech Ltd.,UK)

The machining aspect of this work was performed using an excimer laser system Series 8000 (Exitech Limited, UK) equipped with a LPX210i (Lambda Physik, Germany) laser source as shown in Figure 3.21.



Figure 3.21: Excimer laser Series 8000 Exitech Ltd.

The beam delivery system contained beam shaping and homogenization optics to create a uniform, square beam at the plane of a mask (chrome-on-quartz or Nd:YAG contour metal shim mask). The mask was held on an open frame with a CNC X-Y stage set. The double fly's eye homogeniser had a numerical aperture (NA) of 0.01 and produced a 10 x 10 mm uniformly illuminated region at the mask plane. An on-line beam profiler monitored the pulse energy, of which, 80% has an intensity variation of less than $\pm 5\%$ RMS in the plane of the mask. The fluence at the sample position was measured as a function of attenuator setting using a pyroelectric energy monitor (Molelectron Type JD25) and it was found varies no more than $\pm 10\%$. The lens used for this work had a 1:10 demagnification factor, NA of 0.3, a 1.5 mm diameter field and an optical resolution of $0.8\mu\text{m}$. The arrangement of the homogeniser and the projection lens produced a partial

coherence factor of 0.2. In order to understand the effect of the fluence and number of laser shots, the fluence was varied in the range of 0.2 to 1.6 J/cm². This was done by adjusting the attenuator, which consisted of dielectrically coated plate and an uncoated compensator plate angularly rotated in the beam to continuously change the optical transmission value [79]. A schematic of the optical arrangement of the excimer laser mask projection system is shown in Figure 3.22.

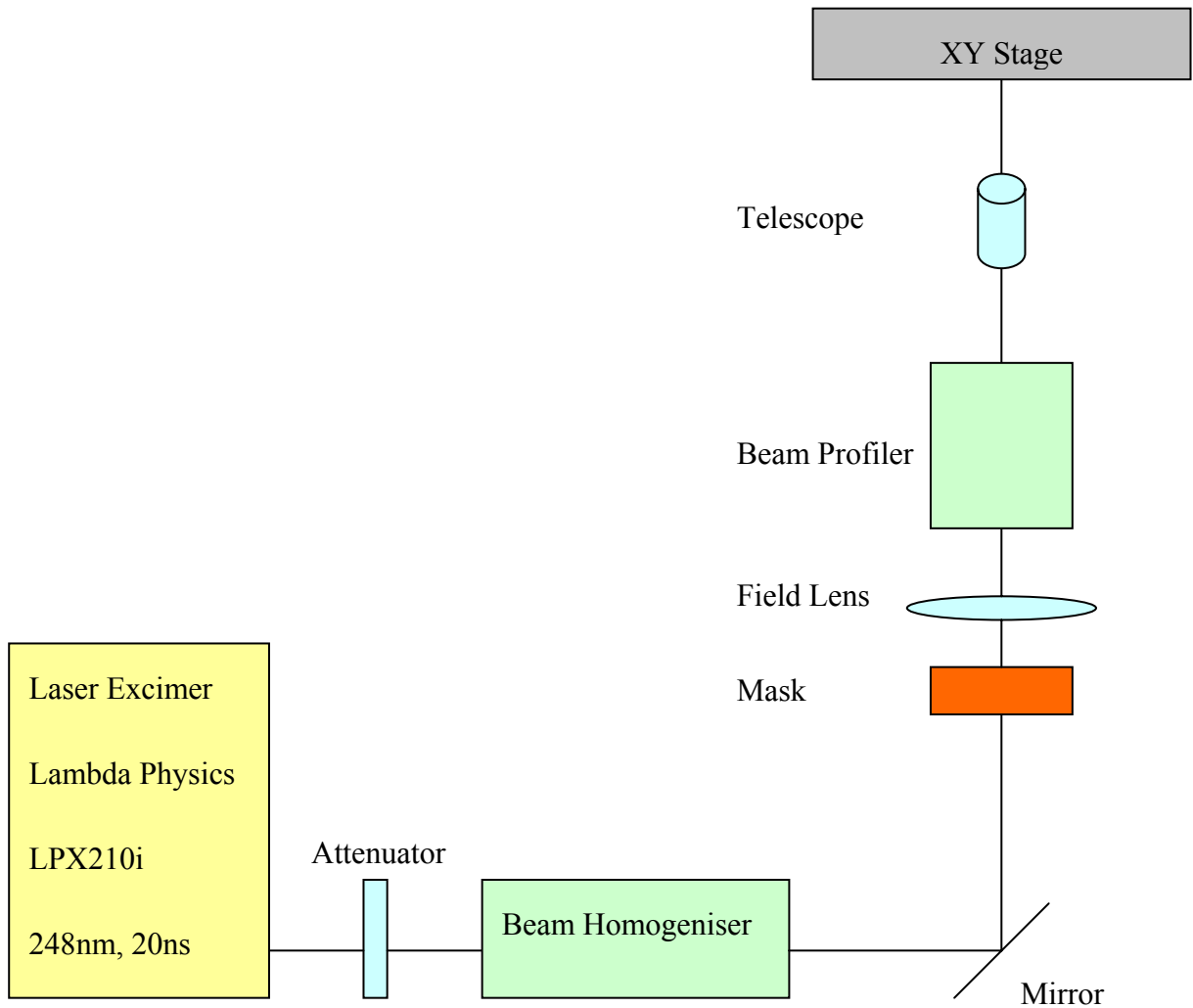


Figure 3.22: Optical arrangement of the excimer laser micromachining system.

3.7.4..1 *Excimer Laser Machining*

The microstructures were fabricated by UV laser photo-ablation process at 248nm using step-and-repeat and workpiece-dragging technique and following set up procedures previously described [79].

All the experiments were achieved with a 1.58 mm thick PC, 0.250 mm thick PET.

Table 3.3 summarized experimental work undertaken in this research and lists the main process parameters applied in each experiment.

Table 3.3: Experimental investigations undertaken in this research.

Experiment		Laser Parameters (F_d , PRF , n)	Mask dimensions (mm)	Chapter
Edge Error	15° Sample	1.6 J/cm ² , 5 Hz, 50 laser pulses	4,2,1	4
	30° Sample			
	45° Sample			
Material Characterization for PC		0.2-1.1 J/cm ² , 10 Hz, (8,16,32,64,128) laser pulses	8,4,2,1	5
Material Characterization for PET		0.2-1.1 J/cm ² , 10 Hz, (8,16,32,64,128) laser pulses	8,4,2,1	5
Stitching Error	Type 1, OL = 0	1.1 J/cm ² , 5 Hz, 100 laser pulses	2, 1	5
	Type 1-5	1.1 J/cm ² , 5 Hz, 500 laser pulses		
DOE optimisation	Square	0.5 J/cm ² , 80 Hz, 70 laser pulses	1	5
	Square _{DOE}			
	Hexagonal			

CN Method	Y-Shape	1.3 J/cm ² , 5 Hz, 50 laser pulses	1, 0.5	6
	Simple Serpentine			
	Complex Serpentine			
Cell Transportation Device	Design1 90°	1.1 J/cm ² , 50 Hz, 25 laser pulses	0.5	7
	Design 2 Circular			

3.7.5 Laser Scanning Confocal Microscopy

The evaluation of the results of excimer laser micromachining was performed by a laser scanning confocal microscope (LSCM) (Olympus Pty. Ltd., OLS1200) (see Figure 3.23).



Figure 3.23: LSCM (OLS 1200, Olympus Pty.Ltd.).

The basic optical principle behind a Laser Scanning Confocal Microscope (LSCM, sometimes CLSM) is to scan the specimen with an illuminating spot, and at the same time have a small detector aperture follow that illuminating spot. This is usually achieved by having a laser as illumination source and a small aperture in front of the detector, which usually is a photomultiplier tube (PMT) [80]. A schematic of a simplified system is shown in Figure 3.24.

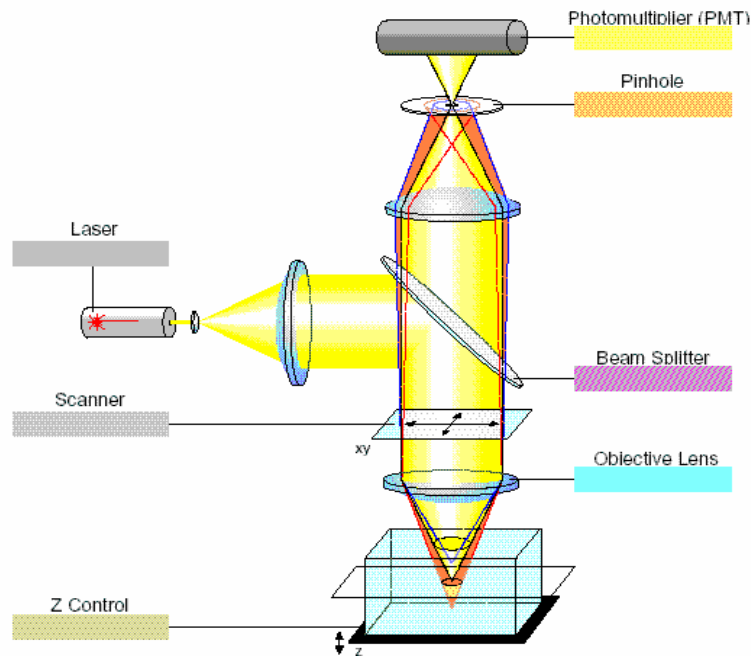


Figure 3.24: A schematic of LSCM.

A 2D image of a small partial volume of the sample centered on the focal plane is generated by performing a raster sweep of the sample at that focal plane. As the laser scans across the specimen, the analog light signal, detected by the photomultiplier, is converted into a digital signal, contributing to pixel-based image displayed on a computer monitor attached to LSCM. The relative intensity of the light emitted from the laser hit point, corresponds to the intensity of the resulting pixel in the image (typically 8-bit grayscale). The plane of focus (Z-plane) is selected by a computer-controlled fine-stepping motor, which moves the microscope stage up and down. Typical focus motors can adjust the focal plane in as little as $0.1\ \mu\text{m}$ increments. A 3D reconstruction of a sample can be generated by stacking 2D optical sections collected in series [81].

This unique microscope enables measurement of depth of the microstructures with high resolution ($0.01\ \mu\text{m}$), due to its very short depth of field. With this device non-contact 3D surface data acquisition is possible. It can be used as a common microscope in order to get 2D images of the surface. The advantage of a confocal microscope in comparison to other 3D information systems like interferometers, or fringe projections is

the possibility to reproduce quantitative information from surface with a range of roughness, high aspect ratios, and varying reflectivity. Filtering and leveling operations are provided to post-process generated image data. The quality of these images and time taken to acquire images is in between a scanning electron microscope (SEM) and an optical microscope [81]. The Multiple Image Acquisition Module of the software allows stitching together a large number of adjacent images with higher magnification, hence images of high resolution can be produced for large scanning areas. This is particular useful for acquisition of data with high resolution for long microchannels or complete MEMS devices.

3.7.6 Optical Microscopy

For cut profile characterization, samples were visualised with an optical microscope with Z-axis calibration (Olympus BX60) (see Figure 3.25) using 5x objective magnification lens [82].



Figure 3.25: (a) Optical microscope (Olympus BX60).

3.8 Evaluation of the System

The CAD/CAM system has a standard tool set of multiple mask sizes (0.01, 0.5, 1, 2, 4 and 8 mm). The system also has a cleaning cycle feature for removal of re-deposited ablated debris: i.e., machining with less pulses (5-10) per pass and multiple pass control.

Table 3.4 compares main process steps required to accomplish a microstructure or device from early design to final machining stage using existing systems and the CAD/CAM system developed in this research. The numerical data was established from a survey of experts in the field. It is noticeable that the new system provides a cost effective

solution especially when quick changes in design are essential. Other capabilities are discussed in more detail in the following sections.

Table 3.4: Comparison of the process steps in the existing and new approach from early design stage to final product.

	Existing approach process steps	New approach process steps
Design Tools	AutoCad, CorelDraw	Fully parametric 3D CAD interface Solidworks
Design Time	½ hour (\$60/per hour)	½ hour (\$60/per hour)
Mask Design	Chrome-on-Quartz Mask patterns specific to a particular design.	Chrome-on-Quartz Mask patterns a standard tool set (1, 2, 4, 8 mm) to produce any features.
Mask Fabrication Time	2 weeks (\$800-2000)	Standard mask
Part program generation	Manual (\$45/ per hour)	Automatic
3D Microstructuring	Limited design range	Multi layered approach
Quick design changes	Poor flexibility	High flexibility

Costs	Additional for each new mask, extra design time, error prone part programming	One off cost for many design changes.
Machining Time	No optimization	Pulse and toolpath optimization algorithms.
Accuracy and feature resolution	Better surface texture when whole design is contained in one mask.(i.e. synchronized scanning technique).	Optimisation of stitching error effects automatic.
Total Process Time (no changes in design).	2 Weeks	1 Day
Total Cost (no changes in design).	\$905	\$60
Total Process time (one change in design).	4 Weeks	2 Days
Total Cost (with one design change).	\$1810	\$120

3.8.1 Step and Repeat Algorithm

The first phase of development of a CAD/CAM interface for the excimer laser ablation tool was limited to the step-and-repeat ablation technique. In this mode, the workpiece was moved laterally in the XY plane after each process step and a repetitive

pattern was built up. The main details of this technique were discussed in Chapter 2 section 2.5.1..1.

Figure 3.26 illustrates a typical triangular microstructure produced to evaluate the developed system.

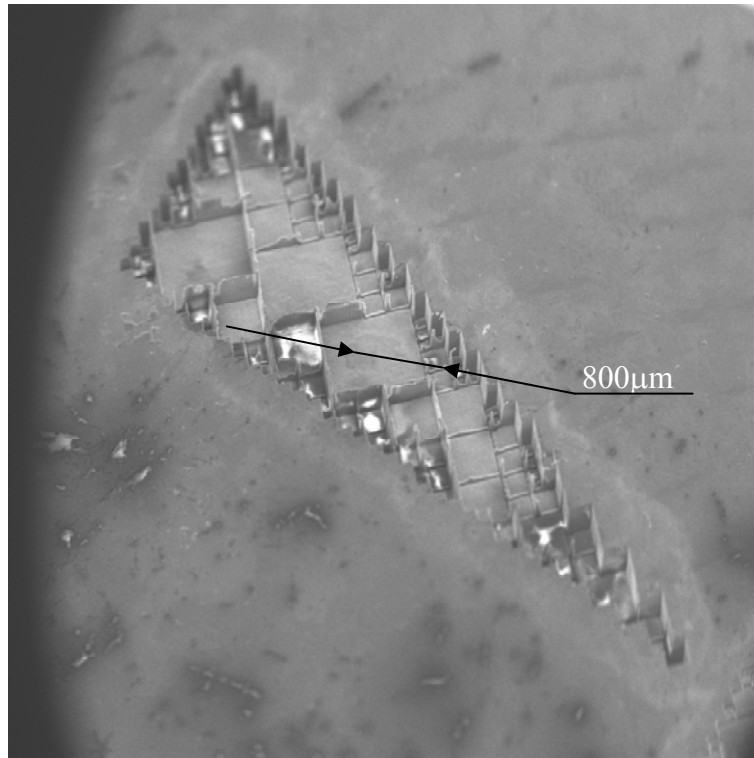


Figure 3.26: SEM image of a triangular structure produced by Step and repeat machining method. Material; PC, $PRF = 5\text{Hz}$, Fluence 1.1 J/cm^2 , Number of pulses per area $n = 100$.

3.8.2 Workpiece-Dragging Technique

Details of workpiece-dragging technique were also explained in Chapter 2, section 2.5.2..2. Figure 3.27 shows a 3D model of a hexagonal microstructure produced using this technique and NC code generated by developed CAD/CAM system. The machined hexagonal microstructure was measured by a LSCM instrument.

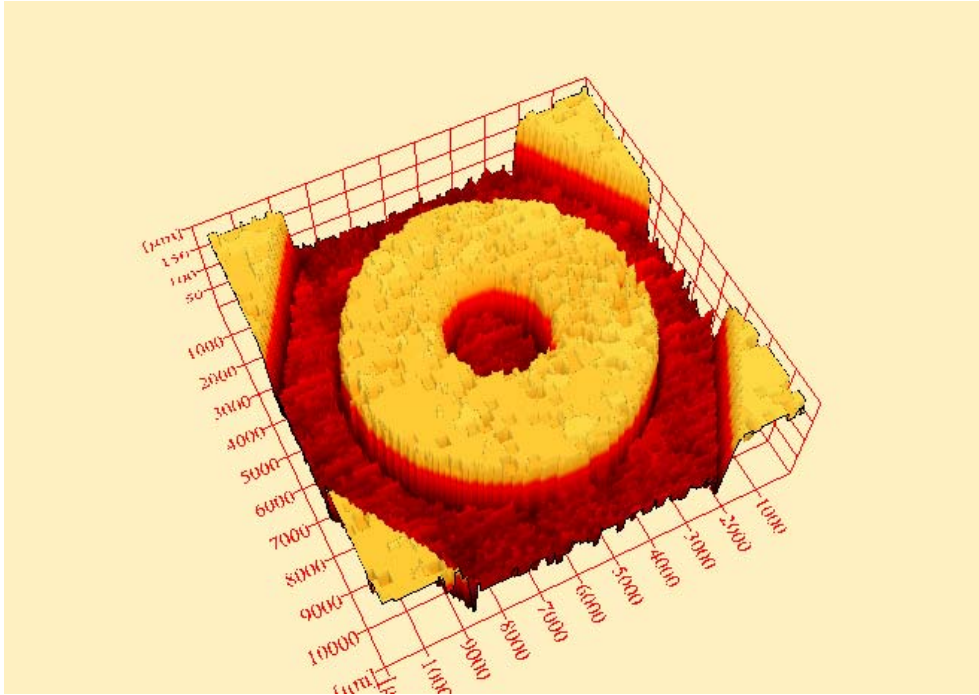


Figure 3.27: LSCM image of an octagonal 3D microstructure. Material; PC, $PRF = 10\text{Hz}$, Fluence 1.2 J/cm^2 , Number of pulses per area $n = 250$.

3.8.3 Multi-Layer Technique

Another important feature of the system is the possibility to produce 3D microstructures using a multi-layered approach. Figure 3.28 illustrates a complex pyramidal structure machined in this fashion. Figure 3.28 (a) shows a CAD model produced by the system and Figure 3.28 (b) shows the 2D LSCM image of the actually machined structure.

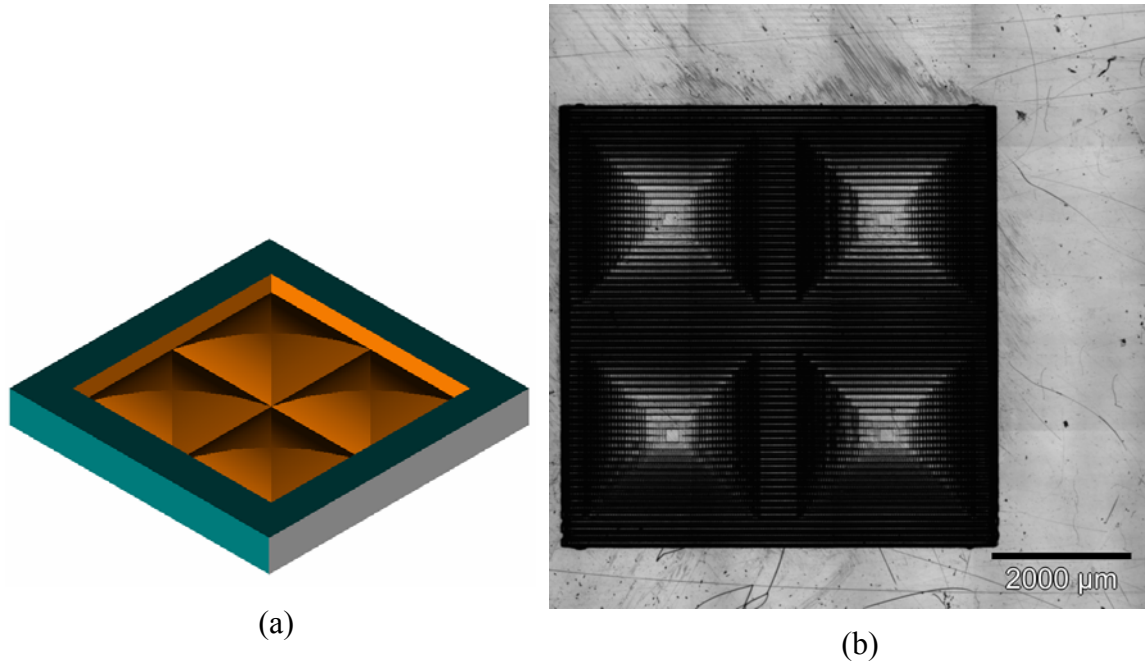


Figure 3.28: (a) CAD model and (b) LSCM image of a 3D multi-layered pyramidal microstructure. Material; PC, $PRF = 70\text{Hz}$, Fluence 0.5 J/cm^2 , Number of pulses per area $n = 100$.

3.8.4 Ramp Removal using Synchronised Mask Scanning Technique

The ramping effect is noticeable on all structures produced using workpiece-dragging technique, because of the nature of the excimer laser machining process where the number of pulses per area determines the entrance and exit of the laser tool. This will cause ramping on the walls of the structures. By employing the Synchronised Mask Scanning technique this error could be removed. This feature was also implemented in the system. The pyramidal structures shown in Figure 3.28 (b) were produced using the workpiece-dragging technique, but after each row has been machined, the mask and workpiece are offset, hence, the mask pattern to be applied comes outside at the edge of the beam. The workpiece was offset in accordance with the demagnification factor 10x. The position of the mask and workpiece is entered into memory registers, hence, they can be retraced back to their exact locations after each machining step. Synchronized movement of the mask stage and workpiece stage in opposing direction was used to remove the ramps. The velocity speed of the stage and workpiece is calculated based on the mask size, number of shots per area and pulse repetition frequency. One setback of

this process is that ramp removal has to be performed at the beginning and end of each dragged line. This additionally increases processing time but leaves the structure with straight walls at the boundaries, not taking wall angle into consideration.

3.8.5 Material Database System

Before the machining module is activated, material properties, mask size and laser process parameters have to be taken into account. The database system (Microsoft Access DB) was developed as a background application that contains all relevant process parameters. For example in multi-layered approach, the slice thickness is a function of etch rate (function of material properties and laser process parameters applied), and influences the accuracy of the CAD model replication. Theoretically, smaller layer thickness should approach the CAD model. Part of GUI for selection of optimal process parameters, depending on material used, was taken directly from database developed and embodied into the ExExp v1.0 system as explained in Appendix B.

3.8.6 System Limitations

The algorithms have been developed only for square and hexagonal shape mask tools. This will introduce staircase error effects at the contours of the part. These edge error effects are directly dependent on the minimum mask size used for machining. To control this error a mathematical model has been developed to determine the edge error, and the model is presented in the following chapter.

3.9 Summary

This chapter has explained the methodology used to develop a novel CAD/CAM system for the excimer laser ablation process named ExExp v1.0. The system's algorithms use the 3D geometry of a microstructure, defined in a CAD model, and the main parameters that influence the process, to automatically generate a precise NC part program for the machine. Two different approaches have been discussed. STL file approach that enables the system to exchange CAD model data with other CAD/CAM

systems and the BMP file approach that was developed to overcome deficiencies of the STL file approach.

The design component of the system enables both “external” and “internal” CAD modelling. The system algorithms have been developed for the step-and-repeat laser ablation technique and extended to include the workpiece-dragging technique to achieve a higher surface accuracy (smoothness) within the sub-micron range. The details of the algorithms for pulse number minimisation using the bit-map approach have been presented. The algorithms enable various mask sizes to be used to control the accuracy of the machined part and reduce the machining time. Development includes different machining techniques and a heuristics approach for tool path optimisation.

The system capabilities and limitations are presented and will be further discussed in the following chapters.

Chapter 4. *Mathematical Model for Edge Error*

4.1 Overview

This chapter describes a mathematical model for edge error calculation inherited as a staircase effect produced by a square shaped laser micromachining tool. The theoretical background for the approach developed is presented in sections 4.2. Edge error calculation is introduced in section 4.4. The algorithm used in edge error calculation for any shape appears in section 4.4.1. The experimental work carried out to verify the approach used is presented in section 4.4.2. The comparison between theoretical model and experimental results is explained in section 4.4.3 and finally, in section 4.5, a summary of this chapter is presented.

4.2 Introduction

In general, the outer edge of the layer machined with a square tool mask patterns will show the staircase defects. This is due to the fact that the boundary of an excimer laser machined part, using a square mask as a machining tool, is a stepped approximation of the boundary of the part surface from a CAD model. Mathematical equations can be developed to determine the edge error in any part. In general, the technique involves the determination of staircase area error on the outer edge of each layer of the object. The calculation was based on the Center Line Average Area Error (C.L.A.) standard [84]. Normally, this standard is used as a surface roughness determination method and represents surface height profile defined in a X-Z plane of the Cartesian Coordinate System (CCS). In this work the same principle was applied to boundaries of the part that lies in X-Y plane of the CCS for edger error calculation. By predicting the edge error it is then possible to control the quality of the edge.

4.3 C.L.A. Definition

The Center Line Average (C.L.A.), value is the international standard defined as the average height from a mean line of all ordinates of the surface, regardless of sign.

Thus, referring to Figure 4.1,

$$C.L.A. = \frac{h_1 + h_2 + h_n}{n} = \frac{\sum_1^n h}{n} \quad (4.1)$$

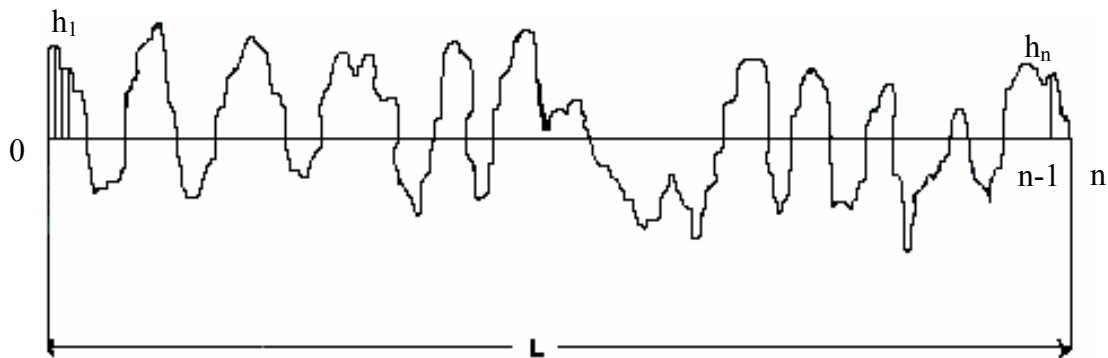


Figure 4.1: Graphical representation of C.L.A. by the collection of ordinates (h_n) [84].

To determine a C.L.A. value by the collection of ordinates would be a laborious process, and if an unfortunate ordinate spacing was chosen a significant point on the surface could be missed. If an irregular area is divided by its length then the value obtained is the average height of the area [84].

Such an area can be measured using a LSCM, thus considering an infinitive number of ordinates, and every point on the surface is considered.

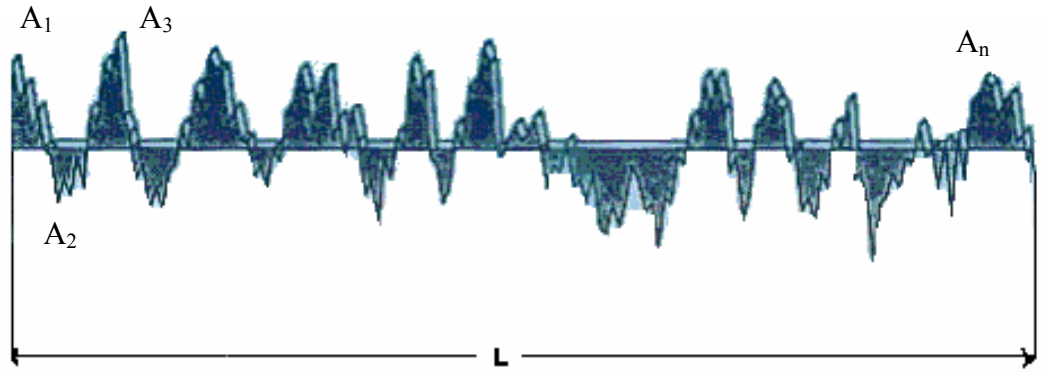


Figure 4.2: Graphical representation of C.L.A. by the collection of areas (A_n) [84].

Referring to Figure 4.2 it is seen that

$$C.L.A. = \frac{A_1 + A_2 + A_n}{L} = \frac{\sum_1^n A}{L} \quad (4.2)$$

where:

$$\sum A = \text{sum of areas in mm}^2$$

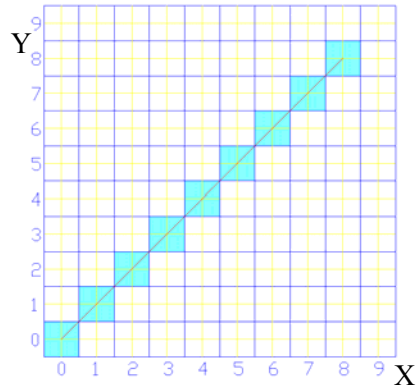
$$L = \text{length of trace in mm}$$

The value thus obtained is the average height of the trace [84].

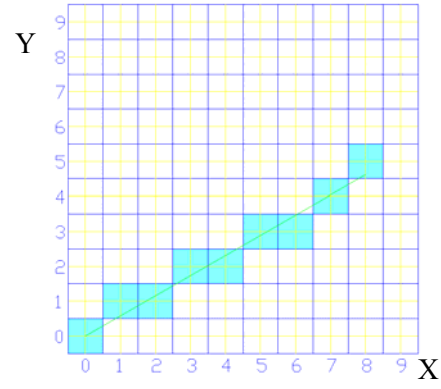
4.4 Edge Error

In a sliced model each layer represents a cross-section of the 3D part. The boundary in each layer is represented as a combination of straight lines. Hence, the edge error model was illustrated in a part by considering a general case of errors in a part with only

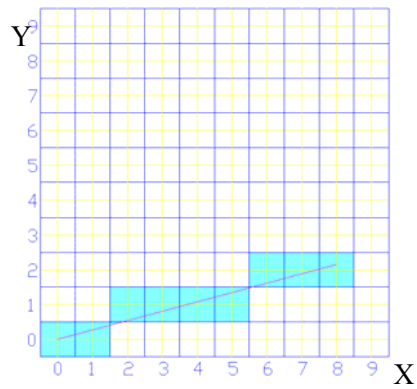
linear contours. The mask layout algorithm was based on an analogy with Bresenham ideal line drawing algorithm as shown in Figure 4.3.



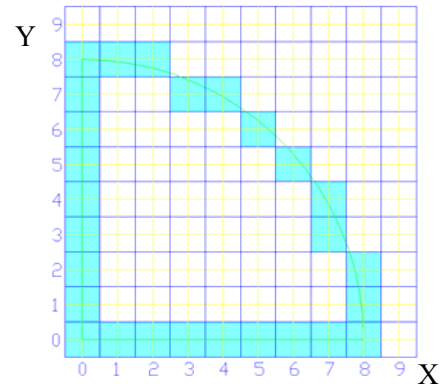
(a) Slope angle 45°



(b) Slope angle 30°



(c) Slope angle 15°



(d) A quarter of circle, angle 0 – 90°.

Figure 4.3: Masks layout in accordance to Bresenham ideal line drawing algorithm. Grid size is equal to mask size, and mask size could be any integer number.

The edge error can be computed in each layer. The edge error for each boundary line can be defined as the area of the triangle formed between a mask and the boundary of the part as shown by the triangle b, d, e or as the area of the trapezoid a, b, c, d in Figure 4.4. The edge error can be represented in terms of mask size and the incline angle. Considering a line with slope between 0 and 1 in Figure 4.4 the area error in each layer:

$$A = \sum_{i=1}^n A_1 + \sum_{i=1}^n A_2 \quad (4.3)$$

where i = the mask column number, $(1 \leq i \leq n)$ and

n = the total number of mask columns

$$A_1 = \frac{(be).(bd)}{2} \quad (4.4)$$

$$A_2 = \frac{(ac) + (bd)}{2} * (ab) \quad (4.5)$$

but $(ab) = M$ (mask size) and $\tan \theta = \frac{(bd)}{(be)}$, therefore area error

$$A_1 = \frac{\tan \theta}{2} * (be)^2 \quad (4.6)$$

$$A_2 = \frac{(ac) + (bd)}{2} * M \quad (4.7)$$

Considering all masks between the start and end point of the line, the average of area error is given by

$$\bar{A} = \frac{\sum_{i=1}^n A_1 + \sum_{i=1}^n A_2}{n} \quad (4.8)$$

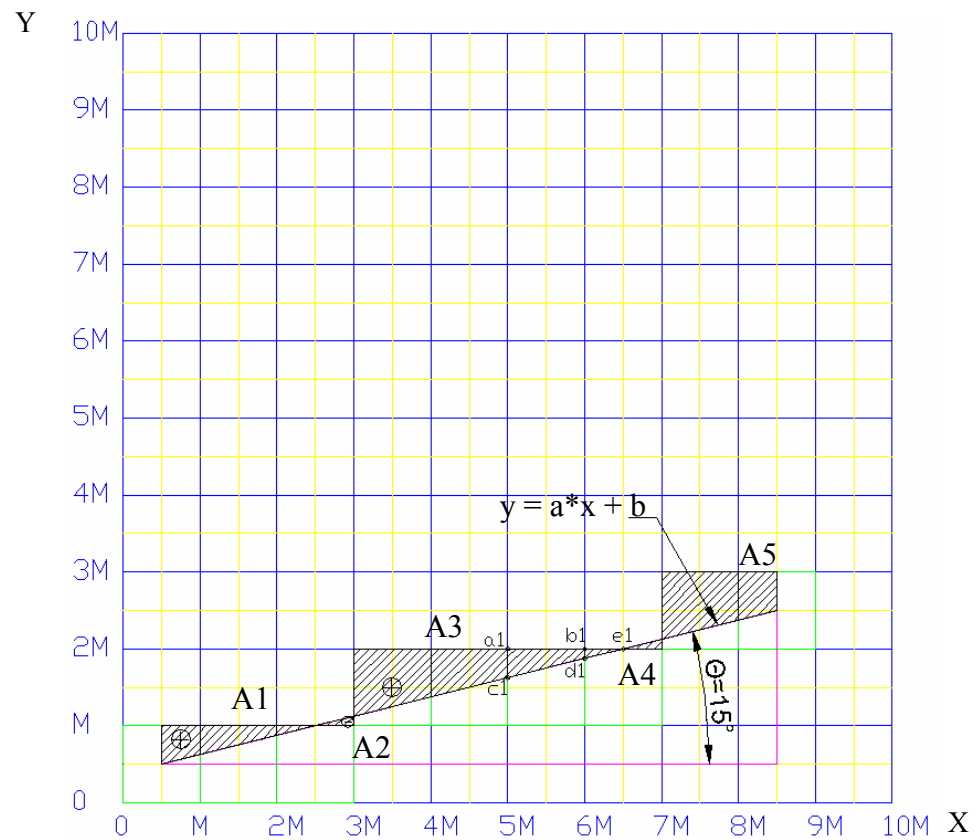


Figure 4.4: Edge error representation for 15° sloped straight lines.

It can be seen from Figure 4.5 that as the slope of the line changes, the area error of the triangles or trapezoids also changes.

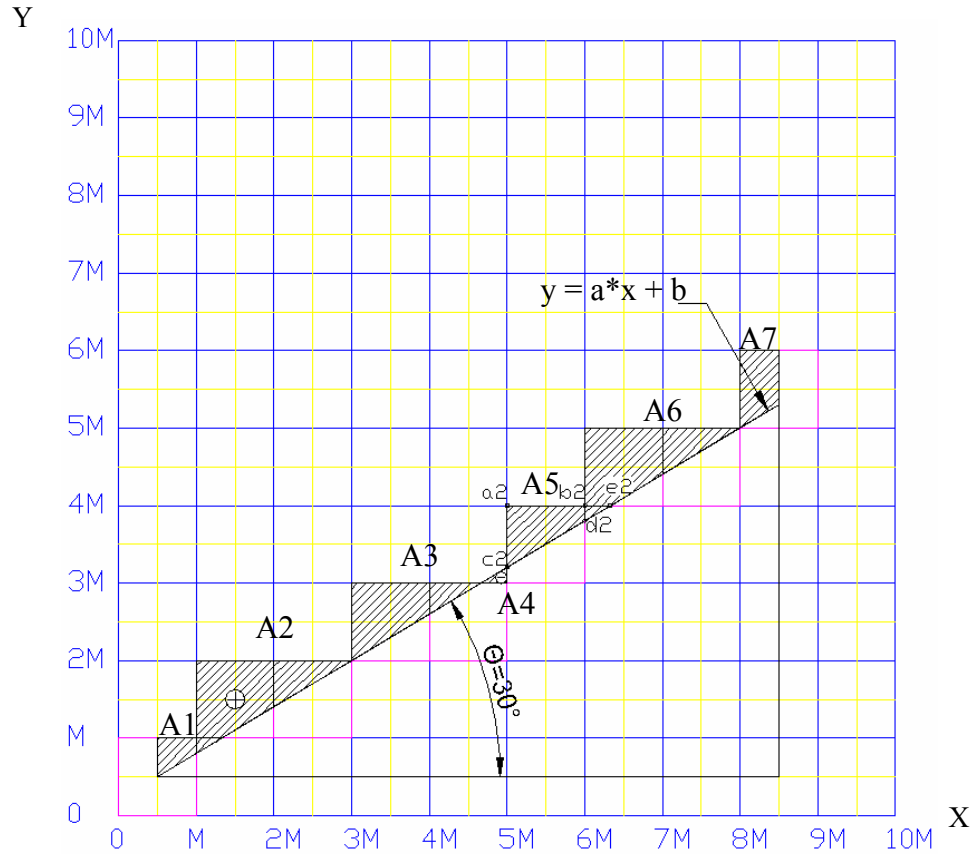


Figure 4.5: Edge error representation for 30° sloped straight lines.

Following the rules for the line drawing using an analogy with the Bresenham line drawing algorithm, the area error in each layer can be calculated as follows:

1) First the line slope has to be determined. The ideal line equation through the start and end point of line segment can be used (Boundary conditions: line slope $m = 0$ to 1).

Ideal line equation:

$$y = m (x - x_s) + y_s, \text{ or rewritten}$$

$$m = y_e - y_s / x_e - x_s \quad (4.9)$$

2) Next the sign of term e_i defined by equation (3.14) has to be determined. This value indicates the position for the next pixel (mask).

3) Area error for each mask position (trapezoid or triangle) is then calculated

The sum of these area errors (cross-hatched area) divided by the length of the line will give the amount of edge error for one segment of the boundary, as shown in Figure 4.6.

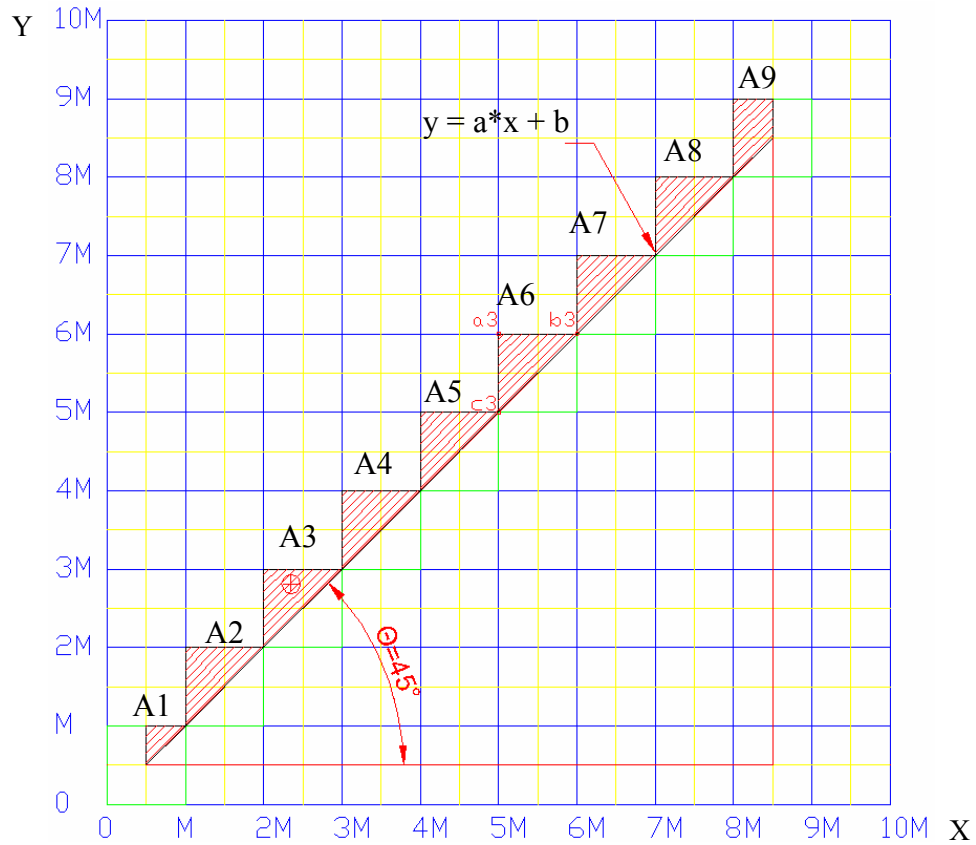


Figure 4.6:Edge error representation for 45° sloped straight lines.

In such a case the edge error in a layer will be the sum of the edge errors for each segment and is given by the expression;

$$E_l = \sum_{i=1}^n (E_i) \quad (4.10)$$

where,

l – current layer

n – total number of segments

E_i – edge error in each segment

4.4.1 Algorithm for Determining Minimum Edge Error

Figure 4.7 shows the flow chart describing mathematical algorithm to determine the least amount of edge error in any shape through selection of mask sizes. The input parameters to the algorithm include the part geometry in form of a slice file and initial mask size. The algorithm shown in Figure 4.7 is only valid for the lines with a slope between 0-1. The values of edge errors are determined for the part at each slope value, and then a mask recommendation can be made based on the minimum edge error.

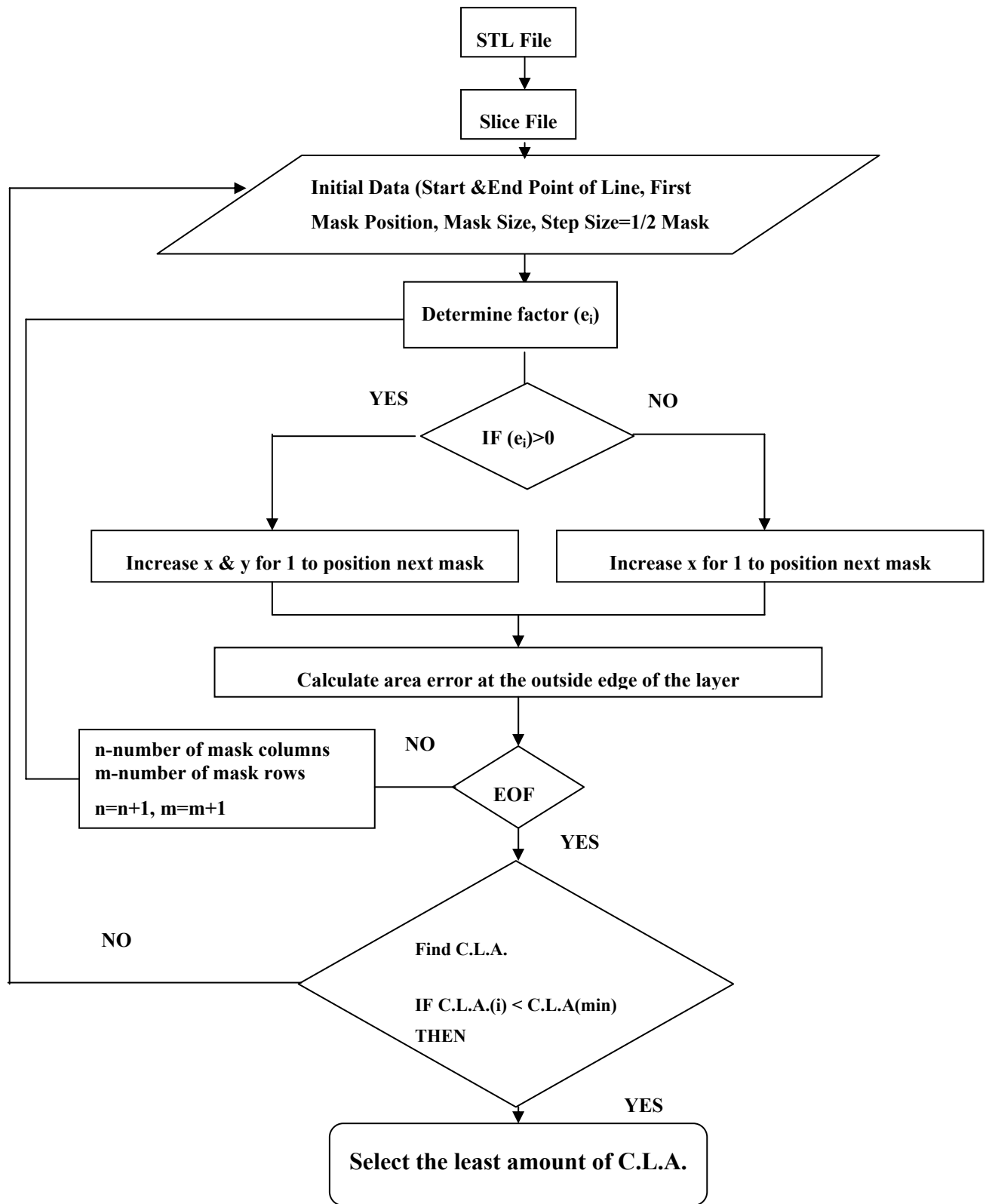


Figure 4.7: Mathematical algorithm to determine minimum edge error for lines with slope angle between 0-45°.

4.4.2 Experiments to Determine Edge Error For Outside Boundaries

The computed values of edge error discussed in previous sections can be verified by comparison with the experimentally determined outside boundaries edge error for a triangular test case. Physical Polycarbonate (PC) prototypes of triangular microstructures with different slope angles 15° , 30° and 45° were machined on the excimer laser system (Chapter 3, section 3.7). The experimental determination of edge error was carried out by measuring the area error of the staircase in each sample. This was accomplished by using a laser scanning confocal microscope (LSCM). The area error used was the average of the area errors measured for several identically machined samples. The calculation was based on the Center Line Average Area Error (C.L.A.) standard for roughness and edge straightness determination method [84].

4.4.3 Comparison of Theoretical and Experimental Results for Edge Error

To determine C.L.A. experiments were conducted and triangular structures were machined that match the theoretical models shown previously in Figure 4.4, Figure 4.5, and Figure 4.6.

Figure 4.8 has been taken by LSCM and represents the experimental ablated area measurements of the PC triangular structure with a 15° slope angle produced by excimer laser Step-and-repeat machining technique using two different square mask patterns: 2 and 1mm respectively. The points of measurements correspond to the same measuring points shown in theoretical model in Figure 4.4. The area measurements (A1-A5) produced by LSCM were summarised in Table 4.1.

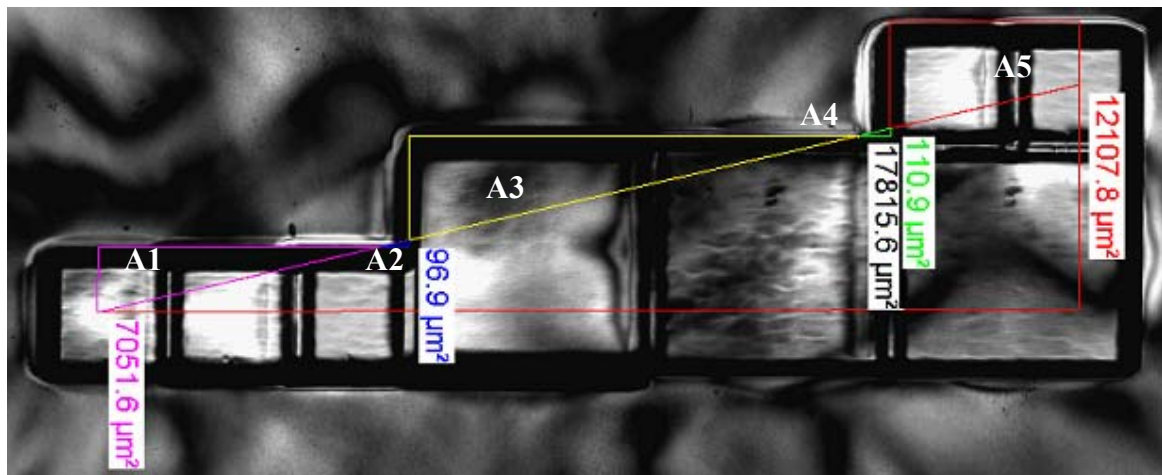


Figure 4.8: LSCM image of edge error measurements when slope angle is 15° . Labels (A1-A5) are area measurements calculated by LSCM.

Table 4.1: Edge error measurements when slope angle is 15° .

Area errors measurements (μm^2)	
A1	96.9
A2	17815.6
A3	110.9
A4	12107.8
A5	96.9
Sum of area errors (μm^2)	
ΣA_i	37182.8
Edge length (μm)	
L	843.72

Using the same analogy, measurements are shown in Figure 4.9 for a slope angle of 30° , and Figure 4.10 when the slope angle is 45° corresponding to measuring points shown in Figure 4.5 and Figure 4.6 respectively. These measurements were summarized in Table 4.2 and Table 4.3 respectively.

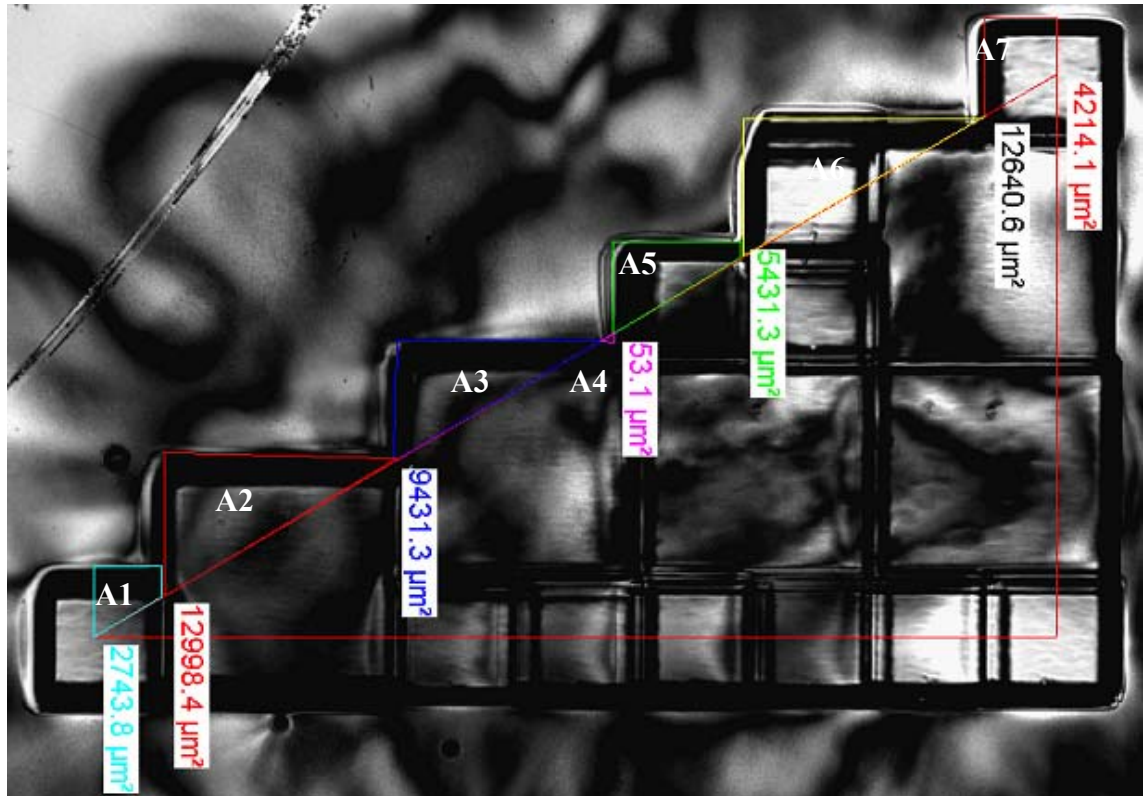


Figure 4.9: LSCM image of edge error measurements when the slope angle is 30° . Labels A1-A7 are area measurements calculated by LSCM.

Table 4.2: Edge error measurements when slope angle is 30° .

Area errors measurements (μm^2)	
A1	2743.8
A2	12998.4
A3	9431.3
A4	53.1
A5	5431.3
A6	12640.6
A7	4214.1
Sum of area errors (μm^2)	
ΣA_i	47512.6
Edge length (μm)	
L	960.9

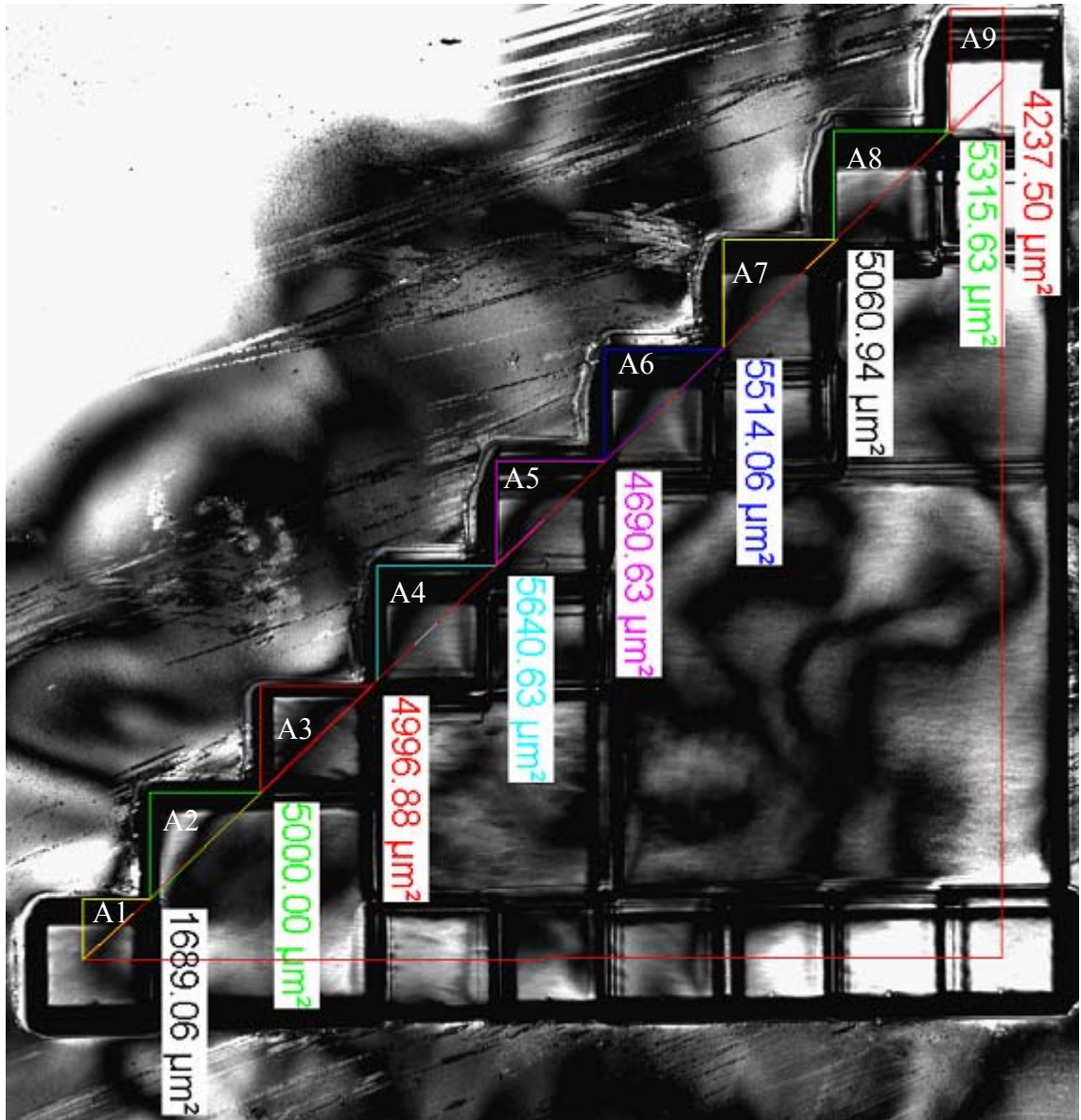


Figure 4.10: LSCM image of edge error measurements when slope angle is 45° . Labels A1-A9 are area measurements calculated by LSCM.

Table 4.3: Edge error measurements when slope angle is 45°.

Area errors measurements (μm^2)	
A1	1689.0
A2	5000.0
A3	4996.8
A4	5640.6
A5	4690.6
A6	5514.0
A7	5060.9
A8	5315.6
A9	4237.5
Sum of area errors (μm^2)	
ΣA_i	42145
Edge length (μm)	
L	1136.6

The difference between theoretical and experimental measurements for these three experiments has been summarised in Table 4.4. Theoretical values for C.L.A. shown in Table 4.4 were produced based on edge error calculations for the mask layouts produced using the Bresenham line drawing algorithm and equation 4.2

Table 4.4: Theoretical and experimental results for C.L.A. values.

Theoretical Values		Experimental Values	
Slope Angle (°) (Bresenham Algorithm)	C.L.A. (μm)	Slope Angle (°) (LSCM)	C.L.A. (μm)
15	367.8	14.69	440
30	465.4	31.87	494
45	353.0	44.90	370

Experimental values were determined using the LSCM microscope measurements of the same area as shown in Figure 4.8, Figure 4.9, and Figure 4.10 respectively. Figure 4.11 shows the experimental and theoretical curves based on data from Table 4.4.

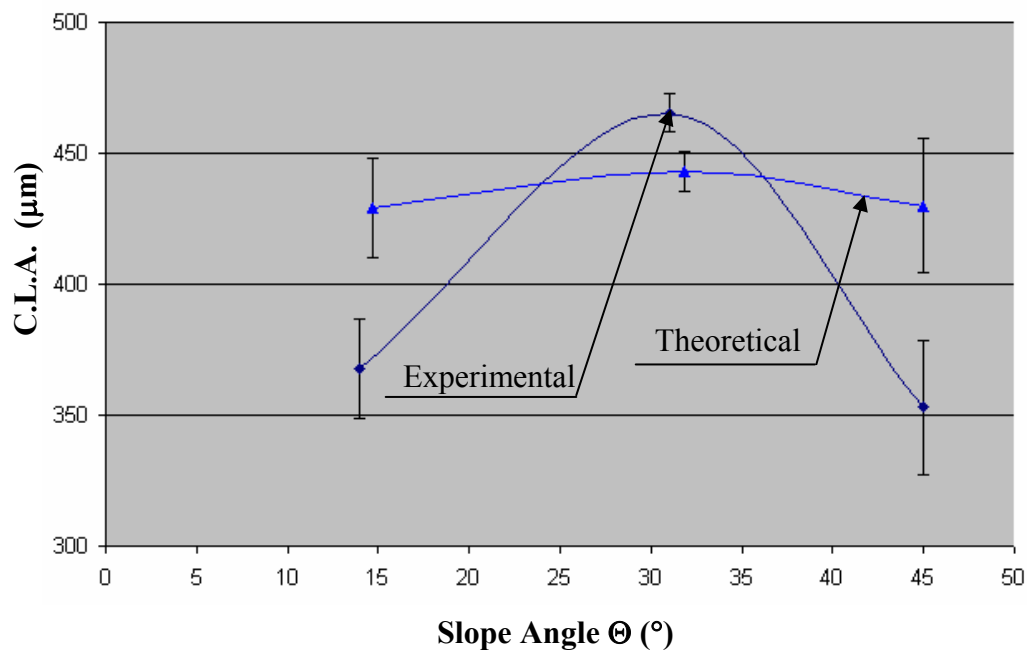


Figure 4.11: Slope angle versus C.L.A. for a constant mask size.

It can be noted that when the slope angle was changed from 15° to 45°, the C.L.A. theoretical value decreased from 367.8 μm to 353 μm . This indicates that lines with a slope angle 45° will produce the part boundaries with better edge quality than lines with a

slope angle 15° or 30° . It is also noted that the theoretical values compare well with experimentally determined values for all three examined inclination angles, especially at 45° , where the angular difference between theoretical and experimental value is only 0.6° (see Table 4.4). This further verifies the accuracy of the mathematical modeling used in this chapter.

Figure 4.11 shows that the average C.L.A. value obtained from 5 different machined samples with a fixed slope angle of 45° is $367.8 \mu\text{m}$. Error bars on these points are standard deviations divided by the value of the square root of sample size (the standard errors) and calculated from scatter of individual measurements.

Although the inaccuracy or relative standard deviation is as high as 16%, the estimated values with relatively high deviations are expected and reasonable because the edge quality and C.L.A. value are strongly dependent on the graphical algorithm used and slope angle and an accurate prediction of these values is difficult, especially when square mask tool was used for machining. The difference between the experimental and theoretical values of C.L.A. can be attributed to the sources of errors encountered in the measurements of staircase areas by LSCM. The other sources of errors could include errors due to alignment of cross-hair with the staircase step edges, error in the actual formation of the staircase steps in the laser Step and repeat machining method, and errors due to approximation in the mathematical modelling (Bresenham graphical algorithm). It was found, as expected, that for the edge error to be minimum, when the square mask was used as a tool for machining, the mask size should be minimum as well. However, this will increase machining time, hence, the best ratio between feature size to be machined and mask size must be carefully determined.

4.5 Summary

This chapter describes the developed mathematical model for edge error control. The method and calculation of edge error was based on the Center Line Average Area Error (C.L.A.) standard for surface roughness determination. The model will be used to determine the best mask size and slope angle in an excimer laser micromachining process based on the minimum edge error in the structure due to staircase effect.

The mathematical model has been shown to work for several simple structures. Mathematical equations for edge error were determined for any outside object boundaries. Theoretical values of edge error are compared with the experimentally determined values for a set of triangular structures machined by the Step-and-repeat excimer laser micromachining technique.

The results of this chapter also shows how it is essential to find best possible relationship between the feature size that needs to be produced and the mask size used. This relationship will directly influence the quality of the produced part, i.e. edge error. The machining time in an excimer laser based machining process where a range of square mask tools were employed to machine any surface profile will also be highly dependent on this relationship. Three different algorithms (left-to-right, zig-zag and star) were employed to find this relationship and they were already discussed in Chapter 3 of this research work. The optimum solution is given by the novel star algorithm where the relationship between feature size and mask range employed provides the best possible edge quality and minimal machining time.

Chapter 5. *Stitching Errors Correction*

5.1 Overview

This chapter presents an investigation in controlling the error effects of stitching and overlap that are inherently present in microstructures made using excimer laser micromachining processes. Section 5.3 describes a laser ablation model in detail, followed by section 5.4 which reports the material characterization process for PC and PET. Details of the mathematical model for overlap error appear in section 5.5, and the overlap size calculation in section 5.6. Optimisation of the main process parameters in this work F_d , PRF , and n for optimum values for wall angle and ablation depth has been carried out using the Taguchi DOE method, and is reported in section 5.7. Experimental verification of the approach is presented in section 5.8. Finally, in section 5.9 the results of this chapter are summarised. The results presented in this chapter have been published by Mutapcic et al.2004 [85].

5.2 Introduction

There are several widely used laser-ablation mask-projection machining techniques as mentioned in the literature review of this thesis (Chapter 2) but they all suffer from wall angle effects between two adjacent ablation sites. These techniques stitch together projected features at the workpiece, and because of the wall angle effect, introduce overlay errors. These stitching errors directly affect the surface roughness and quality of the produced structure, and if they are not successfully controlled then machining microstructures usually requires additional post processing work and operator skills to bring them to an acceptable standard. These types of errors cannot be completely removed but can be controlled to a greater extent by use of a model of the stitching error to optimize process parameters.

Additionally, microstructuring with single excimer laser pulses can cause geometrical imperfections at the boundary between adjacent ablated volumes as a result of mask irregularities and computer numerical control (CNC) errors. Due to the non-ideal shape of the individual ablations, depth irregularities of up to 60% of the depth of ablated layers occur and may adversely effect the desired function of surfaces, for example optical functions [3]. These failures within the structured surface can be reduced by improved control of the main process parameters. To optimize the process parameters, an exact characterization and model of the single ablations is required.

5.3 Ablation Process Model

A good model of the structuring process is essential for developing a system to automatically generate NC code. Modelling the process is based on the precise description of single ablations, as shown in Figure 5.1.

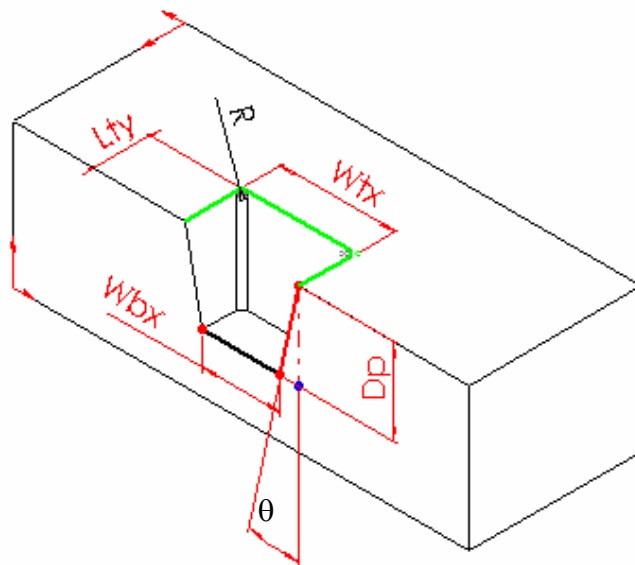


Figure 5.1: Characteristic cross-section of a single ablation site.

The parameters shown in Figure 5.1 are defined as follows:

- Ablation Depth (D_p) [μm]

- Wall Angle (θ) [°]
- Corner Radii (R) [μm]
- Top Width of ablated volume (W_{tx}) [μm]
- Bottom Width of ablated volume (W_{bx}) [μm]
- Top Length of ablated volume (L_{ty}) [μm]

The characteristics of the ablated area depend on several parameters such as material, energy density, number of pulses per area, size of the individual ablation sites, and the surface quality of the processed bulk material [40]. The rate at which material may be machined by an excimer laser ablation can be simplified to be a function of the fluence incident upon the surface.

Hence, simply by knowing the fluence and counting the number of incident laser pulses provides the ability to control the depth of machining [86]. The parameters for PC and PET polymeric materials that can be successfully controlled were determined experimentally and are reported in section 5.4.

5.4 Characterisation of PC and PET

5.4.1 *Dependence of the Ablation Depth on the Number of Pulses*

Selection of a number of pulses at a fixed fluence controls the depth of the structures. This linear relationship is highly dependent on the polymer quality. Different polymers are etched faster or slower depending on their chemical stability, absorption properties at particular wavelength and also depending on the UV sensitizer of the commercially available polymers [14].

Figure 5.2 shows the linear dependency between ablation depth, D_p , and the number of pulses per area, n , at a fluence, $F_d = 1.1 \text{ J/cm}^2$ for two different commercially available polymers PC and PET.

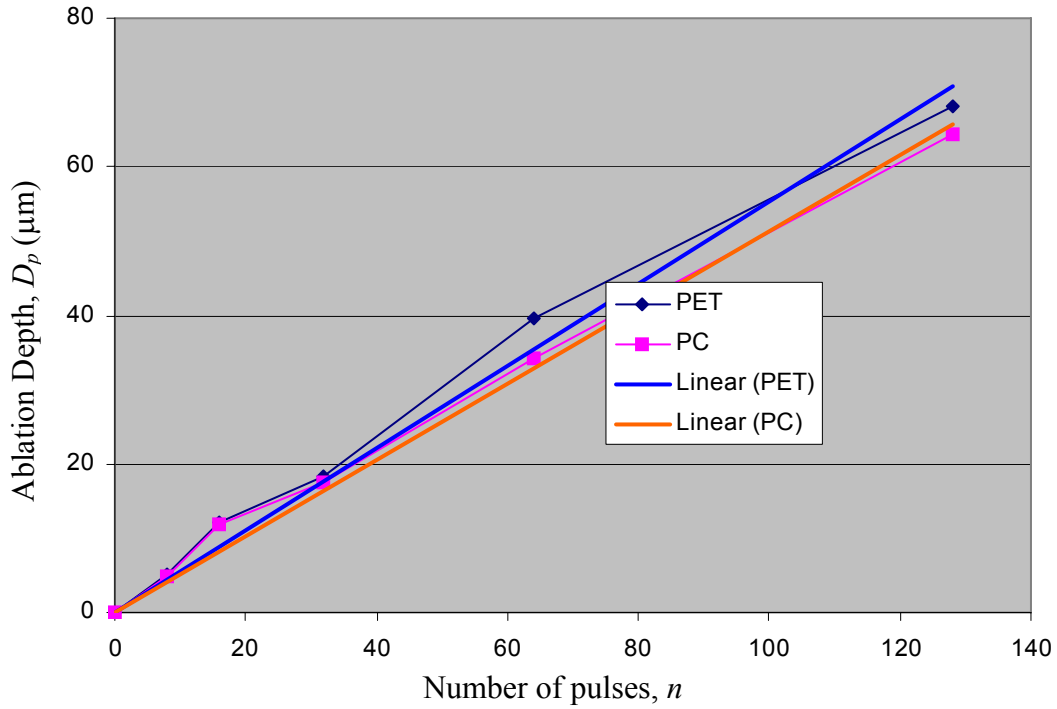


Figure 5.2: Ablation Depth, D_p , versus Number of pulses, n , at a fluence, $F_d = 1.1 \text{ J/cm}^2$ for PC and PET.

5.4.2 Etch Rate versus Fluence.

Etch rate versus fluence recorded for excimer laser ablation of $100 \times 100 \text{ μm}^2$ features in PC using 128 and 8 pulses respectively at 10Hz is shown in Figure 5.3. These trends are in agreement with literature and indicates approximately linear relationship between etch depth and number of shots [10] for the energies above the ablation threshold and below 0.9 J/cm^2 . For deeper microstructures the ablated products are emitted from the site in a 1-D expansion, normal to the surface and back in direction of the incoming laser beam, which shields the target surface from the laser energy [98]. As higher fluences are used, more material is present in the plume; therefore resulting in higher losses and reduced average etch depth per pulse (128 shots curve). Shallower structures allow the beam to expand in 3-D, therefore creating far less dense plume and consequently less shielding of the target surface. Therefore shallower structures usually results in an

observed higher average etch rate per pulse (8 shots curve). Shallower structures are however, also more difficult to measure, and this can increase the reported error. The etch rate was calculated by dividing the depth of ablated region by the number of laser pulses at given energy fluence. Error bars on these points are standard deviations (0.006 for 8 pulses and 0.004 for 128 pulses) calculated from scatter of individual measurements, and in the case of Figure 5.3, suggest that the data are consistent with a linear relationship between etch rate and fluence.

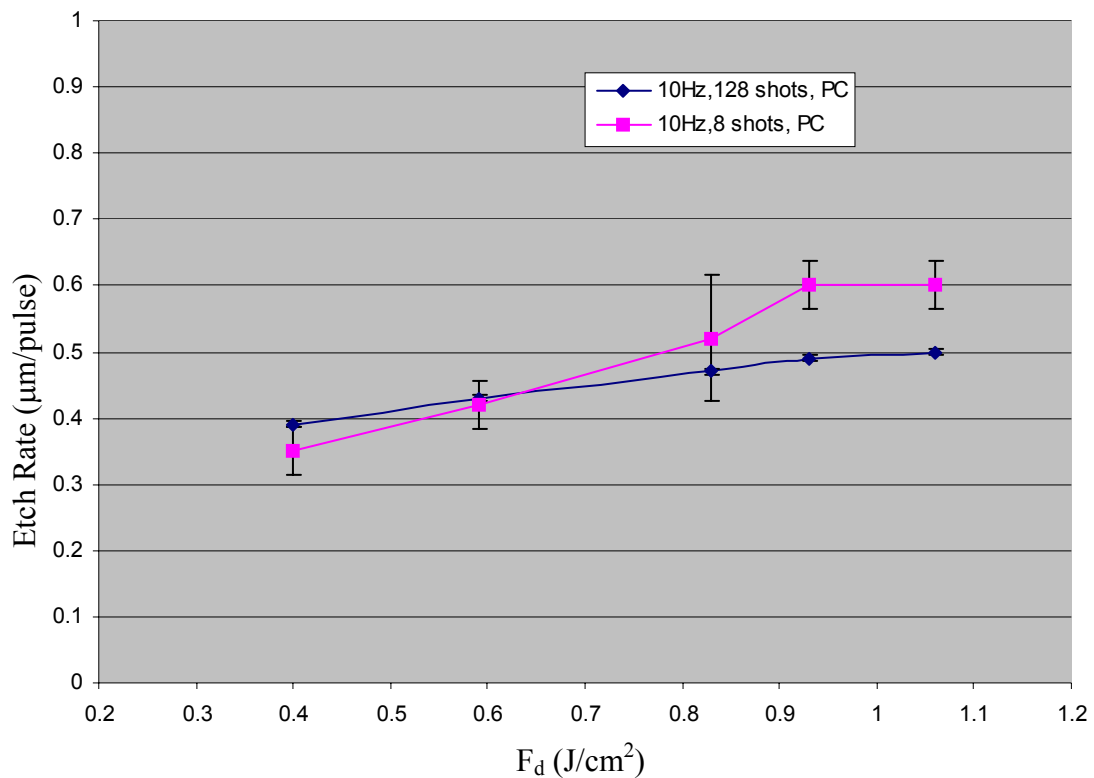


Figure 5.3: The relationship between the etch rate and fluence for the excimer laser firing 128 and 8 pulses respectively at 10Hz showing an etch rate of 0.39μm/pulse and 0.35μm/pulse respectively at fluence of 0.4 J/cm². Sample material was PC.

An interesting phenomenon occurring for a material when irradiated by pulsed lasers is the onset of ablation as a function of the number of pulses what leads to the definition of a n_{th} pulse ablation threshold, F_{th}^n , in such way that when the sample is irradiated with n^t pulses and $n^t < n_{th}$, no ablation occurs. This effect has been defined in

literature as incubation [98,99]. Although the microscopic origin of incubation is still focus of controversy and it is outside the scope of this work, from a practical point of view, incubation plays an important role in micromachining since groove and channel widths clearly depend on pulse accumulation. Hence, the number of pulses, n , is directly connected to the relative movement of the micro machined sample and the laser beam [100].

Figure 5.4 shows etch rate trend lines for both PC and PET materials at a constant frequency (10Hz) and number of pulses (128) applied. It is noticeable that for the same ablation conditions PET material had a slightly higher etch rate compared to PC, and is in agreement with trends found in literature.

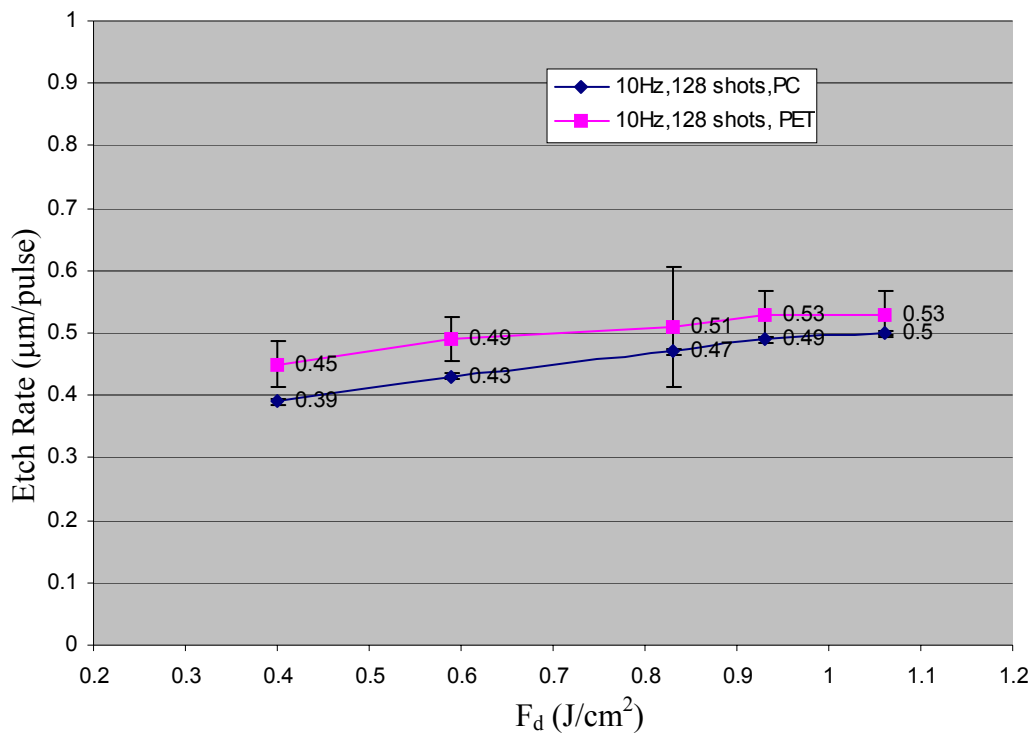


Figure 5.4: The relationship between the etch rate and fluence for the excimer laser firing 128 pulses at 10Hz showing that PET has slightly higher etch rate then PC for the same process conditions.

5.4.3 Wall Angle versus Fluence

Figure 5.5 shows the dependency of the wall angle, θ , for a range of different fluences ($0.2 - 1.1 \text{ J/cm}^2$), and constant number of pulses (100) applied in sample of PC.

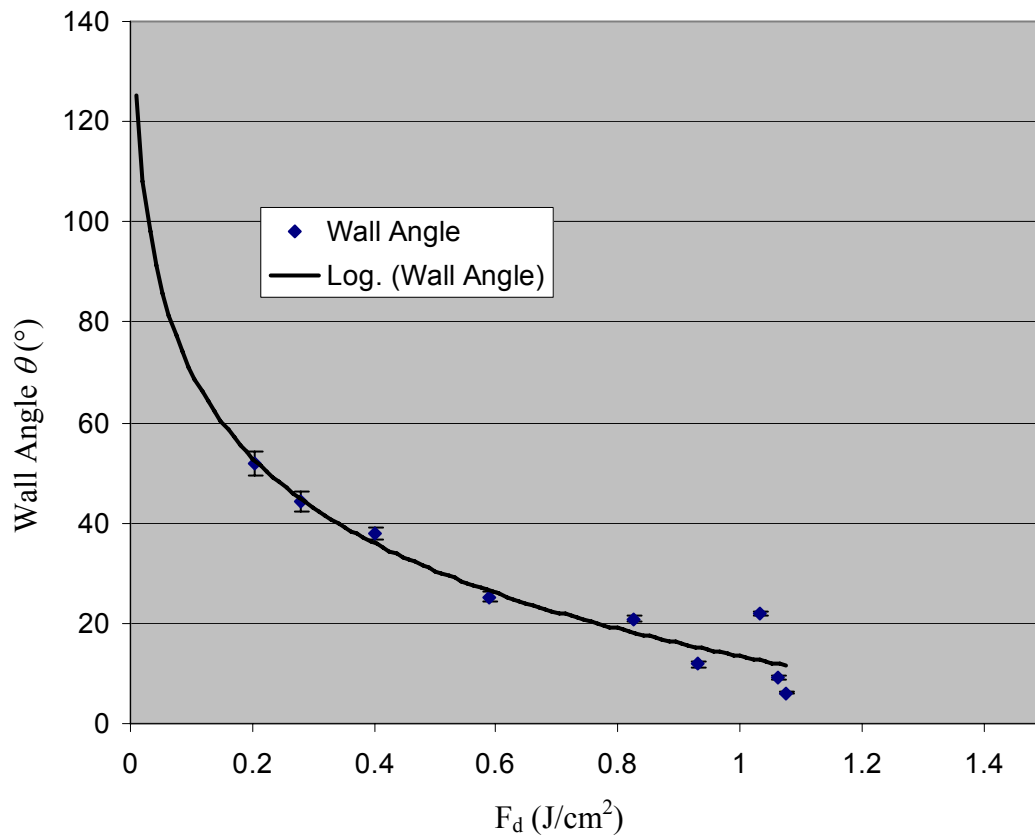


Figure 5.5: Wall angle changes for fluence range from 0.2 to 1.1 J/cm^2 for a constant number of pulses $n = 100$, image size $100 \times 100 \mu\text{m}^2$ in PC.

The Figure 5.5 also shows a curve fitted to the experimental data. It should be noted that the wall angle θ is calculated based on the top and bottom width of the channel, and depth of cut of the materials. It is clear from Figure 5.6 that the wall angle decreases from 51° , measured at fluence of 0.2 J/cm^2 , down to 6° with an increase in fluence up to 1.1 J/cm^2 for PC. This is thought to be due to diffractive effects at the edge of the pattern that produces lower fluences and etch rates in the region. Once initiated the taper is favored by the lower fluence experienced at the wall for non-normal angles of incidence of the beam [87].

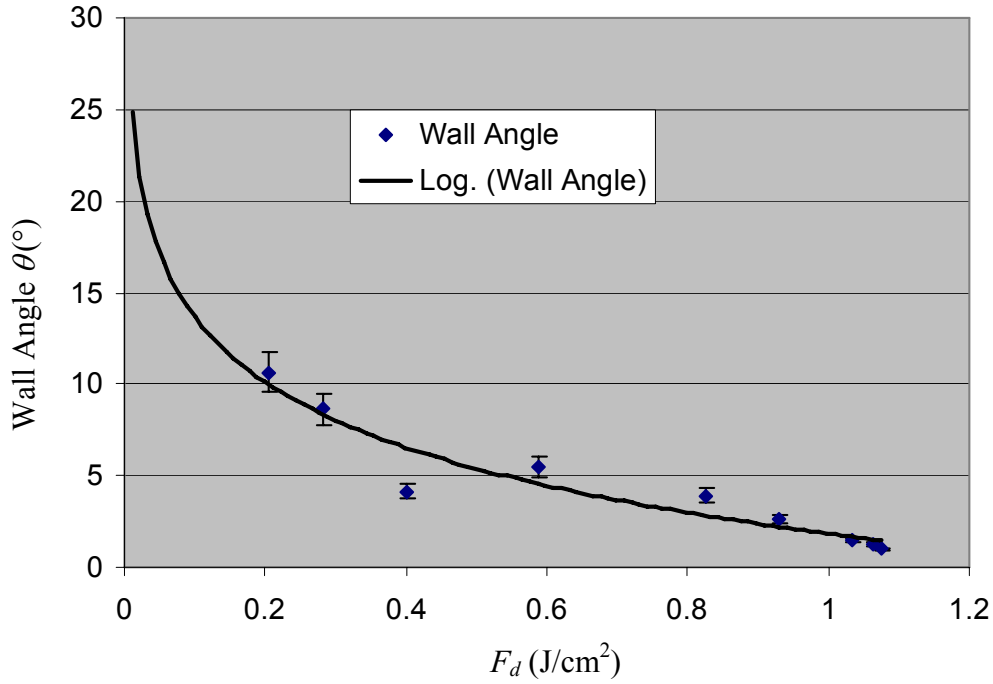


Figure 5.6: Wall Angle vs. Fluence for PET.

Figure 5.6 shows very similar trends obtained for the samples of PET material for the same process conditions. However, it was also noticeable, and in particular for PET material, that a further increase in the fluence causes the angle to cross the zero point and become a negative value. The phenomenon can be explained in two ways. First, the increased fluence is larger than the threshold fluence of ablation even with diffractive effects at the edges, and secondly, the beam size is possibly enlarged due to the defocusing effect but this assumption is not verified yet. However, this phenomenon is not observed when using lower numerical aperture (NA) lenses, which is probably due to the lower divergence of lower NA lenses.

5.5 Theoretical Model of Overlap Error

For the generation of 3D structures, control of the overlap based on the image size and the depth of the ablated region plays an important role for the manufacture of microstructures with surface roughness in the sub-micron range [2].

In order to control this process, a mathematical model dependency based on the image overlap geometry can be established (see Figure 5.7). The figure shows two slightly overlapping volumes created by corresponding pulses. In the figure, the top and front views with the various dimensional characteristics are defined by variables of the model.

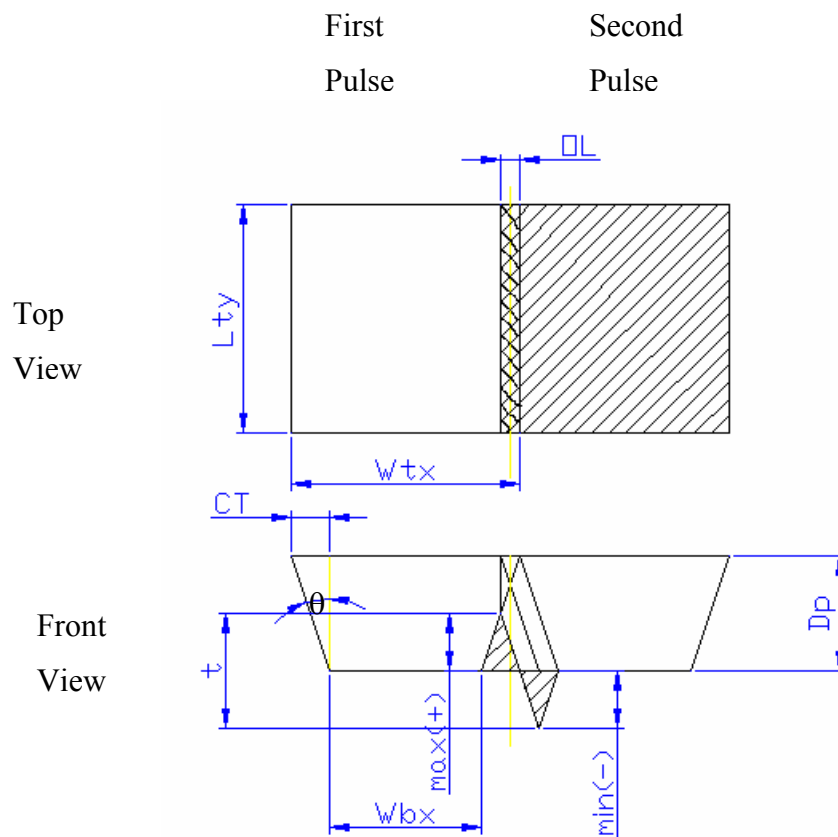


Figure 5.7: Mathematical model based on the laser pulse overlap (*OL*) geometry.

For the overlap error behavior in the two-pulse model shown in Figure 5.7, the total machining error in depth, t , is governed by the equation:

$$t = \max(+) + \min(-) \quad (5.1)$$

and is theoretically equal to the D_p with

$$max(+) = CTI / \tan(\theta) \quad (5.2)$$

and represents the value of the overlay peak error. CTI is determined by:

$$CTI = Abs (CT - OL) \quad (5.3)$$

Where:

$CT (\mu m)$ – Wall Angle Projection on Top Surface

$OL (\mu m)$ – Actual Overlap Size

Based on the geometry of the cross section view of the ablated volume, the value of CT is defined by:

$$CT = \tan (\theta) * D_p \quad (5.4)$$

Where:

$\theta(^{\circ})$ - Wall Angle.

Equation 5.1 can then be rewritten:

$$min(-) = Abs (t - max(+)) \quad (5.5)$$

and represents the value of the second type of error i.e. overlay trough error.

Now, depending on the value of the actual overlap distance (OL), five different cases (types 1-5) can be differentiated that can cause geometrical imperfections and influence surface roughness. They are shown in Figure 5.8 (a-e) where the top view shows the area of the overlap (OL). Figure 5.8 (a) is the case (type 1) where the overlap distance (OL) is equal to zero, only one type of overlap error (peak type) appears and should have its maximum value theoretically equal to D_p . If $OL = 0$ then;

$$max(+)_max = t \quad (5.6)$$

In the case (type 2) where overlap distance (OL) is equal to distance (CT) another extreme where only a trough type of overlay error appears and has its maximum value theoretically equal to D_p . If $OL = CT$ then;

$$\min(-)_{\max} = t \quad (5.7)$$

In Figure 5.8 (c) where the value of the overlap distance OL is less than distance CT , both types of errors exist (type 3), peak and trough, and an optimal value of the overlap distance can be calculated to make the errors even. This is favorable so that roughness of the machined surface is minimised. Figure 5.8 (d) and (e) show how the amount of the trough error type will vary with the overlapping distance taking the value between the CT and $2*CT$ distance value (types 4 and 5).

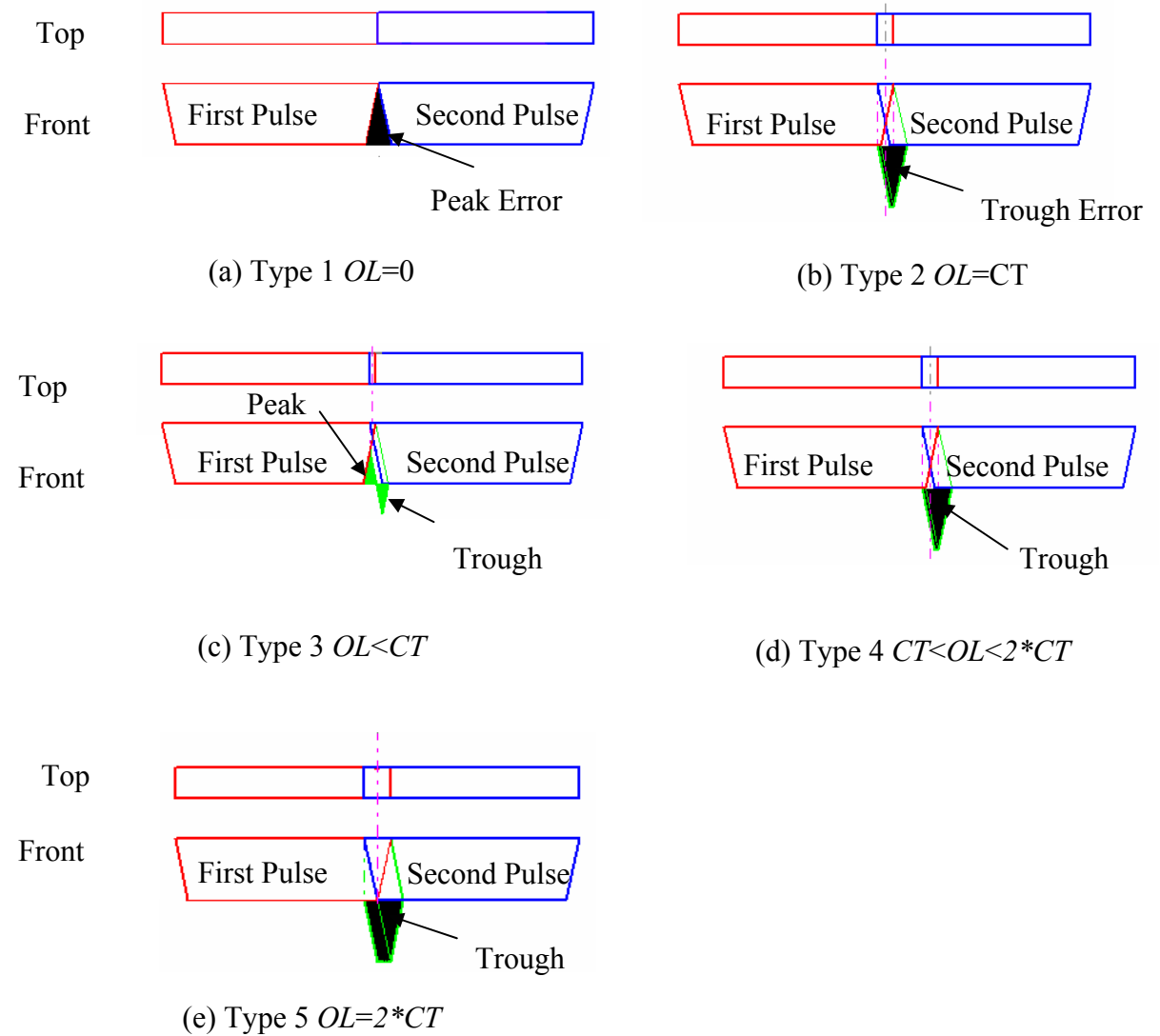


Figure 5.8: Five types of overlay error for different size of overlap OL where (a) $OL=0$, (b) $OL=CT$, (c) $OL < CT$, (d) $CT < OL < 2*CT$, and (e) $OL=2*CT$.

5.6 Overlap Size Calculation

In order to make a comparison between mathematical model data and real machining data, theoretical values for the size of the peaks and troughs were calculated using the model. These values were then compared with measured values produced by machining polycarbonate structures using the parameters suggested by the Ex-Expv1.0. Differences between measurements taken by the LSCM and theoretical values produced by the system were calculated for the wall angle, overlap value, and ablation depth per number of laser pulses. These results for a $210\mu\text{m} \times 210\mu\text{m}$ image size are shown in the Figure 5.9. The wavy kind of shape of the overlap was caused by poor quality of the metal shim mask used to produce this structure.

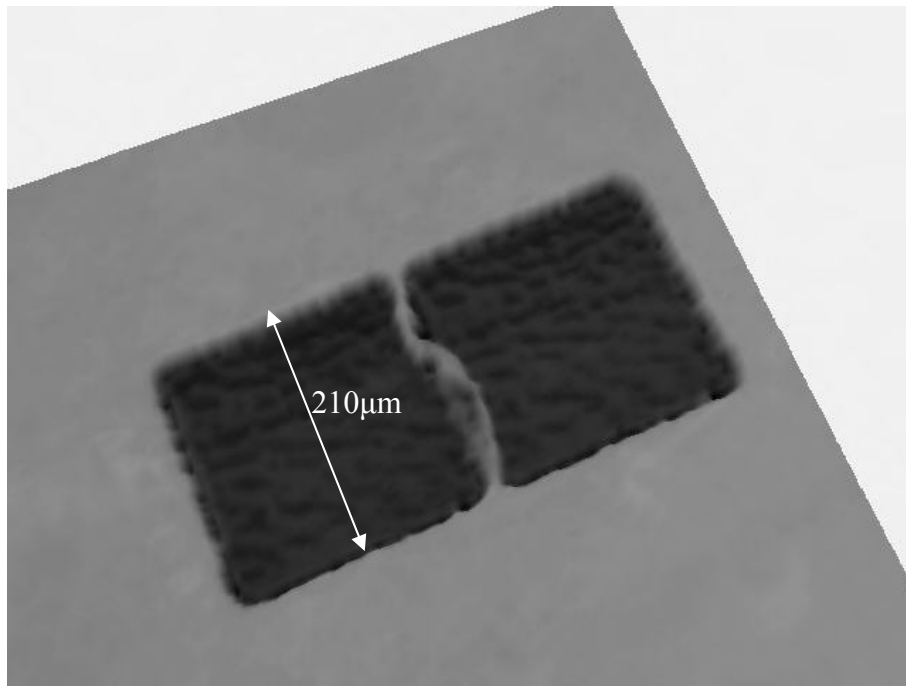


Figure 5.9: Type 1 overlay error where mask image projection overlap $OL = 0$, $n = 100$ laser pulses, F_d is equal to 1.1 J/cm^2 .

Figure 5.10 shows the cross-section view of the ablated surface for the Type 1 overlay error shown in Figure 5.9 and measured by LSCM. The process conditions were: $F_d = 1.1 \text{ J/cm}^2$, $PRF = 5 \text{ Hz}$, $n = 100$, and $OL = 0$.

The ablation depth, $D_p = 36.7 \mu\text{m}$ was measured.

When D_p is known for a given n , the value of the wall angle can be simply determined by measuring the width of ablated area at the start plane of ablation W_{tx} , and width of ablated area at the bottom plane of ablation W_{bx} . Half the difference between the widths, $(W_{tx} - W_{bx})/2$, divided by D_p allows the wall angle θ to be determined.

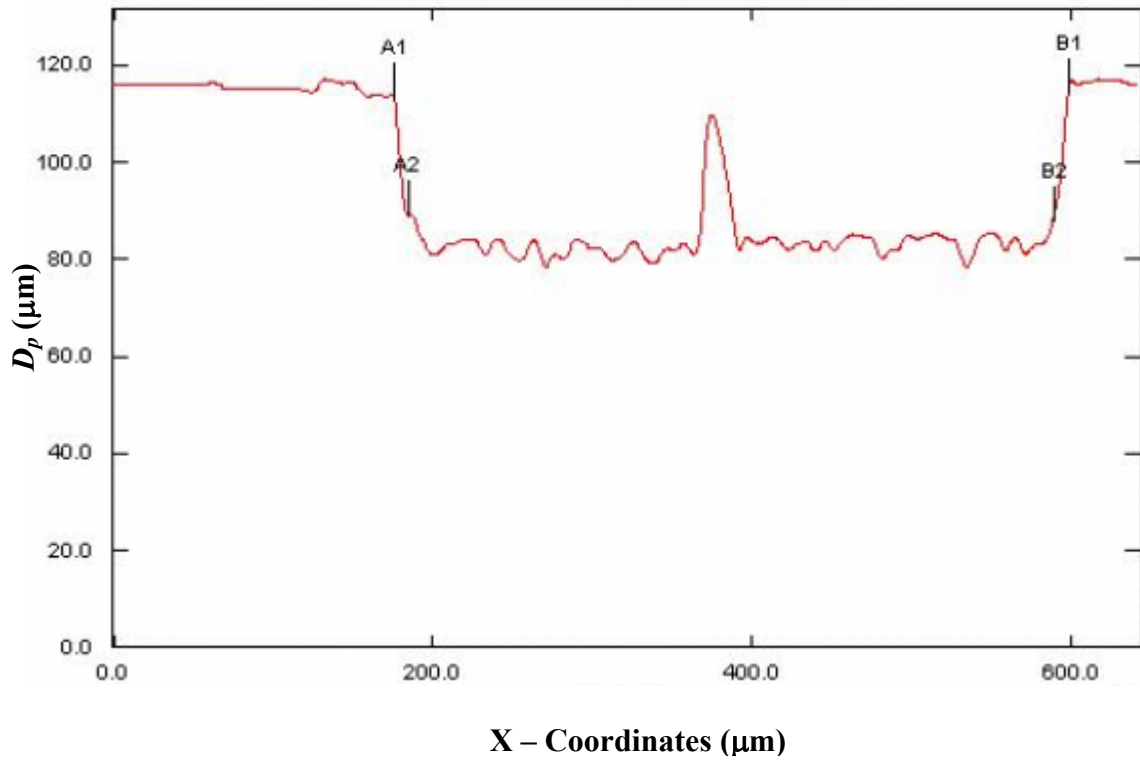


Figure 5.10: Cross-section of ablated surface of Type 1 overlay error where overlap $OL = 0$, image size $210 \times 210 \mu\text{m}^2$, $n = 100$, $F_d = 1.1 \text{ J/cm}^2$. Points A1-B1 and A2-B2 were used to measure wall angle θ .

Table 5.1: Measurements of the wall angle as measured by LSCM.

A1B1 (μm)	A2B2 (μm)	D_p (μm)	Wall Angle θ ($^\circ$)
422.9	404.7	36.7	14

From the data shown in Figure 5.10 wall angle θ can be simply calculated by using equation:

$$\tan \theta = \frac{(A1B1 - A2B2)}{2 * D_p} \quad (5.8)$$

where from Figure 5.10: $W_{tx} = A1B1 = 422.9$, $W_{bx} = A2B2 = 404.7$, $D_p = 36.7 \mu\text{m}$

Hence, $\theta \approx 14^\circ$.

In accordance with the Ex-Expv1.0 system the result shown in Figure 5.11 (a) is predicted value for the maximum height of the peak (Type 1) error when the value of the overlap distance $OL=0$ is $36.7 \mu\text{m}$ correlating with the modelled D_p . Figure 5.11 (b) shows the user interface for the optimised theoretical parameters giving an overlap of $4.6 \mu\text{m}$ needed to distribute the error evenly, a Type 3 error. Equations 5.1 to 5.7 were used to determine optimised theoretical values shown in Figure 5.11 (b).

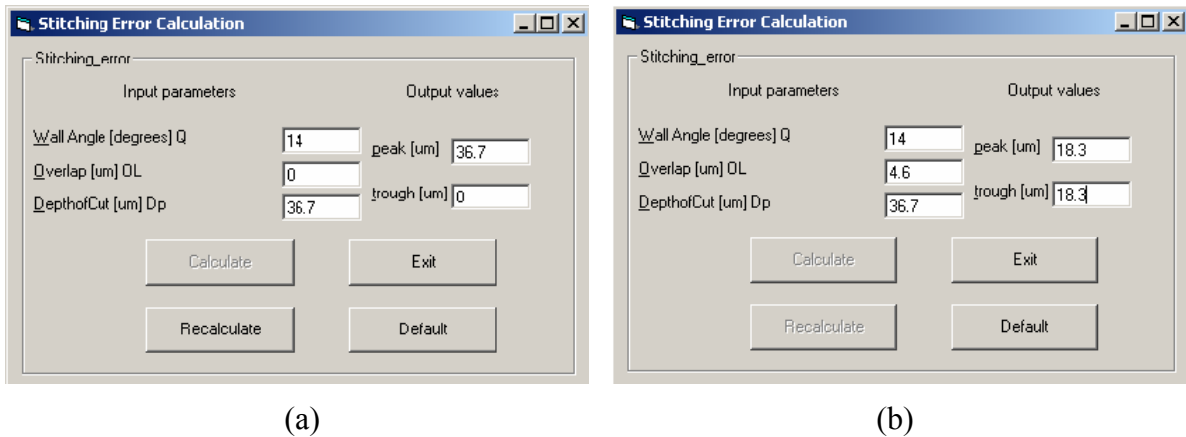
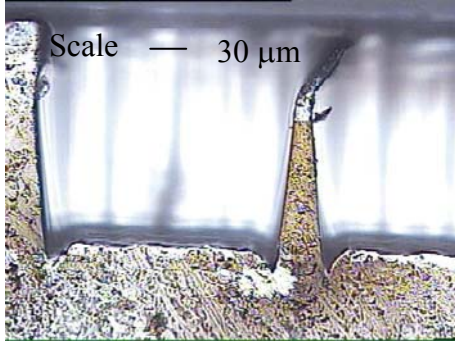
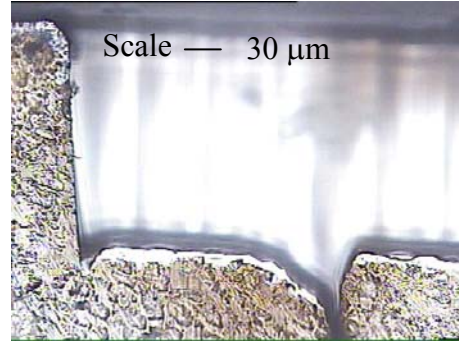


Figure 5.11: (a) Peak error calculation by the ExExpv1.0 when $OL = 0$, (b) Optimised parameters for overlap OL .

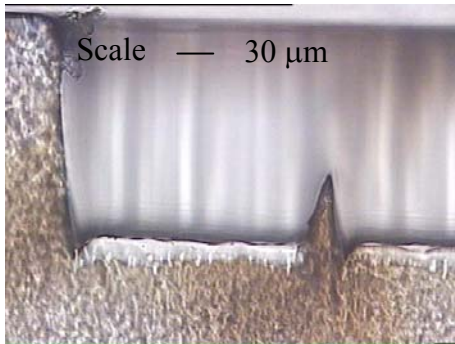
The aforementioned mathematical model and the developed Ex-Expv1.0 system were used to replicate by machining trials types 1-5 stitching errors. Figure 5.12 (a-f) shows different types of overlay errors caused by the overlapping at the boundary of two adjacent sites. The figures represent cross-sections of two square holes. The image is $210\mu\text{m} \times 210\mu\text{m}$ at the surface of the polymer. The sample was held stationary during ablation and focus was not moved during machining even though the distance between the ablating surface and the objective increases as material is removed.



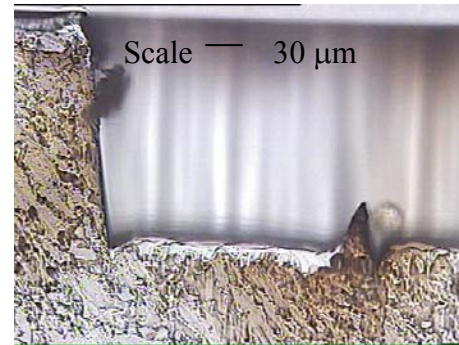
(a) Type 1 $OL=0$



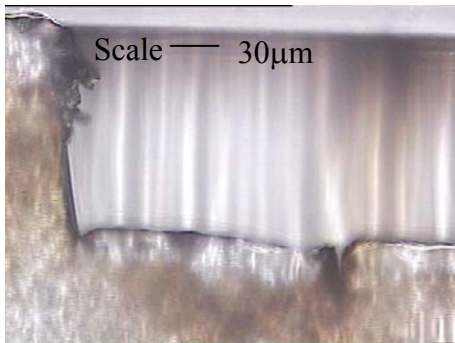
(b) Type 2 $OL=CT$



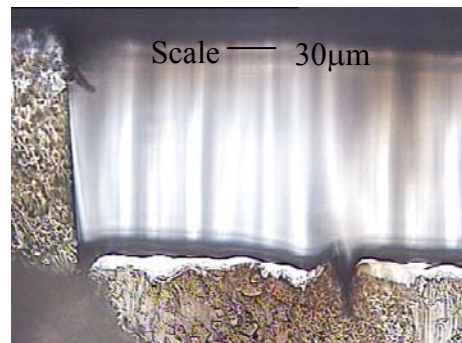
(c) Type 3 $OL < CT$ and $max(+) > min(-)$



(d) Type 3 $OL < CT$ $max(+) = min(-)$



(e) Type 4 $CT < OL < 2*CT$



(f) Type 5 $OL=2*CT$

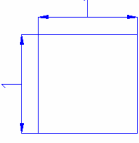
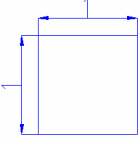
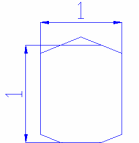
Figure 5.12: Optical images of overlap error with $F_d = 1.1 \text{ J/cm}^2$, $n = 500$, material PC when: (a) Type 1 $OL=0$, (b) Type 2 $OL=CT$, (c) Type 3 $OL < CT$ and $max(+) > min(-)$, (d) Type 3 $OL < CT$ $max(+) = min(-)$, (e) Type 4 $CT < OL < 2*CT$, (f) Type 5 $OL=2*CT$.

5.7 Main Process Parameters

The process parameters for laser micromachining were optimised using the Taguchi Design of Experiments [7] approach to reduce stitching error effects and improve surface

roughness (covered in 3.7.1). Performance was assessed in terms of ablation depth, wall angles, overlap size (stitching error), surface roughness and aliasing effects. Samples were machined using the workpiece-dragging technique [10] with optimised process parameters as shown in Table 5.2.

Table 5.2: Excimer laser optimised process parameters for PC samples.

Experiment	Mask Shape (mm)	Overlap OL (μm)	F_d (J/cm^2)	PRF (Hz)	n
1		0	0.5	80	70
2		1.4	0.5	80	70
3		1.4	0.5	80	70

Optimal process parameters from Table 5.2 are based on preliminary experiments carried out as explained in section 5.7.2.

5.7.1 Taguchi Control Parameters

The average depth of ablation, D_p , and wall angle θ are a function of the number of laser shots per area, n , at fluence level, F_d , and predetermined PRF . Therefore, the values of n , F_d , and PRF were specified by the Design of Experiment software and the ranges were determined by the following tests in section 5.7.2.

5.7.2 Optimisation of Process Parameters

Data in Figure 5.13 were obtained from ablation of a channel using the square features with an image dimension of $100 \times 100 \mu\text{m}^2$, at a fluence of $1.1 \text{ J}/\text{cm}^2$ and PRF of

5 Hz. Figure 5.13 shows the ablation depth when the number of pulses per area increased from 10 to 100 in increments of 10 pulses per area.

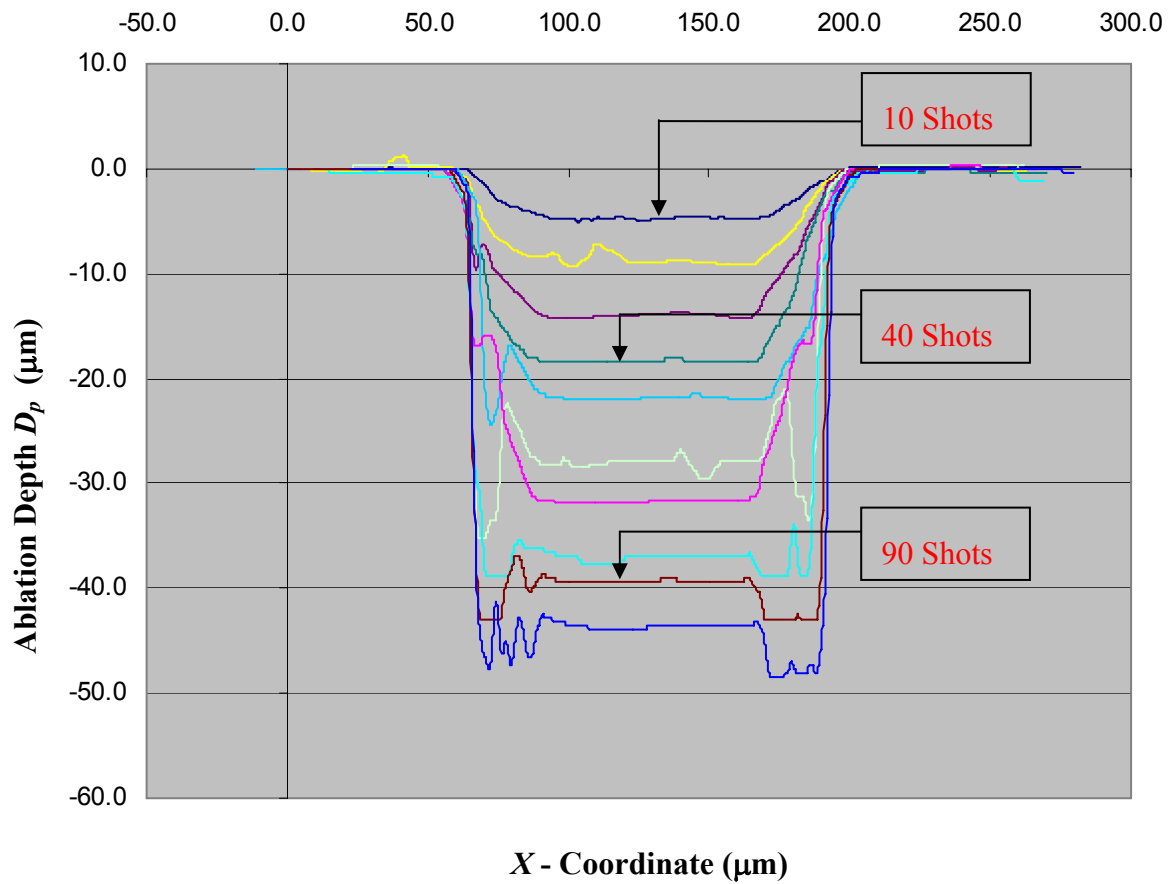


Figure 5.13: Ablation depth of a 100μm wide channel at a constant fluence, 1.1 J/cm^2 , in polycarbonate, when number of pulses per area varies from 10-100.

For the wall angle initial calculation several channels was machined in PC. The main machining parameters are summarised in Table 5.3.

Table 5.3: Ablation parameters for workpiece-dragging machining method of channels in PC.

Process parameters:	Value
On-substrate energy density, F_d	1.1 J/cm ²
Pulse Repetition Frequency, PRF	5Hz
Number of pulses per area, n	100
Feature size at the workpiece	100 μm wide and 1000 μm long

The ablated channel did not have vertical sidewalls due to diffraction effects at the edge of the ablated site. However, the steepness can be controlled to a certain extent by the pulse energy density. Angles as low as 4.8° (high energy densities, 1.1 J/cm²) and up to almost 80° (low energy densities, 0.2 J/cm²) were observed. A cross-sectional view of an ablated channel showing a typical wall angle profile is illustrated in Figure 5.14.

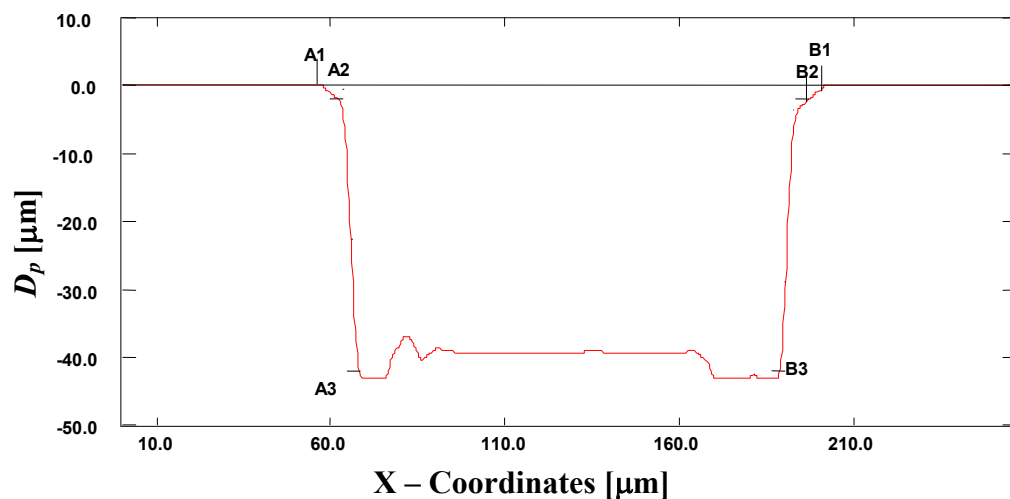


Figure 5.14: Typical cross-section of an ablation site as measured by the LSCM. Points A1-B1, A2-B2, and A3-B3 were used to measure the wall angle.

Figure 5.15 shows the schematic cross-section of a deep ablated area and how the wall angle varies with depth. The wall angle is measured between the top and bottom surfaces, therefore, $\theta_2 > \theta_1$. Calculation data and results of wall angle measurements are shown in Table 5.4 using results in Figure 5.14.

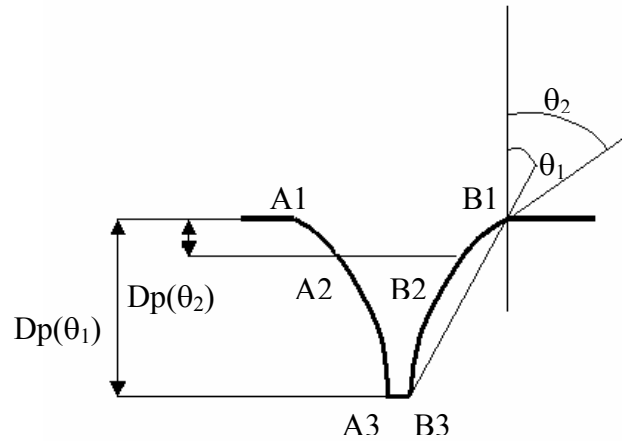


Figure 5.15: Schematic of the wall angles θ_1 and θ_2 .

Table 5.4: Measurements of the wall angle of the channel machined in PC using results in Figure 5.14.

A1B1(μm)	A3B3 (μm)	Dp_{θ_1} (μm)	Wall Angle θ_1 ($^\circ$)
132.58	125.30	42.8	4.8
(a)			
A1B1(μm)	A2B2 (μm)	Dp_{θ_2} (μm)	Wall Angle θ_2 ($^\circ$)
132.58	126.31	1.89	58.9
(b)			

These preliminary experimental results were used to confirm the range of the Taguchi parameters. Three main parameters that affect ablation sidewall angles were used for the Taguchi optimisation. Each of them was varied over three values and the ranges

are shown in Table 5.5. The total number of responses is two, termed as sidewall angle θ and ablation depth D_p .

Table 5.5: Input parameters to the Taguchi Design of experiment and their values.

Inputs	F_d (J/cm ²)	PRF (Hz)	n
Level 1	0.44	5	10
Level 2	0.51	50	50
Level 3	0.57	80	100

Table 5.6 shows the nine experiments conducted with different orthogonal combinations.

Table 5.6: Taguchi Orthogonal Array (OA) for optimising wall angle and ablation depth.

Experiment	Input 1 F_d (J/cm ²)	Input 2 PRF(Hz)	Input 3 n	Output 1 θ (°)	Output 2 D_p (μm)
1	0.44	5	10	51.0	8.0
2	0.44	50	50	11.7	24.0
3	0.44	80	100	26.0	30.0
4	0.51	5	50	26.0	18.0
5	0.51	50	100	12.5	36.0
6	0.51	80	10	45.0	6.0
7	0.57	5	100	2.2	50.0
8	0.57	50	10	39.8	6.0
9	0.57	80	50	26.0	18.0

Also shown in Table 5.6 are the measured wall angle and depth of cut of the channels in nine experiments. The results of the nine orthogonal experiments were used to analyse the influence of the value of each setting of every parameter and generate the results in Table 5.7.

Table 5.7: Predicted results from Taguchi *OA* experiments.

Solution Number	$Fd(\text{J}/\text{cm}^2)$	$PRF(\text{Hz})$	n	$\theta(^{\circ})$	$D_p(\mu\text{m})$
1	0.5	79	64	3.6	52.4
2	0.4	19	89	8.5	101.7
3	0.4	76	71	4.7	62.0
4	0.5	9	56	4.1	112.6
5	0.5	36	39	0.9	64.9
6	0.5	58	75	15.6	90.8
7	0.5	62	55	4.2	50.4
8	0.5	68	61	15.9	68.1
9	0.4	46	69	4.6	67.3
10	0.5	35	83	15.3	111.6

In Table 5.7 the orthogonal array suggests 10 combinations of input parameters that will result in optimal solutions. By looking at the 10 possible solutions, it can be concluded that the higher the fluence, the steeper the wall angle. It is worth mentioning here that the resulting data in the Taguchi method emphasizes the first-order effects: i.e., the main effect of each input parameter on the output function. Based on the wall angle criterion, the laser fluence is the most influential and the laser pulse frequency is the least influential for the range of values chosen for the parameters. Further experimental work confirmed that $0.5 \text{ J}/\text{cm}^2$, 80Hz, with 70 pulses per area gave a wall angle close to 4° and depth of ablation around $40\mu\text{m}$ in agreement with data suggested in Table 5.7 - solution 1, considering variations in fluence at the workpiece of $\pm 10\%$, material properties of polymer and wall angle dependency on ablation depth as shown in Figure 5.15. These optimal conditions were used in fabrication trials to investigate the improvement in the reported defects.

In order to improve surface roughness, stitching error effects had to be minimised. The optimal parameters determined by the Taguchi Design of Experiment method, i.e., wall angle and depth of ablation were used to calculate the size of the overlap (*OL*) in accordance with the mathematical model explained in section 5.5, to reduce the stitching

errors. Using this model it was possible then to express the stitching error effect as a function of the overlap size between adjacent aperture projections at the workpiece only. When the size of the overlap between adjacent images is equal to zero, only “peak” type stitching errors should occur. Therefore, the size of the overlap, for a wall angle equal to 4° and depth of cut equal to $40\text{ }\mu\text{m}$, can be calculated and is equal to $1.4\text{ }\mu\text{m}$. The size of the overlap was used to design a metal shim mask with square and hexagonal features with integrated overlap size. This means that instead of using a $100\text{ }\mu\text{m}$ wide square image at the workpiece, a $101.4\text{ }\mu\text{m}$ wide image and step size of $100\text{ }\mu\text{m}$ were used to achieve desired overlapping effect (see Figure 5.16 (b)).

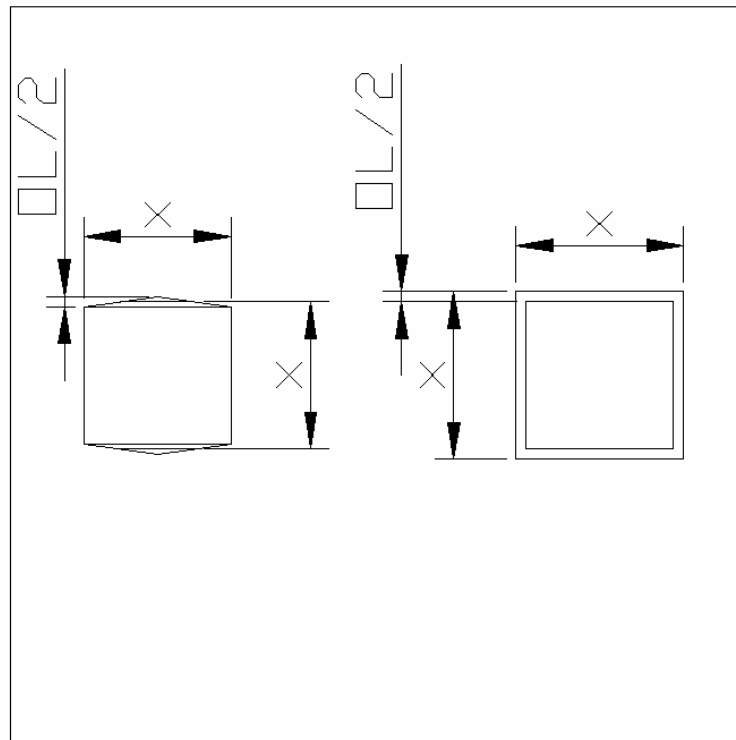


Figure 5.16: Design schematics of (a) Hexagonal and (b) Square mask with integrated overlap size for stitching error minimization.

To further improve the surface roughness and reduce stitching errors, hexagonal shaped masks were tested. These masks were designed to incorporate the size of the overlap. Figure 5.16 (a) and (b) shows the metal shim mask with both types of features mentioned above.

5.8 Experimentation using Optimised Parameters

The process parameters were optimised using the Taguchi Design of Experiments approach and performance was assessed in terms of ablation depth, wall angles, overlap size (stitching error), surface roughness and aliasing effects.

5.8.1 Surface Ablation using Workpiece Dragging Technique

The control sample, shown in Figure 5.17 is a 2.5D microstructure, and was produced by ablation of the surface using a mask with a 1.00 mm square feature and zero overlap (Experiment 1, see Table 5.2).

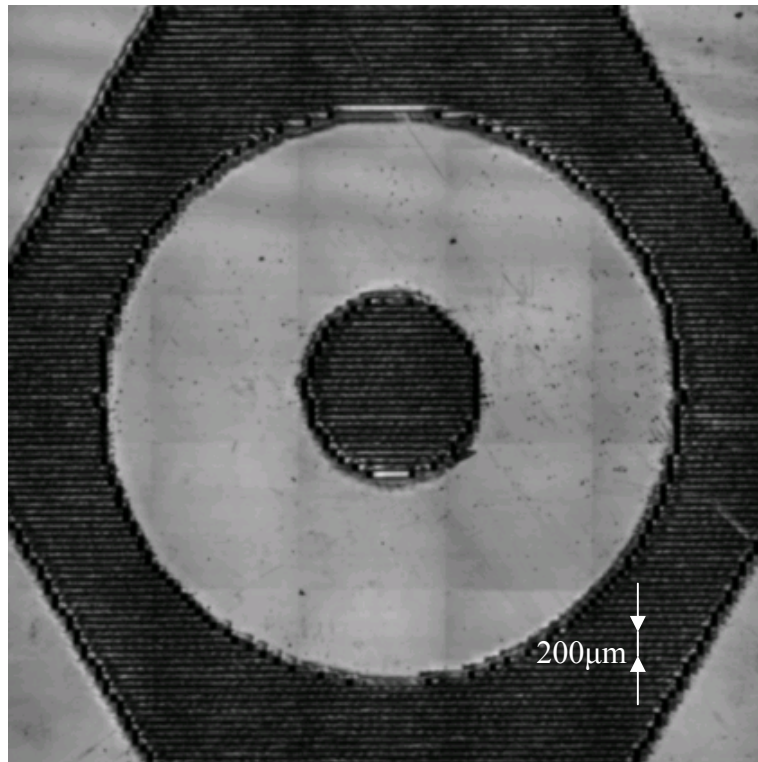


Figure 5.17: LSCM image showing surface texture created by 100x100μm square image at fluence $F_d = 0.5 \text{ J/cm}^2$, $PRF = 80 \text{ Hz}$, $n = 70$ shots per area and material PC.

The surface texture shows stitching errors effects in the form of peaks with a width of $23.4 \pm 2.2 \mu\text{m}$ and a height equal to $3.4 \pm 1.5 \mu\text{m}$. The measurement data in all experiments represents the average value of five measurements and tolerance values were standard deviations calculated from the scatter of individual measurements. Figure 5.18 is a detailed view of part of the surface texture machined using a square mask with included

overlap size calculated as explained in section 5.7.2, i.e. 1.014mm (Experiment 2, see Table 5.2). Figure 5.18 shows that stitching error effects were reduced and it was possible to measure peaks with width equal to $13.4 \pm 2.2\mu\text{m}$ and height equal to $1.4 \pm 0.9\mu\text{m}$.

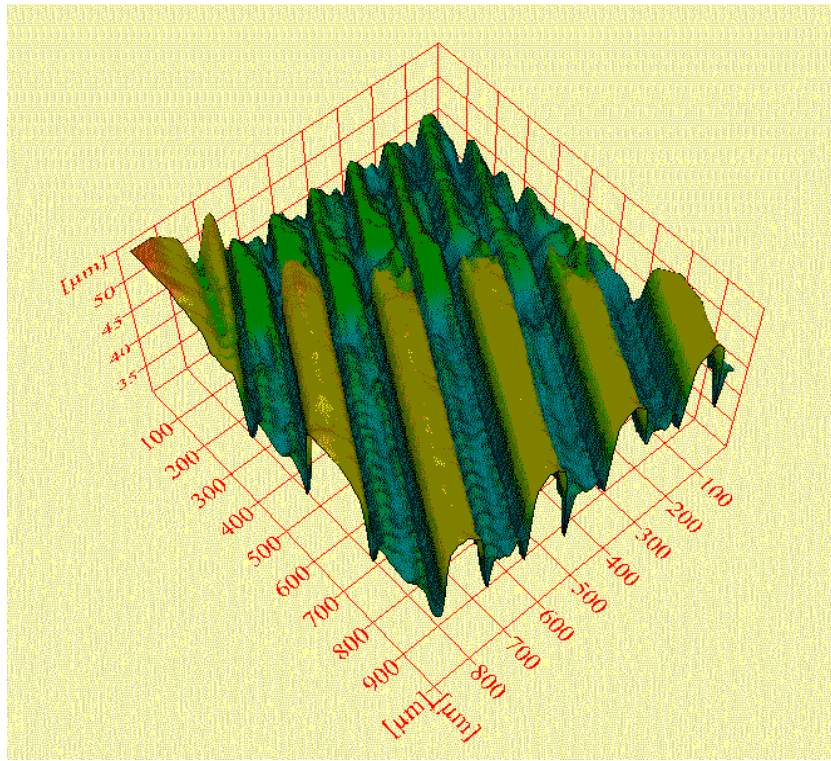


Figure 5.18: LSCM image showing stitching error effect of $13.4 \pm 2.2\mu\text{m}$ width and $1.4 \pm 0.9\mu\text{m}$ height horizontal defects in one axis only during workpiece-dragging ablation process, with square shaped 1.014 mm mask.

A substantial improvement of surface roughness and reduction of stitching errors was achieved by using a hexagonal shaped mask with incorporated overlap size (Experiment 3, see Table 5.2). Figure 5.19 shows that the stitching error effects were reduced along vertical and horizontal axes. Peaks with width equal to $2.4 \pm 0.2\mu\text{m}$ and height equal to $1.4 \pm 0.2\mu\text{m}$ were measured.

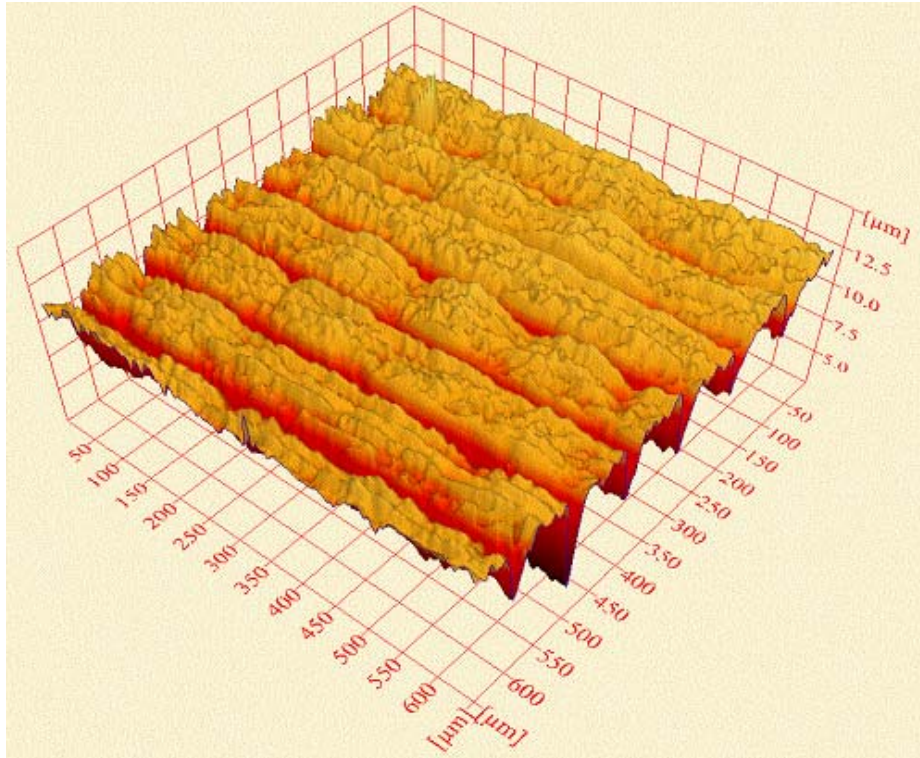


Figure 5.19: LSCM image showing stitching error effect of $2.4 \pm 0.2 \mu\text{m}$ wide and $1.4 \pm 0.2 \mu\text{m}$ high horizontal defects during workpiece dragging ablation process with hexagonal shaped mask.

The results above are summarised in Table 5.8.

Table 5.8: Results summary of stitching error reduction.

Experiment	Feature Shape	OL (μm)	Stitching error (μm)	
			Width	Height
1	Square	0	23.4	3.4
2	Square	1.4	13.4	1.4
3	Hexagon	1.4	2.4	1.4

Aliasing (effect of producing a non-orthogonal path with a square mask) at the contour of the machined structure is also noticeable in Figure 5.20. This error varies with the nature of the contour of the part, i.e., non-orthogonal contours show aliasing effects more predominantly than orthogonal (relative to mask axis) cuts.

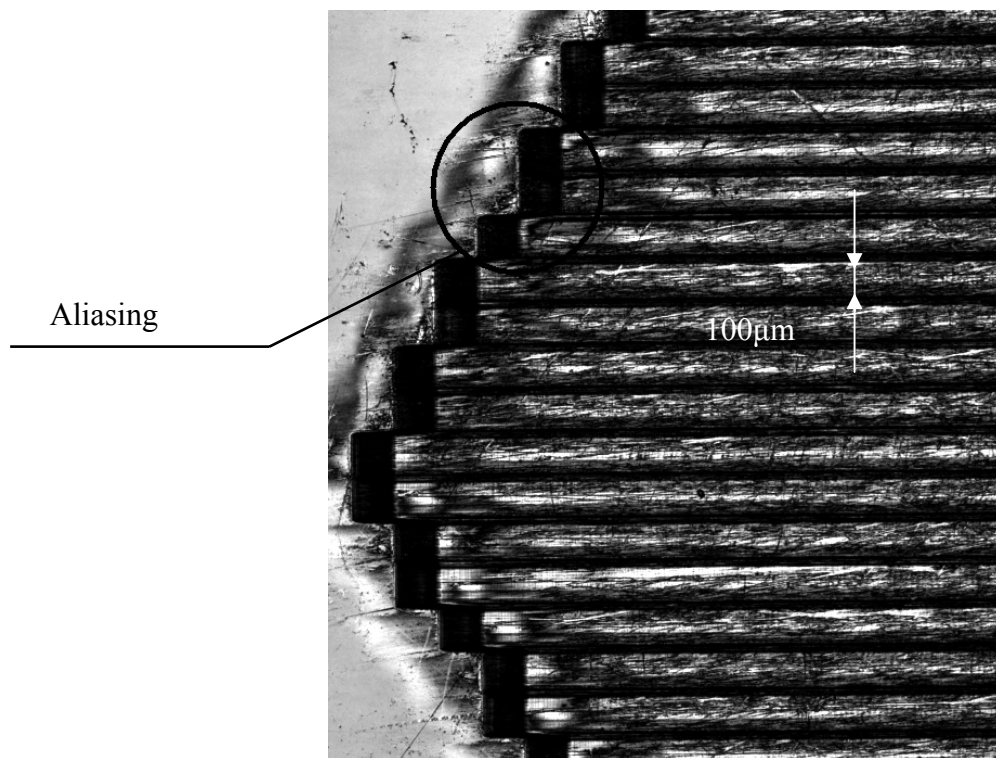


Figure 5.20: LSCM image showing surface texture, with circle around aliasing effects at the edge of machined structure during mask dragging ablation process.

Figure 5.20 also suggests that aliasing effects are directly dependent on the minimum mask feature size used for machining (in this case 100µm), and a smaller mask feature means smaller aliasing, however, this will prolong machining time. Hence, it is necessary to make a compromise between desired feature resolution and effective machining time, and this is also controlled by the CAD/CAM system.

5.9 Summary

In this chapter, the results of work on the geometrical failure effects in the boundary region between the adjacent ablated volumes were reported. The stitching error effects in the boundary area between the adjacent ablated volumes of the polycarbonate (PC) substrate under 248 nm KrF excimer pulsed radiation have been studied with respect to the fluence and the number of pulses. These studies were carried out on the samples created by 210 μm x 210 μm image size with a fluence of 1.1 J/cm² and pulse repetition frequency 5 Hz. The etch rate variation with fluence followed a trend similar to that reported in the literature for polycarbonate.

The effects of different overlay errors on the surface roughness were investigated, and categorised into five different cases. It was found that for a 36.7 μm deep structure the type 1 (*peak*) error height could be converted to more desirable type 3 error $\pm 18.3 \mu\text{m}$ with evenly distributed peak/troughs providing the surface with improved roughness by changing the amount of overlap *OL* from 0 to 4.6 μm . Therefore, an overlap size smaller than the wall angle projection on the top surface appears to be optimum with respect to long-term stability and planarity of the laser patterned structure. Depending on the desired surface quality as well as the accepted processing time, the mask size, the fluence, as well as, the overlap needs to be adjusted [10].

To automatically adjust these parameters a *GUI* for a complete software system for automatic part program generation for an excimer laser ablation tool has been developed. The algorithm in the software GUI is able to calculate the optimal size of the overlapping distance (*OL*) that will produce the surface with peak and trough errors evenly distributed, hence, producing a surface with improved roughness quality. More importantly, two key strategies related to the practical use of excimer laser micromachining process for creation of 3D surfaces for some optical applications have been demonstrated. The first one is the ability to determine fluence and number of shots in order to control surface roughness. Secondly, by controlling the overlapping area in the adjacent layers the amount of error when producing 3D structures can be successfully reduced.

In this research the main process parameters (laser fluence F_d (J/cm²), pulse repetition frequency *PRF* (Hz), and number of pulses per area (*n*) have been used as input

parameters for optimisation by using the Taguchi orthogonal array experimental method [77]. The Taguchi Design of Experiments method reduced the number of process characterization experiments from 27 to 9 and determined that the wall angle is most dependent on the laser fluence, as expected. The optimal output parameters from these experiments were the wall angle $\theta = 4^\circ$ and ablation depth $D_p = 40 \mu\text{m}$, and these have been used as an input to the new system for image overlap optimization. The calculated size of the overlap $1.4 (\mu\text{m})$ was then incorporated into mask features designed for a particular material and process parameters. Samples were machined using two different mask shapes (square and hexagonal). The performance of the system has been verified by NC part program generation and results are reported in terms of width and height measurements of ablated micro textures.

An initial stitching error of $23.4 \pm 2.2 \mu\text{m}$ wide and $3.4 \pm 1.5 \mu\text{m}$ high was observed when the overlap size between adjacent volumes was zero, when ablating $100 \mu\text{m} \times 100 \mu\text{m}$ features in polycarbonate (PC) at a fluence of 0.5 J/cm^2 using a workpiece dragging technique.

When the size of the overlap of a square mask was $1.4 \mu\text{m}$ optimised by a system based on optimal process parameters, and incorporated in the mask design, the maximum stitching error was reduced to $13.4 \pm 2.2 \mu\text{m}$ wide and $1.4 \pm 0.9 \mu\text{m}$ high under the same conditions. Employing the hexagonal shaped mask with incorporated size of the image overlap, horizontal-stitching errors were further reduced to a width of $2.4 \pm 0.2 \mu\text{m}$ wide and $1.4 \pm 0.2 \mu\text{m}$ high.

Chapter 6. *Method for Micromachining using Origin Related Mask Patterns*

6.1 Overview

This chapter describes an approach to mask design as well as a strategy for machining microstructures referred to as “Common Nest” (CN) used to further support this research work. Section 6.2 describes some of the existing approaches in detail, followed by section 6.3 which discusses their limitations. The details of proposed method appear in section 6.4 and a CAD tool concept design for this method is presented in section 6.5. Experiments to evaluate this method are reported in section 6.6. Finally, in section 6.7 the results of this chapter were summarised.

6.2 Introduction

Micro structuring with excimer laser ablation is normally achieved by using non-contact image projection techniques. These techniques require custom-made chrome-on-quartz photo masks as tools for shaping the beam to produce the desired structures. These masks are relatively expensive and making them for every change in design is not practical. Hence, new methods are needed to make this attractive technology a low-cost production process.

Micromachining laser techniques using mask projection methods have become well established as production techniques with improvements limited mostly to enhancements in laser drive technology rather than changes to the basic mask projection, beam handling and motion control systems [45]. Ultra thin inorganic, metallic and organic films are often patterned using mask projection methods with both Nd:YAG and excimer laser ablation tools [19]. Higher features resolution and cut quality can be achieved by excimer laser systems but they are limited to use of expensive lithography

masks. Recently, high harmonic 3ω Nd:YAG lasers have been used as a tool for rapid production of complex patterns on metal shim contour masks that can then be used as a projection tool for excimer laser systems. This is especially practical for rapid testing and prototyping applications [88]. These techniques are mainly limited by stitching error effects between two adjacent ablation sites, mask patterns misalignment problems when trying to stitch together projected features, the need for additional programming for offsets, and expensive projection tools such as lithography photo-masks. These limitations are discussed in more detail in following sections.

6.3 Limitations of Existing Approaches

6.3.1 Stitching Errors

The effects of different stitching errors on the surface roughness were investigated, and categorised into five different cases. A simple mathematical model of how these errors are formed and software how to reduce them was presented in Chapter 4. Figure 6.1 shows a typical stitching error effect at the junction between Y-shape and rectangular shaped patterns. A “trough” type of errors was evident suggesting that the overlap size used was determined in accordance with the mathematical model from Chapter 5 (types of error 2, 4 or 5) as shown in Figure 5.12.

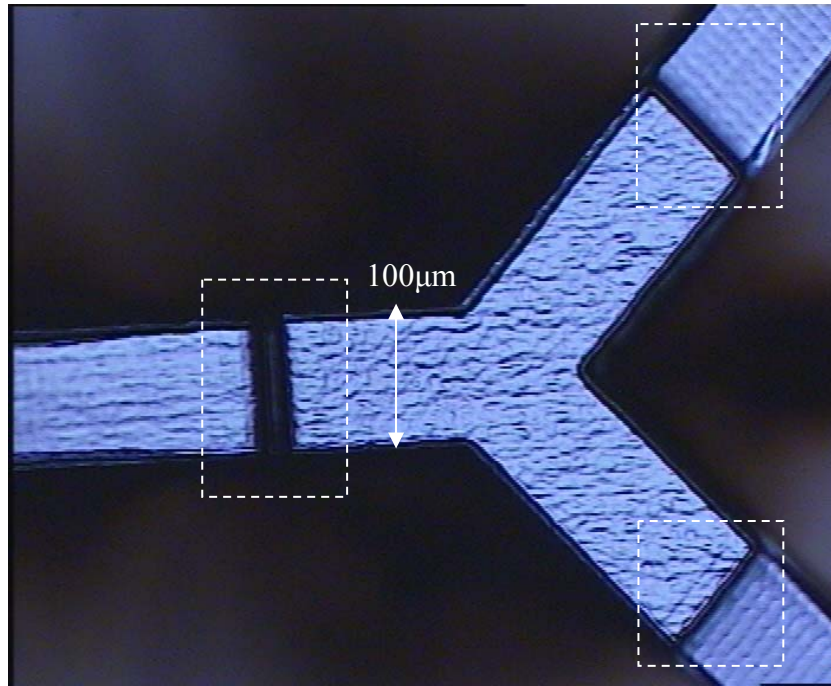


Figure 6.1: Typical stitching error effect (indicated by rectangles) at junction between four imaged patterns. Y-shape channel width is equal to 100 μm .

6.3.2 Additional Programming for Offsets

Micromachining of micromechanical devices usually requires use of more than one mask pattern to machine a complete device. This means that mask pattern projected images have to be properly aligned and offset in order to stitch them together for complete device or microstructure creation. This requires additional programming work and offset calculation to take into account stitching error effects and the necessary pattern alignment. Figure 6.2 (a) shows a desired stitching position indicated by rectangle in order to extend one of the branches of the Y shape and (b) represents a typical offsets calculation and positional error.

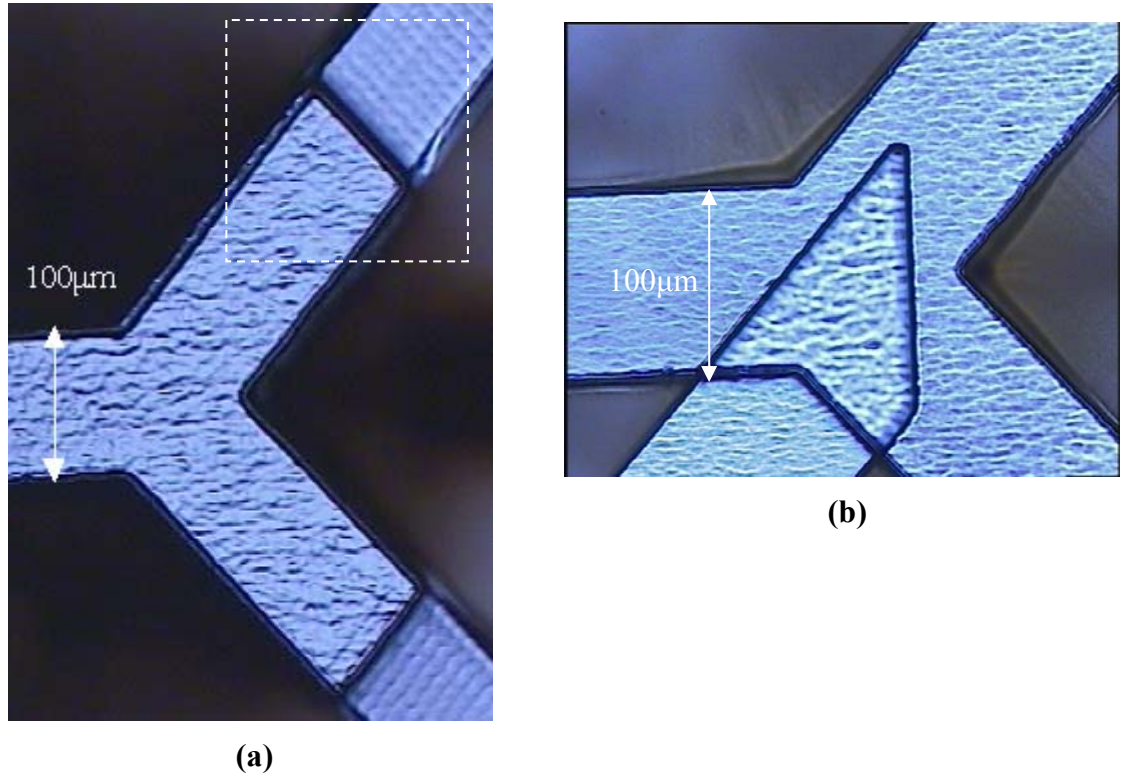


Figure 6.2: (a) Desired alignment position indicated by rectangle and (b) Mask patterns offsets and misalignment problem.

This problem will be illustrated using the microfabrication of a Y-shape microfluidic device that requires several mask patterns and at the same time has to comply with additional design requirements such as proper center distance between holes for placing microfluidic connectors. An example of a Y-shape microfluidic device is illustrated in Figure 6.3 (a) and (b).

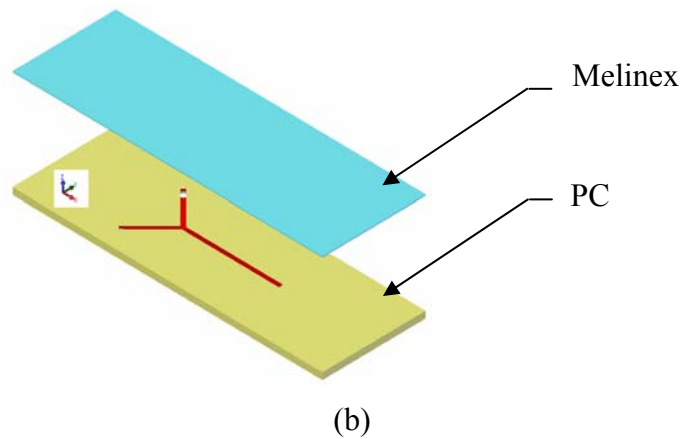
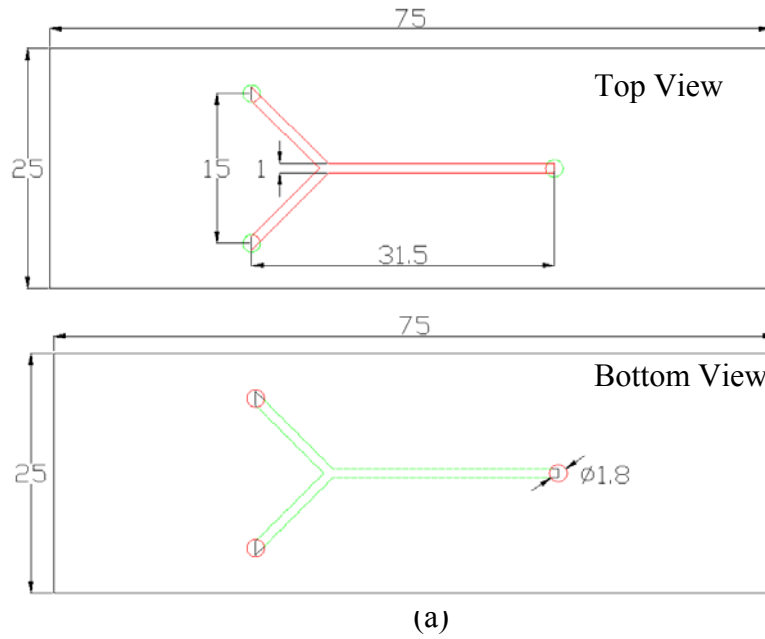


Figure 6.3: (a) Top and bottom view of microfluidic chip layer with dimensions of the channel and holes for fluidic connectors. (b) Y-Shape assembly of two-layered microfluidic device. All dimensions are shown in millimeters.

The PC layers had a thickness of 1.58 mm and sealing layer of 0.035mm. This device can be fabricated using any one of the three different mask layout designs shown in Figure 6.4 (a),(b) and (c). The first solution, as shown in Figure 6.4 (a), is to create the mask for the complete device in one piece, but possible changes in design such as a change in center distance between inlets and outlets holes makes this approach impractical. Especially when the size of the features on the mask is 10x bigger than produced image size. Demagnification is required in excimer laser micromachining as explained in experimental section of this thesis.

The second solution is to create four different patterns and use workpiece-dragging technique to machine the Y-shape device. It is shown in Figure 6.4(b). This solution will be adequate if special care is taken during mask design stage. The main problems with this solution are misalignment and stitching errors. The third solution is shown in Figure 6.4(c), and is a combination of previous two designs and has similar problems.

Fabrication using the design in Figure 6.4 starts by projection of the image of the Y-shape junction mask. Secondly, in accordance with design requirements, the right hand side channel of the junction could be extended using the workpiece-dragging technique. In order to ensure that the channel is continuous the alignment and programming of the offsets is needed. At this stage the amount of overlap at the junction point in order to control the channel machined surface (peaks or troughs errors) needs to be taken into account. After the right hand side of the junction is successfully extended, the same procedure has to be repeated with the other two junction channels, i.e., the offsets have to be recalculated, taking into account the correct size of the overlap. This will require additional programming work that can be time consuming and error prone. The next problem is mask positional error in respect to mask holder and it was discussed in section 6.3.3.

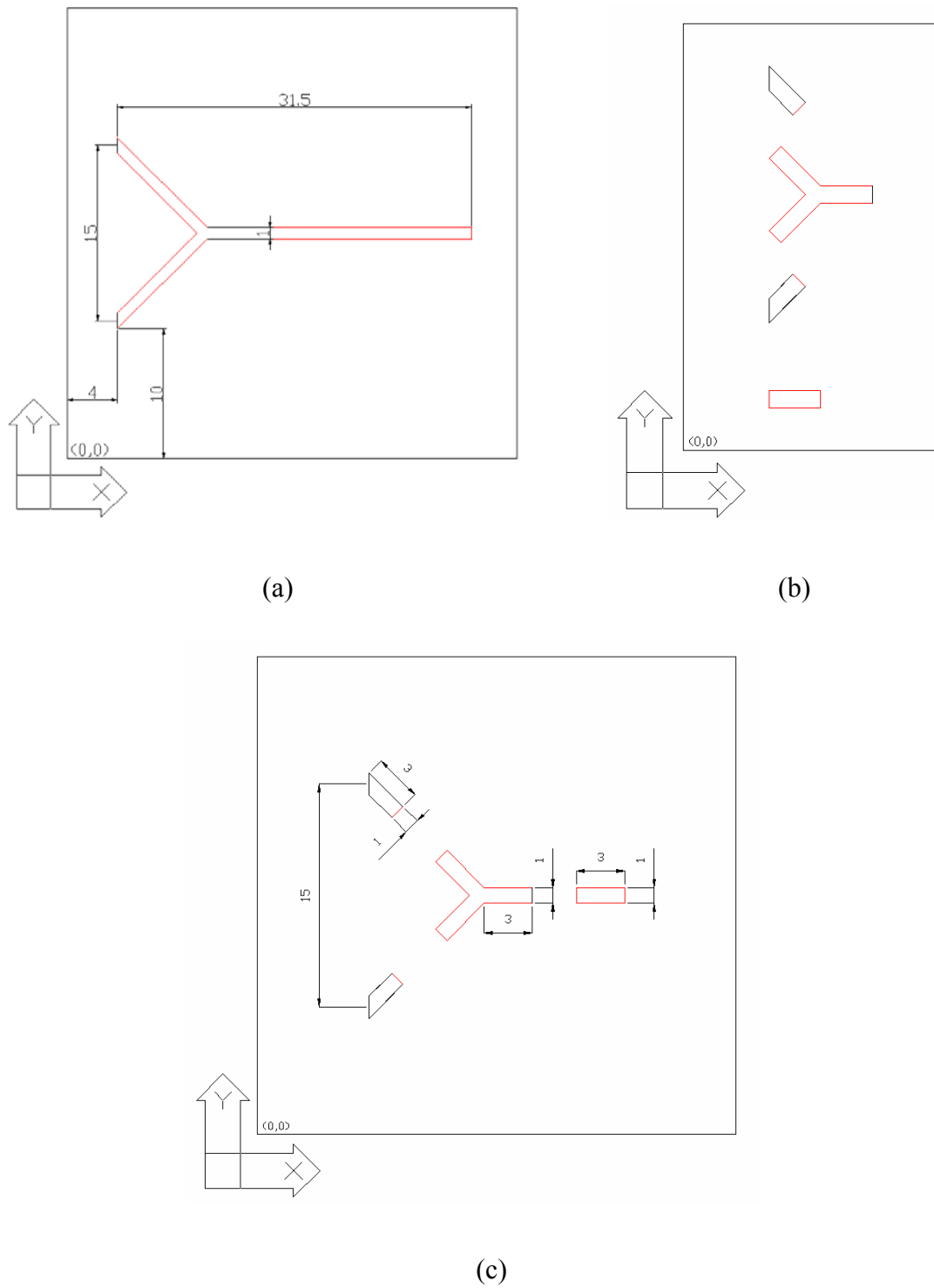


Figure 6.4: Three different mask design solutions. (a) Y-shape made in one mask pattern. (b) Four mask patterns that can be used to produce the Y-shape. (c) Four mask patterns where two of the patterns are spaced in accordance with design requirements for center distance between fluidic connectors.

6.3.3 Mask Positional Error in respect to Mask Holder

The beam delivery system usually contains beam shaping and homogenization optics to create a uniform, square beam at the plane of a mask held on an open frame CNC controlled X-Y stage set. The substrate and mask are mounted on separate planar stages that are capable of moving in both X and Y directions independently. If the mask with multiple patterns is placed in the holder with some rotational error, i.e., the centerlines of each pattern are not parallel to the direction of the stage travel, a rotational error will be introduced. Therefore, mask realignment is necessary. Figure 6.5 shows exaggerated mask rotational error.

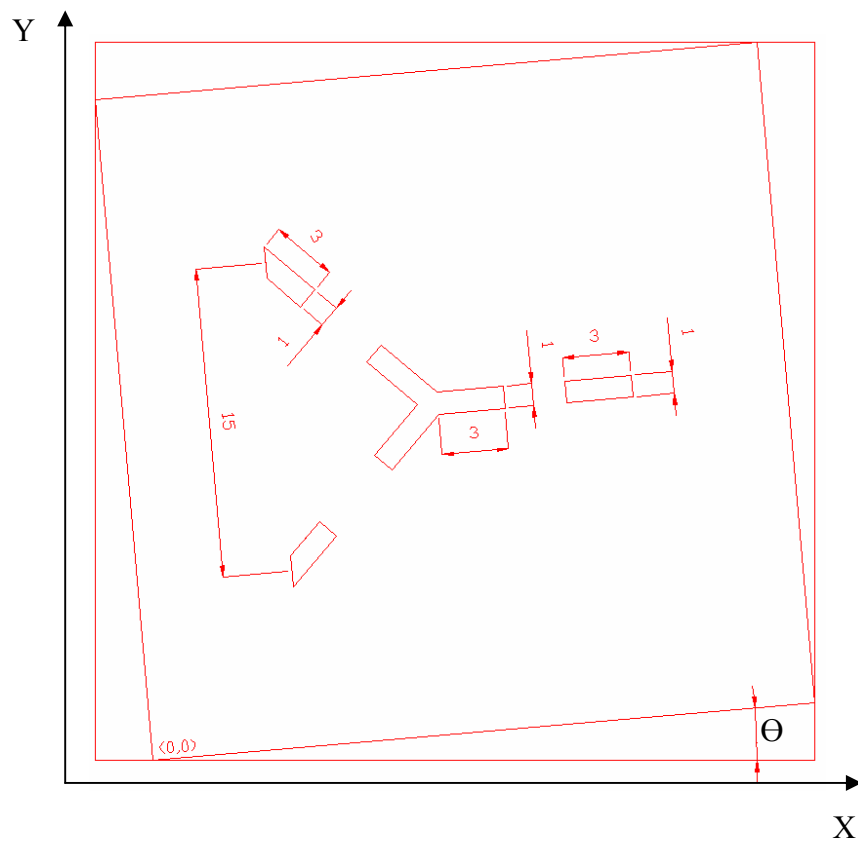


Figure 6.5: Mask rotational error in respect to mask holder.

6.3.4 Chrome-on-Quartz Masks

A conventional chrome-on-quartz mask is traditionally used as a tool for beam shaping in excimer laser mask projection systems. These masks are constructed by lithography processes and they are generally expensive. Also, if they are not well stored and handled they can easily be damaged. Another source of damage to these expensive masks is accidental application of laser fluence higher than the mask ablation threshold of approximately 100 mJ/cm^2 (a poor quality coating has a threshold of $\sim 40 \text{ mJ/cm}^2$). If this happens, the mask is permanently damaged.

One alternative to overcoming this problem is to use custom designed metal contour masks produced by a frequency tripled Nd:YAG laser tool. Mask generation using the frequency tripled Nd:YAG laser offers a rapid and low cost method for fabrication of complex geometries in the excimer laser. This is especially useful for rapid production of low cost prototypes and test structures. Figure 6.6 shows an example of typical chrome on quartz mask and a chemically etched steel mask commonly used as a projection tool in excimer laser ablation process. Nd:YAG laser masks are typically metal shim, low-cost material, contour masks, where patterns are cut through the shim by the laser itself. Resolution of these patterns is limited to $30\mu\text{m}$ by the laser beam size.

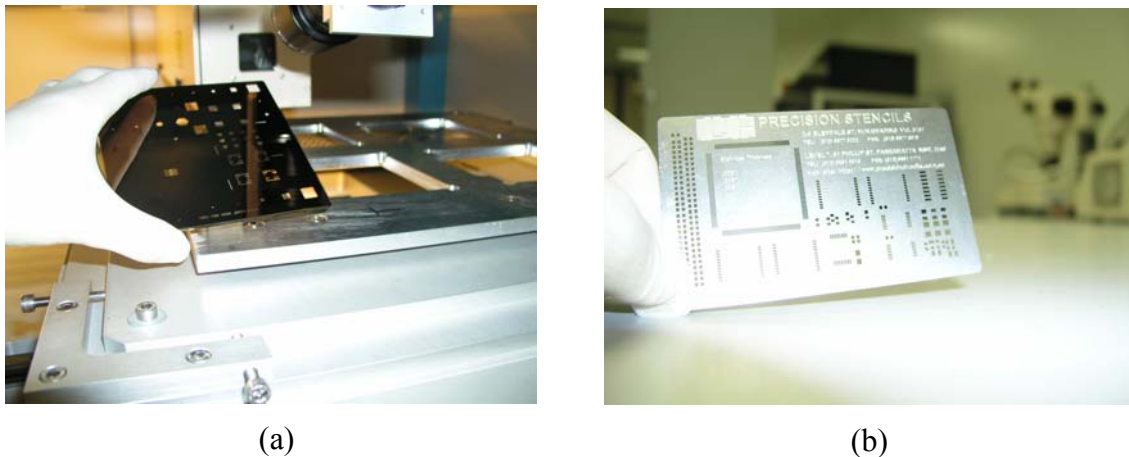


Figure 6.6: (a) Chrome-on-quartz mask, (b) steel mask (precision stencil).

To address all the aforementioned problems, the Common Nested mask design technique is proposed and explained in the section below.

6.4 Description of “Common Nested” Approach

The laser mask projection approach, referred to as Common Nest (CN), has been developed to reduce the coding in part programming and provide flexibility. Whereas, the existing approach is limited to specific single shapes from multiple patterns in a single mask, which are un-related. The new approach eliminates the need for calculation of offsets when using more than one mask pattern to generate complex structures and removes the need for realignment between stitched patterns. The approach is based on a special mask design concept that incorporates allowance for all overlaps directly during the mask design stage. This technique takes advantage of the developed material database described in Chapter 3 section 3.8.5 with process characterization parameters for commonly used materials and design techniques that incorporate stitching error earlier in the mask design stage. It enables the user to tailor the type of stitching error that will best suit the particular device or application. It depends on the material ablation properties and process parameters such as: fluence, ablation depth, number of pulses per area, pulse repetition rate and using the mathematical model explained earlier in Chapter 5, stitching error can be controlled by the amount of overlap chosen to suite particular application. For example stitching errors with only troughs (Types of errors 2, 4, and 5 from Figure 5.8 in Chapter 5) would be preferable for microfluidic channels since the flow of fluid in the channel will not be obstructed with these types of errors.

CN also utilises an economical and flexible laser system for mask production that can be then used by excimer laser tool.

Figure 6.7 illustrates the CN approach. It shows mask design that incorporates overlap and offsets needed already at mask design stage (Step 2). For example, to machine a Y-shape structure as shown in Step 1, a suitable mask pattern array using the CN method would be as shown in Steps 3 to 6. It is important to notice that now all mask patterns have the same/common origin point (hence, the origin of the terminology “common nest”). That is, when all mask patterns (Steps 3 to 6) were overlapped using common CN point the results would be perfectly aligned relative to each other for all mask patterns as shown in Step 7. After laser ablation, the final structure would be a Y-Shape as shown in Step 8.

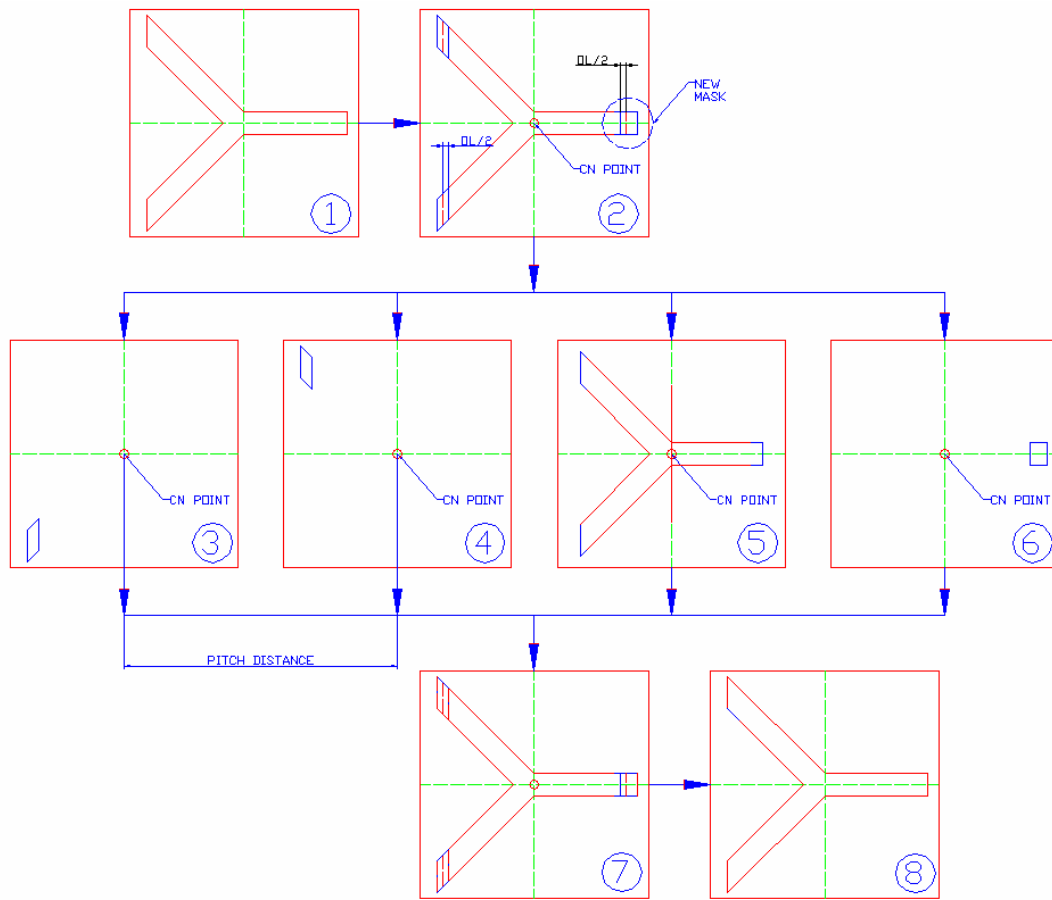


Figure 6.7: The main process steps 1-8 illustrate how CN approach was used to create a Y-shape structure. Four mask patterns were extracted from the main target design and when overlapped using a CN point, they would create the required structure.

Because the size of the overlap is already included in each pattern, there is no need for offset calculation and programming. Time for programming is reduced and a complete device can be manufactured with lower surface roughness and less stitching defects.

In Figure 6.8, the existing approach, and Figure 6.9, the CN method, were used to demonstrate how reduction in part programming was achieved using the latter one. It is obvious from Figure 6.8 that additional programming for offsets is needed to properly position the required mask patterns to be able to machine desired Y-shape when using existing technique.

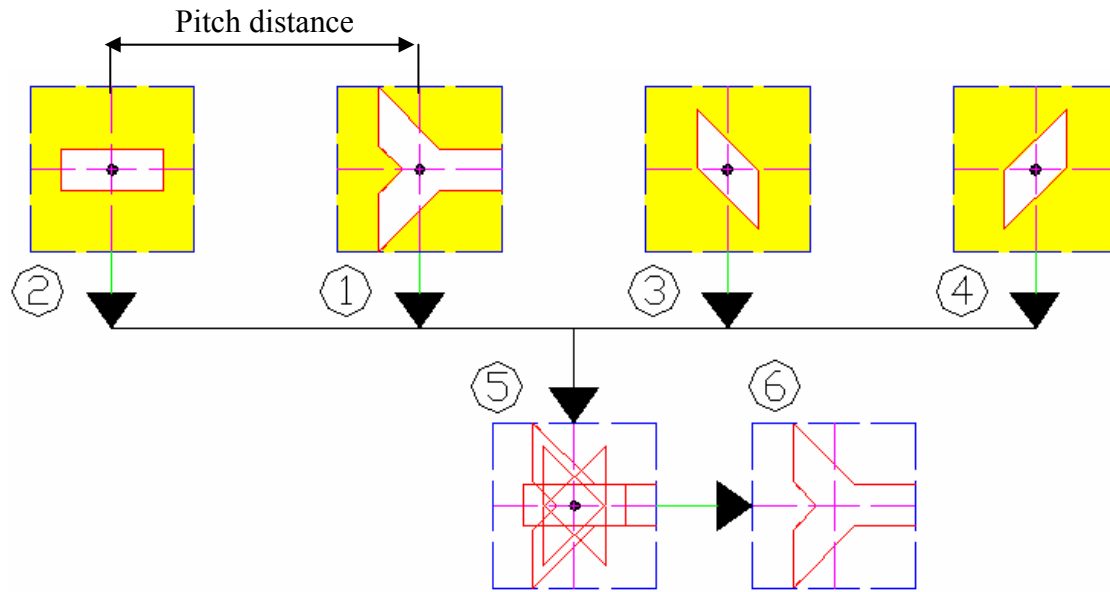


Figure 6.8: An existing approach shows mask patterns with origins unrelated to a common point. Mask patterns offsets and overlaps were not included into design stage.

On the other hand from Figure 6.9 it can be seen that all offsets and overlaps were already included into design stage using the CN method, hence, when any of the four mask pattern was brought into position for laser firing there was no need for additional programming of offsets. At the same time all mask patterns on a mask were always 100% aligned one relative to each other. Furthermore, as long as the whole mask was placed into holder without rotational and positional error, and neglecting the errors such as; NC stages calibration errors, vibration errors, magnification errors and beam pointing stability errors, the total alignment error will be minimum.

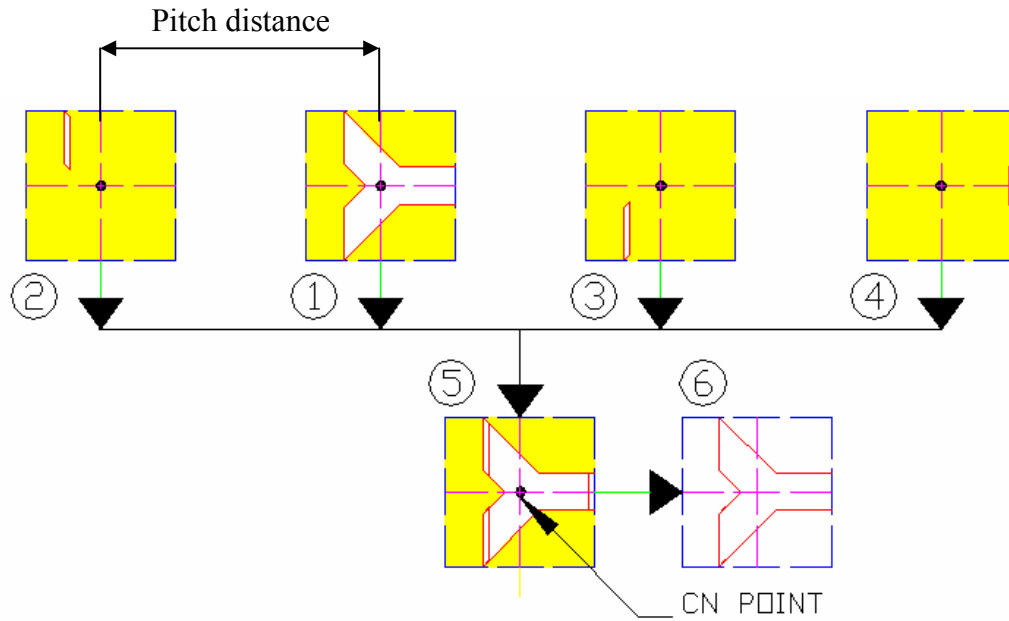


Figure 6.9: Four mask patterns extracted from target design were used to produce same Y-shape structure using principles of CN approach.

In Table 6.1 it was illustrated how a reduction in part programming was achieved by the CN approach compared to the existing approach to produce a Y-shape structure (Figure 6.8 and Figure 6.9). It can be seen from a listing of a segment of part program used to machine desired Y-shape, that the existing approach needs an extra line of coding for each mask pattern to bring workpiece into position for machining and accommodate for the offsets. The listing in Table 6.1 shows part of program just for the first two mask patterns, but for the rest of mask patterns the same steps would apply.

Table 6.1: CN approach reduction in coding compare to existing approach.

Part programming steps		Existing approach (Figure 6.8)	CN approach (Figure 6.9)
1. G90 G1 X100 Y100 F2000	Absolute move of workpiece into position for laser firing.	✓	✓
2. G90 G1 Z282 U134 F2000	Absolute move of first mask into position for laser firing.	✓	✓
3. PSOF,2,50	Fire 50 laser pulses.	✓	✓
4. PSOF,0	Stop Laser Firing.	✓	✓
5. G91 G1 Z15	Relative move of second mask, by pitch distance, into position for laser firing.	✓	✓
6. G91 G1 X(offset value) Y(offset value)	Offsets compensations to bring workpiece into position for laser firing.	✓	NO

Also, mask positional errors are substantially reduced or completely eliminated.

The advantages of the new approach are as follows:

- Reduces the amount of part programming
- Reduces the mask patterns misalignment errors
- Eliminates need for calculation of offsets
- Overlap included with mask design
- Provides control over stitching errors because overlap size is accommodated during mask design stage
- Makes use of metal shim (contour) masks
- Lowers cost of creating complex mask designs for quick prototyping.
- Flexibility. Easy to modify existing or create new designs.
- A standard set of mask patterns can be used to create different structures

Disadvantages:

- Maximum feature size limited to size of the beam ($10 \times 10 \text{ mm}^2$). This is determined by laser projection lens.
- Suitable only for 2.5 D microstructuring techniques.

6.5 CN Mask Design Tool

To support the CN approach a prototype software tool with user interface was developed to assist the mask designer to create a mask design and automatically generate the NC code compatible with excimer laser machine (Exitech S8000 with Unidex 500 Controller, Aerotech Inc). The software is a 2D design tool and is a combination of the existing AutoCAD CAD package and a converter utility program created using the Visual Basic (VB) programming tool kit.

The developed procedure from mask design to creation of the NC-code is outlined below:

- CN mask design and the component patterns are created using AutoCAD
- Machining tool paths are created as a set of lines and curves in AutoCAD using the patterns in the mask
- The tool paths are then converted into a part program using the developed VB software.

The process will start by creating a metal shim mask design using the AutoCAD drawing package. The design has to comply with CN strategy requirements, i.e., each mask pattern has to have a common origin point. Other design requirements that have to be satisfied are simple centering of mask into laser beam and mask alignment with the travel direction of stage axis. Figure 6.10 shows a possible mask design layout to machine serpentine type microstructures, commonly used in design of microfluidics devices.

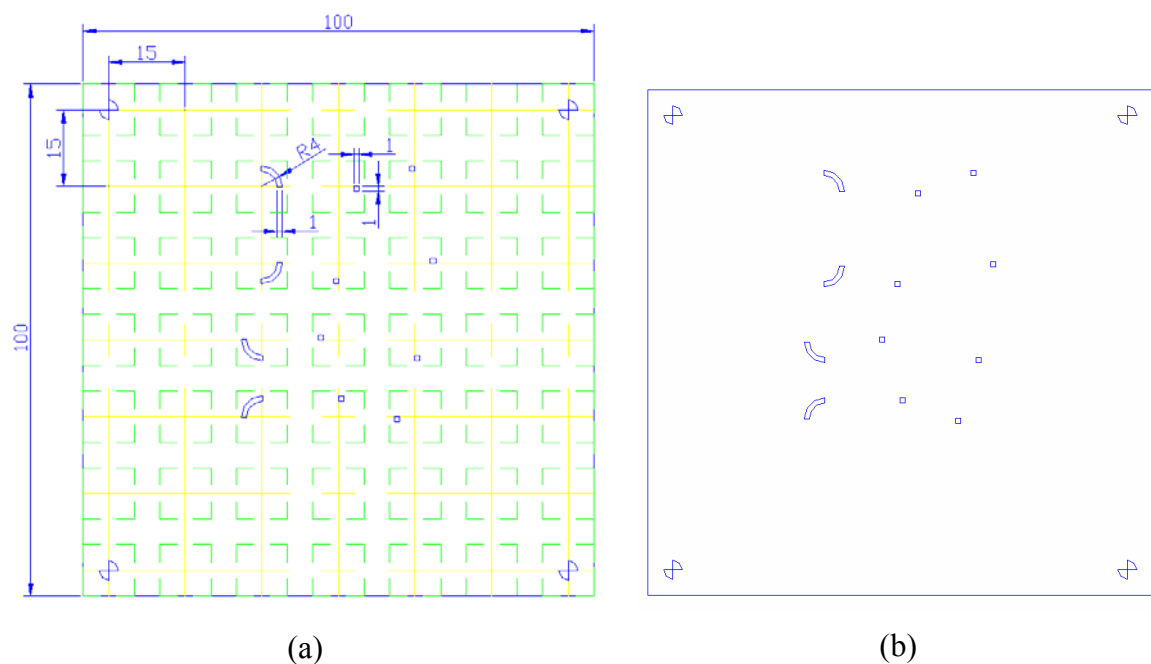


Figure 6.10: (a) Mask design including overlap features. Mask includes features used for correction of mask rotational error in relation to direction of travel of the stage axis. (b) Final mask design.

Four alignment patterns (patterns with alignment marks are located at each corner of the mask) are used for correction of mask rotational error in relation to direction of travel of the stage axis. They are used in conjunction with vision tools (CCD camera and alignment software). The arc patterns with matching small square patterns enable creation of different serpentine microstructures. A standard AutoCAD GUI (user interface and menu layout) has been customised to suit microstructure design needs. All mask patterns are mapped into a matrix, and in this way, a standard set of masks for multipurpose design needs can be created. Mask patterns are created as BLOCKS (standard AutoCAD features) and can be easily recalled when they are needed. BLOCK design and size can be easily changed or scaled to suit design requirements. The desired layout is easily completed by arranging the blocks and lines. Figure 6.11 shows a serpentine toolpath layout designed in AutoCAD using the above mentioned procedure. The layout consists of four arc blocks with different orientation in relation to origin or insertion point and three line patterns. All blocks are implemented using the step and repeat machining method and lines are machined using the workpiece-dragging method. As can be seen from Figure 6.11, by combining different blocks and lines an infinite number of design layouts can be easily accomplished.

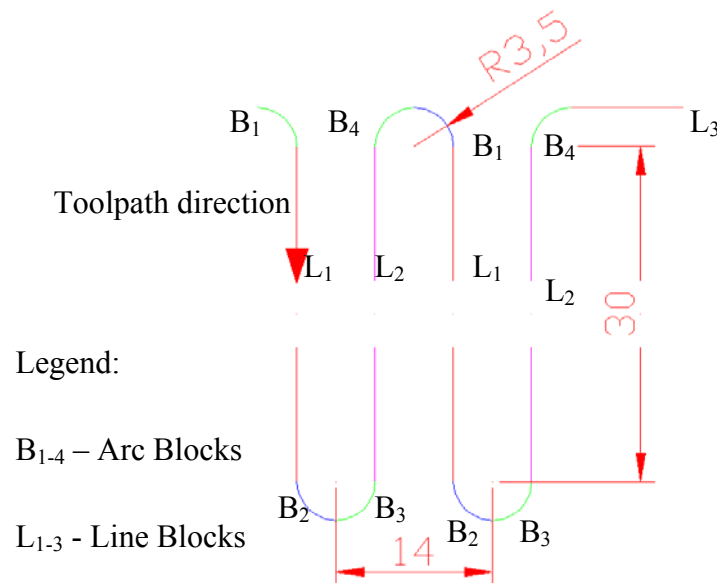


Figure 6.11: Typical toolpath to generate a serpentine structure for microfluidics applications. Arc and line blocks used to make this structure are also shown.

When the design is completed the file is simply exported in DXF file format. This file is then converted using a specially developed visual basic utility directly into NC-code suitable for UNIDEX 500 controller.

6.6 Experiments to Evaluate CN Approach

Various serpentine shaped microfluidic channels were produced using excimer laser micromachining process. The standard operation procedure and material used for the samples produced was explained in Chapter 3, section 3.7.

6.6.1 Results and Discussion

The CAD tool provides GUI for quick and accurate design of microstructures of complex shapes and geometry. To demonstrate the system performance one simple and one more complex serpentine structure were designed and then machined using the NC-code produced by the converter utility. The amount of NC code necessary to produce these structures was significantly reduced in comparison to the amount of code necessary to accomplish designs shown in Figure 6.4 (b) and (c), and it is automatically generated by the software. This method of mask design may be referred to as smart design, and the outcome is a mask that enables a microstructure of complex geometry that can be made without the need for offset calculation and additional alignment. Furthermore, the size of overlap to control stitching error has already been implemented in the mask, and the size and type of overlap depends on process parameters as explained in Chapter 4.

Figure 6.12 shows a simple serpentine microstructure channel 100 microns wide and 100 microns deep machined in a 1.58 mm thick polycarbonate substrate.

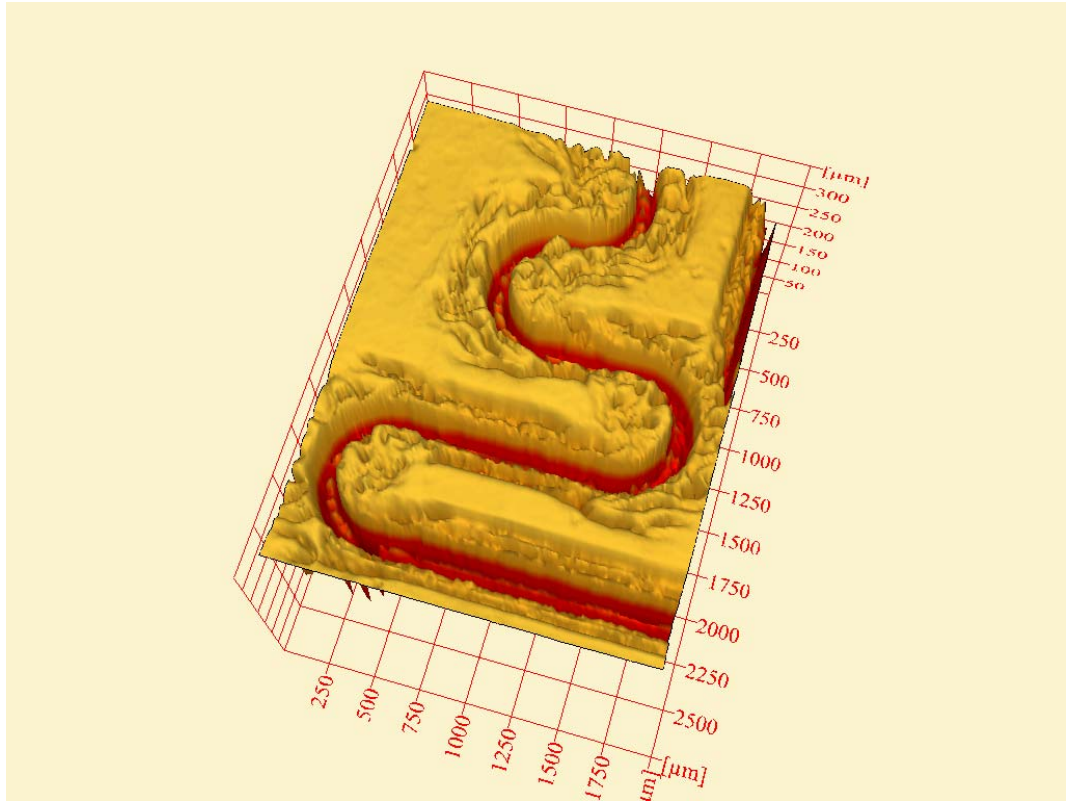


Figure 6.12: 3D LSCM image of a serpentine structure 100μm wide and 100μm deep.

Process conditions: $F_d = 1.2 \text{ J/cm}^2$, $PRF = 5\text{Hz}$, $n = 50$.

Figure 6.13 shows a more complex multi-directional serpentine structure easily accomplished with new CAD tool using the same mask design as shown in Figure 6.10 (b). Only this time the sequence of use of mask patterns was different and was chosen to meet the design requirements from Figure 6.13. This further proved the flexibility of the CN approach where different complex designs can be easily achieved using the mask with standard mask patterns.

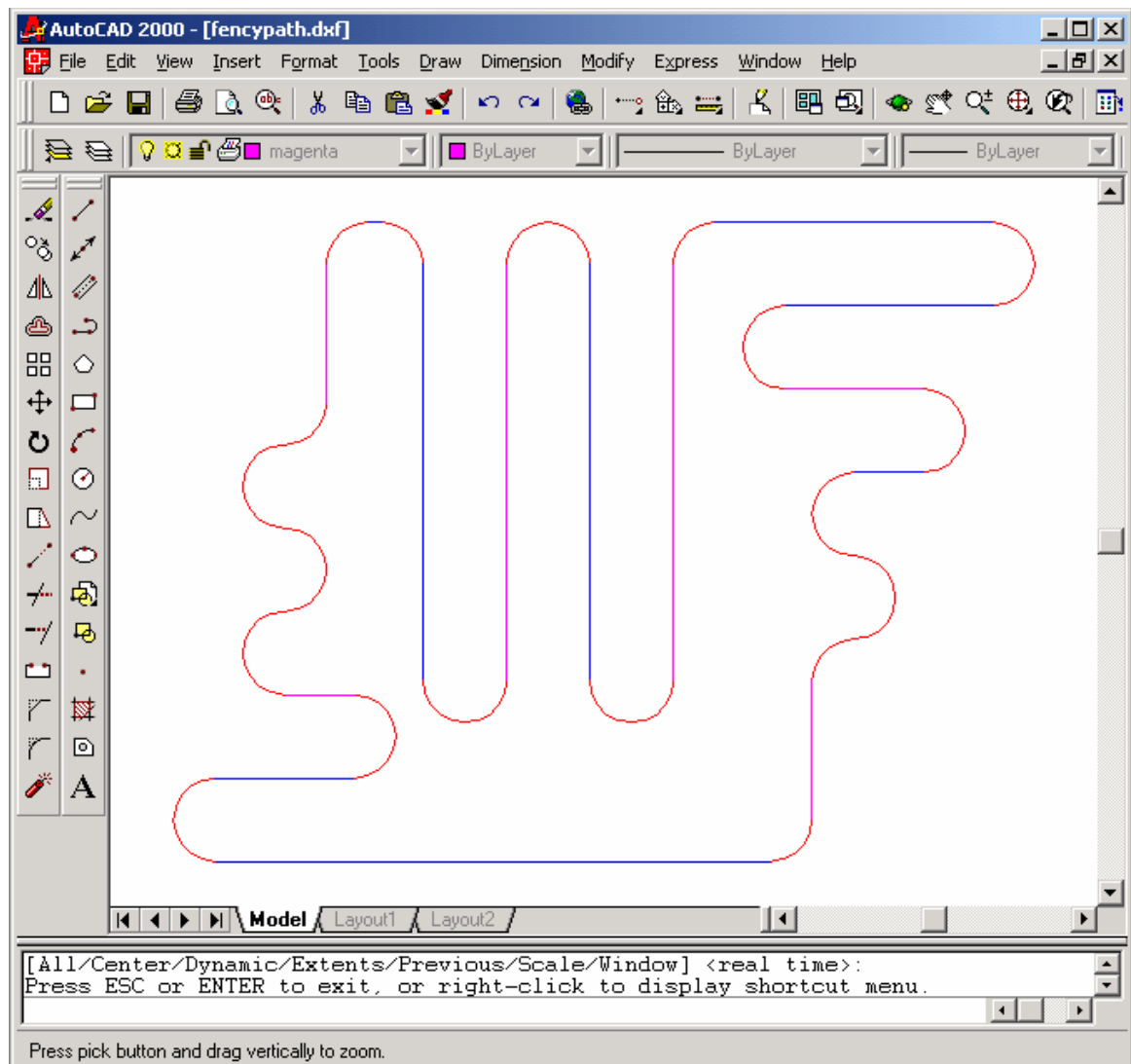


Figure 6.13: 2D CAD model of a more complex serpentine structure designed in accordance with the CN method requirements.

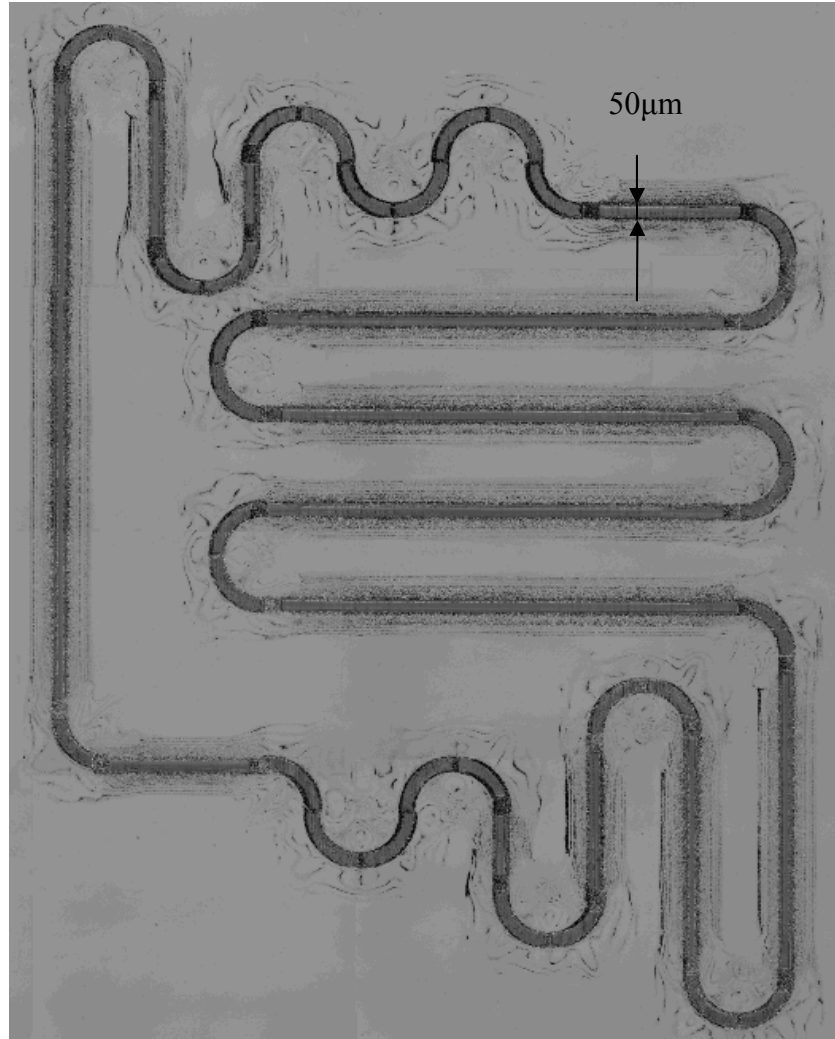


Figure 6.14: 2D LSCM image showing a complex serpentine structure. Process conditions: $F_d = 1.2 \text{ J/cm}^2$, $PRF = 5\text{Hz}$, $n = 50$.

The LSCM images shown in Figure 6.14 demonstrate that it was possible to produce the microstructure that exactly matches the design layout produced by new CAD tool as shown in Figure 6.13.

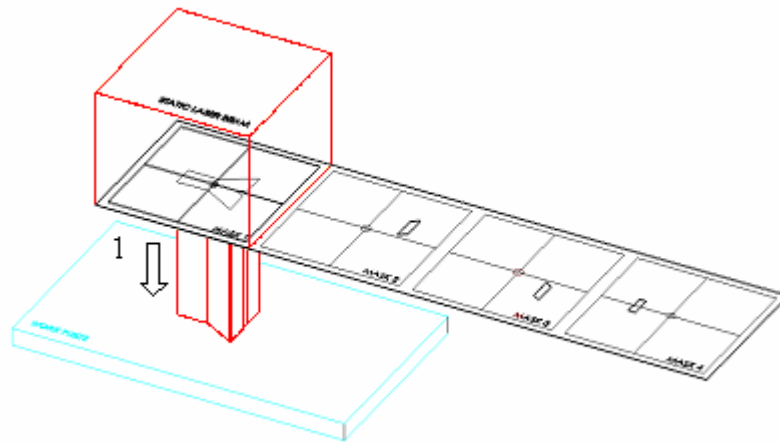
To further support the proposed “nesting” method two examples are presented in the following sections.

6.6.2 Y-Shape Microstructure Produced by “Common Nest” (CN) Technique

In many microfluidic devices, to introduce reagents and samples into the device, the T-type shape of channels were often used. The Y-shape, cross, and other similar shapes follow the same design principles and could be categorized into T-type channels. When the size of micro channel was a few tens of microns, the contacting of two sub streams in a T-type channel was sufficient enough to achieve adequate mixing. Many of electroosmotic driven microfluidic devices use channels that had sizes less than 100 μm , and permit contact between reagent and sample directly in a T-type mixer without any other mixing assistance [89]. A T-type of micro-mixer is one of the most important components of the micro Total Analysis Systems (μTAS) and in Figure 6.15 it was shown how this important design element can be produced using the CN method.

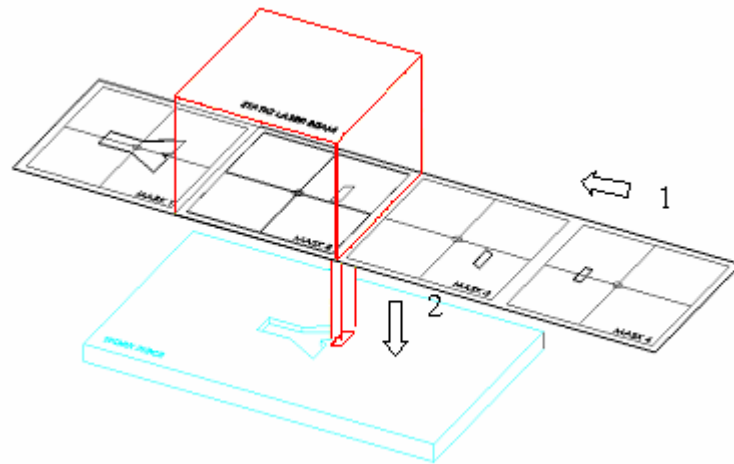
The substrate and mask are mounted on separate planar stages that are capable of moving in both X and Y directions independently (Stages are not shown for clarity). A uniform, square beam (10x10mm²) at the plane of a mask is static during the whole machining process (Figure 6.15 shows the schematic of beam size equal to the maximum possible size of a single opening at the mask (10x10 mm²)). A metal-shim mask with a row of four patterns needed to produce a whole device is also shown in Figure 6.15 and can be easily produced by Nd:YAG laser operating in direct-write mode. The patterns are all equally spaced with a pitch distance of 15 mm and aligned along one axis.

Step 1: Firstly, a proper alignment of the mask to the stage is achieved using the alignment camera. Then a Y-shape pattern is moved under the static laser beam and a train of laser pulses applied to the substrate. Both substrate and mask are held stationary during firing process.



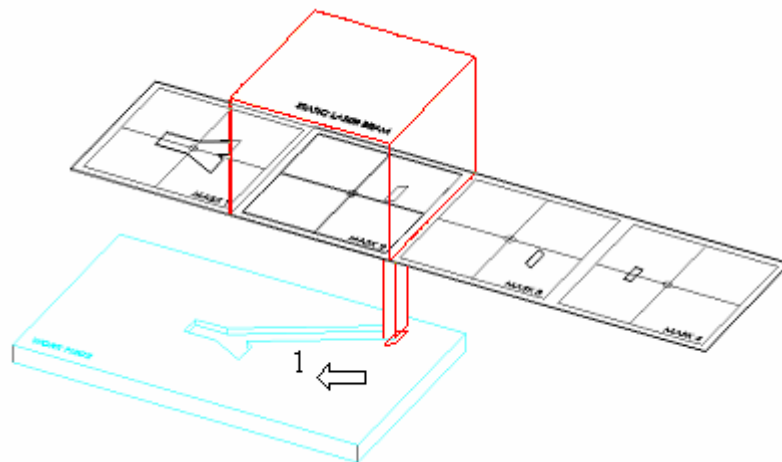
Step 1: Mask projection of Y-shape. Step and Repeat technique.

Step 2(a): The second step aims to extend the left branch of Y-shape to meet design requirements that center distance between two inlet holes is equal to 5.5 mm. To achieve this after the laser stops firing, the mask stage is moved to the left along the same axis for the size of pitch distance (15mm). This brings the second mask pattern now at the same position under the laser beam, as was previously Y-shape pattern. The substrate stays static during this process. This provides centers of the second and first pattern that are identical (common nest), and since the size of second pattern is designed to include the size of the overlap, patterns “clip” into each other and there is no need for additional offsets calculation and programming as well as realignment between mask patterns. This is normally achieved with a trial and error process that can be very time consuming and sometimes not accurate enough.



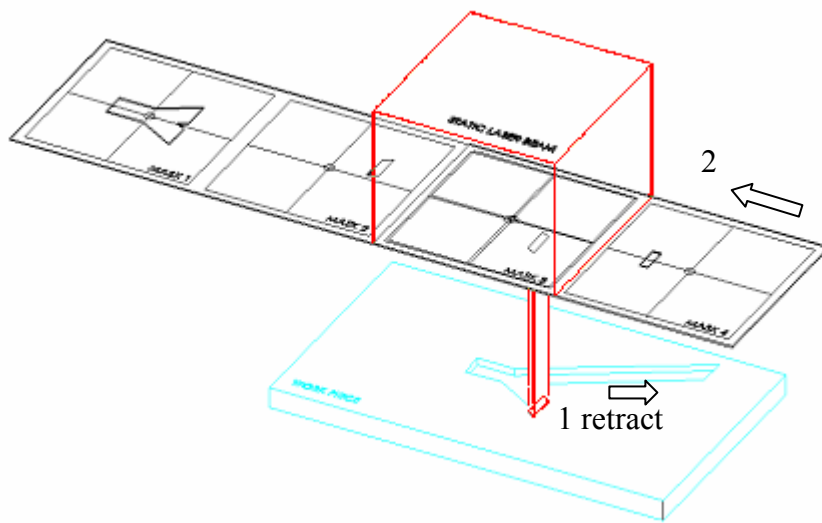
Step 2(a): Workpiece dragging of left part extension of Y joint (start position).

Step 2(b): Now the workpiece-dragging technique was used to extend the left hand side of the Y-shaped channel to the design required length.



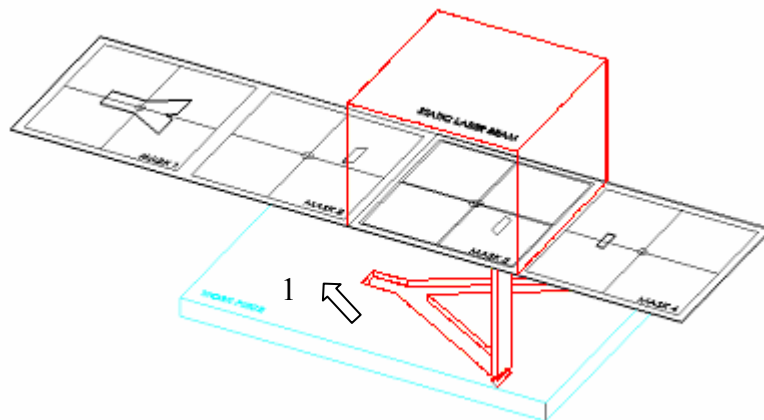
Step 2(b): Workpiece dragging of left part extension of Y joint (end position).

Step 3(a): This step has the goal to extend the right hand side of the Y-shape to match the design requirements. Firstly, the substrate has to be retracted to the starting position. Secondly, the mask stage is moved to the left for the pitch distance (15mm) to ensure that center of third mask pattern is the identical to centers of two previous patterns. This again requires no offsets calculation and additional programming work because the size of the mask pattern already includes the size of overlap needed. Again there is no need for any additional realignment of the patterns as they are already at an exact position necessary for next step.



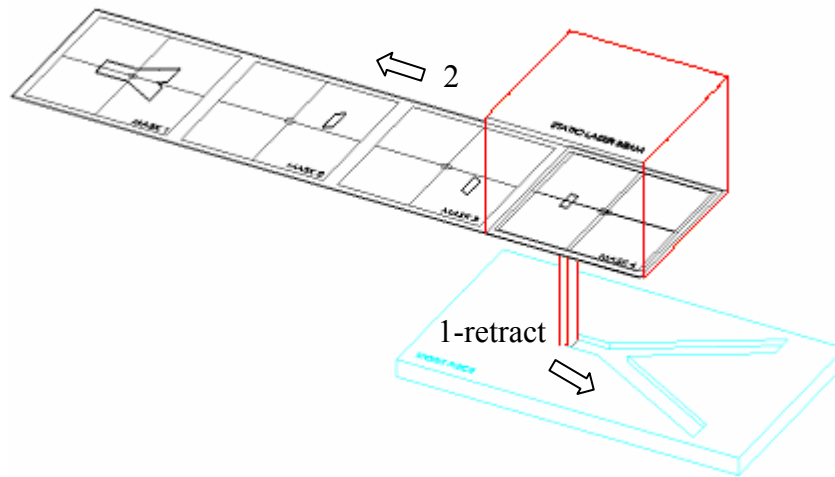
Step 3(a): Workpiece dragging of right part extension of Y joint (start position).

Step 3(b): In this step the workpiece-dragging technique was used to extend the right hand side of the Y-shaped channel to the correct length.



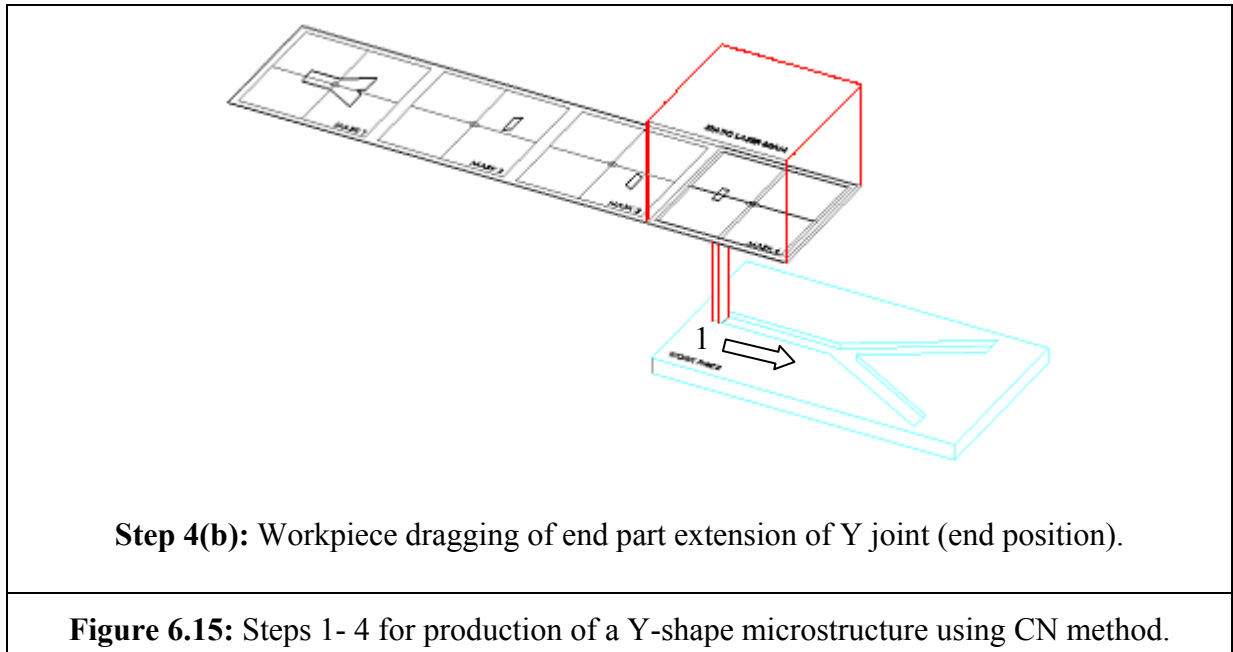
Step 3(b): Workpiece dragging of right part extension of Y joint (end position).

Step 4(a): This step starts with simple retraction of the substrate to the starting position. Next, the third and final mask pattern is now moved the pitch distance to the left hand side to ensure that this pattern as well have the same origin point as other three patterns used before. Again all offsets are already in place and there is no need for any additional programming or realignment work, hence everything is in position for the next step.



Step 4(a): Workpiece dragging of end part extension of Y joint (start position).

Step 4(b): This final step has the goal to extend the third left hand joint of the Y-shape channel to the required length. The workpiece dragging can be used again to achieve this design requirement.



With steps 1-4 , as shown in Figure 6.15, the excimer laser's part of machining of a Y-shaped microfluidic channel commonly used in MEMS application is completed and the substrate is ready now for some additional processing to create inlet and outlet holes by using a micromilling technique.

6.6.3 Serpentine Microstructure

One important strategy to solve the microfluidic mixing problem was to create chaotic advection. Chaotic advection, sometimes called Lagrange chaos, had been studied intensively in Macro-world [90]. The knowledge could be borrowed for the design of microfluidic mixers. For instance, using a twisted pipe, secondary flow occurs at the bends of the pipe [91]. Chaotic advection could be a result of these secondary flows. Inspired by the twisted pipe, 3D serpentine channels were fabricated [92]. The flow in 3D serpentine channels demonstrated chaotic advection at high flow rates ($Re \sim 70$) and good mixing performance [89]. One of the advantages of the serpentine design was to keep the height-to-width ratio near one so that it minimizes the chances of clogging, fouling and loss of sample in the biological analytical applications. However, the challenges of serpentine mixers were the microfabrication of complex 3D structures and the need for a high Reynolds number to stir fluids to generate chaotic advection [93]. This is one of the reasons why serpentine structures could be found as an important design element for many microfluidic devices. Here, it will be shown how this common microstructure

design element can be machined using the CN strategy. Figure 6.16 shows a part of serpentine structure that consists of a 90 degrees entrance channel, serpentine structure and an exit straight channel.

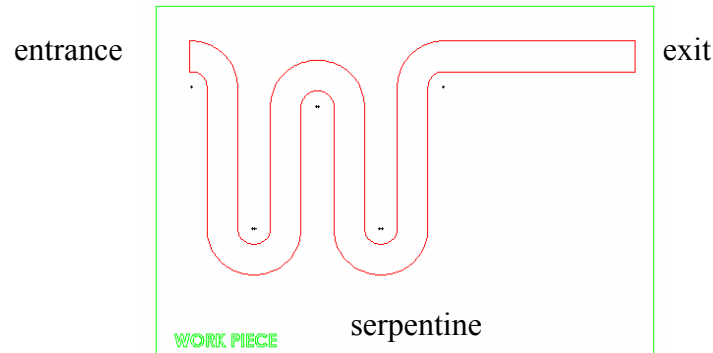


Figure 6.16: Serpentine structure element.

To machine the serpentine structure using the CN technique, first a metal shim mask needed to be made using Nd:YAG laser and layout design as shown in Figure 6.17. Figure 6.17 shows eight mask patterns, but for the case of Figure 6.16, only seven patterns to machine complete structure were needed ¹. The mask was designed following the same rules as explained for Y-shape example. Again all patterns have the same origin point (common nest), hence, calculations of offsets and realignment are not needed.

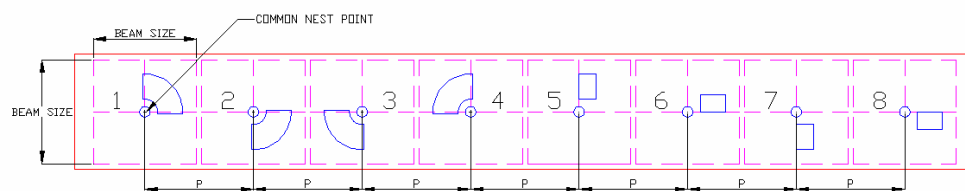
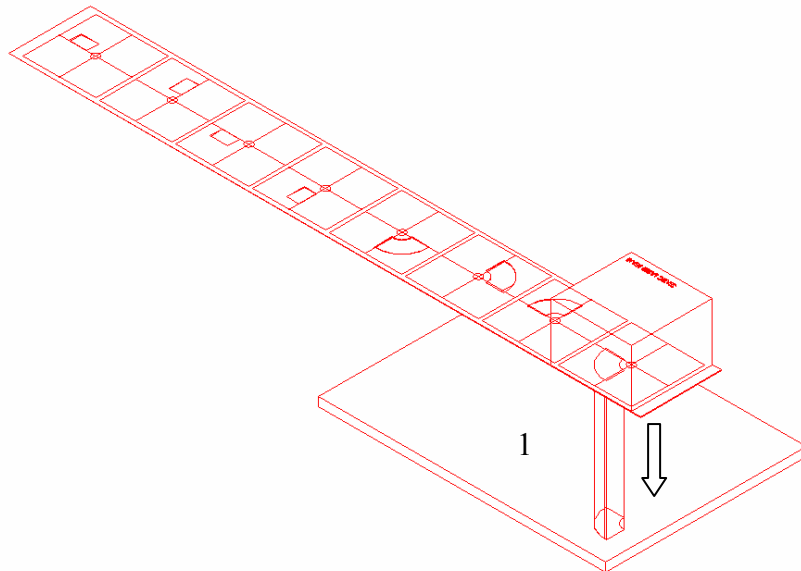


Figure 6.17: Metal shim mask with eight patterns for machining serpentine structure.

¹ Only two mask patterns are needed to complete machining of serpentine structure as shown in Figure 6.16 providing that workpiece or mask stage can rotate.

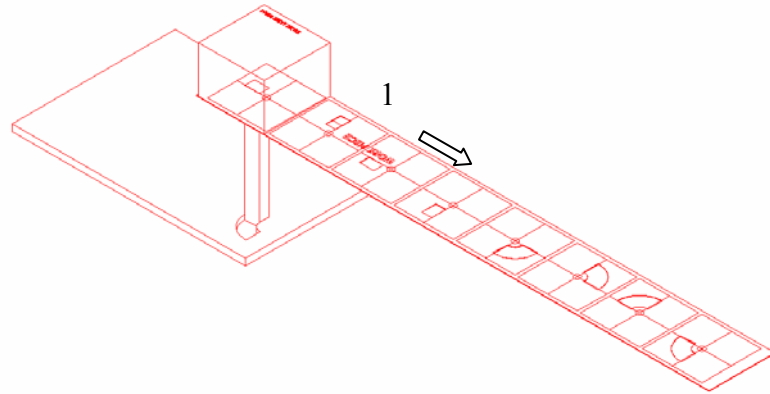
The substrate and mask were mounted on separate planar stages that are capable of moving in both X and Y directions independently (Stages are not shown for clarity). A uniform, square beam ($10 \times 10 \text{ mm}^2$) at the plane of a mask is static during the whole machining process (Figure 6.18). Step 1 shows the schematic of beam size equal to the maximum possible size of a single opening at the mask ($10 \times 10 \text{ mm}^2$). A row of metal-shim mask with eight patterns needed to produce a whole device is also shown in Figure 6.18, Step 1, and can be easily produced by Nd:YAG laser operating in direct-write mode. The patterns are all equally spaced with a pitch distance P and aligned along one axis.

Step 1: Firstly, a proper alignment of the mask to the stage is achieved using the alignment camera. Then a mask pattern 1 (0-90 degrees) is moved under the static laser beam and a train of pulse shots applied to the substrate. Both substrate and mask are held stationary during firing process. Static laser beam position was chosen for a CN position in this example.



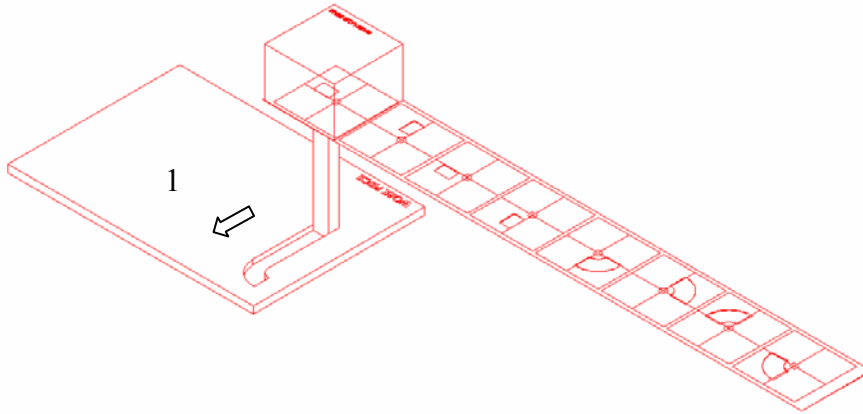
Step 1: Mask pattern 1 (0-90 degrees).

Step 2: Mask stage was moved in direction 1 for a distance $7P$ to bring mask pattern 8 to the CN position. A rectangular mask pattern was designed to include the size of the overlap and was brought to the CN position, perfectly aligned and ready for workpiece-dragging of the first serpentine straight channel.



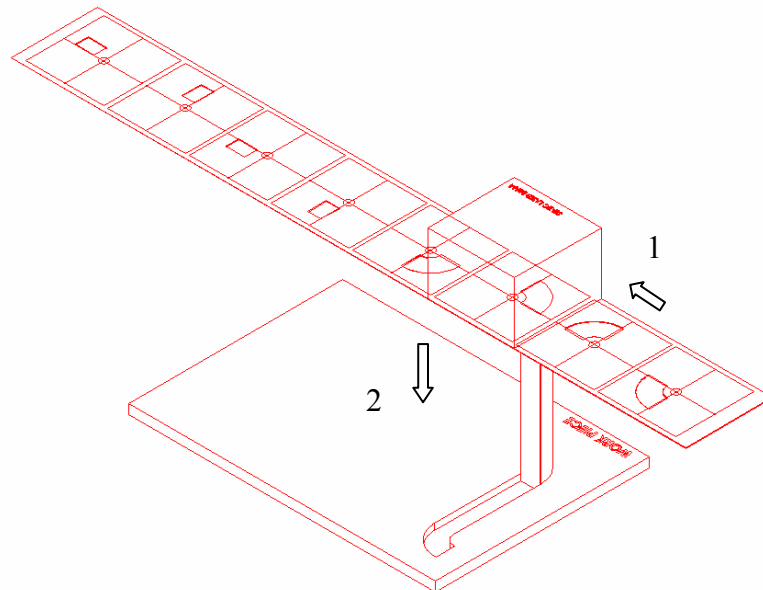
Step 2: Mask pattern 8.

Step 2(a): Workpiece-dragging of the first straight channel is completed by relative motion of workpiece stage in direction 1 of the workpiece.



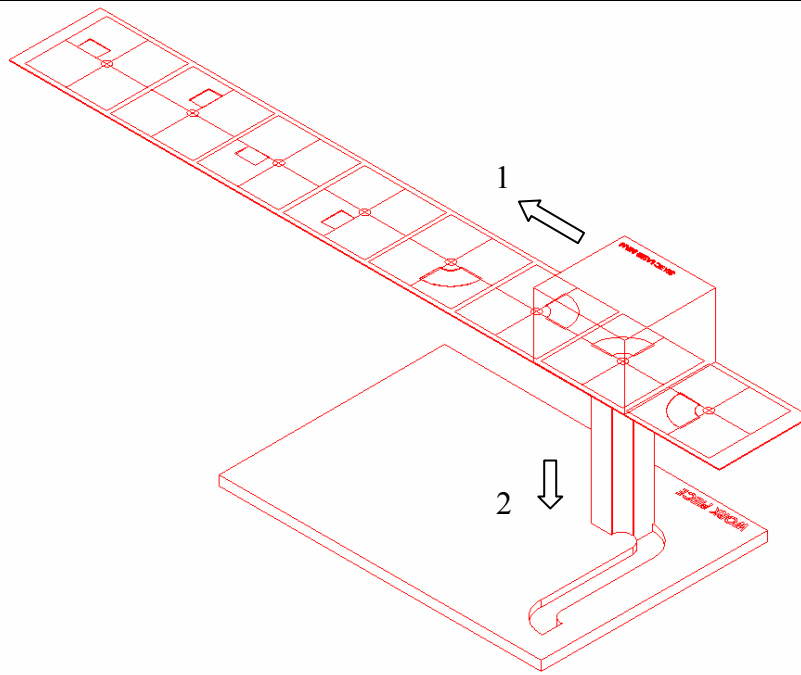
Step 2(a): Mask pattern 8.

Step 3: Relative motion of mask stage in direction 1 for a distance $5P$ brought mask pattern 3 in CN position. Direction 2 shows how mask pattern 3 was applied.



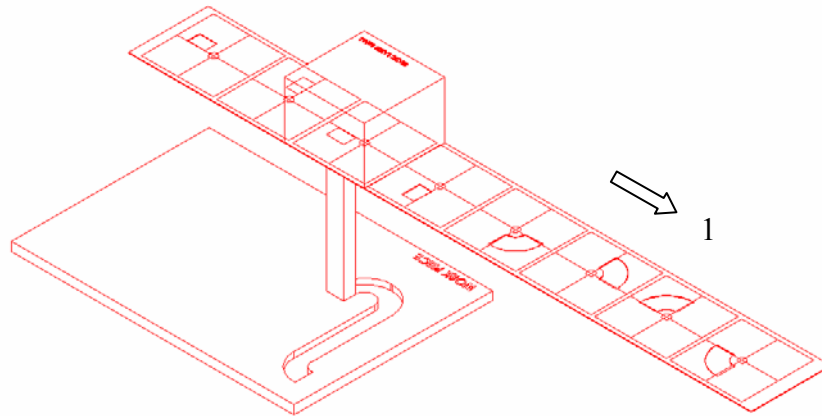
Step 3: Mask pattern 3 (180-270 degrees).

Step 4: Mask pattern 2 is moved to position by relative motion of mask stage in direction 1 for a distance P . Direction 2 shows how mask pattern 2 was applied.



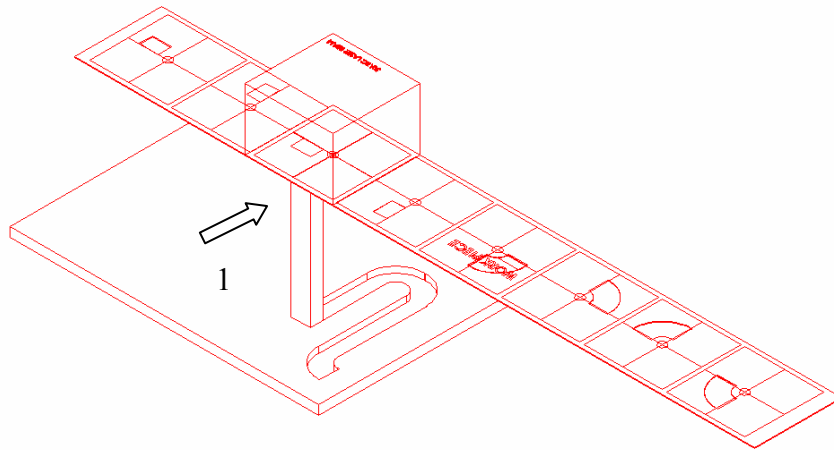
Step 4: Mask pattern 2 (270-360 degrees).

Step 5: Relative motion of mask stage in direction 1 for a distance $4P$ brought mask pattern 6 in CN position.



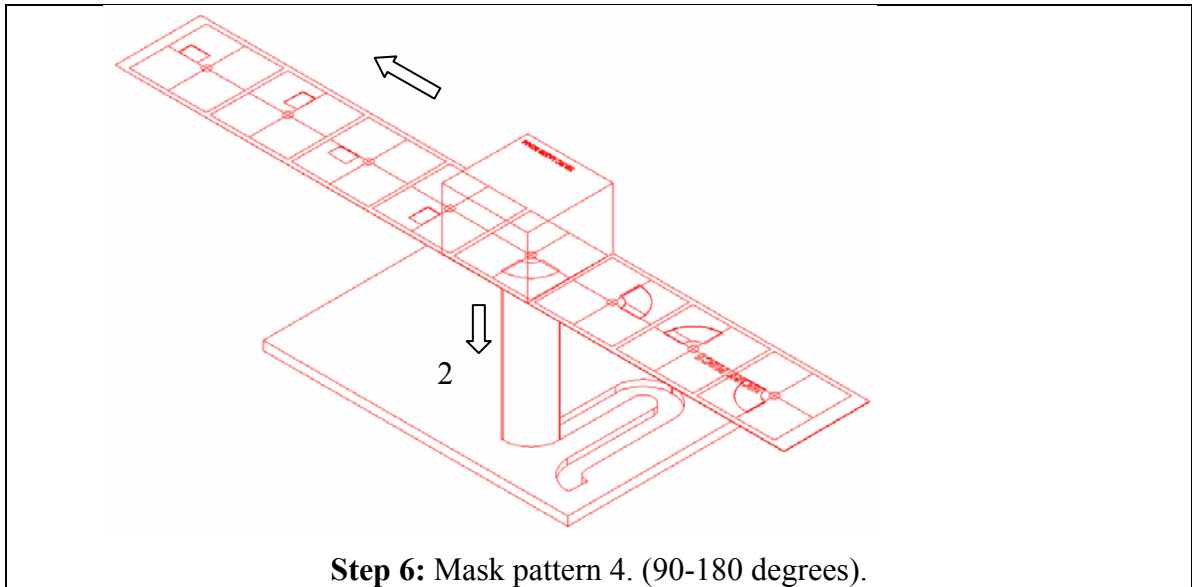
Step 5: Mask pattern 6.

Step 5(a): Workpiece-dragging of second straight channel is completed by relative motion of workpiece stage in direction 1.

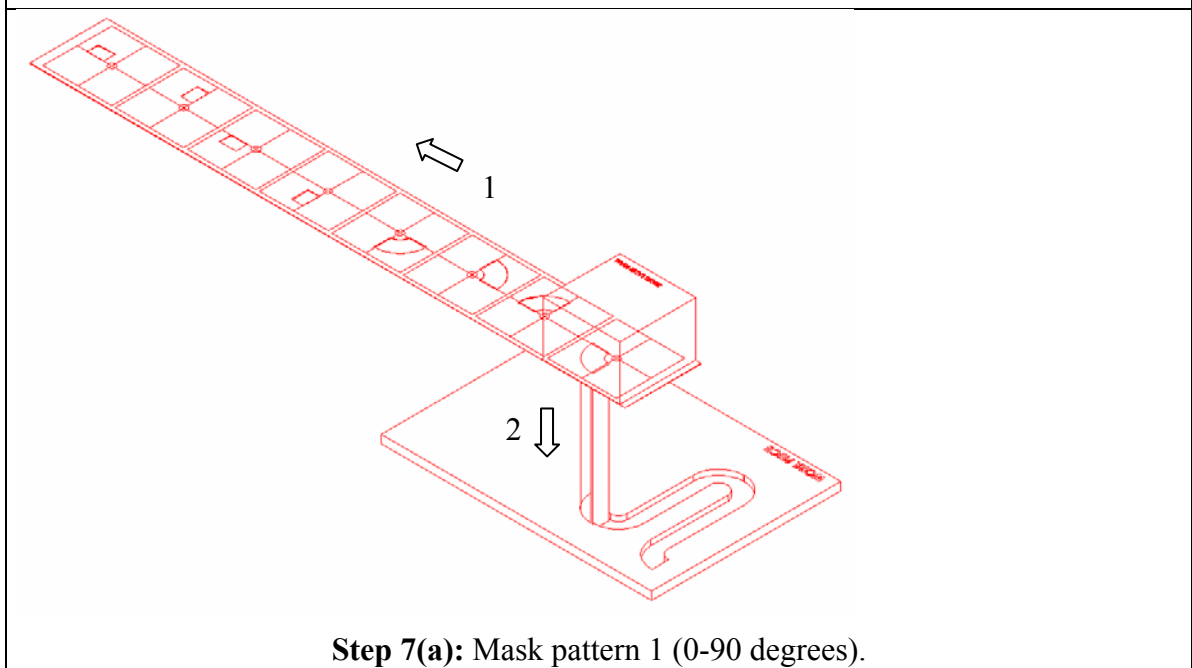


Step 5(a): Mask pattern 6.

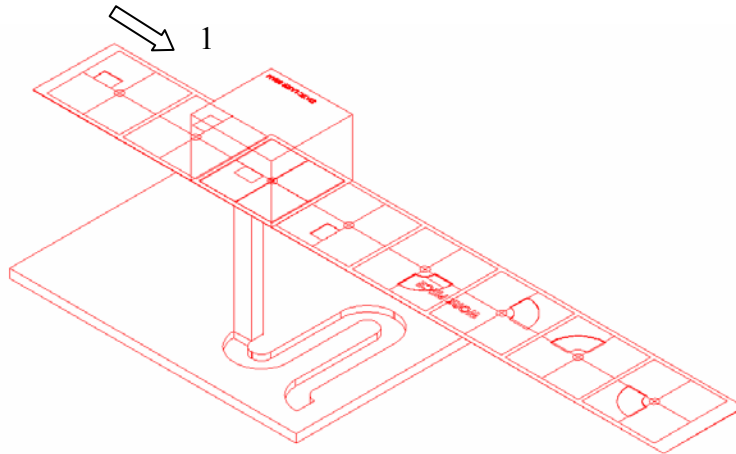
Step 6: Relative motion of mask stage in direction 1 for a distance $2P$ brought mask pattern 4 in CN position. Direction 2 shows how laser beam was applied.



Step 7(a): Relative motion of mask stage in direction 1 for a distance $3P$ brought mask pattern 1 in CN position. Direction 2 shows how mask pattern 1 was applied.

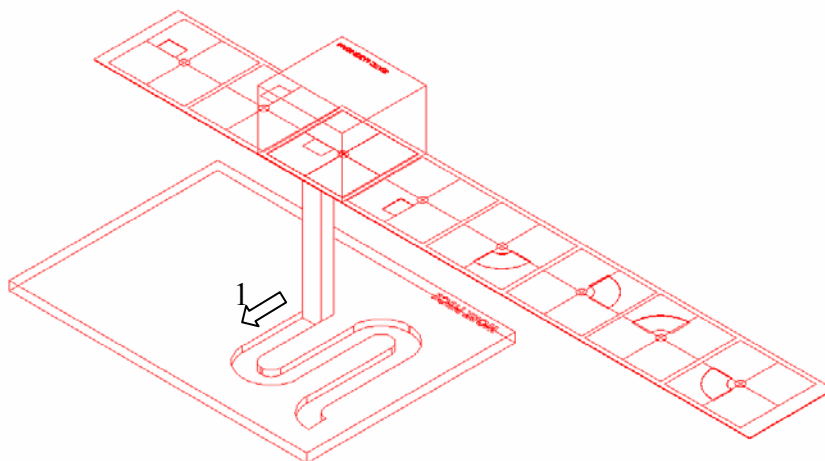


Step 7 (b): Relative motion of mask stage in direction 1 for a distance $5P$ brought mask pattern 6 in CN position.



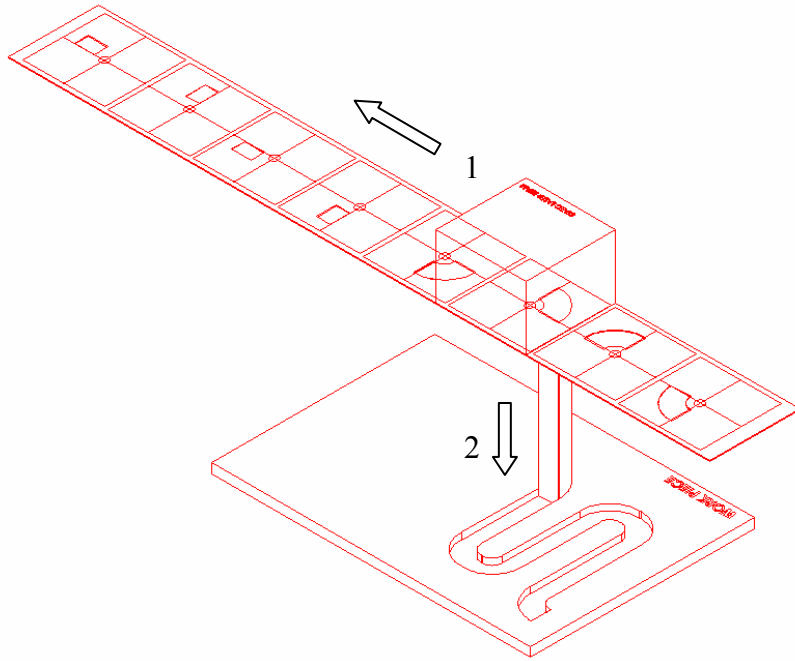
Step 7 (b): Mask pattern 6.

Step 8: Relative motion of workpiece stage in direction 1 was completed using workpiece-dragging of the third straight channel.



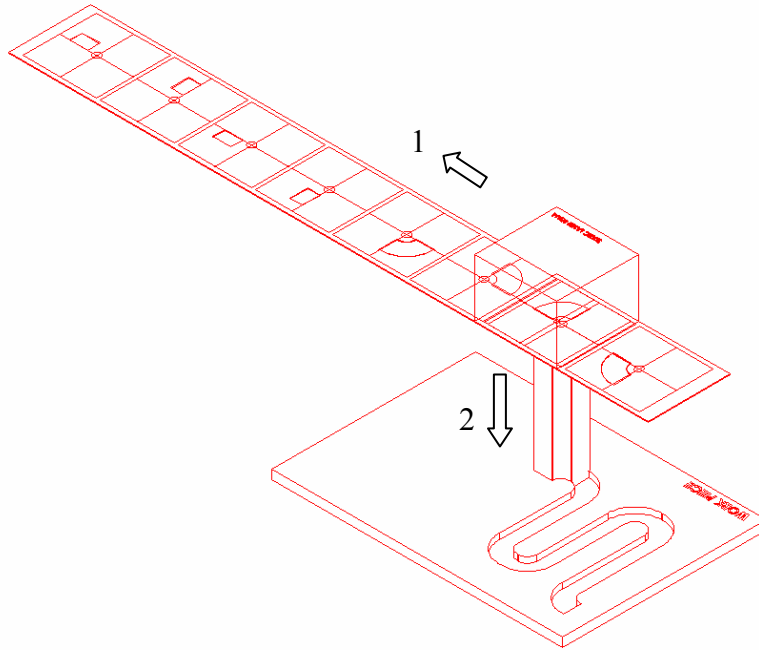
Step 8: Mask pattern 6.

Step 9: Relative motion of mask stage in direction 1 for a distance $3P$ brought mask pattern 3 in CN position. Direction 2 shows how mask pattern 3 was applied.



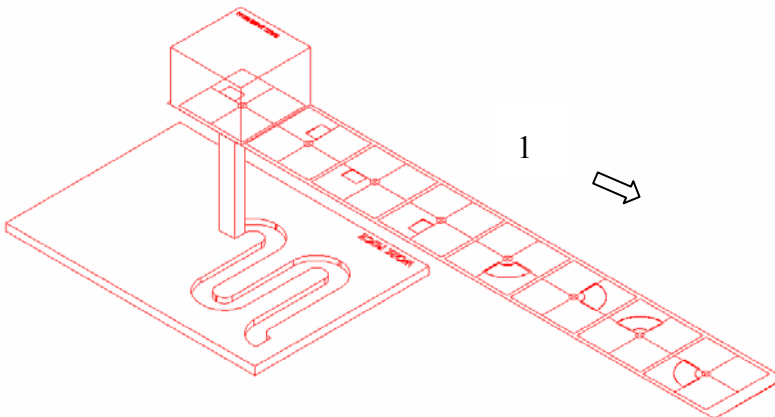
Step 9: Mask pattern 3 (180-270 degrees).

Step 10: Relative motion of mask stage in direction 1 for a distance P brought mask pattern 2 in CN position. Direction 2 shows how mask pattern 2 was applied.



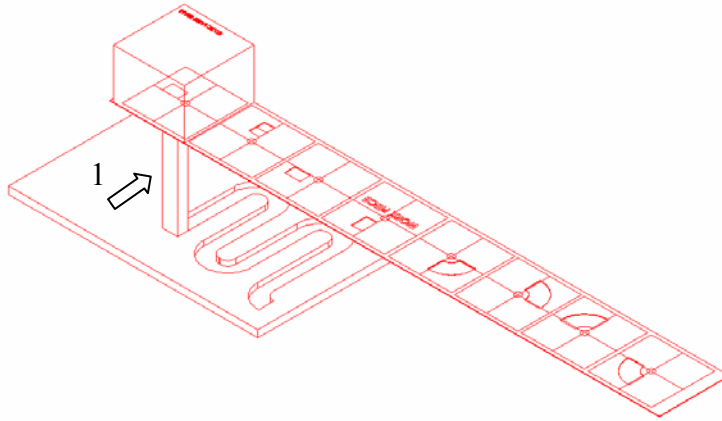
Step 10: Mask pattern 2 (270-360 degrees).

Step 11: Relative motion of mask stage in direction 1 for a distance $6P$ brought mask pattern 8 in CN position.



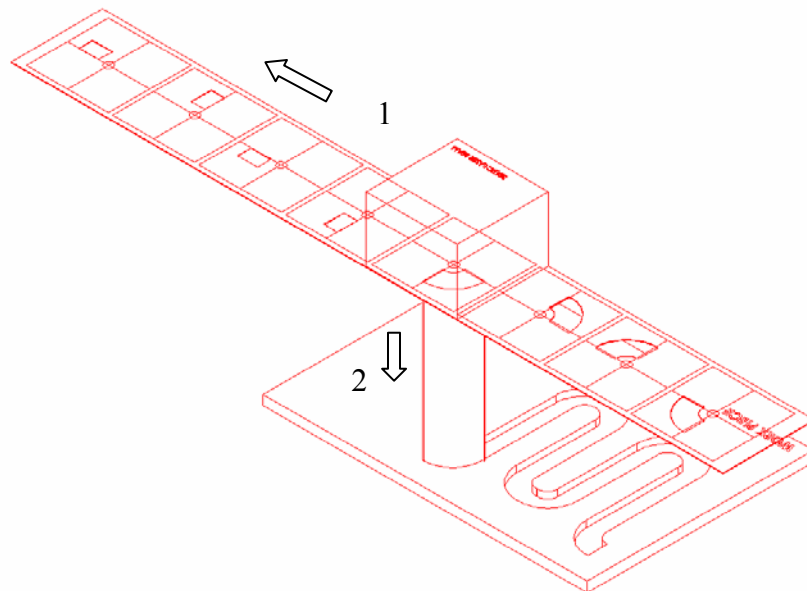
Step 11: Mask pattern 8.

Step 11(a): Relative motion of workpiece stage in direction 1 completed workpiece-dragging of the fourth straight channel.



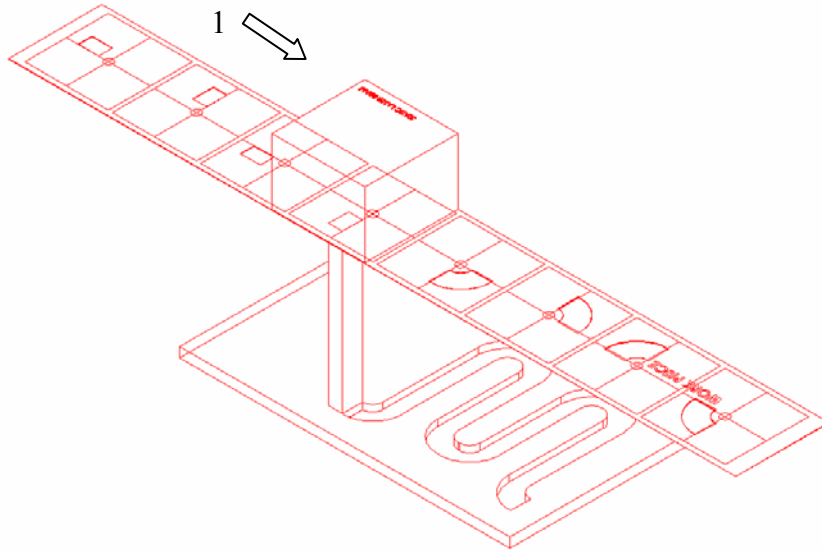
Step 11 (a): Mask pattern 8.

Step12: Relative motion of mask stage in direction 1 for a distance $4P$ brought mask pattern 4 in CN position. Direction 2 shows how mask pattern 4 was applied.



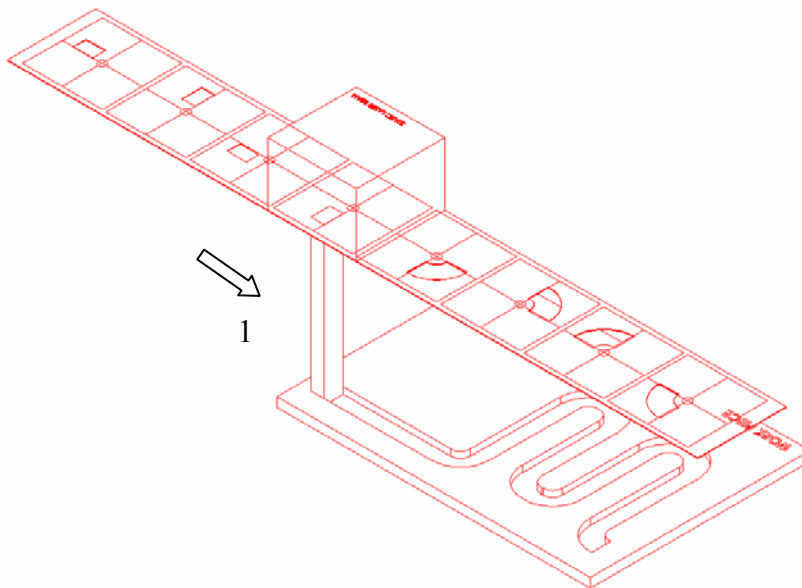
Step 12: Mask pattern 4 (90-180 degrees).

Step 13(a): Relative motion of mask stage in direction 1 for a distance P brought mask pattern 5 in CN position.



Step 13(a): Mask pattern 5.

Step 13(b): Relative motion of workpiece stage in direction 1 completed workpiece-dragging of last straight channel.



Step 13 (b): Mask pattern 5.

Figure 6.18: Steps 1-13 to fabricate serpentine structure using CN method.

6.7 Summary

A flexible and improved mask design and machining technique was presented and demonstrated. The mask design stage incorporates the necessary offsets, removes the need for realignment and reduces the amount of programming work. This method enables improvements in speed and accuracy when manufacturing standard microfluidics structures. The system has been implemented in a new 2D CAD software tool specially developed for the excimer laser ablation process. The tool enables easy fabrication of microstructures of complex microfluidic circuits using a series of patterns in the mask coupled with a layout feature to draw the circuit. A converter utility program enables microstructures designed in the CAD system to generate NC code that is suitable for the excimer laser machine (Exitech S8000 with Unidex 500 Controller, Aerotech Inc). Also, a set of standard masks can be created that can be used for multi-purpose design requirements as demonstrated with a serpentine mask design.

The approach is limited by the laser beam size and is only applicable for 2.5 D microstructures designs.

This technique was explained in greater detail using two examples: the machining of a Y-shape microfluidics device, and the machining of a common microfluidics serpentine structure.

Chapter 7. Case Study: *Fabrication of a Microfluidic Device For Cell Transportation*

7.1 Overview

This chapter reports on a case study to evaluate the performance of the developed CAD/CAM system. The first part of this chapter, section 7.2, covers the design and microfabrication of a microfluidic device for biological cell transportation using a network of micro-channels, followed by section 7.3 where two different concept designs were presented. Section 7.4 discusses the results and compares the actual machined structure data with CAD model data. The details of this case study that explain the development and testing of a second design concept are presented in section 7.4.2. Finally, in section 7.5 the results of this chapter are summarised.

7.2 Cell Transportation Device

The cell transportation device in this study is made up of a network of microfluidic channels. Two designs are reported here, one design incorporates obstacles, which are used to direct the flow of cells whilst allowing a relatively unimpeded flow of the carrier fluid. The various geometric features, including the obstacles, were chosen because the laser machining would pose a challenge using existing NC-code programming techniques. The two-microfluidic concept designs were developed using the CAD/CAM system described in chapter 3, and subsequently tested to determine the system's performance in terms of enabling rapid design changes and its flexibility in prototyping. Typical micro channel designs included channels 50-100 μm deep and 50 μm wide with non-vertical sidewalls.

7.3 Microfluidics System Design using the CAD/CAM Tool

Two microfluidics systems designs were selected for modelling: (1) has in-line obstacles (Design 1), and (2) has a circular layout (Design 2). The 2D schematic structure of the microfluidics device with in-line obstacles is shown in Figure 7.1.

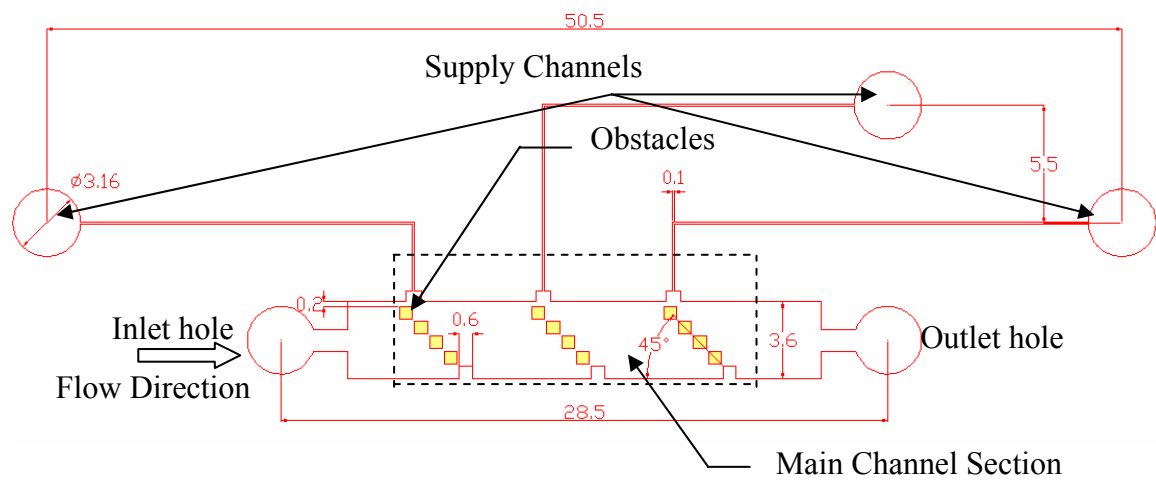


Figure 7.1: 2D model representation of Design 1 - a microfluidic device for cell transportation (in-line obstacles). All dimensions are shown in millimeters after 10x demagnification.

Figure 7.2 shows a circular layout design as a second concept design.

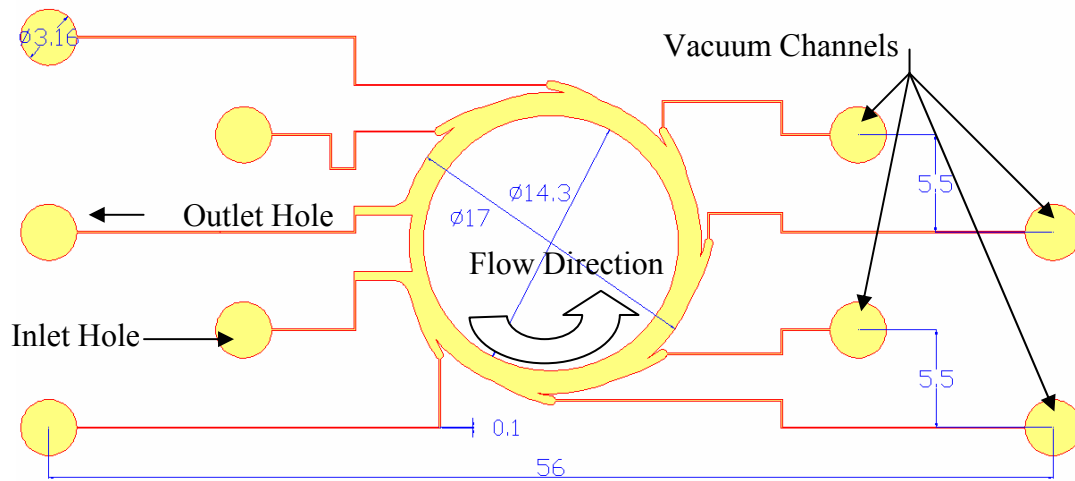


Figure 7.2: 2D model representation of Design 2 - a microfluidic device for cell transportation (circular layout). All dimensions are shown in millimeters after 10x demagnification.

7.4 Comparison between CAD Models and Machined Structures

The aim of this experimental work was to compare the lateral and vertical dimensions determined by the CAD models with the achieved dimensions of the structures after laser micromachining using the NC code produced by the Ex-Expv1.0 system. The other parameters of interest were; wall angle, stitching errors, and edge error and they are also discussed. The experimental set up to evaluate the CAD/CAM system was described in Chapter 3 (section 3.7).

7.4.1 In-line Obstacles - Design 1

Figure 7.3 shows the confocal microscope image of part of the machined polycarbonate structure (Design 1 – detail of channel with obstacles), taken in the indicated area in Figure 7.1 by the dashed box. The largest feature is 600 μm wide. The square obstacle features were designed with straight 90° walls in relation to horizontal

flow direction to avoid aliasing error normally introduced when features were produced using a square mask algorithm.

Figure 7.3 represents a part of the channel (center distance between main inlet and outlet hole of channel equals to 28.5 mm) with 3 columns of square barriers in a staircase arrangement (45°) to direct flow of cells towards one of the sides of the main channel (1800 μm). This way the flow of individual cells can be controlled or directed, since, only cells with a size smaller than 100 μm can travel through the channel. Figure 7.3 was created using the special features of the LSCM software called Multiple Image Alignment (MIA). This feature enabled stitching together a matrix 4x4 of adjacent images taken with a high magnification objective to generate a stitched image of a much larger area with the same magnification.

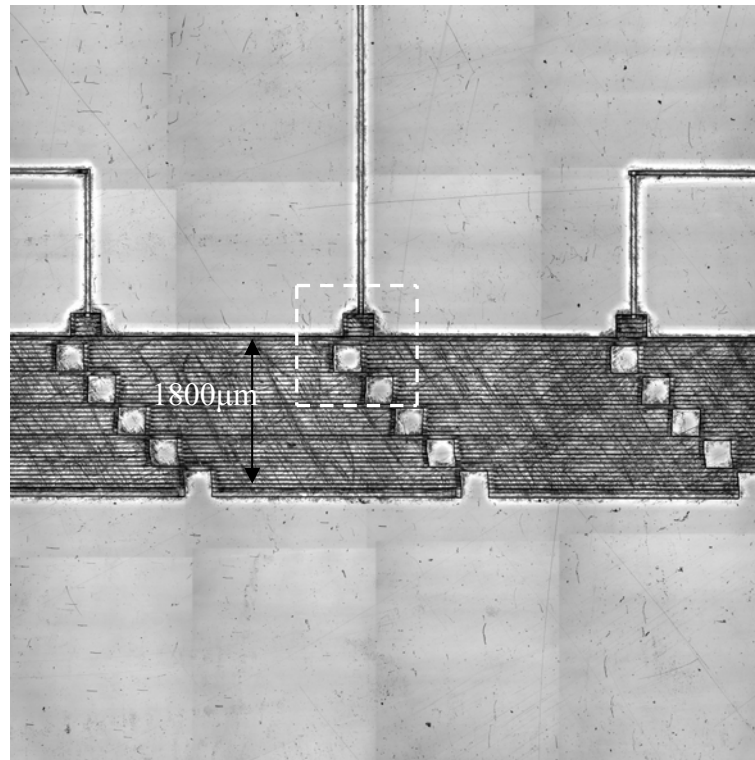


Figure 7.3: 2D LSCM image of micro fluidic device for cell transport – Design 1 produced by workpiece-dragging technique using NC code generated by Ex-Expv1.0.

Process parameters: $F_d = 1.1 \text{ J/cm}^2$, $PRF = 50\text{Hz}$, $n = 25$, material:PC.

This design was machined with frequency $PRF = 50\text{Hz}$, number of pulses $n = 25$, and fluence $F_d = 1.1 \text{ J/cm}^2$. The machining depth was measured using an optical microscope and was approximately $12 \pm 5 \text{ }\mu\text{m}$. This gave an etch rate of $0.48 \text{ }\mu\text{m/pulse}$. (Etch rate from literature for polycarbonate is between $0.35\text{-}0.5 \text{ }\mu\text{m/pulse}$). Taking into account instrumental measurement errors and fluence variations of the laser system set up of $\pm 10\%$ this result was in accordance with literature. Similar depth values were measured using the LSCM.

Figure 7.4 shows a detail view of part of the design 1 concept, taken in the indicated area in Figure 7.3 by the dashed box. Dimensions are all expressed in microns and created using the CAD module of the Ex-Expv1.0 system (internal link to Solidworks GUI).

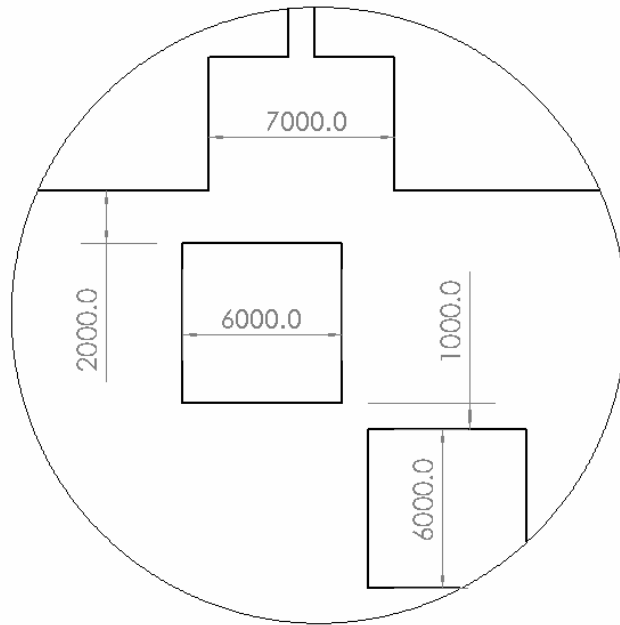


Figure 7.4: A detail view of 2D CAD model of Design 1 with lateral dimensions (μm) for comparison, taken in the area indicated in Figure 7.3 by the dashed box.

Figure 7.5 shows the same detail as Figure 7.4 scaled down by ratio 1:2 by the ExExpv1.0 system and then scaled down 10x by the demagnification lens of the S8000 laser system. This is a limitation of the current version of the Ex-Expv1.0 system where

only a range of 1, 2, 4 and 8 mm mask sizes can be used for NC code generation. If smaller size mask need to be employed, as in the sample above, the system has the option to scale down the complete design created for the mask size of 1 mm by half and then the 0.5 mm mask can be used. However, the produced structure will also be scaled down by half. Hence, this particular design stretched the capabilities of the Ex-Expv1.0 system to its limits. Also, one of the design requirements was that depth of channels is 50 - 100 μm . To achieve this depth the ExExpv1.0 system would require at least 500 pulses per area, a *PRF* of 80Hz and a fluence of 1.1 J/cm². If the workpiece-dragging method is to be used for aforementioned process parameters, then in accordance with equation 2.6 (Chapter 2, section 2.5.2..2), the workpiece-stage velocity speed would be equal to 0.48 mm/min. On the other hand the minimum speed of the workpiece-stages for the current laser system setup (Chapter 3 section 3.7.4) for a stable operation must be at least 3 mm/min. Even with this speed, the processing time for the Design 1 would be extremely long and not practical to run. Hence, for the purpose of the experiment to demonstrate that system is capable of producing this design it was decided that less demanding process parameters were to be used ($n = 25$, *PRF* = 50Hz) to be able to produce the whole structure within a reasonable time framework of 45 minutes, but sacrifice the depth of structure. This of course resulted in a ablation depth of $12 \pm 5 \mu\text{m}$ that was far from the design requirements, but considering that this gave an etch rate of 0.48 $\mu\text{m}/\text{pulse}$, and comparing this with data available from literature for polycarbonate, it can be expected that the desired depth would be achieved if the laser system was setup to run long enough.

Figure 7.5 also shows various measurements taken by the LSCM to verify lateral dimension accuracy for the features fabricated using the excimer laser ablation and NC part program generated by Ex-Expv1.0 system. It was found that the accuracy was in the range of $\pm 2 \mu\text{m}$ without taking into account the influence of the wall angle. The image size used to produce these features was 50 μm square. It is also noticeable that 50 μm gap size between square obstacles in the main channel was easily achieved and this matched exactly with the gap size requested by CAD model.

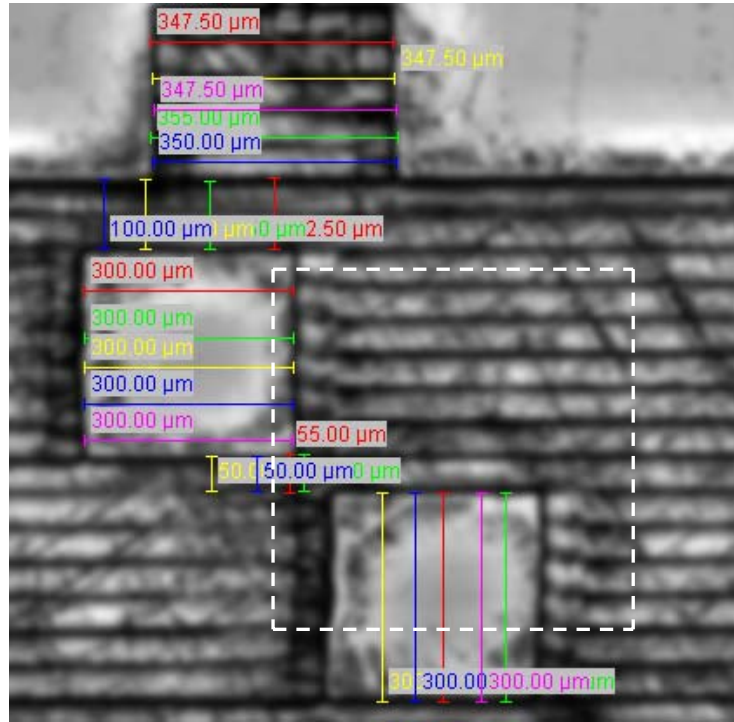


Figure 7.5: 2D LSCM image of microstructures produced by excimer laser micromachining, with lateral dimensions for comparison. The detail is taken in the indicated area in Figure 7.3 by the dashed box.

Figure 7.6 shows that square feature obstacles had a saw-tooth effect along the vertical side walls, and after investigation it was determined that this effect was due to a problem associated with the machine controller where the work piece stages moves first before the laser actually starts firing the pulses. Hence, the adjustment of the Ex-Expv1.0 software system was necessary to accommodate for this case.

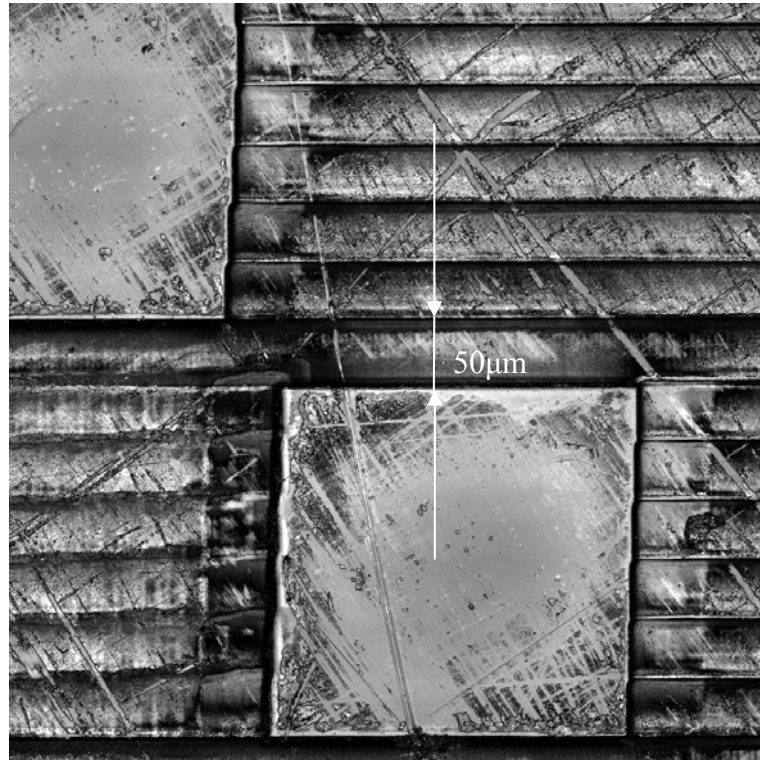


Figure 7.6: 2D LSCM image showing saw-tooth effects, i.e. a problem of straightness along the square feature vertical sides. The detail taken is indicated area in Figure 7.5 by the dashed box.

A stitching error of $8.8 \pm 2.1 \mu\text{m}$ wide and $6.1 \pm 2.3 \mu\text{m}$ high was measured when the overlap size between adjacent volumes was zero ($OL=0$), when ablating $50\mu\text{m} \times 50\mu\text{m}$ features in PC at a fluence $F_d = 1.1 \text{ J/cm}^2$ using the workpiece-dragging technique. This can be also observed in Figure 7.6. Further optimization of stitching error was not carried in these experiments because the focus was more on the rapid prototyping aspect of this work. The edge errors were determined by the image size of $50\mu\text{m} \times 50\mu\text{m}$ because only one mask pattern size was used to machine this sample.

Another section of machined structure is shown in Figure 7.7, which was used for wall angle measurements.

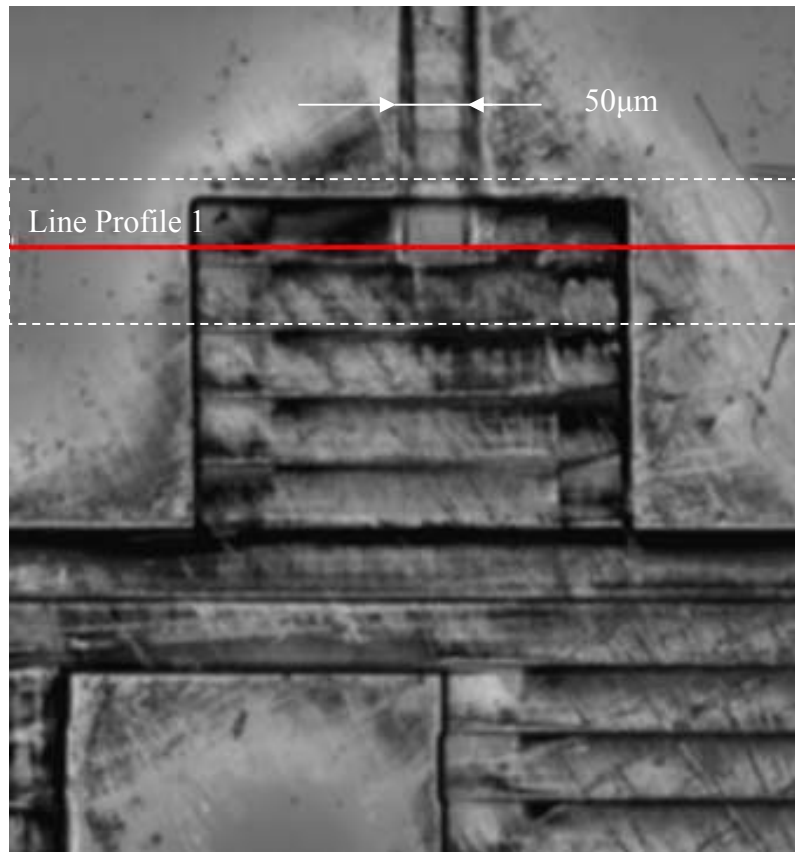


Figure 7.7: 2D LSCM image showing locations for wall angle measurements. The detail taken in the indicated area in Figure 7.3 by the dashed box.

Figure 7.8 shows a typical cross-sectional view of the channel where the width of the channel at top surface and width of the channel on the bottom surface were used to determine the size of the wall angle (non-vertical sidewalls). The values of the measurements taken at the points shown in Figure 7.8, and produced by LSCM are summarised in Table 7.1.

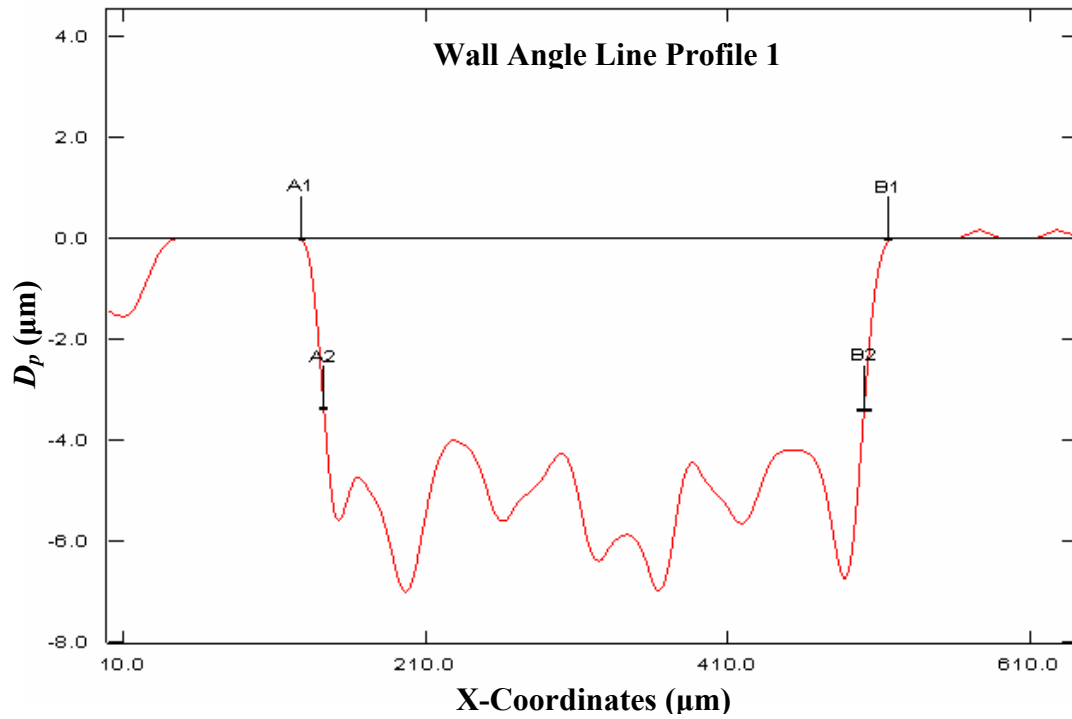


Figure 7.8: LSCM cross-sectional wall angle line profile 1. Line profile 1 was taken in the highlighted area in Figure 7.7 by the dashed box.

Table 7.1: Wall angle measurements data along line profile 1 as shown in Figure 7.8.

A1B1 (μm)	A2B2 (μm)	$D_{p\theta}$ (μm)	Wall Angle θ (°)
366.7	355.4	3.5	58

From the data shown in Table 7.1, and by using equation 4.8, the wall angle $\theta = 58^\circ$. One of the reasons (besides fluence) for the high value of tapered wall angle $\theta = 58^\circ$ was as explained previously in Chapter 5 where it was shown that wall angle changes with the depth of the ablation, i.e., the deeper the structure the steeper the wall angle. Here, the ablation depth measured was only ($D_p = 12 \pm 5 \mu\text{m}$).

7.4.2 Circular Layout - Design 2

Figure 7.9 shows a 3D model of a circular layout design based on the principle of centrifugal fluid dynamics. The CAD model is parametric and can be easily changed to suit design requirements using the newly developed CAD/CAM system.

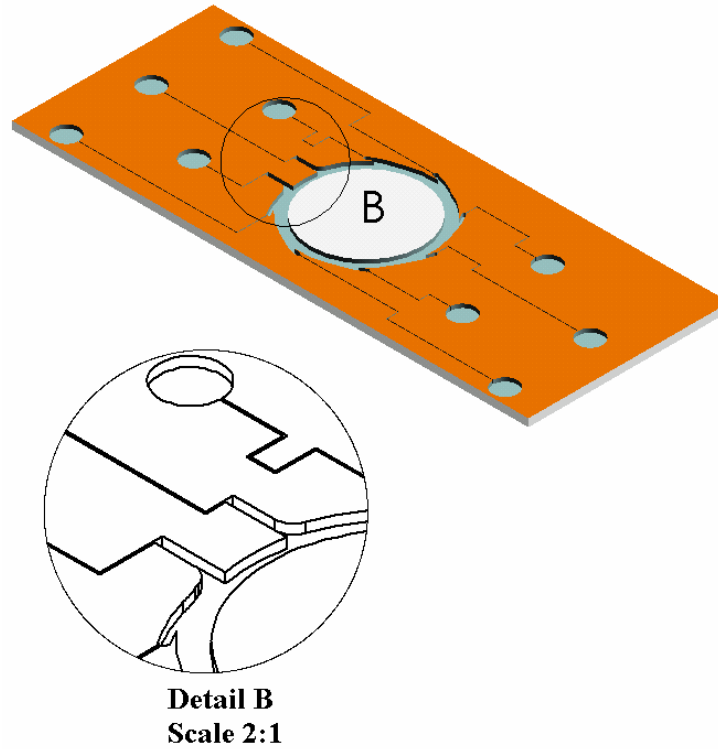


Figure 7.9: 3D model of Design 2 (Circular) produced by developed CAD/CAM system.

Figure 7.10 is generated using the MIA image module of LSCM microscope. It shows a 2D image of the circular concept design generated by LSCM microscope. It is important to notice here that Design 2 has also been scale down by ratio 1:2 by the ExExpv1.0 system and then scaled down 10x by the demagnification lens of the S8000 laser system. Conventional chrome on quartz lithography mask with a square feature pattern of 0.5 mm was used to produce a 50 μ m image size at the workpiece. The same process conditions were employed as for the machining of the Design 1 ($n=25$, $PRF = 50\text{Hz}$, $F_d = 1.1 \text{ J/cm}^2$). But this time to achieve the design required depth it was decided

that after the whole structure was machined once, the same process was repeated another four times. This actually means that total number of pulses per area applied was 125 which gave an etch rate of $0.52 \mu\text{m/pulse}$.

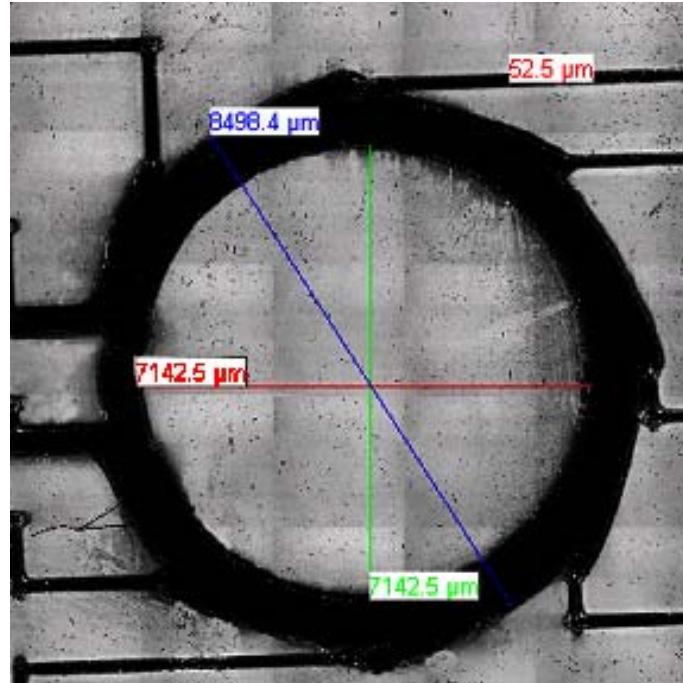


Figure 7.10: 2D LSCM image of a micro fluidics device for cells transportation (Design 2 - circular layout). Process parameters: $F_d = 1.1 \text{ J/cm}^2$, $PRF = 50\text{Hz}$, $n = 25$, material:PC.

Typical trapezoidal shaped channels were generated with a depth of $65 \pm 3.2 \mu\text{m}$ and a width of $54 \pm 2.6 \mu\text{m}$ at the top and $42 \pm 2.7 \mu\text{m}$ at the bottom. The total laser machining time was 55 minutes for one pass. Figure 7.10 also shows various measurements taken by the LSCM to verify lateral dimension accuracy for the features fabricated using the excimer laser ablation and NC part program generated by Ex-Expv1.0 system. It was found that the accuracy was not as good as it was in case of Design 1 and this was expected because the circular edges were hard to produce by the square mask algorithm, and this directly contribute to increase in aliasing errors. The accuracy for Design 2 was in the range of $\pm 7.5 \mu\text{m}$ measured on the internal circular

edge. The value of the outside diameter was measured with difference of $\pm 3.2 \mu\text{m}$ from designed requirements.

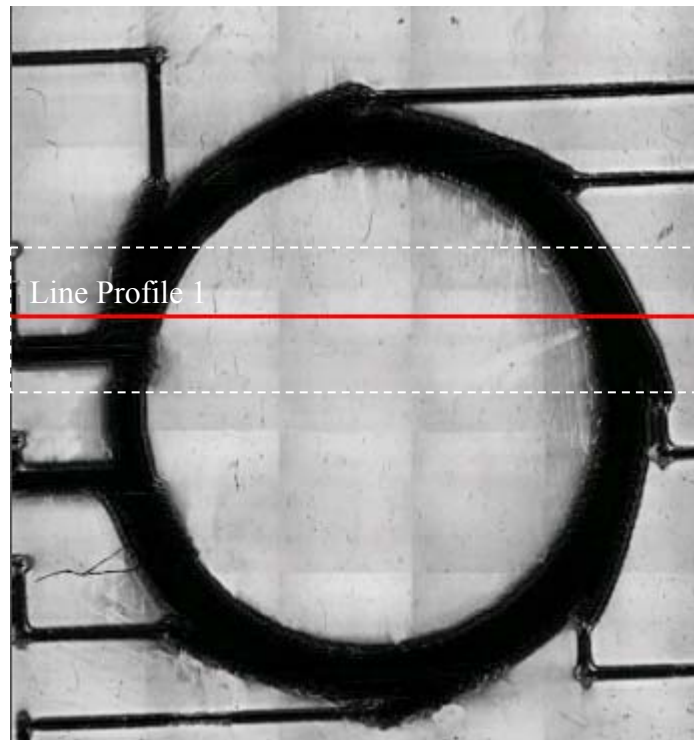


Figure 7.11: 2D LSCM image showing locations for wall angle measurements.

Figure 7.12 shows a typical cross-sectional view of the channel where the width of the channel at top surface and width of the channel on the bottom surface were used to determine the wall angle (non-vertical sidewalls). The values of the measurements taken along line profile shown in Figure 7.11, and produced by LSCM are summarised in Table 7.2.

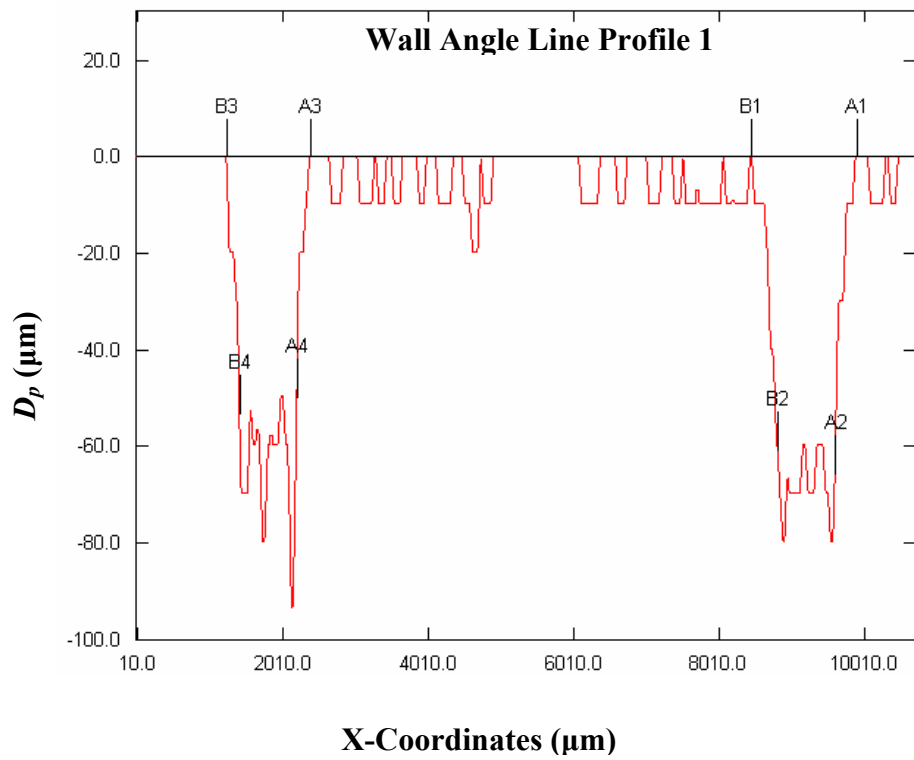


Figure 7.12: LSCM cross-sectional wall angle line profile 1. Line profile 1 was taken in the highlighted area in Figure 7.11 by the dashed box.

Table 7.2: Wall angle measurements data along line profile 1 as shown in Figure 7.12.

A1B1(μm)	A2B2(μm)	D_{pθ} (μm)	Wall Angle θ (°)
1055.3	998.2	59.8	25
A3B3(μm)	A4B4(μm)	D_{pθ} (μm)	Wall Angle θ (°)
1006.3	980.2	57.7	12

The ablation depth $D_p = 65 \pm 3.2 \mu\text{m}$ was observed and wall angle θ of 12° and 25° . This was in agreement with relationship between ablation depth and wall angle stated previously because the increased depth of ablation contributed to a much steeper wall angle this time. Also, a variation in depth was observed causing the wall angle to change as well. Several factors can produce this effect such as; beam inhomogeneity, pulse-to-pulse energy variation of $\pm 10\%$ and even sample material inhomogeneity.

A stitching error of $32.4 \pm 3.2 \mu\text{m}$ wide and $18.4 \pm 2.2 \mu\text{m}$ high was observed with the overlap size $OL=0$ (type 1- only “peaks” errors), when ablating $50\mu\text{m} \times 50\mu\text{m}$ features in PC at a fluence of 1.1 J/cm^2 using the workpiece-dragging technique and NC code produced by Ex-Expv1.0.

Aliasing errors effects were more prominent and harder to avoid because the circular edges were approximated using the square mask algorithm.

7.5 Summary

The purpose of this chapter was to demonstrate the performance and advantages of using the new developed CAD/CAM system for excimer laser micromachining for quick prototyping and microfabrication of complex microfluidic structures. Some complex designs that previously required substantial user effort to complete have been produced with NC code generated in a few minutes by experienced users of the system. It was also possible to demonstrate the accuracy of the NC code by comparing the lateral dimensions determined by the CAD model and measured values of the machined structure produced by LSCM. The results show good agreement between CAD model data and laser machined parts with dimensional accuracy of $\pm 2 \mu\text{m}$ (Design 1).

The main limitation of the system was use of the square mask algorithms to produce sloped structures, and this lead to aliasing errors as in the case of Design 2 where circular edges were a design requirement. The dimensional accuracy was between $\pm 7.5 \mu\text{m}$ at internal circular edges and $\pm 3.2 \mu\text{m}$ at outside diameter of the structure, while the dimensional accuracy of the supply channels was still $\pm 2.5 \mu\text{m}$. These effects particularly influenced the quality of the machined structure when the size of the edge features

approached the size of the mask image ($50\text{ }\mu\text{m} \times 50\text{ }\mu\text{m}$) at the substrate (Design 2). This led to a design with features with vertical sides (90°) in relation to horizontal flow (Design 1). Flow chart with main input and output parameters (for both cases: Design 1 and Design 2) for each CAD/CAM system module used are illustrated in Appendix C.

The CAD/CAM system provides a new tool for rapid changes in microstructure 3D model design. NC programs are generated in few minutes for complex 3D microstructures (see further examples in Appendix B), that are not possible, or are tedious and error prone using current systems. The system interfaces to a SolidWorks GUI environment and design tools for easy and flexible design and visualization. The time from the concept stage to final prototype development was significantly reduced from several days, or hours, to 30 minutes or much less for an experienced user of the system. However, the laser machining time was still long when severe machining requirements were imposed (*PRF* above 70Hz and workpiece-dragging technique), but this can be justified by the time saved on the actual design of the product itself, especially if changes to design are constantly required.

Chapter 8. *Conclusions and Further Research*

8.1 Overview

The research presented here involved the development of a CAD/CAM system for excimer laser mask projection micromachining to automate NC program creation and improve the quality of the microstructures. This was achieved using a unique combination of commercially available software and spatial algorithms developed in this research to suit such a unique machining process. This chapter presents the contributions in section 8.2, section 8.3 covers the limitations of the research, and section 8.4 outlines recommendations for future research to extend this study and improve on the developed algorithms and CAD/CAM system.

8.2 Contributions of the Research

The CAD/CAM system has data exchange capabilities based on the commonly used STL (Stereo Lithography) file format. A significant improvement over existing approaches is that this system enables the use of CAD data from most commercial CAD packages on the market. Algorithms were developed to extract the 3D geometry from STL files and convert the information into layered tool path information. This function permits CAD models to be used directly in the NC part programming stage. The CAM component of the system is used to convert the CAD models into NC data (part programs) compatible with the laser system's (S8000, Exitech,UK) CNC controller.

The STL file approach enabled approximation of any 3D surface and after slicing of the structure created the way for 3D microstructures to be machined using excimer laser machining process. However, as the STL file is based on a triangular approximation process where each surface is represented as a mesh of triangles, and if certain conditions are not met, the file will contain redundancy data that will result in an inaccurate model

representation. In order to overcome these difficulties an alternative approach was developed based on the Bit-Map file. This approach is more suitable to the excimer laser micromachining process, which is in its nature 2D and binary, and an analogy can be drawn between laser micromachining principle and raster graphics theory.

The system contains a unique database of optimised processing parameters, enabling the production of microstructures from a range of different materials including: Polyethylene terephthalate (PET) and Polycarbonate (PC). The user is able to override and modify the optimised processing parameters. Optimisation processes were carried out using Taguchi Design of Experiments technique. The database is used to set machining process parameters when creating part programs. The system implements the following optimised experimental parameters that influence the process, to automatically generate a precise NC part program for the excimer laser machine:

- laser fluence F_d [J/cm^2]
- pulse repetition frequency PRF [Hz]
- number of shots per area [n]
- wall angle θ [$^\circ$]
- ablation depth D_p [μm]
- stitching errors [μm]

The system's algorithms are based on a raster-color programming technique, resulting in substantially reduced mathematical complexity and computational time. This is the first time this approach has been used to support direct conversion of 3D geometry from a CAD model into an NC part program compatible with the excimer laser machine (Exitech S8000 with Unidex 500 Controller, Aerotech Inc).

The system also provides other tools, such as a fully integrated 3D design graphic user interface (GUI), easily expandable materials database with optimal processing parameters for most commonly used materials and laser routines including 3D multi-layer machining, step-and-repeat, workpiece dragging, and ramp removal using synchronised

mask scanning. A set of algorithms for pulse number minimization (Star algorithm) and tool path optimization based on a heuristics insertion method has also been incorporated.

These outcomes are outlined below:

- Development of algorithms and methodologies for the two most exploited excimer laser machining techniques (step-and-repeat and workpiece dragging) for automatic part program generation directly from a CAD model.
- Algorithms were developed for two different approaches STL-File approach and Bit-Map File approach to convert CAD model data into tool path information.
- A mathematical model for edge error control has been developed and presented.
- Quantitative and qualitative analysis of stitching error characteristics was carried out for the excimer laser ablation process. The Taguchi Design of Experiments (DOE) method was used for the parameter optimization process, as the number of experiments needed to determine these parameters using other means was impractically high, owing to the large number of parameters involved. The Taguchi method reduced the number of process characterization experiments from 27 to 9. A mathematical model for controlling stitching errors was also implemented in the system. This model relates the width and height of the stitching error to the mask shape and overlap size. The model may be used to determine the optimal overlap size to achieve minimum stitching error.
- Experimental verification of the prototype system was performed using part programs (NC code), directly generated from CAD models, to machine different geometrical shapes and surfaces for evaluation of the system's performance.
- A new mask design and machining strategy named common nest (CN) was developed which has the potential to significantly change how current mask design is carried out. The major advantages of the CN approach are the reduction of mask misalignment errors and the elimination of the need for offsets calculation when using multiple mask patterns to manufacture a MEMS or microfluidic device. The CN approach is suited to 2.5D geometry microstructures, such as microfluidic channel networks.

- Analytical and experimental verification of the CN strategy was carried out by machining two common microfluidics structures and evaluation of the measurements.
- Development of a new 2D CAD software prototype tool to support the CN strategy. The system prototype is a combination of the AutoCAD GUI and a VB converter utility. The AutoCAD interface enables design of origin related mask patterns and can be used to design different toolpaths in accordance with the CN design rules. The VB converter utility converts a DXF file format to NC code suitable for excimer laser CNC controller.
- The effectiveness of the CAD/CAM system was verified by NC part program generation for several 3D microstructures and subsequent machining trials. Excellent agreement was obtained between the laser machined geometries and the microstructure CAD models. A Laser Scanning Confocal Microscope (LSCM) was used to measure the lateral dimensions tolerance of $\pm 2 \mu\text{m}$.
- The system was also successfully used in a practical case study to machine the microchannel network of a cell transportation microfluidic device.

8.3 Limitations of the Research

The scope of this research was restricted to developing algorithms for only square mask patterns. One limitation of the research was the existing excimer laser machine design and laser controller capabilities, which had no additional stages for flexible laser beam shaping system. In addition, the mathematical model for stitching error takes into account only a two-dimensional problem and expresses these errors in terms of width and height of the peak, or troughs, but does not take into account the laser ablation mechanism to calculate the exact volume of material removed with each laser pulse. This was directly responsible for achieving the surface quality (sub-micron range) that is less than adequate for optical applications (< 50 nanometers). Processing speed and superposition of multiple layers to reduce the number of pulses in the vertical axis still need to be completed and improved. The algorithms for other common geometrical shapes (e.g. circles, triangles, rectangles) still need development. A library of standard tools (i.e., for

example library of different mask shapes mapped into a database) can be developed. The system is also based on purely experimental results and measurements that introduce different sources of errors in the final measurements, rather than trying to produce and numerically simulate the laser ablation mechanism and exactly reconstruct the ablated structure.

The common nest (CN) approach to mask design and machining has been limited in its application to 2.5D structures (i.e., microchannel networks in microfluidic devices).

A concept for a debris cleaning cycle was considered but not tested experimentally to determine effectiveness of such a post machining cleaning cycle. This may offer opportunities to improve quality of surface texture if it is investigated.

8.4 Recommendations for Future Research

An accurate numerical model and closed loop system that can feedback information of each laser pulse ablation back into system. This information will directly influence the other laser parameters that has to be adjusted in order to achieve the desired etch rate and ablated profile.

The algorithms for other commonly used laser ablation techniques such as one summarised in literature review chapter (Synchronised Image Scanning in section 2.5.2..2.1 and Synchronised Overlay Scanning in section 2.5.3) can be developed. It is already shown by other researchers [10, 21, 22] that synchronised movement of the mask and workpiece in both axes will result in reduction of stitching error effects.

In addition to the laser system there should also be an engineering workstation with a knowledge base database system that includes both engineering and manufacturing data. A reverse engineering capability including laser-scanning equipment to capture microstructure 3D geometry after each laser pulse being applied and feedback, in real-time, this information to the system before the next pulse or pulse train is due to be applied. This will enable accurate adjustment of the main process parameters and provide better control of the complete process (uniform etch rate). All system modules should be

able to communicate with each other through a GUI and have common exchange data capabilities.

The model for edge roughness could be extended to predict and control 3D surface roughness which may lead to improved surface finishes for optical components applications, or textured surfaces where required (e.g. passive micromixing).

The generation of correct and efficient plans for machining (micro structural) mechanical components requires the identification of features such as holes, slots and pockets, which are associated with distinctive manufacturing processes (i.e., excimer laser ablation). An automatic feature recognizer that extends the state-of-the-art in several directions will be considered as a possible direction for this problem solution. The recognizer decomposes the total volume to be machined into volumetric (i.e. solid) features that satisfy stringent conditions for manufacturability, and correspond to operations typically performed in the excimer laser ablation process.

Future research should include the development of a simulator to display the laser tool path and machined surface to verify the part program and allow changes to the program. This simulator is a feature in conventional CAD/CAM systems for programming computer numerically controlled metal cutting machines. Work has been carried out by [94] in this area, and the work could be integrated with the present system.

Further investigation of the CN approach to producing 3D structures may offer additional capabilities and should be considered.

Currently, CAD/CAM system was specifically tailored for the excimer (pulsed type) laser processing but can be easily modified to suit the other non-excimer laser systems such as: Laser Engineered Net Shaping (LENS) process, Direct writing machining systems (Solid State Nd:YAG and CO₂ lasers), Laser Deposition Systems (LDS) or any other layer-by-layer type laser processing (rapid-prototyping systems). For any layered manufacturing technology, the overall goal of the control software is to take a CAD representation of the part, slice the model into appropriate thickness layers, and create path instructions for the manufacturing equipment. However, it is important to highlight that each of the aforementioned processes have it's own sensitivity to multiple

software controllable parameters such as substrate velocity, border representation and laser fluence.

Finally, predicting debris accumulation and removal could also be studied and modeled.

8.5 Summary

CAD/CAM tools have become increasingly important in MEMS and microfluidics technology, where they are used to design a product, assess the effect of design changes, evaluate manufacturing and reduce the time to market. Achievement of successful micro-engineered structures requires incorporating the microstructure functionality early in design stage. Many research groups are attempting to address this problem, and correspondingly an active CAD community has developed to help scientists and engineers model and understand MEMS devices. While significant advances have taken place in some areas of microengineering, such as lithographic and chemical-etching techniques, a structured methodology for many other micro-fabrication processes is yet to be developed. In particular, CAD/CAM systems for excimer laser mask projection micromachining tools have received little attention, and indeed, few attempts have been reported on CAD/CAM systems that fully capitalize on the unique capability of the excimer laser process. Fabrication of a 3D structure and surface texture using excimer laser mask projection typically requires the machine operator to develop a specific NC part program for the desired structure geometry and also incorporate appropriate machine parameters to achieve the desired finish. The capability of the laser ablation process could therefore be significantly improved by a CAD/CAM system that automatically generates the NC part program using the 3D information of the CAD model of the desired structure. Accordingly, this research demonstrated such a system – that is, an effective CAD/CAM system specifically for excimer laser mask projection micromachining tools.

The developed system is the first of its kind that extracts information from a STL file to automatically generate NC code data for excimer laser ablation manufacturing using optimised processing parameters. The system simplifies part program creation and is useful for excimer laser operators who currently use a tedious trial and error process to create programs and complex masks to generate microstructure parts. The system enables

good quality components to be produced with acceptable speed and accuracy in the sub-micron domain (down to 10 μ m features resolution possible).

The system algorithms deployed are currently developed only for square and hexagonal mask patterns, however, the algorithms can easily be extended to accommodate a range of different shaped masks and other processes. Furthermore, the system is cost-effective because it does not require additional expensive lithography masks to be produced for every change in design of microstructures. The system was specifically design for fixed mask geometry to shape the laser beam. Additionally, pulse minimization algorithm is integrated, allowing the minimization of manufacturing time by the specific multiple patterned masks.

References

1. Tonshoff, H.K., von Alvensleben, F. and Kulik, C., "Advanced 3D-CAD-Interface for Micro Machining with Excimer Lasers", Symposium on Design, Test, and Microfabrication of MEMS and MOEMS, Paris, France, March, 1999, Vol. 3680, p. 340-347.
2. Tonshoff, H.K., Graumann, C., Hesner, H. and Rinke, M., "NC-controlled production of smooth 3-D surfaces in brittle materials with 193 nm-Excimer Laser", Proceedings of SPIE Conference on Micromachining and Microfabrication Process Technology IV, Santa Clara, California, September, 1998, Vol. 3511, p. 56-66.
3. Tonshoff, H.K., von Alvensleben, F., Ostendorf, A., Korber, K. and Kulik, C., "3-D Micro-Structuring with F2 Lasers", Proceedings of SPIE on Micro-Opto-Electro-Mechanical Systems, 2000, Vol. 4075, p. 159-166.
4. Pratt, M.J., Bhatt, A.D., Dutta, D., Lyons, K.W., Patil, L. and Sriram, R.D., "Progress towards an international standard for data transfer in rapid prototyping and layered manufacturing", Computer-Aided Design, 2002, Vol. 34(14), p. 1111-1121.
5. Zimmer, K., Hirsch, D. and Bigl, F., "Excimer laser machining for the fabrication of analogous microstructures", Applied Surface Science, 1996, Vol. 96-98, p. 425-429.
6. Zimmer, K., Braun, A. and Bigl, F., "Combination of different processing methods for the fabrication of 3D polymer structures by excimer laser machining", Applied Surface Science, 2000, Vol. 154-155, p. 601-604.
7. Taguchi, G., Chowdhury, S. and Wu, Y., "Taguchi's Quality Engineering Handbook", J.Wiley & Sons Inc., New Jersey, U.S., 2005.
8. Madou, M., "Fundamentals of Microfabrication", CRC Press, New York, 1997.

9. Dyer, P.E., Waldeck, I. and Roberts, G.C., "Fine-hole drilling in Upilex polyamide and glass by TEO CO₂ laser ablation", *Applied Physics*, 1997, Vol. 30, p. 19-21.
10. Harvey, E.C. and Rumsby, P., "Fabrication techniques and their application to produce novel micromachined structures and devices using excimer laser projection", *Proceedings of SPIE*, Austin, Texas, USA, 1997, Vol. 3223, p. 26-33.
11. Metev, M., Veiko, V.R., "Laser-Assisted Micro-Technology", *Springer's Series in Material Science*, 1998, Vol. 19, p. 135-148.
12. Gower, M., "Excimer lasers: principles of operation and equipment, in *Laser Processing in Manufacturing*", ed. Crafer RC and Oakley PJ, Chapman & Hall, 1993, p. 196-205.
13. Harvey, E.C., Rumsby, P., Gower, M. and Remnant, J.L., "Microstructuring by Excimer Laser", *Proceedings of SPIE*, 1995, Vol.2639, p. 266-277.
14. Srinivasan, R., Braren, B., "Ultraviolet Laser Ablation of Organic Polymers", *Chem. Rev.*, 1989, Vol. 89, p. 1303-1316.
15. Garrison, B.J. and Srinivasan, R., "Laser ablation of organic polymers: Microscopic models for photochemical and thermal processes", *Journal of Applied Physics*, 1985, Vol. 57(8), p. 2909-2913.
16. Hayes, J.P., "Lasers in microengineering", Industrial Research Institute Swinburne, Swinburne University of Technology, Melbourne, Australia, 2001.
17. Doany, F.E., "Large-field scanning laser ablation system", *IBM J. Res. Develop.*, Vol. 41, No. 1/2, Jan., 1997.
18. Bruck, R., Rizvi, N. and Schmidt, A., "Applied Microtechnology", Carl Hanser Verlag, Munich, 2001.
19. Elliot, D., "Ultraviolet laser Technology and Applications, Academic Press, 1995.

20. Braun, A., Zimmer, K., Hosselbarth, B., Meinhardt, J., Bigl, F. and Mehnert, R., "Excimer laser micromachining and replication of 3D optical surfaces", Applied Surface Science, 1998, Vol. 127-129, p. 911-914.
21. Rizvi, N.H., Milne, D., Rumsby, P. and Gower, M., "Laser Micromachining - New Developments and Applications", Proceedings of SPIE, 2002, Vol. 3933, p. 261-271.
22. Gower, M., Rizvi, N.H., "Applications of Laser Ablation to Microengineering", Proceedings of SPIE, 2001, Vol. 4065, p. 452-460.
23. Zimmer, K., Braun, A. and Bohme, R., "Etching of fused silica and glass with excimer laser at 351 nm", Applied Surface Science, 2003, Vol. 208-209, p. 199-204.
24. Holmes, A.S., " Laser processes for MEMS manufacture", RIKEN Review, 2002, Vol. 43, p. 63-69.
25. Harvey, E.C., Mackin, T.R., Dempster, B.C., Scholten, R.E., "Micro-Optical Structures for Atom Lithography Studies", Proceedings of SPIE, 1999, Vol.3892, p. 266-273.
26. www.resonetics.com, "Review of Laser Micromachining", May, 2002.
27. www.resonetics.com, "Micromachining Seminar", Dec, 2001.
28. Quentel, F., Fieret, J., Holmes, A.S. and Paineau, S., "Multilevel diffractive optical element manufacture by excimer laser ablation and halftone masks", www.exitech.co.uk, 1999.
29. Hayden, C.J., "Three-dimensional excimer laser micromachining using greyscale masks", Journal of Micromechanics and Microengineering, 2003, Vol. 13, p. 599-603.
30. Gower, M., "Laser micromachining for manufacturing MEMS devices", www.exitech.co.uk, 1999.

31. Rizvi, N.H., Rumsby, P. and Gower, M., "New Developments and Applications in the Production of 3D Microstructures by Laser Micromachining", www.exitech.co.uk, 2000.
32. Gower, M., "Industrial Applications of Pulsed Lasers to Materials Microprocessing", www.exitech.co.uk, 1999.
33. Lankard, J.R. and Wolbold, G., "Excimer Laser Ablation of Polyimide in a Manufacturing Facility", Appl. Phys. A, Vol. 54, p. 355-359, 1992.
34. Rizvi, N.H., "Production of novel 3D microstructures using excimer laser mask projection techniques", www.exitech.co.uk, 2001.
35. Rumsby, P., "Excimer laser patterning of thick and thin films for high density packaging in Microelectronic packaging and laser processing", Proceedings of SPIE, Singapore, 1997, Vol. 3184, p.176-187.
36. Harvey, E.C., "The Mysteries of PSO", Industrial Research Institute Swinburne, Swinburne University of Technology, Melbourne, Australia, 1999.
37. Abbott, C., Allott, R., Bann, B., Boehlen, K., Gower, M., Rumsby, P. and Beohlen-Stassen, I., "New techniques for laser micromachining of MEMS devices", www.exitech.co.uk, 2002.
38. Boehlen, K., Boehlen, I.B., "Laser micro-machining of high density optical structures on large substrates", www.exitech.co.uk, 2004.
39. Liao, Y.S., Chiu, Y.Y., "A New Slicing Procedure for Rapid Prototyping Systems", International Journal of Advanced Manufacturing Technology, 2001, Vol. 21, p. 579-585.
40. Davis, S.T., Harvey, E.C., Jin, H., Hayes, J.P. and Ghantasala, M.K., "Characterization of micromachining process during KrF excimer laser ablation of TiNi shape memory alloy thin sheets and films", Smart Materials and Structures, July, 2002, Vol. 11, p. 708-714.

41. Rizvi, N.H., Apte, P., "Developments in Laser Micromachining Techniques", www.exitech.co.uk, 2001.
42. Booth, H., "Recent applications of pulsed lasers in advanced materials processing", www.exitech.co.uk, 2004.
43. Jain, K., "Large-Area, High-Throughput, High Resolution, Projection Imaging System", U.S. Patent 5,285,236 issued Feb. 8, 1994.
44. Jain, K., "High-Throughput, High Resolution, Projection Patterning System for Large, Flexible, Roll-Fed Electronic-Module Substrates", U.S. Patent 5,652,645 issued Jul. 29, 1997.
45. Jain, K., Zemel, M. and Klosner, M., "Large-Area, High-Resolution Lithography and Photoablation Systems for Microelectronics and Optoelectronics Fabrication", Proceedings of IEEE, Vol. 90, Oct., 2002, p. 1681-1687.
46. Lee, Y.C., Chen, C.M. and Wu, C.Y., "A new excimer laser micromachining method for axially symmetric 3D microstructures with continuous surface profiles", Sensors and Actuators A: Physical, 2005, Vol. 117(2), p. 349-355.
47. Choi, K.H., Meijer, J., Masuzawa, T. and Kim, D.H., "Excimer laser micromachining for 3D microstructure", Journal of Materials Processing Technology, 2004, Vol. 149(3), p. 561-566.
48. Jolic, K., Ghantasala, M.K. and Harvey, E.C., "Excimer laser machining of corner cube structures", Journal of Micromechanics and Microengineering, 2003, Vol. 14, p. 388-397.
49. Boehlen, S.I., Fieret, J., Holmes, A.S. and Lee, K.W., "CAD/CAM software for an industrial laser manufacturing tool", Photon Processing in Microelectronics and Photonics II, San Jose, California, USA, SPIE, Vol. 4977, 2003, p. 198-206.
50. Perkins, D., "CAD/CAM system for an Excimer 8000 Series Laser Micro Machining System", Master of Engineering Thesis, Computer Systems Engineering, University of Wales, Bangor, 2000, p. 120-126.

51. Mayer, F., "Laser Zentrum Hannover: Introduction Notes and Presentation", Personal Communication, May, 2004, Laser Zentrum Hannover, Hannover.
52. Zhao, W., Yang, Y., Wang, Z. and Zhang, Y., "A CAD/CAM system for micro-ED-milling of small 3D freeform cavity", Journal of Materials Processing Technology, 2004, Vol. 149, p. 573-578.
53. Takayuki, Y., Mutsuya, T., Takashi, O., Satoshi, T. and Takayuki, G., "Novel fabrication method for 3-D microstructures using surface-activated bonding and its application to micro-mechanical parts", Proceedings of SPIE, 2002, Vol. 3467, p. 105-112.
54. He, Y., Marchetti, J. and Maseeh, F., "MEMS Computer-aided Design", 1997 European Design and Test Conference and Exhibition Microfabrication, Paris, 1997, p. 275-282.
55. Maseeh, F., Harris, R. and Senturia, S.D., "A CAD architecture for microelectromechanical systems", Proceedings of IEEE Micro Electro Mechanical Systems, 1990, p. 1567-1576.
56. Harris, R., Maseeh, F. and Senturia, S.D., "Automatic Generation of a 3-D Solid Model of a Microfabricated Structure", Proceedings of IEEE Solid-State Actuator Workshop, 4th Technical Digest, 1990, p. 1161-1168.
57. Koppelman, G.M., "Oyster, a three-dimensional structural simulator for microelectromechanical design", Sensors and Actuators A: Physical, 1989, Vol. 20, p. 179-185.
58. Chen, Y.H., Ng, C.T. and Wang, Y.Z., "Generation of an STL File from 3D Measurement Data with User-Controlled Data Reduction" International Journal of Advanced Manufacturing Technology, 1999, Vol. 15, p. 127-131.
59. Sheng, X., Hirsch, B.E., "Triangulation of trimmed surfaces in parametric space", Computer-Aided Design, 1992, Vol. 24(8), p. 437-444.
60. Dolenc, A., Makela, I., "Slicing procedures for layered manufacturing techniques", Computer-Aided Design, 1994, Vol. 26(2), p. 119-126.

61. Mani, K., Kulkarni, P. and Dutta, D., "Region-based adaptive slicing", Computer-Aided Design, 1999, Vol. 31(5), p. 317-333.
62. Kulkarni, P., Dutta, D., "Adaptive Slicing for Parametrizable Surfaces for Layered Manufacturing", Proceedings of ASME Design Automation Conference, Boston, MA, 1995, p. 211-217.
63. Suh, Y. and Wonzy, M.J., "Adaptive Slicing of Solid Freeform Fabrication Processes", Proceedings of Solid Freeform Fabrication Symposium, Austin, Texas, 1994, p. 404-411.
64. Mutapcic, E., Iovenitti, P. and Hayes, J.P., "Automated generation of NC part programs for excimer laser ablation micromachining from known 3D surfaces", Proceedings of SPIE Conference on Biomedical Applications of Micro-and Nanoengineering, Melbourne, 2002, Vol.4935, p. 445-453.
65. Mutapcic, E., Iovenitti, P., Hayes, J.P., "A prototyping and microfabrication CAD/CAM tool for excimer laser micromachining process", International Journal of Advanced Manufacturing Technology, published online 25 November 2005.
66. Trimmer, W., "Computer aided design for MEMS/MST", Micromachine Devices, 1998, Vol. 6(6), p. 1-14.
67. Stratasys.INC, "FDM Procedures 2000/3000/8000 Release 2.0", www.Stratasys.com, Dec., 2001.
68. Cooley, P., "The Essence of Computer Graphics Computing", Prentice Hall, Harrow, England, 2001.
69. Richardson, M., "Practical Computer Graphics", Second Edition, McGraw Hill, London, 1999.
70. Angel, E., "Interactive Computer Graphics: a top-down approach with OpenGL", Addison Wesley, Massachusetts, 2000.
71. Ammeraal, L., "Computer Graphics for Java Programmers", Wiley, Chichester, (U.K.), 1998.

72. Hearn, D., Baker, M.P., Computer Graphics, Second Edition, Prentice Hall International, London, 1994.
73. Parent, R., "Computer Animation: Algorithms and Techniques", Morgan Kaufmann, San Francisco, 2002.
74. Golden, B. and Stewart, W. "Empirical analysis of heuristics", In Lawler, E., Lenstra, J., Kan, A.R. and Shmoys, D. (Eds.), The Travelling Salesman Problem - A Guided Tour of Combinatorial Optimization, John Wiley & Sons, Chichester (U.K.), 1985.
75. Evans, J.R., Minieka, E., "Optimization Algorithms for Networks and Graphs", Prentice Hall, England, 1992.
76. Rosenkrantz, D.J., Stearns, R.E. and Lewis, P.M., "An analysis of several heuristics for the traveling salesman problem", SIAM Journal of Computer Science, 1997, Vol. 34, p. 563-581.
77. Li, J., Ananthasuresh, G.K., "A quality study on the excimer laser micromachining of electro-thermal-compliant micro devices", Journal of Micromechanics and Microengineering, 2001, Vol. 11, p. 38-47.
78. Atkin, M., Mutapcic, E., Hayes, J.P. and Harvey, E.C., "A comparison of 355nm and 248nm Laser Ablation of PET for Microfluidic Applications", Picalo Conf., Laser Institute of America, Melbourne, April, 2004, p. 353-361.
79. Ghantasala, M.K., Harvey, E.C. and Sood, D.K., "Excimer laser micromachining of structures using SU-8", Micromachining and Microfabrication Process Technology V, SPIE, Vol. 3874, Santa Clara, California, September, 1999, p. 85-91.
80. Boyde, A., "Memoir on Inventing the Confocal Scanning Microscope by Marvin Minsky", International Journal of Scanning Applications, 1988, Vol. 10, p. 128-138.
81. Sheppard, C.J.R. and Shotton, D.M., "Confocal Laser Scanning Microscopy (Microscopy Handbook)", BIOS Scientific Publishers Ltd., Oxford, (U.K.), 1997.

82. Olympus Optical Co. Ltd., "Instructions BX60M system microscope", Tokyo, Japan, p. 1-31, 1990.
83. Olympus Optical Co. Ltd., "CAMEDIA Olympus digital camera basic manual C-5050 Zoom", Tokyo, Japan, 2002.
84. Galyer, J.F.W, Shotbolt, C.R., "Metrology for Engineers", Third Edition, Camelot Press Limited, London, 1969.
85. Mutapcic, E., Iovenitti, P. and Hayes, J.P., "Overlay error effects on polycarbonate structures produced by 248nm UV laser ablation tool", Third Asia-Pacific Forum on Precision Surface Finishing and Deburring Technology, Melbourne, 2003, p. 269-280.
86. Sexton, B.A., Hayes, J.P., Brian, D. and Harvey, E.C., "Electroplated Microstructures from Excimer Laser Micromachined Moulds", Proceedings of 12th International Federation of Heat Treatment and Surface Engineering Congress, Melbourne, Australia, 2000, p. 119-126.
87. Chen, Y.H., Zheng, H.Y. and Tam, S.C., "Excimer laser drilling of polymers", www.sintecoptronics.com, Dec., 2001.
88. Atkin, M., Hayes, J.P., Brack, N., Poetter, K., Catrall, R. and Harvey, E.C., "Disposable biochip fabrication for DNA diagnostics", Proceedings of SPIE on Biomedical Applications of Micro and Nanoengineering, 2002, Vol. 3453, p. 125-135.
89. Wang, H., "Passive Mixing in Microchannels with Geometric Variations", Doctor of Philosophy Thesis, Industrial Research Institute Swinburne, Swinburne University of Technology , Melbourne, Australia, 2004.
90. Aref, H., "Stirring by chaotic advection", Journal of Fluid Mechanics, 1984, Vol. 143, p.1-21.
91. Jones, S.W., Thomas, O.M., and Aref, H., "Chaotic advection by laminar flow in a twisted pipe", Journal of Fluid Mechanics, 1989, Vol. 209, p. 335-357.

92. Beebe, D.J., et al., "Passive mixing in microchannels: Fabrication and flow experiments", *Mecanique & Industries*, 2001, Vol. 2(4), p. 343-348.
93. Wang, H., Masood, S., Iovenitti, P. and Harvey, E.C., "Application of Fused Deposition Modelling Rapid Prototyping System to the Development of Microchannels", *Proceedings of SPIE, Smart Electronics and MEMS*, Adelaide, Australia, 2001, Vol. 4590, p. 213-220.
94. Hume, R., Iovenitti, P. and Hayes, J.P., "Laser Cut Examples", *Industrial Research Institute Swinburne*, Swinburne University of Technology, Melbourne, Australia, 2002.
95. Rattanawong, W., "An Intelligent Generic Part Orientation System Based on Volumetric Error in Rapid Prototyping", *Doctor of Philosophy Thesis*, Industrial Research Institute Swinburne, Swinburne University of Technology, Melbourne, Australia, 2000, p. 201-205.
96. Tseng, A., Chen, Y.T., and Ma, K.J., "Fabrication of high aspect ratio microstructures using excimer laser", *Optics and Lasers in Engineering*, 2004, Vol.41, p.827-847.
97. Chen, Y.T., Naessens, K., Baets, R., Liao, Y.S., and Tseng, A.A., "Ablation of transparent materials using excimer lasers for photonic applications", *Optical Review*, 2005, Vol.12, p.427-441.
98. Kruger, J., Martin, S., Madebach, H., Urech, L., Lippert, T., Wokaun, A., and Kautek, W., "Femto- and nanosecond laser treatment of doped polymethylmethacrylate", *Applied Surface Science*, 2005, Vol.247, p.406-411.
99. Burns, F.C., and Cain, S.R., "The effect of pulse repetition rate on laser ablation of polyimide and polymethylmethacrylate-based polymers", *J.Phys. D: Appl. Phys.*, 1996, vol. 29, 1349-1355.
100. Baudach, S., Bonse, J., Kruger, J., and Kautek, W., "Ultrashort pulse laser ablation of polycarbonate and polymethylmethacrylate", *Applied Surface Science*, 2000, Vol.154-155, p.555-560.

101. Charrier, M. et al., "Manufacture of a conformal, multi-layer RF antenna substrate using excimer mask imaging technology and a 6-axis robot.", Thomson-CSF, Laboratoire Central de Recherches, Domaine de Corbeville, Orsay Cedex, France, www.exitech.co.uk, 2004.

Appendix A

A List of Publications

A.1 Journal Publications

Mutapcic, E., Iovenitti, P., Hayes, J.P., “A prototyping and microfabrication CAD/CAM tool for excimer laser micromachining process”, *International Journal of Advanced Manufacturing Technology*, published online 25 November 2005.

Mutapcic, E., Iovenitti, P., Hayes, J.P., “A 3D-CAM System For Quick Prototyping And Microfabrication Using Excimer Laser Micromachining”, *Journal of Microsystems Technologies*, December, 2005, DOI: 10.1007/S00542-005-0009-7 Vol. 12(1), p. 128-136.

Hume, R., Mutapcic, E., Iovenitti, P., Hayes, J.P., “Rapid prototyping of polymer Microfluidics Devices using CAD/CAM tools for laser micromachining”, *International Journal of CAD/CAM*, 2006, ISSN: 1598-1800, No:4/25.

A.2 International Conferences Publications

Mutapcic, E., Iovenitti, P., Hayes, J.P., “A 3D CAM system for automating NC part programming for excimer laser micromachining”, *DTIP of MEMS & MOEMS*, Montreux, Switzerland, 2004, p. 155-160.

Mutapcic, E., Iovenitti, P., Hayes, J.P., “A Novel CAD/CAM Tool for Excimer Laser Ablation-Machining Process”, *PICALO*, Melbourne, 2004, p. 312-318.

Atkin, M., Mutapcic, E., Hayes, J.P., Harvey, E.C., “A comparison of 355nm and 248nm Laser Ablation of PET for Microfluidic Applications”, *PICALO*, Melbourne, 2004, p. 318-324.

Mutapcic, E., Iovenitti, P., Hayes, J.P., “Overlay error effects on polycarbonate structures produced by 248nm UV laser ablation tool”, *Third Asia-Pacific Forum on Precision Surface Finishing and Deburring Technology*, Melbourne, 2003, p. 269-280.

Mutapcic, E., Iovenitti, P., Hayes, J.P., “Automated generation of NC part programs for excimer laser ablation micromachining from known 3D surfaces”, *Proceedings of SPIE Conference on Biomedical Applications of Micro-and Nanoengineering*, Melbourne, 2002, Vol. 4935, p. 445-453.

Birchall, I.E., Mutapcic, E., “Excimer laser ablation micro-patterning of bovine pericardium”, 15th Annual Conference of the Australian Society of Biomaterials, Victor Harbor, South Australia, 2005.

A.3 Local Publications and Presentations

Mutapcic, E., Iovenitti, P., Hayes, J.P., “A software approach for control of overlay error effects on polycarbonate structures produced by 248nm UV laser tool”, in D. Toncich (ed.), Profiles in Industrial Research Knowledge and Innovation 2003, Industrial Research Institute Swinburne, Hawthorn, p. 261-268, ISBN 1876 567 04 X.

Mutapcic, E., Iovenitti, P., Hayes, J.P., “Automatic NC Part Programming Interface for a UV Laser Ablation Tool”, in D. Toncich (ed.), Profiles in Industrial Research Knowledge and Innovation 2002, Industrial Research Institute Swinburne, Hawthorn, p. 248-254, ISBN 1876 567 04 X

Appendix B

NC Part Programs and Actual Microstructures Produced by Ex-Expv1.0 System.

This appendix provides an introduction to CAD/CAM system developed. Through a series of step-by-step instructions the appendix explains how to get started with the new system and covers the following topics:

- Creating 2D and 3D geometry (section 3.4.2)
- Creating STL file (section 3.4.2)
- Creating of sliced structure (section 3.4.3..3)
- Samples of part programs and machined structures using different machining techniques
- User-interface for selection of materials and machining process parameters
- Aerotech Unidex 500 programming language

B.1 Creating 2D and 3D Geometry

Development of complex 3D microstructures by manual programming of positioning axes and beam shaping makes use of excimer lasers uneconomical especially for small batches and single parts. By developing a CAD/CAM interface and algorithms to automatically control CNC unit, mask stages movements and a workpiece handling system, this limitation can be overcome.

Modelling of a prototype system was reported in Chapter 3 and in Figure B.1.1 the four steps process behind it was briefly illustrated.

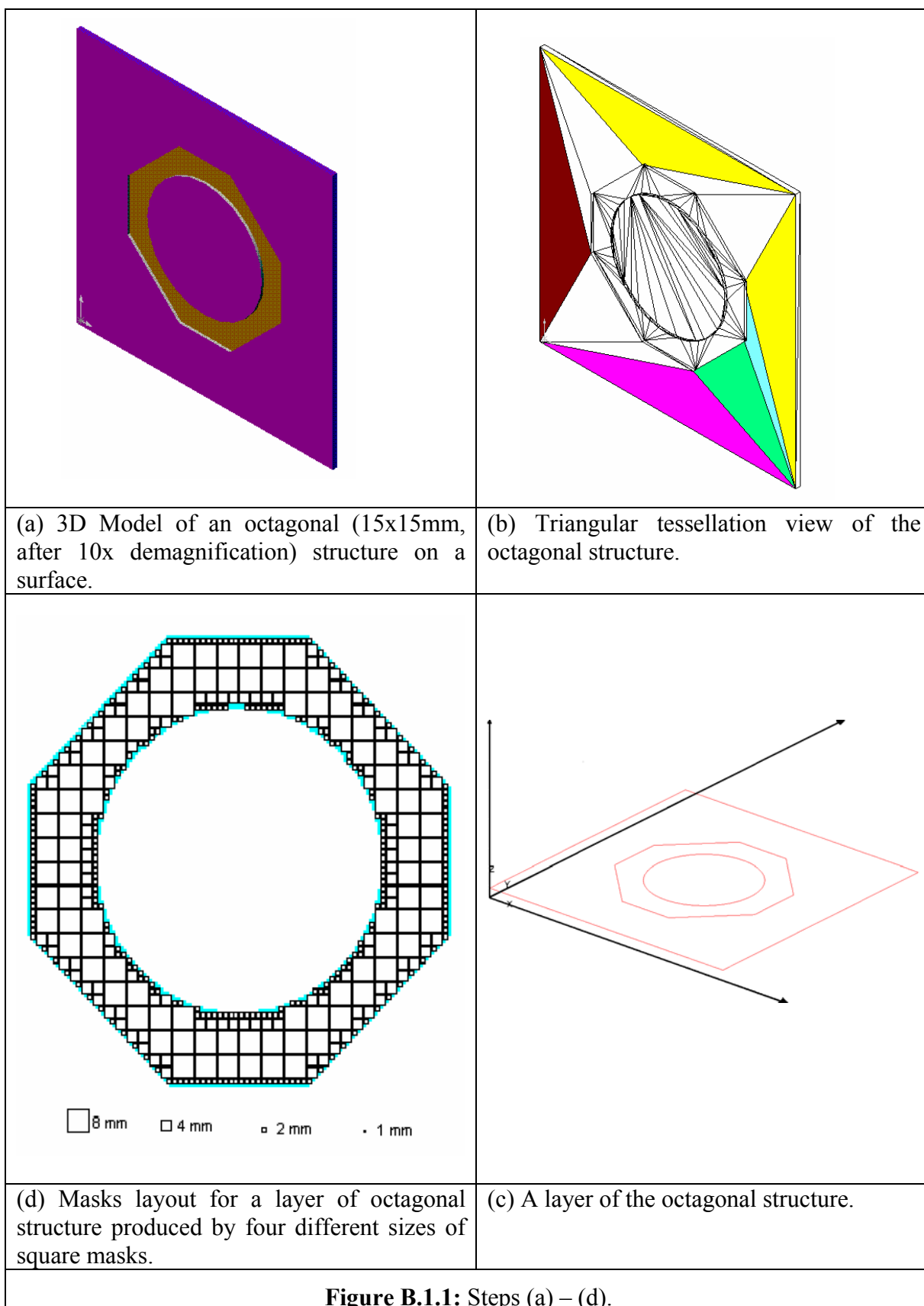


Figure B.1.1: Steps (a) – (d).

B.2 Creating STL File

STL File is an ASCII or binary file normally used in Rapid Prototyping process. It is a tessellated description of a CAD generated model. ASCII file must start with the lower case keyword **solid** and end with **endsolid**. Within keywords are listing of individual triangles that define the faces of the solid model. Each individual triangle description defines a unit normal vector directed away from the solid's surface followed by the XYZ components for all three of the vertices. These values are all in Cartesian coordinates and floating-point values [95].

STL File listing used to produce structure shown in Figure B.1.1 is given below.

Listing B.2.1: STL File Structure.

Description: A part of STL file structure to produce Figure B.1.1.

```
OctagonBoss.STL

solid boss
  facet normal 0.000000e+000 0.000000e+000 1.000000e+000
    outer loop
      vertex 3.496757e+001 2.580466e+001 8.900000e-001
      vertex 3.500000e+001 2.500000e+001 8.900000e-001
      vertex 4.000000e+001 2.000000e+001 8.900000e-001
    endloop
  endfacet
  facet normal 0.000000e+000 0.000000e+000 1.000000e+000
    outer loop
      vertex 4.000000e+001 2.000000e+001 8.900000e-001
      vertex 3.500000e+001 2.500000e+001 8.900000e-001
      vertex 3.496757e+001 2.419533e+001 8.900000e-001
    endloop
  endfacet
  facet normal 0.000000e+000 0.000000e+000 1.000000e+000
    outer loop
      vertex 4.000000e+001 2.000000e+001 8.900000e-001
      vertex 3.496757e+001 2.419533e+001 8.900000e-001
      vertex 3.470942e+001 2.260684e+001 8.900000e-001
    endloop
  endfacet
  facet normal 0.000000e+000 0.000000e+000 1.000000e+000
    outer loop
      vertex 1.551464e+001 2.183332e+001 1.780000e+000
      vertex 1.500000e+001 2.500000e+001 1.780000e+000
      vertex 1.512950e+001 2.339589e+001 1.780000e+000
    endloop
  endfacet
endsolid
```

B.3 Creating Sliced File Structure

Sliced file used to produce octagon structure shown in Figure B.1.1.

Listing B.3.1: Sliced File Structure.

Description: Part of sliced file structure:

```
Slice V19
STEP 0.00700787
HEIGHT 0.07008
G (0 DEFAULT)
G (1 BaseFast)
G (2 BaseTop)
G (3 Part)
G (4 PartFast)
G (5 PartSmall)
G (6 PartMating)
G (7 SupportFace)
G (8 Support)
G (9 SupportBottomSmall)
G (10 SupportBottom)
G (11 SupportSparse)
G (12 SupportPerf1)
G (13 SupportPerf2)
G (14 SupportSmall)
G (15 SupportBox)
G (16 SupportBoxPerf)
G (17 PartXHatch)
G (18 PartXtended)
G (19 PartTooSmall)
FILE(0,E:/SolidWorksFiles/stl/boss.ST
L,boss)
Z 0.007008 0.007008 F
O 0
3
3
4
1.968504 1.968504
O 1.968504
O 0
1.968504 0
CVIMNN0 0 1.968504 0 1.968504
7.8740158 3.8750078
*
Z 0.014016 0.007008 F
3
3
4
1.968504 1.968504
O 1.968504
O 0
1.968504 0
...
...
...
CVIMNN0 0.5905512 1.3779527 0.5908705
1.3776335 2.471072 0.48488448
*
*
*
END
```

B.4 Samples of Part Programs and Machined Structures using Different Machining Techniques

Listing B.4.1: NC code.

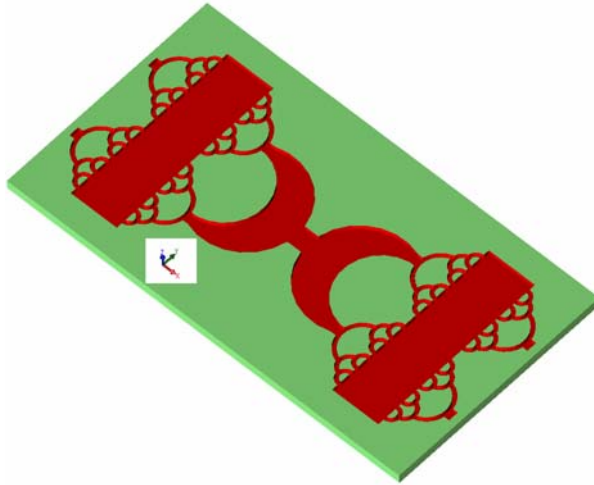
Description: Part program to produce octagonal structure shown in Figure B.1.1.

OctagonBoss.prg

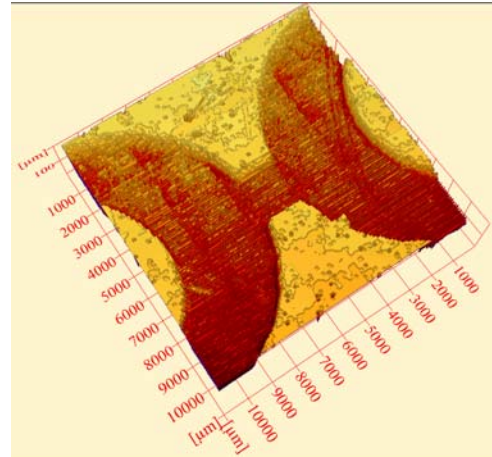
```
bo2
g90 g1 y2.55 f200
g90 g1 z0 f50
bo1
g90 g1 z282.535 u134.2199
g90 g1 x109.9 y105.5
psop,1,0,(10000/100)-50,50
v50=250
v61=48
v62=160
psod,0,160
psof,2,1
psof,3,x
g91 g1 x=52 f=48
psof,0
g90 g1 x109.5 y105.9
psop,1,0,(10000/100)-50,50
v50=250
v61=48
v62=160
psod,0,160
psof,2,1
psof,3,x
g91 g1 x=60 f=48
psof,0
g90 g1 x109.1 y106.3
psop,1,0,(10000/100)-50,50
v50=250
v61=48
v62=160
psod,0,160
psof,2,1
psof,3,x
g91 g1 x=68 f=48
psof,0
...
...

Exit
```

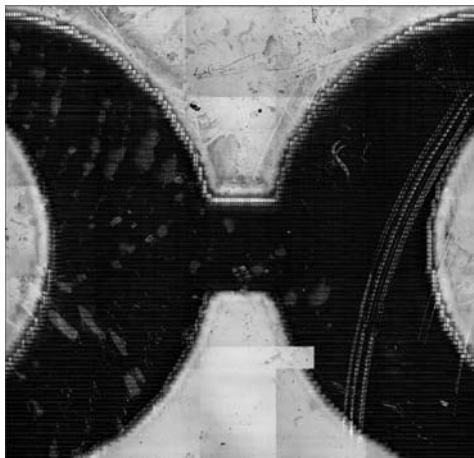
Figure B.4.1 shows a complex microfluidic channel network programmable with different sizes of channels that can be used for studying of concentration gradients. Two dyes can be injected from the top and two from the bottom before combining in a single channel in the middle.



(a)



(b)

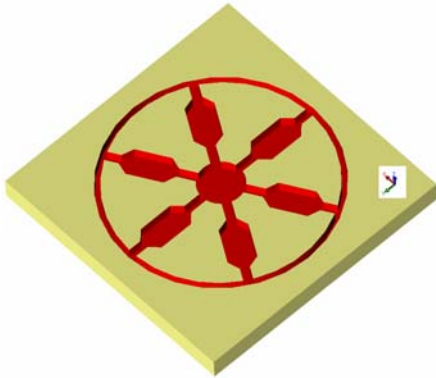


(c)

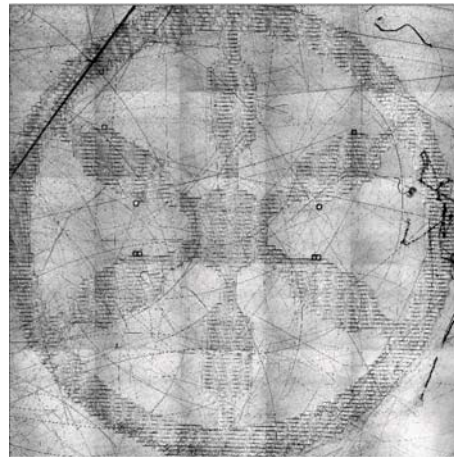
Figure B.4.1: (a) CAD model of a complex microfluidics channels network, (b) and (c) 2D and 3D LSCM image of the machined structure.

Figure B4.2 (a) and (b) represent the micro mixer array where ten mixer units are arranged in a star-like configuration, thus achieving a compact overall construction.

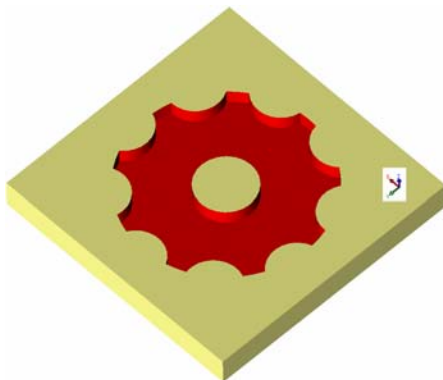
Figure B4.2 (c) and (d) show a CAD model and micromachined structure of a standard mechanical part, a micro-gear, and finally (e) and (f) represent a structure with different geometrical shapes for testing purpose.



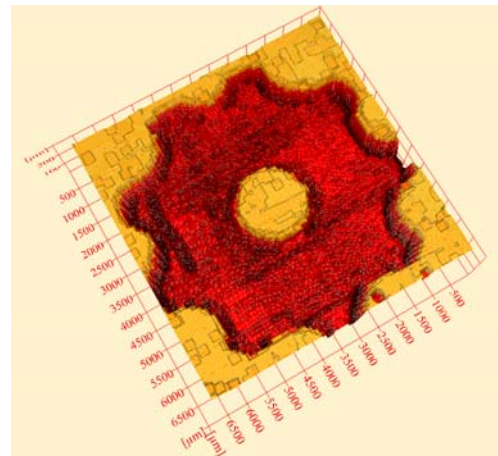
(a) CAD model of a micro mixer array.



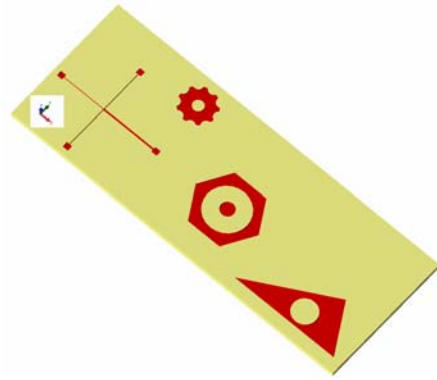
(b) 2D LSCM image of micro mixer array shown in (a).



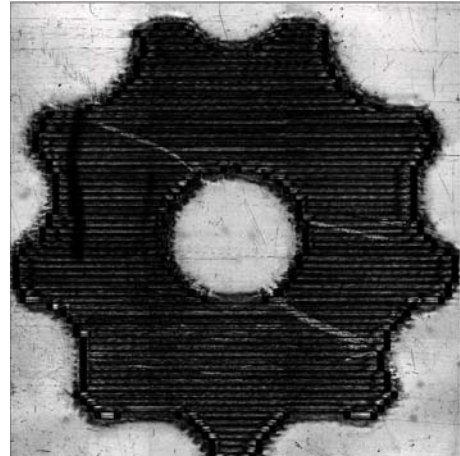
(c) CAD model of a micro gear.



(d) 3D LSCM image of micro gear shown in (c).



(e) CAD model of a test structure.



(f) 2D LSCM image of a part of test structure shown in (e).

Figure B.4.2 (a)-(f): CAD models and 2D LSCM images of different machined structures produced by Ex-Expv1.0 system.

B.5 User-interface for Selection of Materials and Machining Process Parameters

Figures B5.1 and B5.2 show part of GUI interface for machining parameters and material data selection from database respectively.

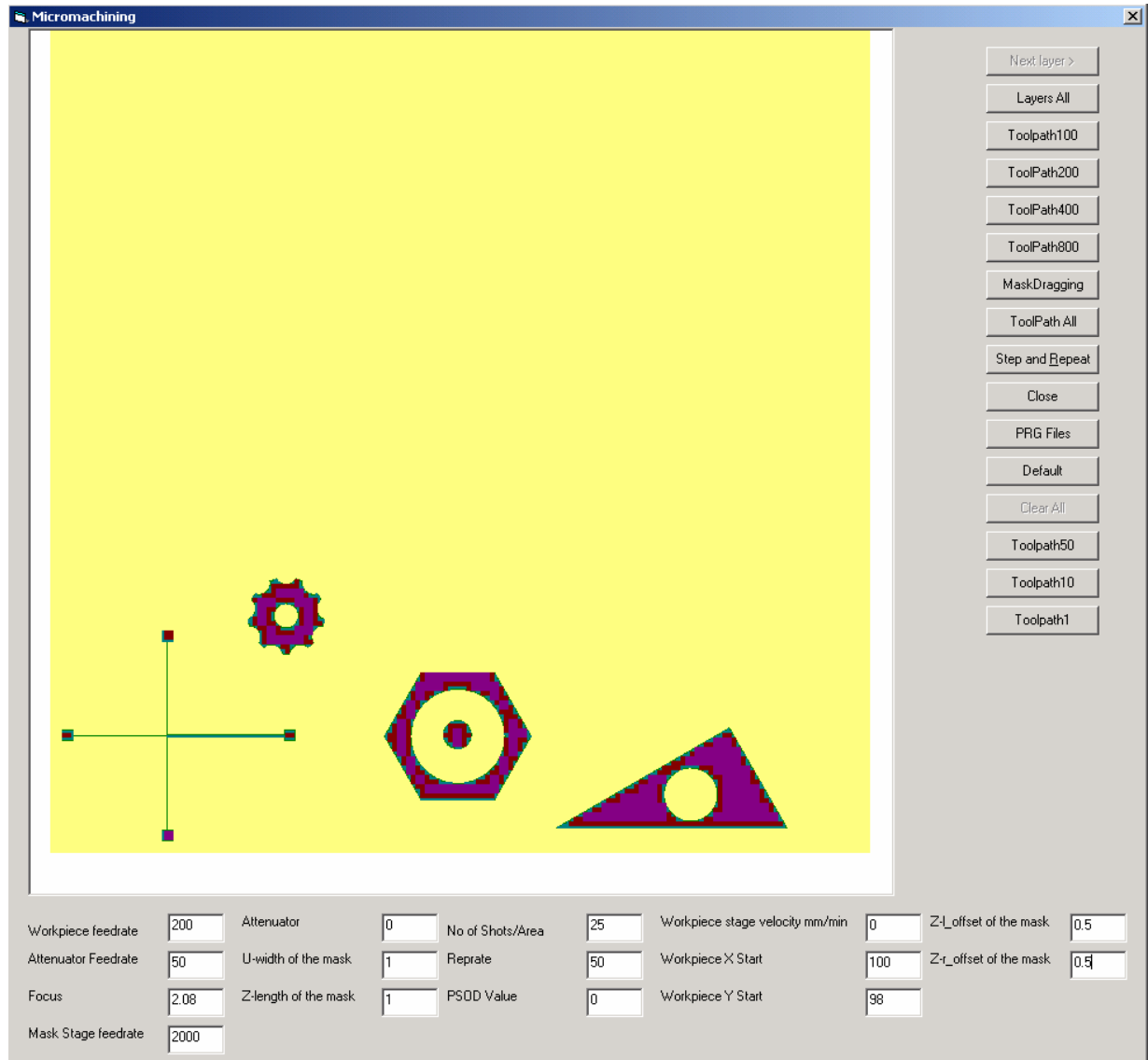


Figure B.5.1: Part of GUI for machining.

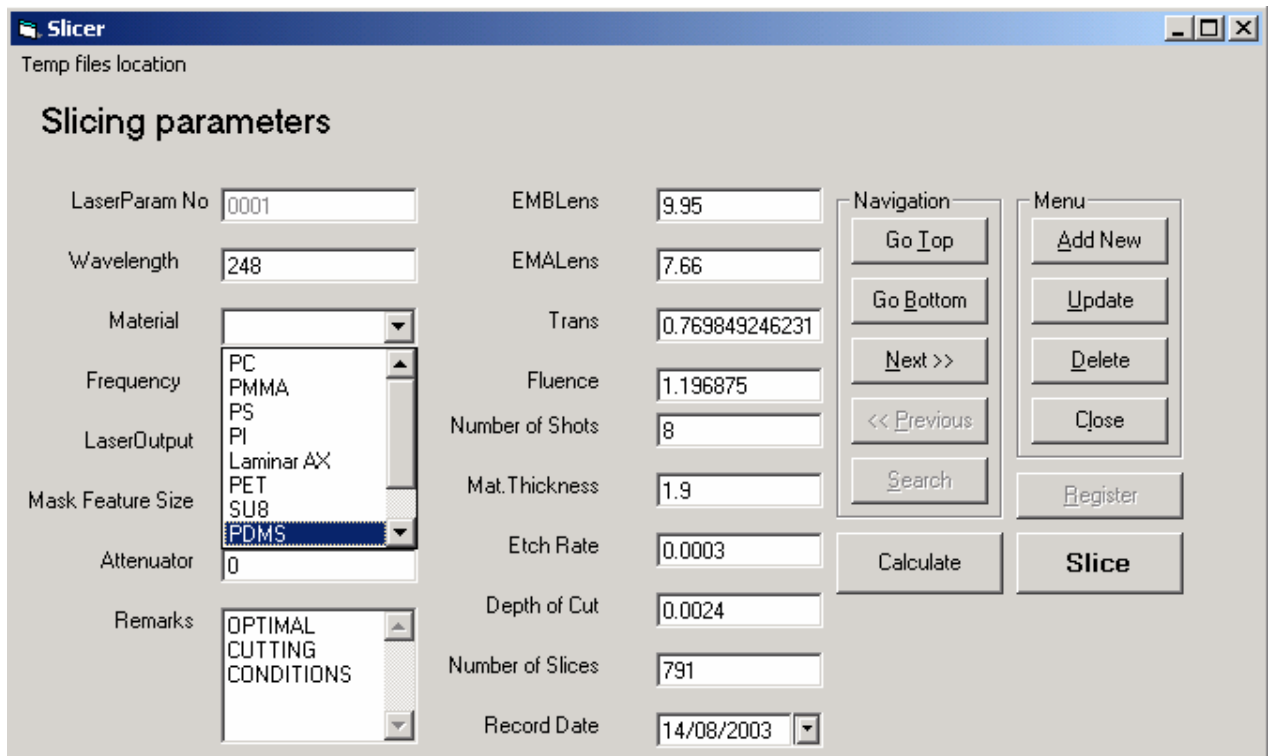


Figure B.5.2: Part of GUI for selection of process parameters from database of the system.

B.6 Aerotech Unidex 500 Programming Language

This section introduces the Aerotech Unidex 500 programming language as applies to Exitech Series 8000 laser machines. Full details of the Unidex 500 RS-274 “G” and “M” code CNC programming language are to be found in the Aerotech Unidex 500 manual. The listing below is a summary of a few of the most useful commands. The format examples show equivalent RS-274 “G”-code commands [36].

Table B.6.1: Exitech Series 8000 laser machine.

Axis	Function	Units	Resolution	Max Feedrate (units/min)
Board 1				
X	Workpiece X motion (0-200mm)	mm	0.0001 mm	6000 mm/min
Y	Workpiece Y motion (0-200mm)	mm	0.0001 mm	6000 mm/min
Z	Mask X motion (0-400mm)	mm	0.0001 mm	6000 mm/min
U	Mask Y motion (0-400mm)	mm	0.0001 mm	6000 mm/min
Board 2				
X	Workpiece Rotation	Degrees	$\pm 45^\circ$	1000 deg/min
Y	Workpiece Elevator	mm	0-5 mm	300 mm/min
Z	Beam Attenuator	Arbitrary (0-1)	0.01 mm	100 mm/min
U	Spare Axis	mm	0.0001 mm	6000 mm/min

Table B.6.2: RS-274 “G” code and Aerotech commands.

U500 Command	RS-274 code	Example Format	Explanation
LINEAR	G1	G1 F100 x55	Moves X-axis 55 mm at federate of 100 mm/min
INDEX	G0	G0 x55	Moves X-axis 55mm at top feedrate.
Program AB	G90	G90 G1 F100 x5	Moves X-axis to absolute position 5 mm from HOME
PROGRAM IN	G91	G91 G1 F100 x5	Moves X incrementally 5 mm from present position
DWELL	G4	G4 100	Program pause for 100 msec.
ENABLE		EN x y	Drive amplifiers for X and Y axes are enabled
DISABLE		DI x	Drive amplifier for X-axis disabled
HOME		HO x y z u	X, Y, Z and U axes all move to home

			position
LOOP		LOOP 10	The lines between this and the NEXT command will be repeated 10 times.
NEXT		NEXT	The closing command for a loop.
:		:CYCLE	Used for GOTO or SUBROUTINE.
;		;This is comment	Comment Line
GO TO		GO TO CYCLE	Go to label marker CYCLE.
M0	M0	M0	Program paused until “Step” key pressed.
M2		M2	Program end.
V0-V255		V12=V12+10	Variables 0 to 255 Variable V12 increased 10. X-axis moves to position V12.

The PSO is a special Position Synchronised Output card, which generates the laser trigger pulses.

The PSO may be used as a simple pulse generator using the PSOP and PSOF commands.

The PSO may be used as a pulse generator delivering a programmable number of pulses using the PSOP and PSOF,2,n commands.

The most powerful use of the PSO is as a position synchronised trigger source using the PSOP, PSOD and PSOF,3 commands. In this mode the PSO counts stage encoder pulses and issues a pulse at a programmable incremental number of encoder counts (or stage steps) [36].

Table B.6.3: PSO Commands.

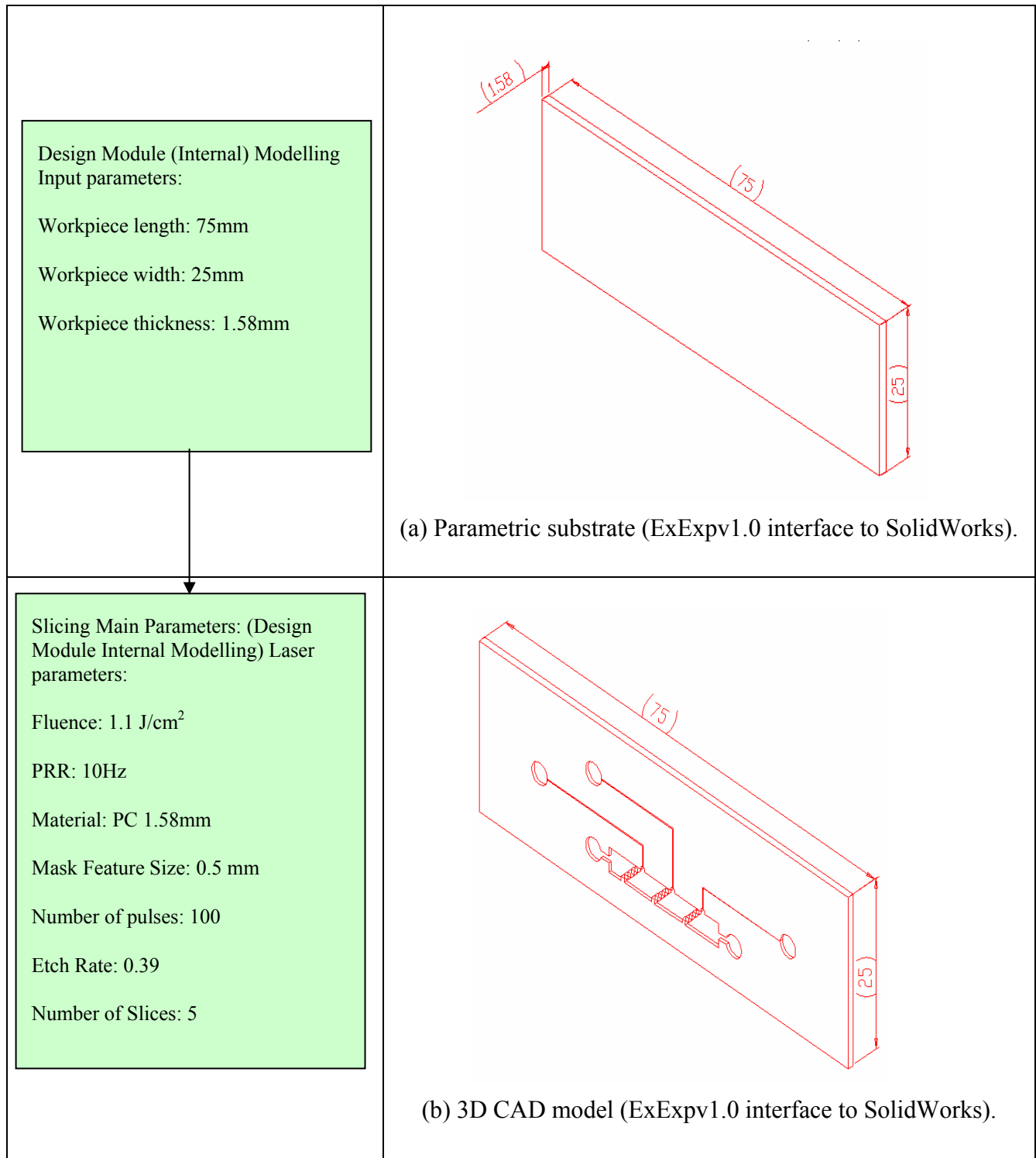
PSO Trigger Commands	Arguments	Example Format	Explanation
PSOP,c,l,w,t	c = case(usually=1) l = lead-in time (0.1ms) w = pulse width (0.1 ms) t = pulse tail time (0.1 ms)	PSOP,1,0,5,955	PSO Pulse train Case=1 Lead-in time = 0 ms Pulse width = 0.5 ms Pulse tail = 95.5 ms Pulse period = 100 ms (10 Hz).
PSOD,c,n	C = case (usually = 0) n = number of machine steps between trigger pulses	PSOD,0,50	Enable the PSO to fire every 50 machine steps. (also PSOF,3) (for workpiece X and Y 1 machine step = 0.1 μ m).
PSOF,1		PSOF,1	PSO Fire. Start trigger pulse train.

PSOF,0	G91	PSOF,0	PSO Fire. Stop trigger pulse train.
PSOF,2,n	n = number of pulses	PSOF,2,10	PSO Fire. Fire 10 trigger pulses.
PSOF,2,0		PSOF,2,0	A very useful version of PSOF, which causes the Unidex to pause program execution until the previous PSO commands have been completed.
PSOF,3,n	n = axis name	PSOF,3,x,y	PSO Fire according to PSOD. Trigger on X and Y motion.

Appendix C

Flow chart of main input and output parameters for Design 1 (in-line obstacles) and Design 2 (circular layout).

Design 1: In-line obstacles (Flow Chart)

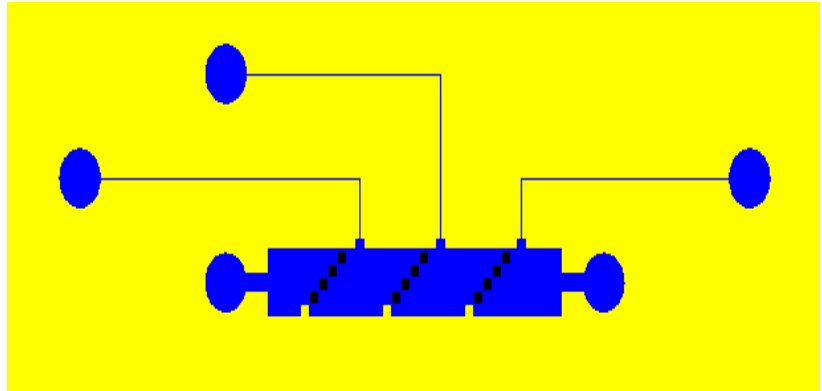


Machining Module:

First Slice:

Input parameters:

1. Toolpath (Left-Right, Zig-Zag, Star Algorithm)
2. Machining Method (Step and repeat , Workpiece-dragging)
3. Mask Stage feedrate:
4. Workpiece Stage feedrate:
5. Workpiece X-start:
6. Workpiece Y-start:
7. Attenuator position:
8. Attenuator feedrate:
9. Focus:
10. No of Shots/Area:
11. PSOD Value:
12. Z-mask length:
13. U-mask width:
14. Reprate:



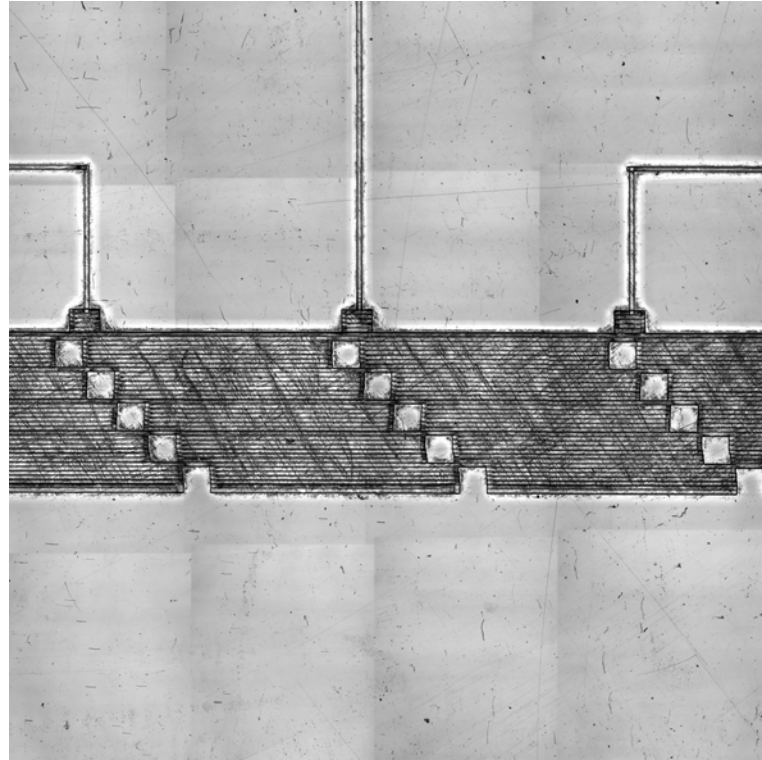
(c) BMP File representation of the first slice (ExExpv1.0 – Machining Module).

Machining Module:

```
bo2
wait all
g90 g1 y2.08 f200
g90 g1 z0 f50
wait all
bo1
g90 g1 z332.685
u178.55 f2000
;mask=Mask1
pattern=Pattern1
wait all
g90 g1 x111.8 y87.15
f2000
psop,1,0,(10000/100)-
50,50
v50=25
v61=12.06
v62=40.2010050251256
psod,0,40.201005025125
6
psof,2,0
dw100
psof,3,x
g91 g1 x=0.2 f=12.06
psof,0
dw100
```

Output parameters:

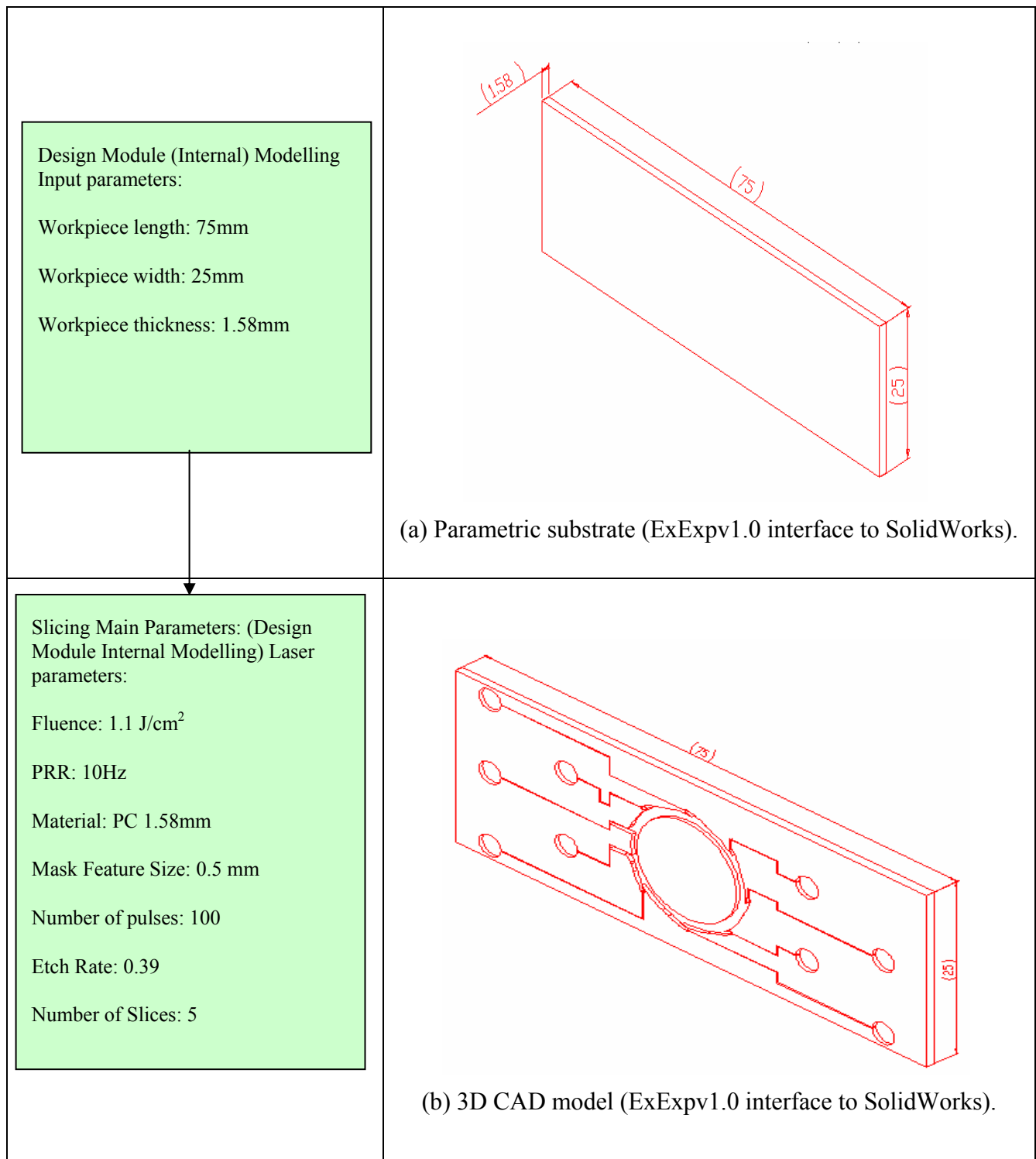
1. Part program to machine structure as per Design1. (only part of complete program listed here).



(d) LSCM picture of machined Design 1.

Figure C.1: Design 1: In-line obstacles - Flow Chart.

Design 2: Circular Layout (Flow Chart).

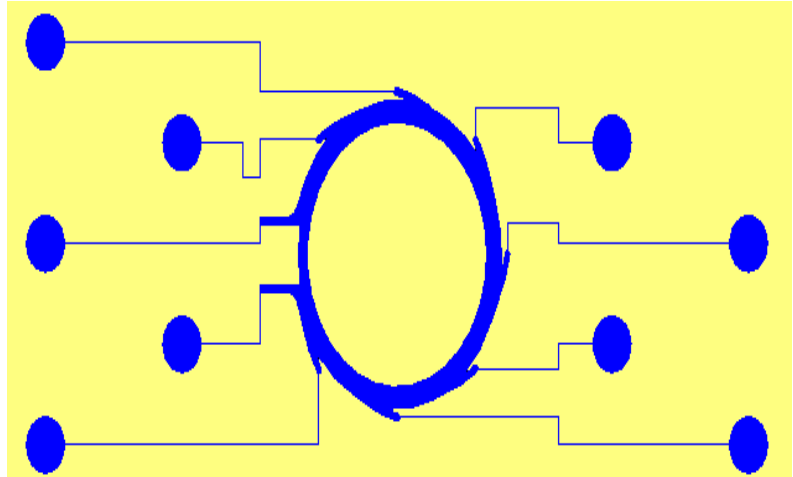


Machining Module:

First Slice:

Input parameters:

15. Toolpath (Left-Right, Zig-Zag, Star Algorithm)
16. Machining Method (Step and repeat , Workpiece-dragging)
17. Mask Stage feedrate:
18. Workpiece Stage feedrate:
19. Workpiece X-start:
20. Workpiece Y-start:
21. Attenuator position:
22. Attenuator feedrate:
23. Focus:
24. No of Shots/Area:
25. PSOD Value:
26. Z-mask length:
27. U-mask width:
28. Reprate:



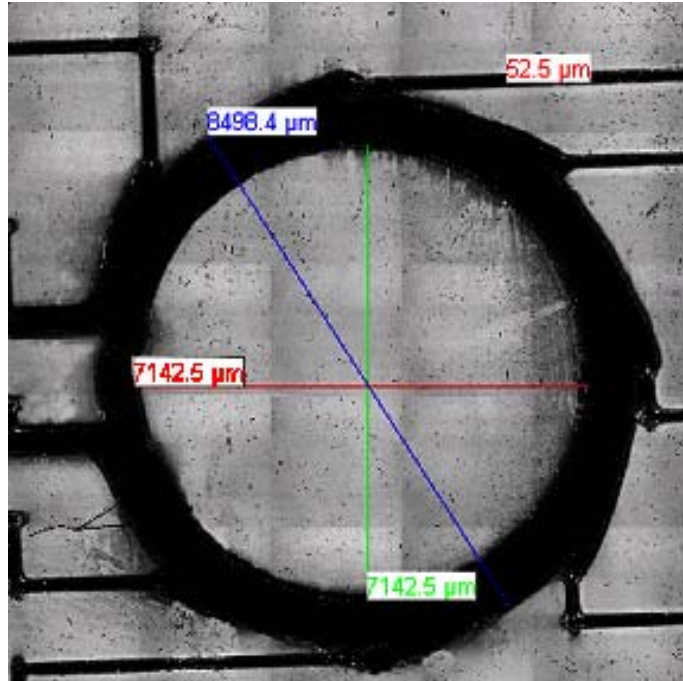
(c) BMP File representation of the first slice (ExExpv1.0 – Machining Module).

Machining Module:

```
bo2
wait all
g90 g1 y2.08 f200
g90 g1 z0 f50
wait all
bo1
g90 g1 z332.685
u178.55 f2000
;mask=Mask1
pattern=Pattern1
wait all
g90 g1 x111.8 y87.15
f2000
psop,1,0,(10000/100)-
50,50
v50=25
v61=12.06
v62=40.2010050251256
psod,0,40.201005025125
6
psof,2,0
dw100
psof,3,x
g91 g1 x=0.2 f=12.06
psof,0
dw100
```

Output parameters:

2. Part program to machine structure as per Design 2. (only part of complete program listed here).



(d) LSCM picture of machined Design 2

Figure C.2: Design 2: Circular Layout - Flow Chart.

Appendix D

Comparison between functionalities and similarities of the main modules described in Charrier et al. [101] approach and this research work.

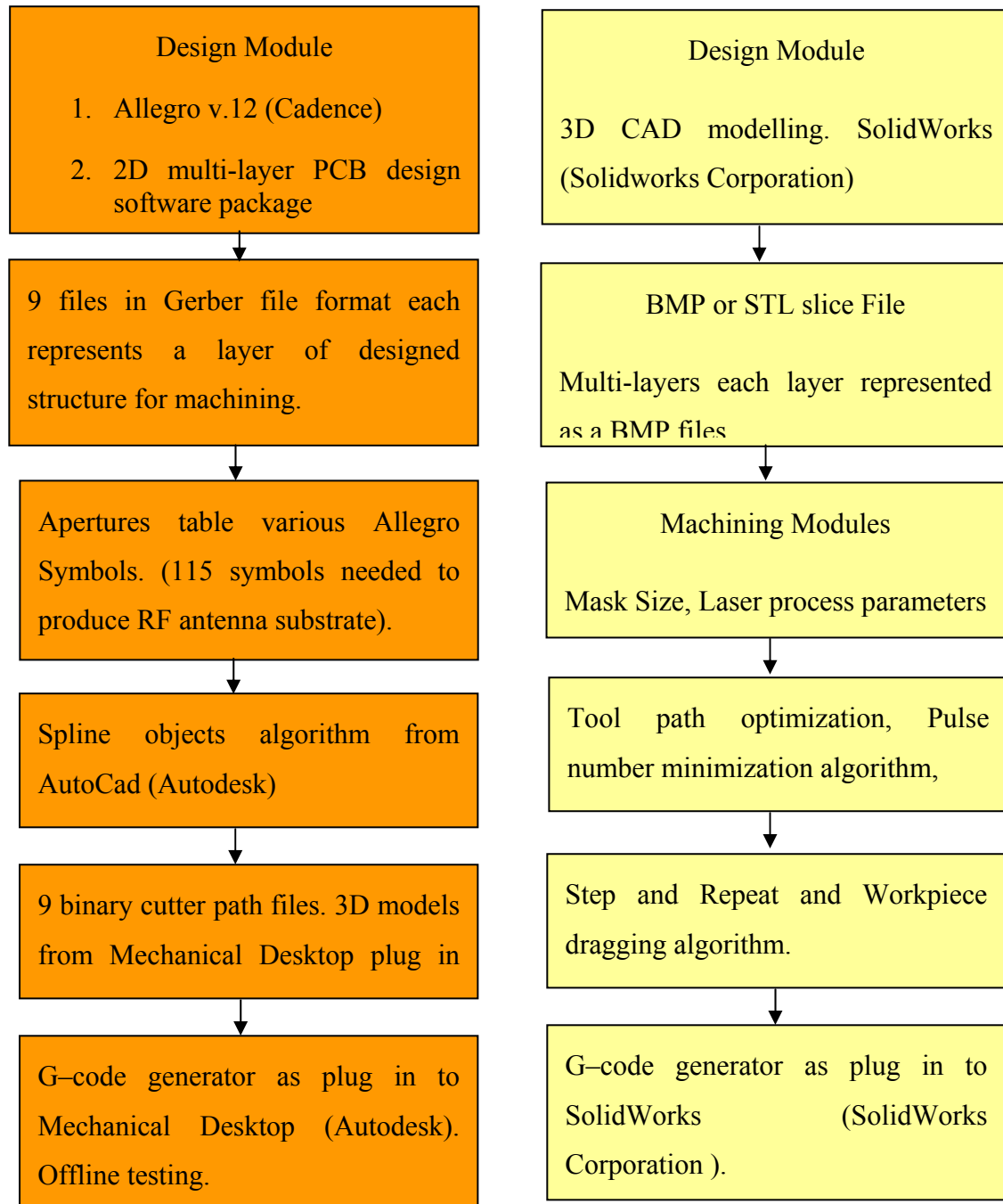


Figure D.1: Comparison between Charrier et al. [101] approach and this research work.